Creating the Electric and Magnetic Fields for the nEDM@SNS Experiment

Thesis by
Marie Blatnik

In Partial Fulfillment of the Requirements for the
Degree of
Doctor of Philosophy in Physics

CALIFORNIA INSTITUTE OF TECHNOLOGY
Pasadena, California

2024
Defended 05/22/2024

Marie Blatnik
ORCID: 0000-0003-3496-0010

ACKNOWLEDGEMENTS

This thesis is dedicated to the "once and future" nEDM@SNS Collaboration. Senior scientists, seasoned engineers, junior faculty, postdoctoral scholars, graduate students, and undergraduate interns from 22+ institutions have all come together (since before 2006) to give their sweat, blood, and brainpower to realize this next-generation nEDM experiment with the power (we think) to surpass the current nEDM limit by two orders of magnitude. We meant what we were doing—we wanted this experiment—and though it never gave us a measurement, it did give us joy, triumph, and so many hard-fought inventions and technological breakthroughs on the way.

And so, firstly, I write this thesis to the future Dr. Marie Blatnik (senior scientist) and that future nEDM collaboration, whatever we might call it and where it will call home, who will need this information. This is an important enough measurement that we will resurrect it when the competing less-sensitive measurements have run their course, and we need new techniques for the next generation of measurements (these techniques).

Secondly, the present-day people that this experiment brought together were nothing short of amazing. I hesitate to call them out by name, as I must leave out so many examples. I want to highlight the humorous wit of Doug Beck, the enriching stories of Brad Plaster, and the essential good sense of Ekaterina Korobkina. Larry Bartoszek is my partner in mischief and mayhem, from Star Trek silliness to jump-scaring our collaborators out of lava-tubes. I especially enjoyed working with Leah Broussard, and Vince Cianciolo, and John Ramsey—each of them were not only powerful in their work and aided mine, but also helped me grow as a person as I wrestled with the duality of physics and motherhood, stress and sleep-deprived triumph, human emotions and physics powerhouse. This collaboration felt like family—a nurturing support system tied by a common goal (by the measurement instead of by blood).

I would like to thank my fellow graduate students Eric Fries, Xuan Sun, and later Raymond Tat and Alston Crowley; from brainstorming, to building, to problem sets, I really appreciate the camaraderie and things I learned with you. I would like to thank Chris Swank, who was not only my postdoc, but also my first friend in Pasadena—thank you for the physics and the adventures. I would also especially like

to thank Alina Aleksandrova, who was, as a powerful physics and instrumentation force as well as a kind and understanding person, such a joy to work with. If I had to move a mountain, I would choose Alina as my teammate.

I would like to thank Jessica, who taught me how to mentor an undergraduate. And to my post-baccalaureate mentee, Theresa Sandborn, who has astounded me with her technical sense and fortitude even before she attends graduate school. She has allowed me to stay active with the Cavallo progress even as I must focus on writing; I am jealous of the graduate school research group that she will choose.

I would especially like to thank everyone who helped me with finishing this dissertation. Thank you, Pat, for listening, motivating me, and keeping me company as I wrote. Thank you to my mom and my sister-in-law, Samantha, who helped me focus on writing by feeding and entertaining my daughter.

The people who impacted me the most include Steven Clayton and Takeyasu Ito, who took me under their wings at Los Alamos National Laboratory to open my mind to high-voltage possibilities, instrumentation and electronics manipulation, and understanding the balance between finding an interesting data artifact and pursuing meaningless puzzles.

The most important person in my physics journey is Brad Filippone, my research advisor. I not only relied on his physics and laboratory experience (and his grant money), but also on his even-keeled wisdom, shrewd sense of priorities, and his never-ending patience. He allowed me the space to grow as a scientist and as a person, while being ever-available when I needed his input. I cannot thank him enough for mentoring me and adopting me into his family, feeding me in every sense of the phrase. His commitment to my success helped me find the confidence in myself that is imperative in becoming an "independent researcher" and surviving the journey from physics-cogwheel to the deep thinker that the "PhD" represents.

And lastly, finally, and most importantly, I would like to thank my husband, Matt Buck. In all of the chaos of graduate school, I discovered my "forever" with whom I made a family of our own. He saw me through this crazy journey—deciding to be my "teammate" even before graduate school began. As I moved to California, he flew out last-minute to be there for me as I experienced mechanical issues in the desert. He uprooted his life and relocated to California three months after I started graduate school. When I went to Los Alamos, he applied for positions there. Funny enough, the day of his interview was the day that I left; he beat me to Los

Alamos permanently by 3 months. He supported me and loved me, as I studied for the qualifying exam, struggled with my work, cried at the pandemic, dragged our newborn daughter to Oak Ridge, commuted between two National Labs, endured the final months of writing angst, and finally graduated.

Financial supports include Caltech and the Virginia Gilloon Graduate Fellowship, the United States Department of Energy (DOE), Office of Science, Office of Nuclear Physics LANLEEDM DE-AC52-06NA25396 and 89233218CNA000001, the Los Alamos National Laboratory Integrated Contract Order No. 4000129433 with Oak Ridge National Laboratory, and the National Science Foundation "Fundamental Studies in Nuclear Physics" Grants 1812340 and 1506459. The DOE Office of Science Graduate Science Research Fellowship (SCGSR) funded my expenses in Oak Ridge, TN, and the Caltech Groce Travel Fund helped support my conference travel.

ABSTRACT

The neutron's electric dipole moment (nEDM) remains one of the most important quantities to measure due to its sensitivity to new sources of CP violation. The nEDM@SNS Collaboration aims to improve this measurement by 2 orders of magnitude by using a novel measurement technique. This thesis focuses on two of the key challenges that this ambitious experiment must address, electrostatically and magnetostatically, respectively: the production of high voltage for the nEDM measurement using a Cavallo multiplier, and the magnetic environment created for the polarization and transmission of the cold neutron beam through the many nested components of the experimental apparatus. A series of Cavallo prototypes is developed, including a room-temperature apparatus and a cryogenic apparatus with two sets of electrodes. The created high voltage will be monitored without physical contact using a designed and prototyped field mill. Transmission and polarization measurements of the cold neutron beam through the nested components of the experimental apparatus are discussed.

PUBLISHED CONTENT AND CONTRIBUTIONS

A list of the author's published articles that contributed to the thesis is below. The first publication is adapted for Chapter 2, and the author's contributions were supplemental to the high voltage system, and editorial to the magnetic field system.

The second publication is adapted for Chapter 3, Sections 3.3, 3.4, and 3.6.1. The author's contributions were co-leading in the data acquisition, analysis, and editing.

[1] M. W. Ahmed et al. "A New Cryogenic Apparatus to Search for the Neutron Electric Dipole Moment". In: *Journal of Instrumentation* 14.11 (Nov. 2019), P11017–P11017. ISSN: 1748-0221. DOI: 10.1088/1748-0221/14/11/P11017.

[2] Steven M. Clayton et al. "Cavallo's Multiplier for in situ Generation of High Voltage". In: *Journal of Instrumentation* 13.05 (May 2018), P05017–P05017. DOI: 10.1088/1748-0221/13/05/P05017.

Three more publications are in process based on Sections 4.1.1, 3.5 (3.5.1–3.5.3), and 3.5.5/3.6. The author is first author and corresponding author on two of these publications, taking a lead in the data acquisition and simulation effort. The third publication, the author takes a supporting role in the construction, data acquisition, and analysis, and a co-leading role in editing.

CONTENTS

LIST OF FIGURES

Chapter 1

BACKGROUND AND MOTIVATION

The universe is made of matter. Do not take this for granted, because whenever we* make matter in an accelerator, it comes with equal parts antimatter: quark-antiquark pairs literally pop out of the vacuum from high energy collisions that turn energy into mass using quark confinement and Einstein's famous $E = \sqrt{(mc^2)^2 + p^2c^2}$.

But why did the Big Bang and our universe's subsequent evolution leave us with only matter? Where is our "equal parts antimatter?" An amount of antimatter was created during the Big Bang—part of the opaque, messy quark gluon plasma [1]—but all the antimatter annihilated to contribute to the cosmic microwave background (which has been redshifting ever since as the universe expands), leaving the extra matter behind. As one looks into the cosmos, one notices that there are no buffer regions where the interstellar medium annihilates and emits annihilation gamma rays in our direction; there are no matter or antimatter domains that one might expect from a balanced universe. The rest of the visible matter in the universe must also be matter like us.

A more rigorous argument [2] shows that any hypothesized antimatter domains are negligible. Riotto and Trodden demonstrate how much combined matter and antimatter would remain if the expansion of the universe simply froze out the post-Big Bang annihilation interactions [2]. Using η_b/η_γ as baryon density and $\eta_{\bar{b}}/\eta_\gamma$ as antibaryon density, the equation for their abundance in equilibrium as a function of temperature T is given by:

$$\frac{\eta_b}{\eta_\gamma} \approx \frac{\eta_{\bar{b}}}{\eta_\gamma} \approx \left(\frac{\mathrm{m}}{\mathrm{T}}\right)^{3/2} e^{\mathrm{m/T}} \tag{1.1}$$

where m is the mass of the baryon. The leftover matter is frozen out when the universe expansion rate (H(T)) outpaces the rate at which particles and antiparticles can interact and annihilate, given by:

$$\Gamma_{annihilation} = \frac{\eta_b}{\eta_\gamma}\langle\sigma|v|\rangle \tag{1.2}$$

where $\langle\sigma|v|\rangle$ is the thermally averaged cross section times the relative velocity [3]. Therefore, we can have a leftover abundance if $\Gamma_{annihilation} <$ H(T) and m/T is small.

*Experimenters running sufficiently high energy particle collision experiments

That transition temperature [found by solving for T in H(T) $\approx \Gamma_{annihilation}(T)$] is about 20 MeV. Plugging T = 20 MeV into Eq. (1.1), one calculates:

$$\frac{\eta_b}{\eta_\gamma} = 10^{-18} \tag{1.3}$$

Compare that with the measured $\frac{\eta_b}{\eta_\gamma}$ on the order of 10^{-10}. A satellite called PLANCK directly measures baryon and cosmic microwave densities, giving us a measurement of their difference, $\frac{\eta_b}{\eta_\gamma}$ - $\frac{\bar{\eta_b}}{\eta_\gamma} \equiv \eta = (6.19 \pm 0.14) \times 10^{-10}$ [4]. Big Bang Nucleosynthesis gives an independent consistency check on this measurement, with limits of $4{\times}10^{-10} < \eta < 7{\times}10^{-10}$ [5]. These come from light element abundances related to the cosmological processes involved with the Big Bang. For example, we know that most of the deuterium in the universe is from the Big Bang due to its low binding energy (2.22 MeV); it requires an environment that favors producing it without immediately destroying it. The only cosmological process that can produce that much deuterium is during Big Bang Nucleosynthesis, but its current abundance is an underestimation of the amount created during the Big Bang because it is very easy to burn. This gives us a conservative estimate for Big Bang abundance, and therefore an upper bound for η. On the other side, Helium-3 (^{3}He) can be made from deuterium and is more difficult to destroy without producing heavy elements in the process; cosmologists estimate that stars astrated the ^{3}He by no more than a factor of 2 [5]. Figuring out how much Helium-3 (plus deuterium) existed before the stars gives a lower bound to η.

There must be a process that creates matter in the universe—an interaction that violates baryon number. The theorist community needed to invent some ideas to produce this baryon asymmetry, all of which need the Sakharov conditions.

1.1 The Sakharov Conditions

The Sakharov Conditions, proposed by their namesake and published in 1967 [6], are three simple ingredients that a theory requires to create a matter-antimatter asymmetry:

1. Process takes place out of thermal equilibrium.
2. Process explicitly violates Baryon number.
3. Process violates C and CP symmetry.

The first two are not difficult to visualize in the Big Bang—For the former, one could easily imagine non-equilibrium within a hyper-inflating hot mess; for the latter, a theorist can create promising ideas about hypothetical baryon-violating mechanics, such as sphalerons [7].

The remaining criterion, C and CP symmetry, refers to discrete operations on a physical system—in our case ones describing the physics of the particles in our universe. It was once thought that the C, P, and T operators (defined below) were all separately symmetries of nature; when you apply one of these operators to a system, the physics would not change. These symmetries are violated when you apply the operator to the system, and the physics changes.

The C operator stands for "charge (conjugation)" and flips all charges in the system to their opposite polarity—essentially turning all particles into their antiparticles. For example, two negative electrons in space repel, with their force described by Coulomb's Law. Applying the C operator to that system, the two electrons become positively charged, but their behavior is described by the exact same math. Therefore, these two electrons have C symmetry.

The P operator stands for "parity" and flips all space in the system to its negative—essentially flipping all vectors to their opposite direction. Many people like to think of "parity" like a mirror, but a mirror only flips two of three axes; parity is a three-dimensional, three-axis mirror. Applying the P operator to the above electron example, the physics of two charged particles looks exactly the same if you switch all the space in the coordinate system to its negative. While this example feels trivial, parity becomes especially important in the context of spin and handedness or chirality—a vector becomes its negative under a parity transformation, but a pseudovector like a particle's spin does not.

C and P violation in the Standard Model takes the form of charged weak interactions. An example is the decay of a muon into an electron and a pair of neutrinos—all of those particles have spin-1/2. One needs to understand chirality for this example: when a particle's spin is aligned with its momentum, it is called a "right handed particle" (a right hand's thumb is the momentum direction, and the curling fingers are the spin), and when a particle's spin is anti-aligned with its momentum, it is called a "left handed" particle. Neutrinos are intrinsically left handed, and antineutrinos are intrinsically right handed (which by themselves also violate C and P).

The muon decay is:

$$\mu \rightarrow e^{L} + \bar{\nu}_{e}^{R} + \nu_{\mu}^{L} \tag{1.4}$$

Note that because the $\bar{\nu_e}$ is right-handed, the electron is left handed, which I have denoted with superscripts here. Applying the C operator to Eq. 1.4, we get:

$$\mu^{+} \rightarrow e^{+L} + \nu_{e}^{R} + \bar{\nu_{\mu}}^{L} \tag{1.5}$$

If we do not ALSO apply the P operator, we now have left-handed antineutrinos and right-handed neutrinos. The above process does not happen in nature; the muon decay violates C symmetry. Applying the P operator to Eq. 1.5:

$$\mu^{+} \rightarrow e^{+R} + \nu_{e}^{L} + \bar{\nu_{\mu}}^{R} \tag{1.6}$$

This is the correct reaction for the μ^+ decay; the muon violates C and P symmetry, but conserves CP symmetry. In fact, Sozzi claims that "the two symmetries [of P and C] are tightly linked in weak interactions [8]" which is very important when measuring C violation as the weak decays are also P violating.

CP violation occurs most prominently in the standard model in the neutral K and B mesons. The 1980 Nobel Prize was awarded for the discovery of CP violation in Kaons [9], where two processes of perfectly CP-symmetric decays were being produced at different rates. The BaBar experiment was created at the Stanford Linear Accelerator to measure the CP violation of B mesons [10].

The third discrete operator, the T operator, flips time to its negative. The physics community assumes that CPT—the application of all three discrete operators—is conserved for all particle physics. There is no evidence yet to the contrary.

A Sakharov Example: The Georgi–Glashow Particle

The Sakharov Conditions give us an indirect way to see the baryogenesis happening without directly measuring it; in order to produce a baryon asymmetry like that which we see in our universe, we need to have interactions out of thermal equilibrium, CP and C violation, and a process that violates baryon number (even for only a very tiny amount). These conditions are not some demand proposed by a particle genesis theory, like proposing a symmetry on a Lagrangian and inspecting the results. Instead, these three conditions are the baseline logic by which all baryogenesis theories are measured. The logic is as follows:

A theorist proposes a process—any hypothesis that results in baryon asymmetry. Let's call it process X or particle X as a nod to the Georgi–Glashow model, a grand unified theory with baryon number violation [11]. The 2nd of the three conditions listed above is the most obvious, and so let us start with imposing that—the violation of baryon number. If we assign X an ambiguous baryon number, such that it can decay to two quarks or one quark, the process breaks baryon number symmetry. The Georgi–Glashow Model breaks baryon conservation by having X go to either two quarks or a quark and a lepton. The model proposes two bosons analogous to the W and Z bosons but calls them X and Y. To keep this logic as simple as possible, let us limit our example to X, and only break baryon and lepton number:

$$X \to qq \quad \text{and} \quad X \to ql \tag{1.7}$$

If these two processes occur, then the antiparticle also decays into the antiparticle of these states:

$$\bar{X} \to \bar{q}\bar{q} \quad \text{and} \quad \bar{X} \to \bar{q}\bar{l} \tag{1.8}$$

Next, we impose small differences of Δ_q between the process and its anti-process to violate C and CP symmetries in the theory. The left hand side process and the right hand side process will be, respectively:

$$\begin{cases} \Gamma_{X\to qq} = (1+\Delta_q)\Gamma_q & \text{and} \quad \Gamma_{X_L\to q_L l_L} = (1-\Delta_l)\Gamma_l \\ \Gamma_{\bar{X}\to \bar{q}\bar{q}} = (1-\Delta_q)\Gamma_q & \text{and} \quad \Gamma_{\bar{X}_R\to \bar{q}_R \bar{l}_R} = (1+\Delta_l)\Gamma_l \end{cases} \tag{1.9}$$

Explicitly, what these four equations in Eq. 1.9 are saying is as follows: Charge symmetry requires that if I convert all of my particles to antiparticles in the Hamiltonian, I should get exactly the same dynamics. Obviously, the theory is violating charge symmetry if the anti-process does not have the same decay width as the process itself—our example here in the left-hand column is violating on the order of 2 Δ_q. Similarly, CP is violated (by similar definition) when the number of left-handed baryons does not equal the same number of right-handed antibaryons. This violation is on the order of 2 Δ_l as codified in the right hand column.

CPT symmetry is believed to be a symmetry of nature, and so in addition to imposing the above four equations, we require $\Gamma_X^{total} = \Gamma_{\bar{X}}^{total}$. This means that when you sum

the two processes and equate them to the sum of the anti-processes, the condition imposed is $\Delta_q \Gamma_x = \Delta_l \Gamma_x$. With this extra constraint, the equations become:

$$\begin{cases} \Gamma_{X\to qq} = (1+\Delta_q)\Gamma_q & \text{and} \quad \Gamma_{X\to ql} = (1-\Delta_q)\Gamma_q \\ \Gamma_{\bar{X}\to \bar{q}\bar{q}} = (1-\Delta_q)\Gamma_q & \text{and} \quad \Gamma_{\bar{X}\to \bar{q}\bar{l}} = (1+\Delta_q)\Gamma_q \end{cases} \tag{1.10}$$

Now we can see that more often ("more often" because the decay width is larger by Δ_q), we get two quarks instead of one quark, and more often (again by Δ_q), we get one antiquark instead of two antiquarks. Summarily, with these 2 conditions, the matter-over-antimatter choice of the universe is a simple side-consequence.

However, there is one more very important condition: the process needs to happen out of equilibrium. In equilibrium, the process $X \to qq$ will happen just as often as $qq \to X$, and so the slight preferences in the cross sections of Δ_q will simply be smeared away, and no asymmetry will manifest.

In conclusion, it is a natural consequence of the three Sakharov Conditions to produce a matter asymmetry in the universe. Where do we find these conditions?

First, it seems safe to assume that during and after the inflationary period of the big bang, particles are not in equilibrium, but go from a color-glass condensate in a very small space, to a quark gluon plasma in a still small but slightly larger space, to hadrons in a large space, etc. It is not a large leap to think that things were occurring on timescales much faster than the relaxation time of the system. Secondly, some amounts of C and CP violations are present in the Standard Model and observed in experiment. Is it sufficient?

Thirdly, the leading mechanisms for baryon number violation employ a mathematical quanta of the electroweak field called a sphaleron, which is a particle in the same way that we call a phonon a particle. These particles mediate the conversion of three antileptons into three baryons—conserving "B - L" but breaking both baryon number (B) and lepton number (L). Similarly to how fermions are treated as excitations of a Dirac field, sphalerons are viewed as excitations in the electroweak field. However, unlike the delta functions that fermion quantum field theory uses for excitations, sphalerons utilize sinusoidal barriers through which the three antileptons essentially "tunnel through" in order to convert their baryon number by three and become baryons. Tunneling in multiples of 3 is required because there are three families of quarks [12].

With the invention of baryon-number violating processes, and hopeful experiments looking for neutrinoless double beta decay and a proton lifetime, a naive graduate student may think that the mystery is solved. The Sakharov Conditions appear to be met; they are not.

1.2 Challenging the Sakharov Conditions

Using the Sakharov Conditions, theorists have proposed many ways to generate the matter asymmetry of our universe. The first problem these hypotheses must overcome involves when the asymmetry materialized. Grand Unified Theories have fallen into disfavor because all the forces were unified before inflation (10^{-35} s), which would then "blow the asymmetry away [13]." Kolb and Turner claim that treating the small excess of baryons as an "initial condition" is incompatible with the cosmological inflation [14]. Theories of inflation have been able to predict the temperature anisotropies in the sky, and this convinced the majority of scientists that inflation happened despite not having an understood quantum field theory mechanism for it.

Two popular theories include the leptogenesis model and the electroweak baryogenesis model, both of which produce an antimatter asymmetry at (10^{-11} s). The leptogenesis model involves adding extra Majorana right-handed neutrinos that do not interact with the W or Z bosons, but only with the Higgs boson instead [15]. A Majorana particle is by definition its own antiparticle; the idea is to create a lepton asymmetry by making its Higgs interaction CP-violating, and then to use sphalerons to convert the leptons into baryons. This theory could also explain why the observed neutrino masses are so small [16], but these theories struggle to produce testable predictions. Finding Majorana neutrinos through neutrinoless double beta decay experiments could contribute to this theory's credibility [17].

The electroweak baryogenesis model includes an electroweak phase transition as the universe cooled/expanded, where sphaleron transitions happen easily in the symmetric electroweak phase, but are suppressed when the electroweak symmetry is broken [13]. Bubble walls between the two phases bias the sphalerons towards matter over antimatter, and experimentally found CP violation could inform these wall interactions. Sadly, the hypothesized first order electroweak phase transition may not exist; calculations of the phase transition require the mass of the Higgs Boson to be less than 80 GeV [18]. The heavy Higgs Boson measured in our universe pushes the transition to 2nd order, with no temperature-sensitive barrier

between the local and absolute minima of the finite temperature effective potential. The bubbles cannot form, killing two out of three Sakharov conditions.

1.2.1 Where is Baryon Number Violation?

As a fledgling experimentalist in a class on quantum field theory, I laughed at my professor when he told us that he believed in proton decay. However, my short-sighted derision was incompatible with the fact that our universe is entirely made out of matter.

Most processes that theorists hypothesize for baryon symmetry breaking have the natural consequence that the proton is unstable at some level. Experiments like "Super-K" (super-Kamiokande, in Japan), an enormous Cherenkov detector, were used to put limits on hopeful hypothetical processes like dark matter and proton decay. They measured a proton half-life > 1.67 $\times 10^{34}$ years [19]. For comparison, the age of the universe is 1.4 x 10^{10} years.

The experiments that "simulate" the hot time post-Big Bang (10^{-6} s) cannot get hot enough to produce measurable baryon symmetry breaking. Experiments taking place at the LHC and RHIC (the Relativistic Heavy Ion Collider at Brookhaven National Lab in New York) smash heavy ions like gold and lead together at high speeds to "melt" the nucleons into a quark-gluon plasma (QGP) on the order of 10^{12}K [20], falling short of the 10^{27}K expected by the unification models [21]. The rehadronization of this new state of matter therefore produces an equal amount of matter and antimatter. Even in other deep inelastic scattering experiments at these large accelerators, the mesons and exotic hadrons produced conserve baryon number. Baryon number MUST have been violated at some point because matter is everywhere, but no way has been conceived to directly see the process happen.

While proton decay occurs in Grand Unified Theories (GUTs), large detectors with many protons search for the signal. The source of proton decay is not observable in accelerator-based experiments. Outside of our matter excess, no one has ever seen—directly or indirectly—evidence of a process that violates Baryon number.

1.2.2 Insufficient CP Violation

Using the amount of matter that we have seen in the universe through cosmological studies, the baryon asymmetry produced through our "X-decay" model above (or, more accurately, for the X and Y mesons in the Georgi–Glashow model) is orders of magnitude greater than that which the C and CP violation calculated from the

Standard Model would produce [13]. Somehow, there is not enough C and CP violation to account for our universe.

There are three places in the Standard Model that can create CP violation:

- A complex phase in the Cabibbo–Kobayashi–Maskawa matrix (CKM matrix): The CKM matrix describes how quarks mix—the fundamental driving description of the weak force coupling. This is the complex phase driving the observed CP violation in the neutral K and B mesons.
- A complex phase in the Pontecorvo–Maki–Nakagawa–Sakata matrix (PNMS matrix): The PNMS matrix describes how neutrinos mix; neutrinos are difficult to measure and so their matrix has large error bars, but experiments show that they mix significantly more than quarks. The complex phase measured here, while error bars are large, favors CP violation for only one sequence of the neutrino masses (called the "normal ordering"). [22]
- Terms in the quantum chromodynamics (QCD) Lagrangian that suggest the strong force should violate CP. However, no measurements have found any CP violation in quantum chromodynamics.

The Jarlskog determinant (A_{CP}) [23] [24] [13] is a convenient way to quantify the amount of CP violation in the CKM matrix, and its concept can be applied to the PNMS matrix as well. It takes the form of:

$$A_{CP} \propto J_{CP} \frac{\Delta m^2}{T^2} \tag{1.11}$$

where $J_{CP} = \mathrm{Im}(V_{us} V_{cb} V_{ub}^* V_{cs}^*)$ is the Jarlskog invariant, which vanishes proportionally to the area of the unitarity triangle when CP violation in the standard model goes to zero. The Δm^2 are the differences in quark masses over their generations; $\Delta m^2 = (m_u^2 - m_c^2)(m_c^2 - m_t^2)(m_t^2 - m_u^2)(m_d^2 - m_s^2)(m_s^2 - m_b^2)(m_b^2 - m_d^2)$ [23].

At the transition temperature of our particle-generating theories, the calculated A_{CP} is on the order of 10^{-17} [13]. Theorists treat this as a convenient "measure" of the amount of CP violation, expecting it to be of the order of our baryon asymmetry [13]. However, our baryon asymmetry is on the order of 10^{-10}; there is not enough CP violation in the standard model. We turn to our theorists to create more CP-violating ideas.

1.3 A Theory Smorgasbord

The theorists invented all sorts of ways to tweak the amount of CP violation in the standard model, which we will quantify as φ^{CP} below. Maybe there are multiple Higgs bosons. Maybe there are supersymmetric complements to every single particle in the standard model. Maybe there are more hidden scalar particles. While none of these things have been observed, we need SOMETHING to tweak this parameter to get the baryonic density η to agree with reality. Consequently, every time we tweak η, the neutron could acquire a larger electric dipole moment—just enough to put it just barely in the reach of measurable:

$$\begin{aligned} \eta &= \sum_j G_j[m_\alpha, g_\alpha] \sin \varphi_j^{\mathrm{CP}} \\ d_n &= \sum_i F_i[m_\alpha, g_\alpha] \sin \varphi_i^{\mathrm{CP}} \end{aligned} \tag{1.12}$$

For example, the nEDM predicted with supersymmetry falls in the range 10^{-23} to 10^{-29} e cm, and the Multi-Higgs theory puts it in the range of 10^{-25} to 10^{-28} e cm [25]. The beauty of Electroweak Baryogenesis is that it gives us precisely these sorts of fingerprints to see the CP-violating interactions in action.

Not only that, but the physics of a neutron with both an electric and magnetic dipole moment precessing in electric and magnetic fields violates CP symmetry. The result is a race to measure an nEDM to the highest sensitivity.

Other "fingerprint" experiments include searches for electric dipole moments in other fundamental particles and magnetic quadrupole moments in nuclei. A misconception to avoid is water's dipole moment; it has an induced electric dipole moment created by its atoms, NOT the CP-violating physics for which we search. On the other hand, a detection of an electric dipole moment in a fundamental particle such as an electron is significant [26]. An example of a search for magnetic quadrupoles that are CP-significant is the search for a magnetic quadrupole moment in a nucleus, such as in an optically trapped YbOH experiment [27].

1.4 An Experimental Smorgasbord

It is conceptually simple to measure an nEDM:

1. Polarize some neutrons.

2. Precess them under the influence of a magnetic field: $H_o = \mu B$

3. Add or flip a suitably large electric field, and see if the rate of precession changes: $H = H_o + d_n E$

Between the compelling theoretical motivation, and the above simplicity, it is no wonder that so many scientists want to measure the nEDM. However, the more precision we require, the more difficult the measurement actually gets. Recall that our desired nEDM sensitivity is of order of 10^{-28} e cm. A neutron's diameter is on the order of a femtometer (10^{-13} cm), so such a dipole is equivalent to a positive and negative quark(s) separation of 10^{-15}th the physical size of the neutron. Such a tiny number breeds hardships.

These hardships can be somewhat quantified by the statistical uncertainty of an nEDM measurement:

$$\delta = \frac{\hbar/4}{\sqrt{n}EPT} \tag{1.13}$$

where n, E, P, and T are the number of neutrons, electric field, the polarization, and the transverse coherence time, respectively. All nEDM experiments try for high sensitivity by maximizing the denominator of this quantity, making it a great figure of merit by which to judge nEDM experiments. The other set of hardships are systematic errors, which are characterized by the experimental technique used.

The first measurement of the nEDM ($< 10^{-20}$) came before this theoretical motivation when discrete symmetries were getting scrutinized, using a beam of neutrons from Oak Ridge National Lab's Graphite Reactor [28]. Beam measurements like this were conducted over the next 30 years, hitting the limit of $< 3 * 10^{-24}$ e cm[29]. These experiments were limited by the measurement time and velocity of the neutrons, because the motional magnetic field v $\times$ E will not perfectly align with the applied magnetic field B. This results in different precession rates when the fields are flipped, obscuring the nEDM with a powerful systematic error.

Since then, nEDM experiments have increased measurement times and largely suppressed the v $\times$ E systematic error by moving from more cold beams to ultracold neutrons. Ultracold neutrons (UCN) are free neutrons that have been cooled to the millikelvin range by a superthermal process. Their de Broglie wavelengths are long enough to interact with material surfaces, allowing them to be totally internally reflected and contained ("bottled") for long observations. Their ideal gas behavior results in an average velocity of 0 m/s, and a velocity perpendicular to the magnetic field in the trap of a few m/s. (It is that perpendicular velocity that contributes to the v $\times$ E systematic error [30]).

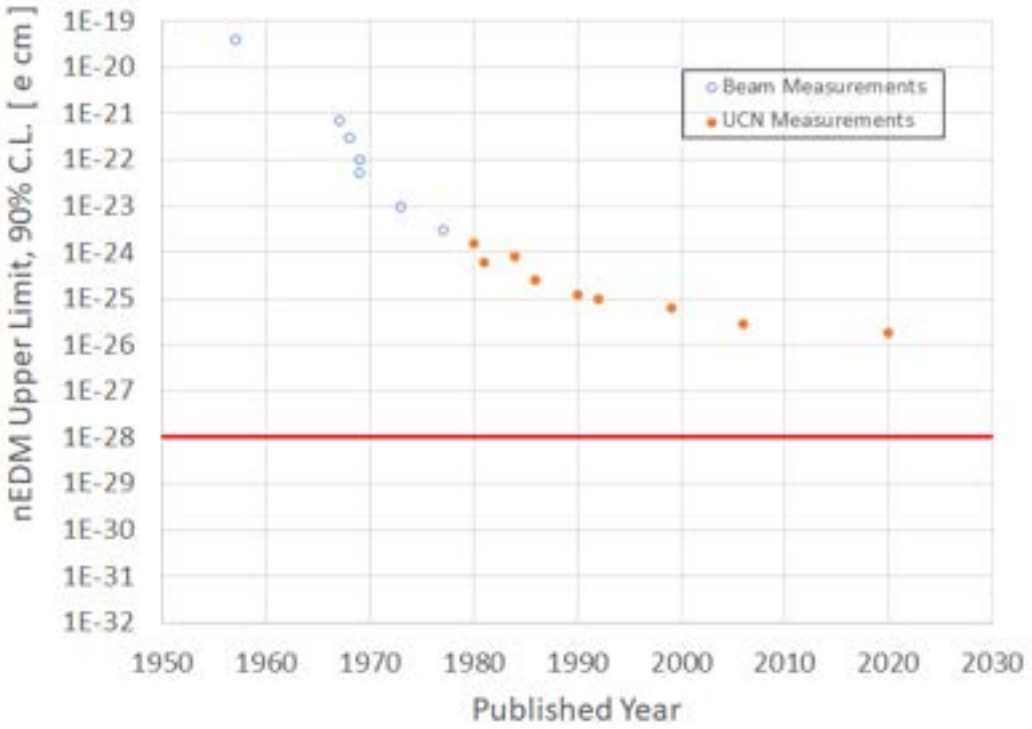

Figure 1.1: History of the nEDM limit. The published nEDM upper limit, at the 90% confidence level, across several collaborative experiments include beam experiments at Oak Ridge National Laboratory and Brookhaven National Laboratory, and UCN experiments at the Paul Scherrer Institut and the Institut Laue–Langevin. A compilation of these published results (minus [31]) can be found at [36].

The nEDM experiment at the Paul Scherrer Institute (PSI) recently won the record for the most sensitive measurement from the Institut Laue–Langevin (ILL), with a measurement of 1.8×10^{-26} e cm [31] to ILL's 2.9×10^{-26} e cm [32]. More UCN experiments continue to develop, attempting to overcome the biggest limitation of these types of nEDM measurements: statistics. The number of ultracold neutrons produced is low, and the number transported and trapped in the experimental measurement cell even less. The PSI experiment is adding another measurement cell to double their neutrons, forming the n2EDM collaboration [33]. The Los Alamos's Neutron Science Center became motivated to measure the nEDM with their source upgrades [34], and TRIUMF (Canada's TRI-University Meson Facility) is also creating what they hope to be the greatest UCN source in the world [35]. All these collaborative efforts hope to push the nEDM sensitivity by another order of magnitude.

The progress in the nEDM upper limit over the years is graphed in Fig. 1.1. The white space between 10^{-26} and 10^{-32} e cm is provocative, as it represents the gap between the current measurements and the standard model prediction. In between these two values lay the beyond-the-Standard-Model predictions of the theorists.

As the trend of the measurements in Fig. 1.1 seems to flatten, it becomes clear that the next huge leap in nEDM measurements must involve novel, clever techniques to beat down the systematic errors and the statistical uncertainty. Doing this, the nEDM@SNS experiment aims to measure the nEDM to the order of 10^{-28} e cm, depicted as a red line in the graph.

Chapter 2

THE NEDM EXPERIMENT

The nEDM@SNS experiment[a] is the only fully cryogenic neutron electric dipole moment (nEDM) experiment in the world[b]; our collaboration aims to leverage the advantages of cryogenics to gain two extra orders of magnitude of sensitivity on the current nEDM limits set by the room-temperature competitors discussed at the end of the previous chapter.

This is a large endeavor, with 23 institutions[c] coming together to create nine quasi-independent, interwoven subsystems around two 3000 cm^3 measurement cells (of dimensions 10 cm × 40 cm × 7.5 cm). These small cells and related subsystems are enclosed or attached to a ≈4 m tall cryostat inside of a ≈7 m (almost 3 story) magnetic shielding enclosure. The effort is large enough to require a second external building at the fundamental neutron physics beamline at the Spallation Neutron Source (SNS), and a 40 m cold neutron guide bringing the neutrons into the apparatus, depicted in Fig. 2.1.

The impetus for this apparatus (in addition to the cryogenic advantages to achieve the greatest nEDM sensitivity) was Golub's and Lamoreaux's idea for a novel measurement technique [40]: "direct detection" using the spin-dependent capture cross section of neutrons in ^{3}He [41]:

$$n + {}^3He \rightarrow p + {}^3H + 765\ keV \tag{2.1}$$

Neutrons have a gyromagnetic ratio of 29 MHz/T [42], and ^{3}He nuclei have a gyromagnetic ratio of 32 MHz/T [43]. Under the same uniform magnetic field B_0, a coherent polarized population of neutrons and ^{3}He atoms perpendicular to that field will precess at slightly different rates. For our B_0 field of 3μT, this is ≈90 Hz and ≈100 Hz, respectively. The capture cross section is maximized when the spins of the neutrons are anti-aligned with the ^{3}He spins, and minimized when they are aligned, producing a beat frequency of released protons and tritons:

[a] nEDM@SNS = neutron Electric Dipole Moment measurement at the Spallation Neutron Source at Oak Ridge National Laboratory

[b] A previous cryogenic nEDM experiment called "CryoEDM" [37] was commissioning at the Institut Laue–Langevin in Grenoble before funding ran out[38]. Its previous home on the beamline now belongs to the SuperSUN ultracold neutron source [39]

[c] A list at https://nedm.caltech.edu/collaborators, plus the newest, Georgia Institute of Technology

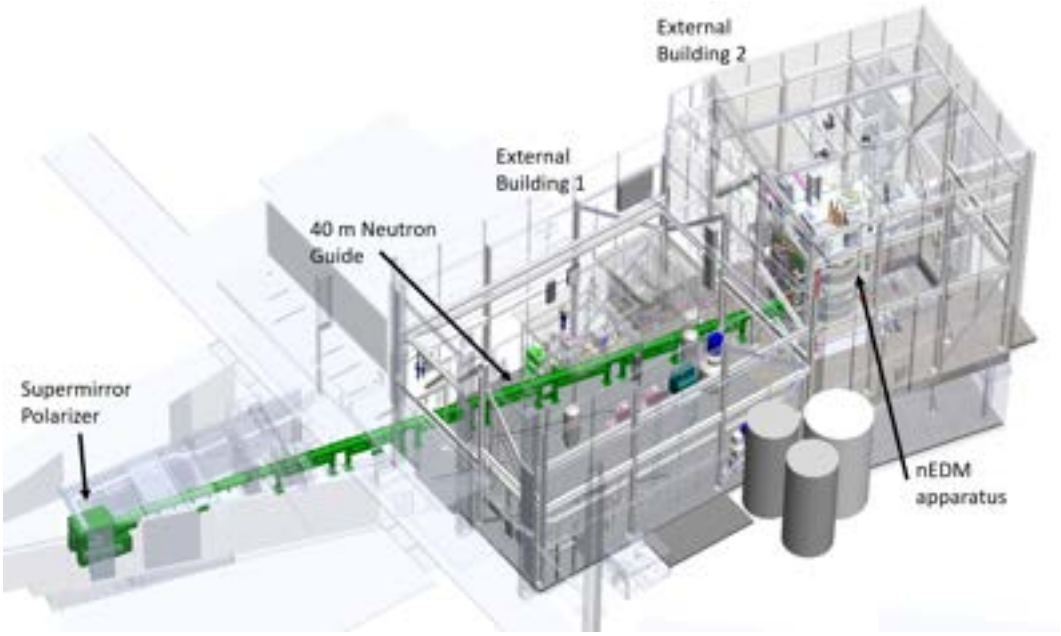

Figure 2.1: Overview of the nEDM@SNS experiment at Beamline 13 of the Spallation Neutron Source. Note that two external buildings are required off of the beamline itself, with the nEDM apparatus housed in the 2nd building. Original figure by Wolfgang Korsch of the nEDM@SNS collaboration, provided by Kavish Imam.

$$\sin(\omega_n t) + \sin(\omega_3 t) = 2\cos(\frac{\omega_n - \omega_3}{2})\sin(\frac{\omega_n + \omega_3}{2}) \tag{2.2}$$

where ω_n and ω_3 are the rotational frequencies of the neutrons and ^{3}He, respectively.

The helium scintillates with each proton and triton, releasing their leftover energy of 765 keV in the measurement cell. The goal is to monitor that light as the measurement signal of the experiment: does the scintillation beat frequency shift as an electric field is applied and flipped?

The measurement cells have a dual duty in the experiment: they must trap both the neutrons and the ^{3}He for a time in excess of 600 s, but they also act as the first collection/transition step in the process of measuring the scintillation light. Made of acrylic to be nonmagnetic and transparent to certain wavelengths of light, they are coated in deuterated Tetraphenyl Butadiene to shift the scintillation wavelengths from $\sim$ 80 nm to $\sim$ 400 nm. Wavelength shifting fibers further lengthen the wavelength of light on its way to be read out by Silicon Photomultipliers. This effort is spearheaded by a team including Montclair University. Even more care needs to be taken to ensure that neither the neutrons nor the helium depolarize (requiring an

additional coating of deuterated polystyrene), and that the cells are leak-tight with long trap times (requiring deuteration to prevent neutron upscattering) [44]. The final signal is simulated in Fig. 2.2 a.

The "great commandment" of precision science (according to Nobel Prize Winner Arthur Schawlow), is "Never measure anything but frequency" [45] because the electronics world is built on frequency. This technique directly measures not just a frequency, but a beat frequency.

That beat frequency can then be used to calculate the neutron precession frequency with the addition of the ^{3}He precession frequency measurement. The ^{3}He atoms have electron clouds that shield their nuclei from experiencing the change of the electric field, yielding a constant frequency (with respect to electric field) that can be directly detected with sensitive magnetic monitors, in this case the Superconducting Quantum Interference Devices (SQUIDs) developed by Los Alamos National Lab [46]. This means that they can be used to correct for any drift and irregularities in the magnetic field environment (called a "comagnetometer") in addition to calculating the neutron's precession frequency.

Contrast this with room temperature experiments, which use the Ramsey Separated Oscillating Field Method (RSOFM). This method involves coherent polarized neutrons in a magnetic field initially aligned with their spins, and then using magnetic "tipping" pulses to control the amount of time they spend precessing in that field. The idea is to start the neutrons parallel to the field, and then use the magnetic pulse to tip the neutrons perpendicular to that field to begin precessing. After some time, the magnetic pulse is applied again to "complete" or "reverse" the flip, depending on how much the neutron has precessed in the perpendicular plane. If the time between tipping pulses is "on resonance" or equal to (or a multiple of) the precession time of the neutron, the two half-pulses will add up to a full spin flip of the neutron. If the time between tipping pulses is half the neutron precession time, the neutron will not have flipped its spin. Intermediate tipping frequencies quantum-mechanically choose some neutrons to flip and others to return to their original spin state, resulting in "Ramsey fringes" depicted in Fig. 2.2 b [47].

These Ramsey fringes are the signal for other nEDM experiments; when an electric field is applied, do the fringes shift? While our experiment measures a frequency in the signal from silicon photomultipliers (SiPMs), these experiments apply a frequency and measure spin-state-dependent neutron counts—they are still effectively probing a frequency. Furthermore, the signal of an nEDM for them is also a fre-

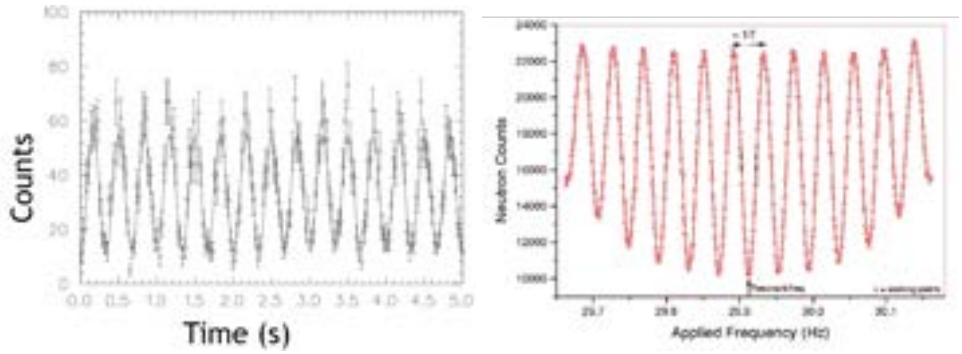

Figure 2.2:
a) Left: A Monte Carlo calculation simulating the silicon photomultiplier output of the nEDM free precession mode; the sinusoid's frequency is the beat frequency of the neutron-^{3}He precession frequencies. Courtesy of Professor B. Filippone.
b) Right: Sample Ramsey Fringes for a RSOFM-type experiment (used by all other UCN nEDM experiments). Taken from Wong [47].

quency shift. However, the measurement of a full set of fringes takes many neutron runs, and production data requires at least four spin-flip frequency runs [31].

One may imagine that statistical uncertainty associated with populating Ramsey fringes ($1/\sqrt{n}$) are intuitively larger than a well-measured beat frequency in statistics-starved ultracold neutron physics. However, requiring the precession frequency measurement of ^{3}He detracts somewhat from that advantage. For this reason, Golub and Lamoreaux[40] [48] invented a way to force the neutrons and ^{3}He to precess at the same frequency using AC magnetic fields, called critical dressing. The concept is to tip the neutrons and the ^{3}He such that the effective spin projected perpendicular to the B0 field is the same size—$S_n \times B_0 = S_3 \times B_0$—based on the dressed spin method of Harouche and Cohen-Tannoudji [49]. With both methods, we not only have a cross-check of results, but we have different sensitivities to some of the systematic uncertainties.

This novel method requires a measurement cell with a maximum number of polarized neutrons and ^{3}He atoms, surrounded by well-controlled and uniform magnetic fields to manipulate the neutron and ^{3}He spins, and a huge electric field. An nEDM's statistical uncertainty is dependent on the number of neutrons measured (n), the coherent measurement time (T), and the electric field applied (E):

$$\delta \propto \frac{1}{\sqrt{n}ET} \tag{2.3}$$

Cryogens are employed to enhance all of these quantities.

2.1 Maximize the Number of Neutrons and Measurement Time

Recall from Chapter 1 that Ultracold neutrons (UCN) are free neutrons that have been cooled to velocities corresponding to the millikelvin range by a superthermal process to make them maximally controllable—trappable, easily polarized with superconducting magnets, and velocity-controlled with gravity. Ultracold neutrons are usually created externally to an experiment and then transported through neutron guides to the measurement apparatus, suffering significant population losses on their journey. However, the cryogenic nature of the experiment allows us to downscatter cold neutrons in situ in superfluid helium, creating the ultracold neutrons directly in the measurement cell and suffering no transport losses.

Pure ^{4}He has essentially no capture cross section with neutrons, and superfluid helium downscatters 8.9 angstrom neutrons at 1 atm by a single-phonon process [50] [51]. Phonons and rotons are quanta of motion inside a medium—here, the motion states of the superfluid helium. Below a momentum of 1 Å^{-1}, the only motion states available to superfluid helium are phonons[52]. A cold neutron of about 8.9 Å has the correct momentum to excite a phonon in the helium, depositing effectively all its energy into the helium and becoming a UCN. That phonon is then frozen out of the helium, preventing the reverse process. Multiphonon scattering also contributes to UCN production significantly less (about a factor of three less) than the single-phonon process [53].

Finally, this process is also pressure dependent, with higher pressures suppressing UCN production and squeezing the phonon-roton curve to require higher momentum cold neutrons for the single-phonon process [53]. However, this effect is negligible for us as we operate under a few atmospheres.

Furthermore, neutron losses also occur due to upscattering on impurities such as gasses in our competitors' vacuum, or on the walls of the experiment. By running the experiment at a fraction of a kelvin in polarized ^{3}He, we minimize these losses.

The neutrons that will downscatter into UCN come from the Fundamental Physics Cold Neutron Beamline at the Spallation Neutron Source at Oak Ridge National Laboratory [54], also known as Beamline 13. These neutrons are produced by a pulsed 1.8 MW, 1 GeV proton linear accelerator beam impinging on a liquid mercury target [55], then moderated by water followed by supercritical hydrogen to about 20 K [54]. The beamline contains two choppers to limit the number of higher energy neutrons outside of the downscattering envelope. They will then encounter a supermirror polarizer, such as the one utilized in a previous experiment

[56]. A 40-m engineered beam guide will bring these neutrons to the experimental apparatus, dividing them between two measurement cells full of the helium needed to downscatter.

The population density of neutrons in the cell are:

$$\rho_{UCN} = R\tau_{UCN} \tag{2.4}$$

where τ_{UCN} is the total lifetime of the neutrons in the cell, including their beta decay, capture onto ^{3}He, and upscattering or wall losses. R is the rate of production of UCN, based on the flux with respect to energy of the cold neutron beam. The more flux at the desired cold neutron energies, the more neutrons downscattered into the measurement cell.

2.2 Maximize the Electric Field

Eq. 2.3 shows that the statistical uncertainty of an nEDM measurement is inversely proportional to electric field. The current leading limit from PSI achieved 11 kV/cm across their measurement cell in vacuum [31]. While other mediums can withstand higher electric fields than vacuum, it is imperative that the medium does not upscatter or capture the stored neutrons in the apparatus.

Not only is liquid helium useful for UCN generation, but it can also withstand high electric fields as demonstrated by Phan [57]. Tolerating 120 kV/cm in the apparatus allows us to put 75 kV/cm inside the measurement cell. For our measurement cell electrodes, this requires 650 kV on the high voltage electrode.

While it sounds simple, a high voltage feedthrough for this electrode is problematic for two reasons: its heat load on the sub-kelvin region especially by the leakage currents and also by thermal conduction from outside the cryostat, and those large leakage currents producing magnetic fields. Eddy currents from the magnetic dressing fields and suitable nonmagnetic materials could also be a problem in the design. Instead, an electrostatic induction machine invented in the 18th Century [58] called the Cavallo Multiplier, can provide the required voltage for this nEDM measurement [59].

Furthermore, the eddy currents plaguing a hypothetical feedthrough would also plague a set of metal electrodes. Because the nEDM experiment uses sinusoidally driven magnetic fields to control the spin states of the neutrons and ^{3}He [60] (including critical dressing), a set of metal electrodes will create competing magnetic fields and a significant heat load on the sub-kelvin region near the measurement cell.

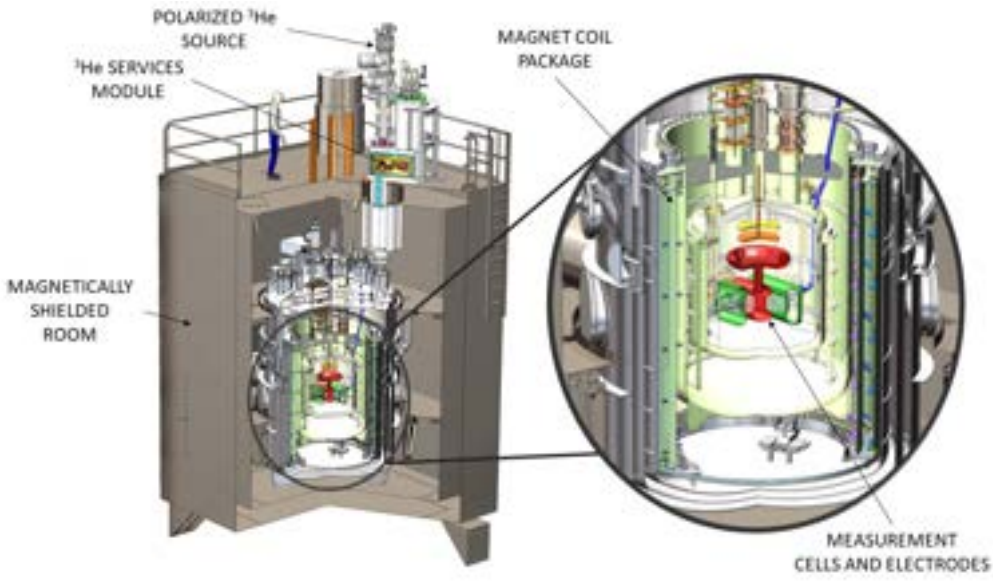

Figure 2.3: Overview of the nEDM@SNS apparatus. The magnetic shield enclosure surrounds the large cryostat, which houses the magnet package and central system containing the measurement cells and the colorfully depicted electrodes (yellow, orange, red, and green). Original CAD by John Ramsey of the nEDM@SNS collaboration, republished from [60].

Therefore, the Cavallo electrodes for the nEDM experiment will be created out of non-conducting composite with a thin alloy coating with a high resistivity. This will limit the eddy currents, thereby limiting the heating and the stray magnetic fields. This thin resistive coating is very delicate, so these electrodes need to be protected from any damaging electrical discharges. All of these constraints and other design considerations are outlined in the next chapter; the goal is to create our electric fields with a magnetically pure and minimally heating design.

2.3 Control the Magnetic Fields

At the beginning of this chapter, a description of the scale of this project contrasted the size of the measurement cell with the size of the magnetic shielding enclosure. This huge disparity underlines the effort required to ensure that the experiment takes place in a magnetically quiet, controlled environment—from shielding the entirety of the apparatus (including the dilution refrigerators above the cryogenic magnet) from earth's magnetic field and any changing magnetic disturbance, to maintaining the high polarization of the ^{3}He along its entire load-unload cycle, to careful spin manipulation inside of the cryomagnet, to minimizing a key systematic effect.

The apparatus is depicted in Fig. 2.3 with the electrodes colorfully depicted around

the measurement cells. The magnetic shield enclosure is only two layers (as opposed to competitors' 5–7 layers) due to the large magnetic shielding afforded by the superconducting lead shield inside of the magnet cryostat. In the heart of the cryostat,

Magnetic disturbances give rise to systematic errors. The most concerning systematic error is the geometric phase effect because it mimics the same linear electric field dependence of a true neutron electric dipole moment. Also known as the Bloch–Siegert Induced False EDM, this false EDM arises due to the interaction of the motional magnetic field ($v \times E$) of the neutron with magnetic field gradients in the neutron's sample volume [60]. To suppress this systematic error and achieve the target nEDM sensitivity on the order of 10^{-28} e cm, magnetic field gradients in the volume need be less than 10^{-11} T/cm. The B0 magnet package is equipped with shim coils to fine-tune the magnetic field gradient, and an array of magnetic field probes, designed and created by Alina Aleksandrova, surrounds the heart of the cryostat to monitor the magnetic field and its gradients [61].

Another leading systematic error is due to the leakage currents mentioned in the previous section. Not only can leakage currents create magnetic field disturbances that can affect the experienced magnetic field in the measurement region, but temperature gradients in the cells can create a nonuniform ^{3}He population. A population gradient will contribute to the pseudo-magnetic field experienced by the neutrons [40], and also increase the statistical uncertainty by decreasing coherence times; we aim for leakage currents less than 1 pA [60].

The manipulation of the magnetic field environment is done by not only the magnetic shielding, but also by the cryogenic magnet package surrounding the central detector system (the measurement cells, the electrodes, etc.). It includes the B0 magnet of 3 μT inside the superconducting lead shield, its flux return, the AC spin-dress coils and copper AC shield, and a <6 K helium cooling system. Chapter 4 discusses these systems and an effort to measure their effect on the incident cold neutron beam passing through them.

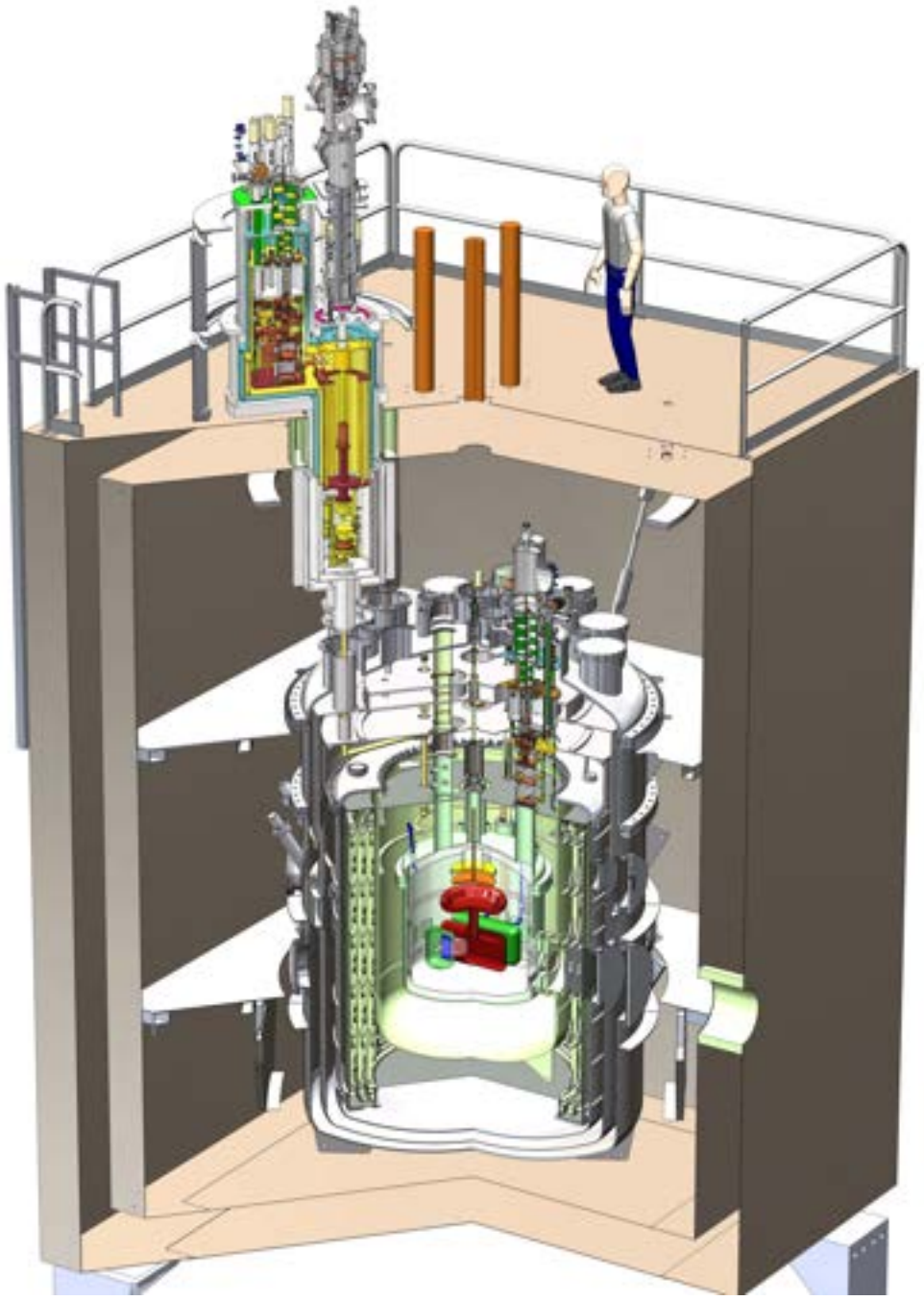

Figure 2.4: Overview of the nEDM@SNS apparatus, enlarged from Fig. 2.3. Original CAD by John Ramsey of the nEDM@SNS collaboration, republished from [60].

Chapter 3

MANIPULATING THE ELECTRIC FIELDS

3.1 Historical Introduction

The electrostatic voltage multiplication device known as the "Cavallo apparatus" or "Cavallo multiplier" dates back to the Scientific Revolution, a period roughly spanning the 16th through the 18th centuries where the conventional observation-driven Scientific Method [62] was used to advance knowledge from gravity [63], to calculus [64], and most importantly for this section—electricity [63]. Electrical knowledge advanced from the ancient observation that amber, when rubbed, can attract light objects [65], to William Gilbert's 1600 publication of a list of "electrifiable materials" in De Magnete [66], to using voltaic electricity for street lights and electric motors [65].

Tiberius Cavallo lived during a slice of this period (from 1749 to 1809 [67]), where electricity was being studied extensively but had not yet reached a level of practicality in daily life [65]. Charles Du Fay had already shown that electricity could be positive or negative [68], and Jean-Antoine Nollet and Stephen Gray had already demonstrated electrical induction [65]. Cavallo summarized the understood electrical phenomena of his time in a several-volume textbook, and described the "two well-known laws of Electricity" as "a body presented to another body electrified, acquires thereby the contrary electricity, proved it be made [to] communicate with other bodies or with the earth; and secondly, that the capacity of a body for holding electricity, is increased by being placed with its surface contiguous to another body not insulated. [58]" In addition to writing this treatise, Cavallo improved upon the machines he described in his book.

While Benjamin Franklin demonstrated that lightning was electricity when Cavallo was 3 years old [65], the sources of electricity for study during Cavallo's lifetime were either triboelectric or produced by weak chemical batteries. Otto von Guericke's electrostatic machine was a sulfur ball rotating against a cloth [67]. In 1800, Volta wrote about his copper-zinc-salt "piles" [69], and silver-zinc batteries also made it into Cavallo's Treatise [58]. Both of these methods produced weak amounts of electricity; sensitive electrometers and voltage multiplication schemes were useful. Cavallo improved on both [58], calling "the Doubler . . . at present by some persons,

considered . . . one of the most useful instruments in electricity [58]."

Cavallo's multiplication scheme was based on Bennett's doubler, which he discussed at length in his Treatise [58]. He claimed that a "defect arose" in the physical touching of the initially charged electrode and the transfer electrode. The apparatus bearing his name fixes that "defect" by allowing the two electrodes to become close but not touch [58]. He saw that "the effect [of the multiplier on the voltage] seemed to be somewhat more constant, yet it was far from being uniform and certain [58]."

Other physicists then improved on his design. William Nicholson animated the Cavallo apparatus in 1788 by placing the plates on a winch [70] [58], and in 1804 Wilson published a "compound Electrical Instrument for condensing and doubling [71]" which worked like a double-Cavallo apparatus, among its configurations of six plates. This machine could accumulate charge at a much larger multiplication rate than Bennett's Doubler or Cavallo's apparatus [71].

Unlike Cavallo or his Scientific Revolution compatriots, we now have the technology to predict the apparatus's voltage behavior using measured capacitances, a precise initial voltage, and an actuator to move the transfer electrode. Furthermore, Cavallo's apparatus is still relevant today as we intend to implement the device in the nEDM@SNS experiment to produce the required high voltage.

3.2 Further Motivation for an Electrostatic Induction Machine

High voltages in cryogenic experiments are a challenge embraced by many experiments and engineering companies, often requiring a high voltage feedthrough. All feedthroughs balance many requirements. First, they are rated for certain voltages (the larger the voltage, the larger the required diameter of their conductor). Secondly, they are engineered for certain temperatures by managing the differential length contraction and minimizing their heat loads with thermal intercepts (and minimizing their leakage currents across their insulators). Thirdly, they must take into account other important aspects of the experiment, such as material requirements and other compatibilities. Our experiment requires 650 kV in a sensitive 0.4 K superfluid, bulk-conductor-free, magnetic-material-free zone, and a heat load budget by the high voltage system of about 1 mW. Any voltage fed in will need to traverse the boundary between this sensitive, superfluid-filled region and the outside vacuum.

Directly feeding 650 kV from outside is problematic; first of all, the size of the conductor needed is large. If one wanted to store 650 kV on an imaginary sphere (not unlike a feedthrough terminator) and keep the electric fields less than 120

kV/cm, one would want over a 5 cm radius (via E = V/R). Even neglecting the conductive heat load from a thermal intercept at 4 K, the surface leakage current across the feedthrough would have to be below 1.5 nA (via 1 mW/650 kV = 1.5 nA); how big of an insulator will leak so little? In reality, a feedthrough with a large conductor from 300 K (or even thermally intercepted at our heat shields at 4 K and 40 K), and an insulator with leakage currents due to the high voltage, will either exceed our heat budget or our size requirements. Furthermore, a huge amount of material research would need to be done to meet the other requirements of this area: completely nonmagnetic (no stainless steel or kovar), superfluid-helium tight while withstanding thermal cycling from 300 K to 4 K, etc.

However, Ito et al. demonstrated that it is possible to feed up to 50 kV in a way that is compatible with these requirements [72]. Commercially available 50 kV feedthroughs exist, even superfluid-tight and low leakage current (< 1 nA) [73]. A nonmagnetic prototype was created out of G10 and phosphor bronze [74] for the nEDM system, but a more commercially available magnetic 50 kV was installed in the cryogenic prototype [75]. All one needs is a way to multiply the 50 kV to 650 kV.

Furthermore, an electrostatic multiplication scheme allows for the power supply to disconnect from the high voltage system. This is advantageous for the measurements using the Superconducting Quantum Interference Devices (SQUIDs). Recall from the previous chapter that these SQUIDs are measuring the precession frequency of the ^{3}He, with a magnetic field signal estimated to be about 6 fT at 100 Hz. Any ripple or noise from a direct feedthrough by the power supply, or even by the feedthrough cable acting as an antenna, can overwhelm this sensitive signal. An electrostatic multiplier charging up an internal electrode disconnects the high voltage power supply from the high voltage electrode, thereby protecting the SQUIDs from this noise.

Further motivation for the Cavallo Multiplier as the electrostatic induction machine includes the simplicity of movement and ways to manage the heat load and electrical breakdown of the device. These will be discussed as part of the operation of the machine itself.

3.3 The Cavallo Apparatus

The Cavallo Multiplier consists of three electrodes and a ground electrode as shown in Fig. 3.1 used to multiply a nominal voltage using capacitive induction. The A

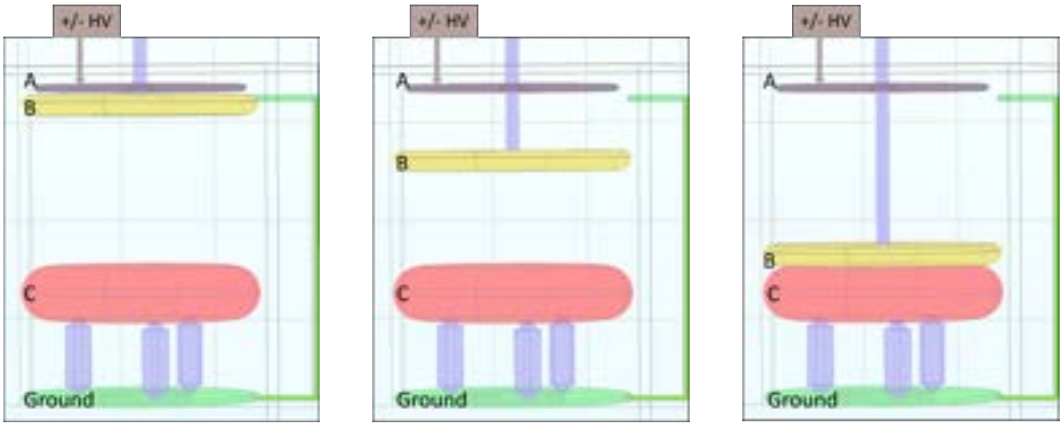

(a) Induce charge on B (b) Move charge (c) Transfer charge to C

Figure 3.1: A Model of the Cavallo High Voltage Multiplier: The charge is transferred to the B electrode in Fig. [a], then physically moved with the B electrode in Fig. [b], and transferred to the C electrode in Fig. [c]. Then the B electrode returns to the position in Fig. [a] to complete the cycle and recharge for the next cycle.

electrode holds the nominal voltage (from an externally controlled source such as a power supply) and stays fixed above a ground ring or grounding pin. The C electrode is the collector electrode, which gets charged to the required output high voltage. The B electrode is the charge transfer electrode moving mechanically between two positions; the mechanical energy supplied to the B electrode converts to the energy stored by the charges on the C electrode.

Its operation is as follows: First, when the B electrode is docked to ground, its close proximity to the A electrode voltage induces an image charge on the B electrode. When the B electrode loses contact with that ground, that induced charge remains on the B electrode. Secondly, the B electrode moves to come into contact with the C electrode, and the charge is distributed in proportion to the B and C capacitances with everything else in the system. Finally, the B electrode cycles between these two positions to continue to transfer charge, limited by either the electric field produced or the residual charge remaining on the B electrode.

The initial charge deposited on the transfer electrode B is dominated by its capacitance with electrode A in the docked position (denoted by the superscript “a”):

$$Q_B^a = C_{AB}^a(-V_A) + C_{BC}^a(-V_C^a) \tag{3.1}$$

As the B electrode loses contact with ground and moves towards the C electrode, its charge remains constant while its voltage changes linearly with the change in capacitance. To solve for this mathematically, we start by generalizing the above equation

using an analogue to Kirchoff's Node Law, summing over the charge indicated by the voltage differences between an electrode and all the electrodes/conductors in the system:

$$\begin{cases} Q_B = C_{AB}(x)[V_B(x) - V_A] + C_{BC}(x)[V_B(x) - V_C(x)] + C_{BG}(x)[V_B(x) - V_G] \\ Q_C = C_{AC}(x)[V_C(x) - V_A] + C_{BC}(x)[V_C(x) - V_B(x)] + C_{CG}(x)[V_C(x) - V_G] \end{cases} \tag{3.2}$$

From this system of equations, we solve for the voltage on B and C as a function of the displacement of electrode B, which we call x above:

$$V_B(x) = \frac{Q_B + C_{AB}(x)V_A + \eta(Q_C + C_{AC}(x)V_A)}{C_{AB}(x) + C_{BG}(x) + C_{BC}(x)(1-\eta)} \tag{3.3}$$

$$V_C(x) = \frac{Q_C + C_{AC}(x)V_A}{C_{AC}(x) + C_{BC}(x) + C_{CG}(x)} + \eta V_B(x) \tag{3.4}$$

where $\eta = C_{BC}(x)/(C_{AC}(x) + C_{BC}(x) + C_{CG}(x))$.

One might notice from Eq. 3.2 that the initial charge and the initial voltage on the C electrode cannot both be zero due to the parasitic capacitance C_{AC}. This capacitance is negligible, on the order of 0.3 pF. Neglecting it, equations 3.3 and 3.4 reduce to:

$$V_B(x) = \frac{Q_B + C_{AB}(x)V_A + Q_C\frac{C_{BC}(x)}{C_{CG}(x)+C_{BC}(x)}}{C_{AB}(x) + C_{BG}(x) + C_{CG}(x)\frac{C_{BC}(x)}{C_{CG}(x)+C_{BC}(x)}} \tag{3.5}$$

$$V_C(x) = \frac{Q_C + C_{BC}(x)V_B(x)}{C_{BC}(x) + C_{CG}(x)} \tag{3.6}$$

The B electrode completes its journey downwards by touching the C electrode (denoted by the superscript "c"), imposing $V_B = V_C = V_{BC}$ in this configuration and sharing its charge based on the mutual capacitances of the B and C electrodes with the other electrodes in the system:

$$Q_{total} = (Q_B + Q_C) = (C^c_{AC} + C^c_{AB})(V_{BC} - V_A) + (C^c_{BG} + C^c_{CG})(V_{BC} - V_G) \tag{3.7}$$

which yields:

$$V_{BC} = \frac{Q_{total} + V_A(C^c_{AC} + C^c_{AB})}{C^c_{AC} + C^c_{AB} + C^c_{BG} + C^c_{CG}} \tag{3.8}$$

Separating Q_B from Q_C (by separating each of the capacitance terms in Eq. 3.7 with respect to the B or C electrode):

$$\begin{cases} Q_B = [C_{AB} + C_{BG}]V_{BC} - C_{AB}V_A \\ Q_C = [C_{AC} + C_{CG}]V_{BC} - C_{AC}V_A \end{cases} \tag{3.9}$$

Note that plugging in V_{BC} here turns this set of equations into terms involving the total charge and terms involving V_A, e.g.:

$$Q_C = \frac{(C_{AC} + C_{CG})Q_{total}}{C_{AC} + C_{AB} + C_{BG} + C_{CG}} + V_A \left[-C_{AC} + \frac{(C_{AC} + C_{CG})(C_{AC} + C_{AB})}{C_{AC} + C_{AB} + C_{BG} + C_{CG}} \right] \tag{3.10}$$

The first term involving Q_{total} is a satisfying "charge divider" (e.g., as an analogue to a voltage divider). Note that neglecting C_{AC} still yields us with some influence on the charge distribution by the voltage on the A electrode, but that it is also negligible because C_{AB} is very small compared to $(C_{BG} + C_{CG})$.

Weeding out the negligible terms leaves us with:

$$Q_C = \frac{Q_{total}C_{CG}}{C_{BG} + C_{CG}} \tag{3.11}$$

The B electrode then travels back up to its initial position near the A electrode to reload with more charge. As seen in Eq. 3.1, the charge acquired is now slightly less than the previous cycle because V_C has increased in magnitude. If we neglect that difference, we can express these iterative cycles as a geometric series with $r = C_{CG}/(C_{BG} + C_{CG})$, so Eq. 3.11 for each successive Q_C^n becomes:

$$Q_C^n = Q_B r \frac{1 - r^n}{1 - r} \tag{3.12}$$

Eventually, however, $Q_B^a = Q_B^c$; the amount of charge "loaded" on the B electrode satisfied by Eq. 3.1 is equal to the amount of residual charge left on the B electrode after the electrode B-C contact transfer. In the limit of infinite cycles, Eq. 3.12 reduces to:

$$\lim_{n \to \text{inf}} Q_C^n = Q_B \frac{r}{1 - r} = Q_B \frac{C_{CG}}{C_{BG}} \tag{3.13}$$

A more precise way to approach the final theoretical gain of the system would be to impose $Q_B^a = Q_B^c$ on Eq. 3.2, yielding four equations for Q_B^a, Q_B^c, Q_C^a, and Q_C^c. Solving for the gain $G_C^c = V_C^c/V_A$ yields:

$$G_C^c = \frac{C_{AB}^c - C_{AB}^a}{C_{AB}^c + C_{BG}^c + C_{BC}^a C_{CG}^c/(C_{BC}^a + C_{CG}^a)} \tag{3.14}$$

A distinction must be made between this theoretical gain in Eq. 3.14 and the realizable gain of the system due to high voltage breakdown and/or corona discharge in the electrodes' medium. This apparatus is limited both in gain geometrically through the capacitances in Eq. 3.14 (the "geometric gain"), and by the ability to withstand the electric fields in operation. The geometric gain cannot be fully realized if the electric fields produced by the apparatus would cause breakdown.

To further understand the Cavallo apparatus's charging behavior, Fig. 3.2 and Fig 3.3 illustrate simulated charges and voltages for an example set of Cavallo electrodes with the A electrode set to 50 kV using a finite element analysis program [76]. It is especially interesting to note the two-tone nature of the graphs—the half-cycles corresponding to the B electrode touching the C electrode, and complete integer cycles corresponding to the B electrode returning to its initial charging position near the A electrode.

For the B electrode charge, one can see that the B electrode starts with a large charge-up (over 6 μC) in Fig. 3.2. However, as the C voltage increases in Fig. 3.3, the B electrode can pick up less charge (as we can see in the upper integer-cycle trend-line) and leaves with more charge (initially < 0.5 μC as we see in the lower half-integer trendline). Eventually, in the infinite cycle limit, the residual charge on the B electrode leaving the C electrode will equal the amount of charge picked up leaving the A electrode—this is the geometric gain. Note, however, in that infinite cycle limit, the C electrode reaches almost 1 MV, which the geometry may not be able to sustain.

Note that these sample electrodes have a G_C^c approaching 20. Electrode shapes, their capacitances and geometries, and design methods will be discussed in depth in section 3.5.1.

3.3.1 Energy Losses, Heating, and Sources of Error

Energy losses can occur by electrical breakdown in the system, by charge conduction heating across the electrodes, by drag from the B electrode's movement in

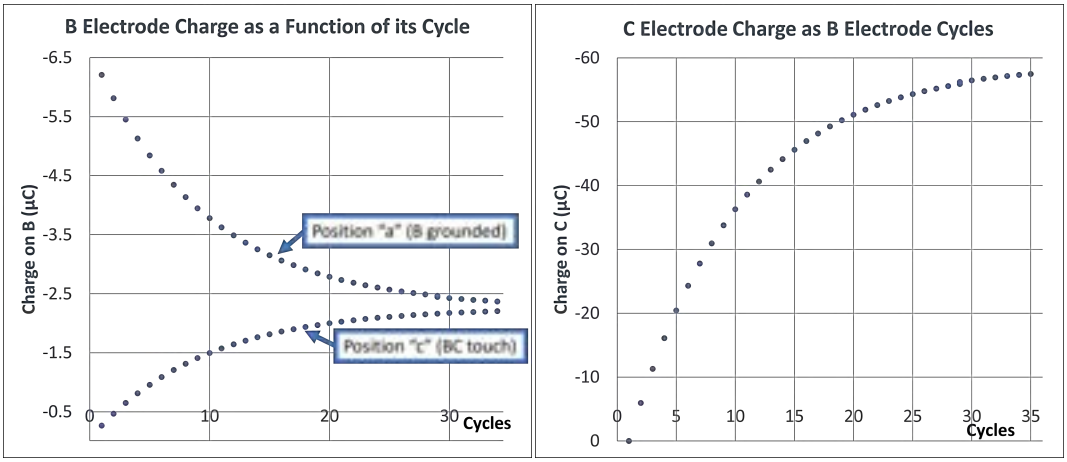

(a) Charge on the B Electrode (b) Charge on the C Electrode

Figure 3.2: Charges on the B Electrode (traveling electrode) or C Electrode (high voltage electrode) as a function of B Electrode Travel Cycles. Note how the half-cycles correspond to the B electrode touching the C electrode, and the integer cycles correspond to the B Electrode returning to its charging position near the A electrode.

that medium, and by leakage currents through the insulating standoffs and/or fluid medium.

First, electrical breakdown can occur as the Cavallo apparatus charges up, especially at high electric field regions on the C electrode (the high voltage, collector electrode). This breakdown profile can be optimized by design; Phan et al. [57] showed that electrical breakdown depends, not only on the strength of the electric field at the electrode's surface, but also on the integrated surface area at that field strength. A comprehensive method to calculate the probability for electrical breakdown can be implemented for arbitrary electrode geometries using data on breakdown field distributions for a small set of electrodes that take into account the other variables of electrical breakdown (material, surface quality, LHe pressure, etc.).

Secondly, electrical breakdown could occur with the charge transfer to or from the B electrode. The charge transfer to the B electrode from the ground ring as it returns to the A electrode can be eliminated by changing the nominal voltage on the A electrode. At the other extent of the B electrode's journey, the B and C electrode approach the same voltage as the B electrode physically approaches the C electrode. In a perfect world, that means there is no breakdown when the B electrode approaches the C electrode. However, any imperfections or surface features could create a localized high field and therefore a breakdown. The energy available to that spark is proportional to square of the difference in their voltages, so the closer

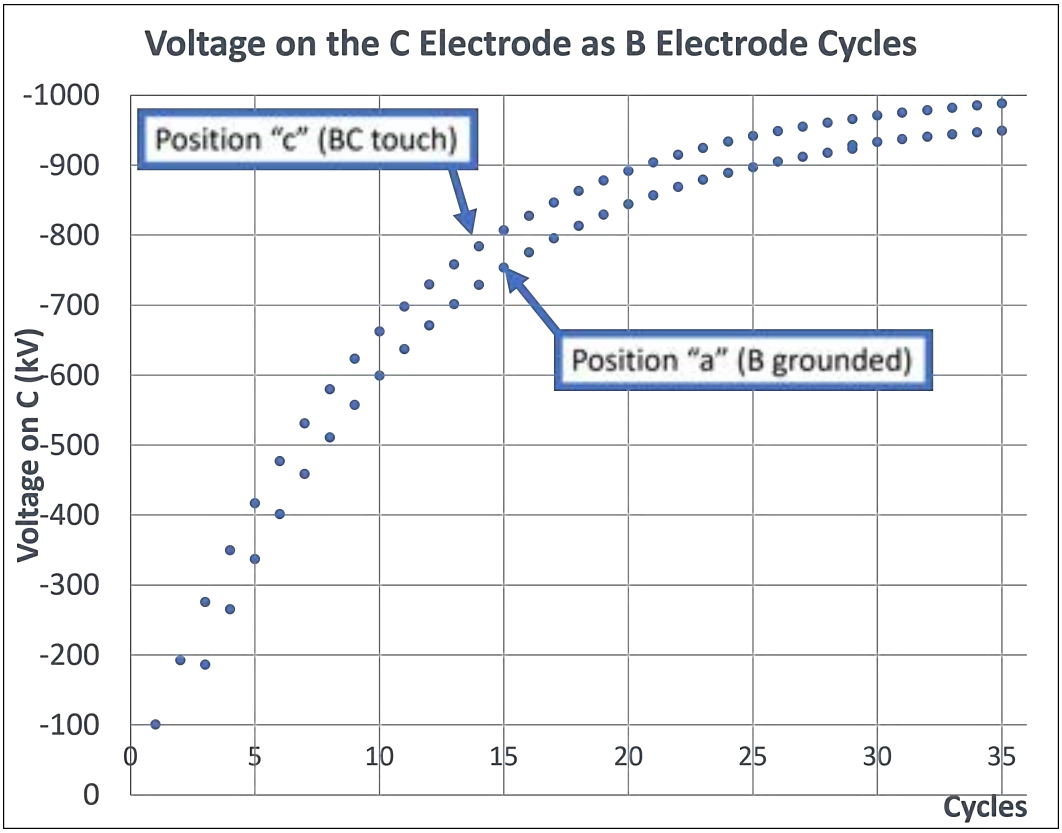

Figure 3.3: Voltage on the High Voltage (C) Electrode as a function of B Electrode Travel Cycles. Note how the half-cycles correspond to the B electrode touching the C electrode, and the integer cycles correspond to the B electrode returning to its charging position near the A electrode (and its residual charge moving away from the C electrode, lowering its voltage.)

the two electrodes are when they spark, the safer they are to damage, and the less energy (and heat) released.

Thirdly, the realization that as the B electrode physically approaches the C electrode, they approach a common voltage means that their surface charges are also rearranging. The heat produced by this activity is dependent on the amount of charge and on the rate at which we drive the B electrode downward, such as the charges moving from the top to bottom of the B electrode:

$$\begin{aligned} W &\propto (I^2\rho)\Delta t \\ &\propto ((Q_B/\Delta t)^2\rho)\Delta t \\ &\propto (Q_B^2\rho)/\Delta t \end{aligned} \tag{3.15}$$

where ρ is the surface resistivity of the electrode, Q_B is the charge on the B electrode, and Δt is the time it takes the charge to rearrange (related to the time it takes for

us to drive the B electrode downward). The C electrode is also responding with a mirror charge, with its top surface charge approaching $-Q_B$ as B and C approach. Managing the heat load from this surface charge "self-current" is simply slowing the B electrode down as seen in the above equation.

Slowing the B electrode down also has an effect on the friction and heating due to drag through the medium. Assuming turbulent flow, the force is proportional to the square of the velocity v, and so the power loss is v^3. Experience working with a Cavallo apparatus in liquid helium would allow us to tune this rate of speed, but extrapolations from quantum turbulence measurements of oscillating spheres [77] suggest that running at 3 cm/s would produce <1 mW of heating [59].

Finally, leakage currents in any standalone Cavallo system will be different than the leakage currents in the final experiment, due to the support structures for the Cavallo apparatus differing significantly without a measurement cell electrode system attached. However, we can still measure them by creating a 4th electrode (called the "D" electrode) within the ground return, isolating the C electrode's standoffs from the rest of the ground. A picoammeter can be installed between this new electrode and the rest of the ground return.

3.4 The Room Temperature Demonstration Prototype

The purpose of the room temperature demonstration prototype was to verify the mathematical understanding of the Cavallo voltage multiplication, test some non-contact voltage measurement schemes, and gain operational and troubleshooting experience applicable to future nEDM-specific designs.

The electrodes were chosen by convenience (recycled from previous experiments), and affixed in a grounded aluminum enclosure as shown in Fig. 3.4 using electrically insulating G10 standoffs. The A (nominal seed voltage) electrode was attached to an external power supply[a], and the B (transfer) electrode was attached to a G10 rod driven by a linear actuator with a 29 cm stroke length. We found that installing a nylon bushing to guide the B electrode rod created unacceptable triboelectric charge up, and was removed. Fig 3.5 is a closeup of the inside of the enclosure, to better see the electrode layout. When the B electrode stopped at the top of its stroke near the A electrode, a solenoid extended a grounded pillow to ground the B electrode as depicted in Fig. 3.6. The ground near the C (high voltage) electrode was isolated as a separate standoff for picoammeter measurements and to be able to change the

[a] first the Keithley 617 Electrometer, then a Bertan 377X 7.5 kV High Voltage Supply

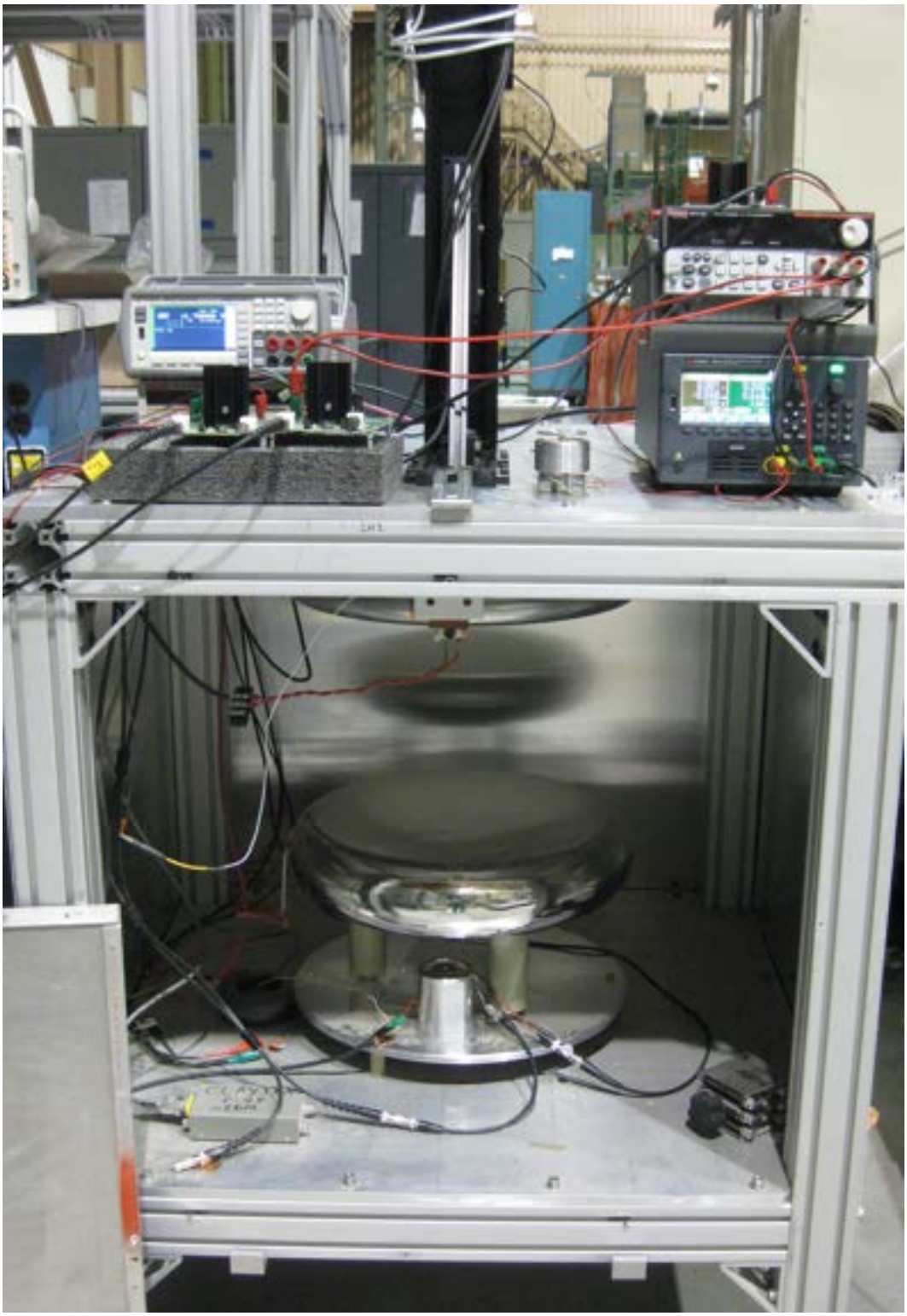

Figure 3.4: Photograph of the Room Temperature Demonstration Apparatus. The electrodes were electrically shielded in an aluminum enclosure, with an actuator rod moving a G10 rod feeding into the enclosure to move the B electrode.

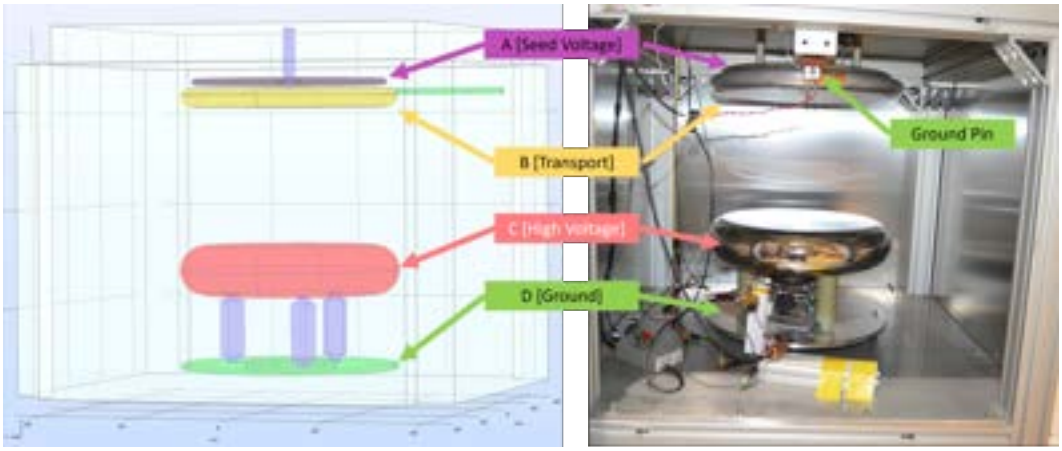

Figure 3.5: Inside the Cavallo Demo Apparatus Enclosure. Note the electrodes and the grounding pin, with a no-contact voltage measurement device on the floor of the enclosure.

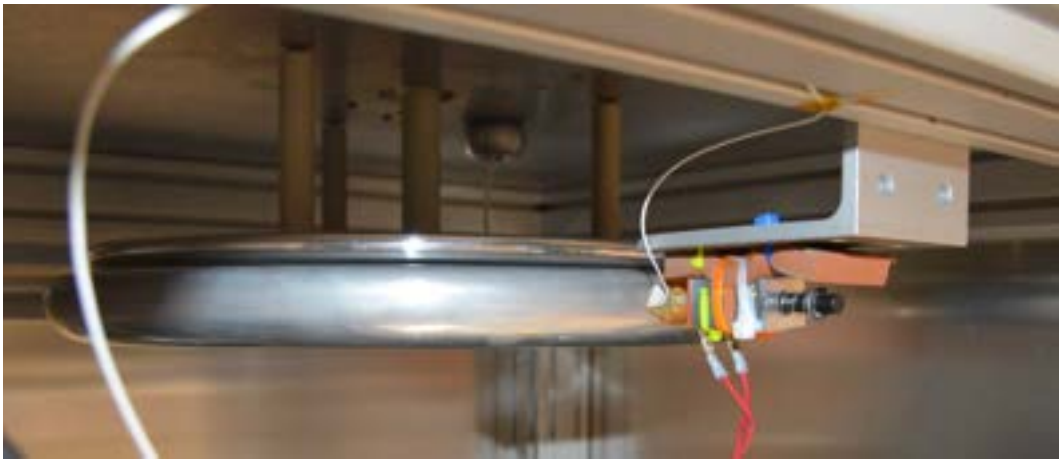

Figure 3.6: Photograph of the B electrode at its closest position to the A electrode; note the solenoid mechanism on the right, which extends a grounded spring-pin cushion to the surface of the B electrode, effectively grounding it. It retracts before B moves again.

C_{CG} capacitance.

The electrodes' mutual capacitances were measured by attaching shielded coaxial cables to each electrode and recording them with a Handheld Agilent U1733C LCR meter as the B electrode made its 29 cm journey. All parasitic capacitances were minimized using the guard input on the capacitance meter; the guard was electrically connected to the coaxial cable shields and all conductive surfaces aside from the two electrodes measured. The results in Fig. 3.7 plug into Eq. 3.3 and Eq. 3.4 to predict the voltage-charging behavior of the Cavallo apparatus. The results are included with Fig. 3.8.

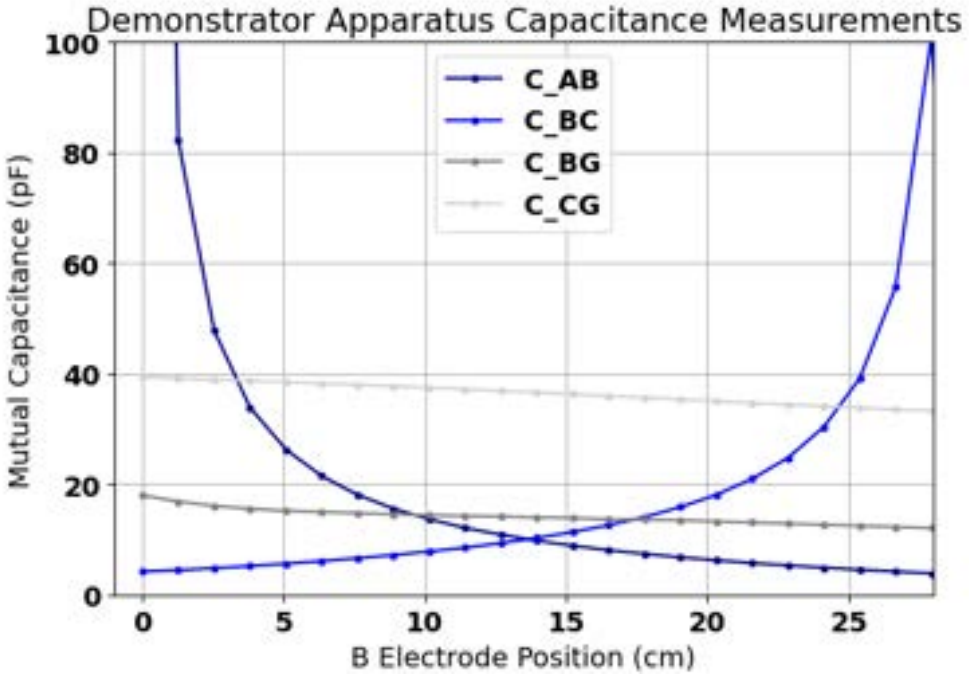

Figure 3.7: Mutual Capacitances of the Cavallo Demonstrator electrodes. The B electrode was chosen to stop at a distance 2.5 mm below the A electrode, meaning that C_AB reaches a maximum of 399.3 pF ± 0.5 pF.

The capacitance meter was also useful in calibrating the position of the B electrode when measuring the electrical impedance (LCR) between B and C; as the B electrode slowly approaches the C electrode a few thousand steps at a time[b], the edge of contact occurs when the meter output oscillates between a mH and a nF. This position is 2.3 million steps (11.5 inches) from the "zero" of travel corresponding to the A-B electrode distance of 2.5 mm.

Direct measurement of the C electrode voltage was undesirable even for a low-voltage demonstrator apparatus. It is better to avoid the cable's capacitance, the device's leakage current, and noise from the cable and device by creating a prototype for non-contact voltage measurement useful for future voltmeters. Instead, the electrometer was used to calibrate a non-contact voltage measurement device discussed in subsection 3.6. The voltage measurements plotted in Fig. 3.8, as well as the decay curve in Fig. 3.9, were taken using the "Wiggling Capacitive Voltmeter" from that subsection.

Fig. 3.8 contains two graphs of the voltage on the C (high voltage) electrode as a

[b]The actuator yields 0.0127 mm/step.

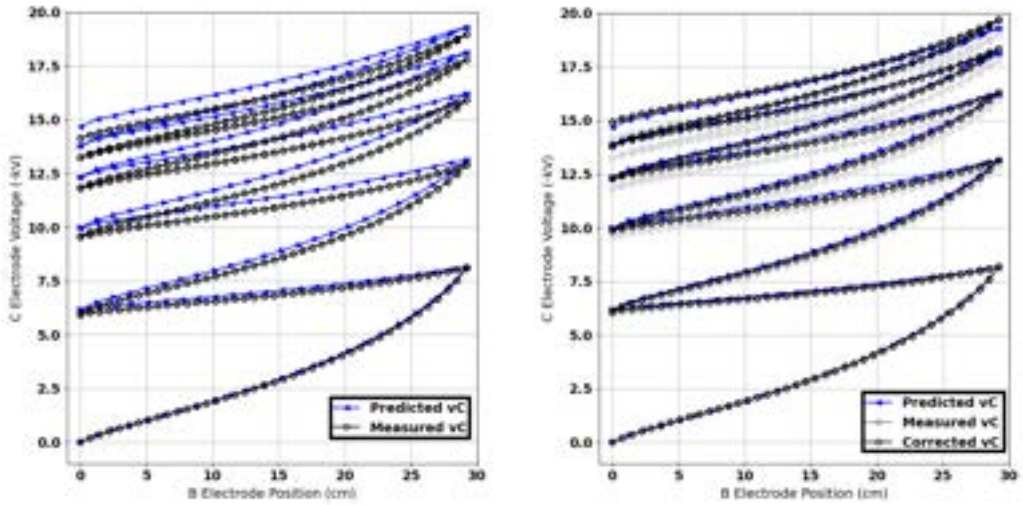

Figure 3.8: C Electrode Voltage for five cycles of the B electrode with V_A = 1 kV. The blue curves (arrows) are mathematical predictions of the C Electrode Voltage calculated using the measured capacitances.
Left: the black dots are the measured voltages from the wiggling capacitor voltmeter discussed in section 3.6.
Right: the black dots are the measured voltages corrected for the charge leakage, with the faint grey dots representing the raw measured voltages seen on the right.

function of the B electrode's position, or where B is in its journey from 2.5 mm from the A electrode (x = 0) to touching the C electrode (x = 29 cm). The predicted voltages (in blue, with arrows) are derived from the measured capacitances with the application of equations in subsection 3.3. Note that in Fig. 3.8 (a), the predicted voltage and the measured voltage (black circles) agree well for the beginning cycles, and start to fall out of alignment towards the end of the five cycles. This is NOT due to our approximations involving C_{AC}, which yields a difference of only 2.2 V at the end of cycle 5, and a maximum of 30 V (cycle 4.5, when B and C touch at x = 29 cm). The measured discrepancy is of the order of 526 V.

This discrepancy is due to the charge leaking from the electrode, both by the water in the air and leakage currents through the three posts holding up the C electrode. For the timescales of these Cavallo cycles as seen in Fig. 3.10, the charge bleed-off is approximately linear as seen in Fig. 3.9. This linear fit was used to correct for the charge bleed-off while charging in 3.8 (b). The uncorrected voltage measurements were greyed out for reference, with the corrected data graphed on top in black. This corrected data better agrees with the predicted voltages (blue, arrows).

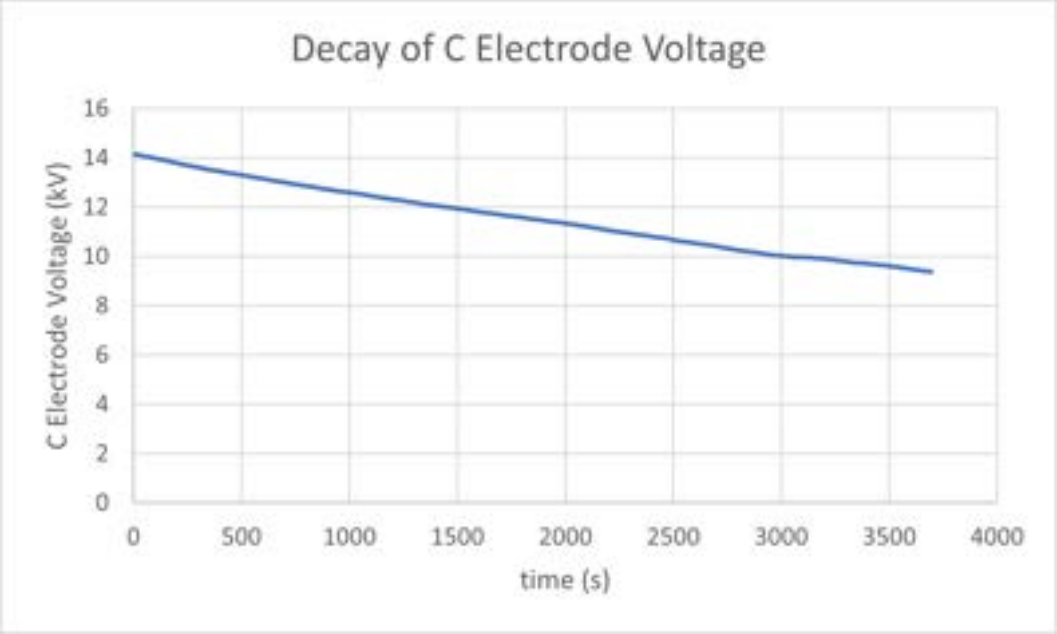

Figure 3.9: C Electrode Voltage Decay Curve. Note that its linearity on Cavallo charging timescales lends itself to correcting the charging data.

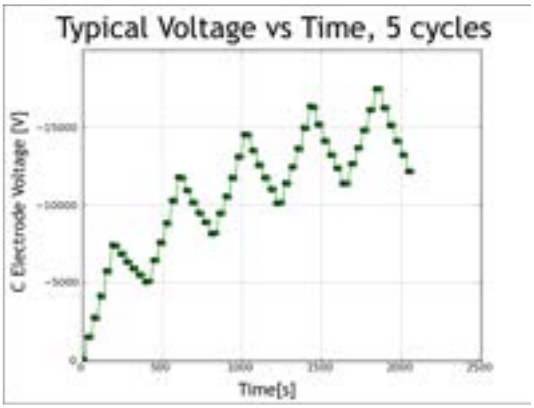

(a) C Electrode Voltage vs. time:
V_A = 1 kV, $C_{CG} \approx$ 30 pF

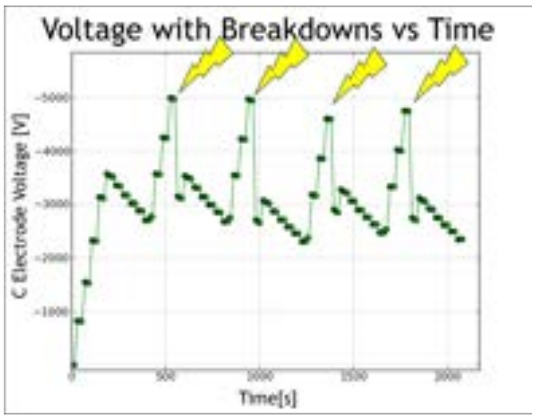

(b) C Electrode Voltage vs. time:
V_A = 1.001 kV, C_{CG} = 160 pF

Figure 3.10: Measured C Electrode Voltage for five cycles of the B electrode with V_A = 1 kV and different C_{CG} values. On the left is a typical charging cycle for Cavallo multiplier as a function of time. On the right, breakdown occurs between the C electrode and the ground electrode underneath.

A cursory attempt was made to measure the leakage current from the C (high voltage) electrode through the G10 standoffs, as the electrical isolation of the ground return under the C electrode from the rest of the grounds created that option. It was instead connected to ground through the picoammeter (virtually grounding it) as opposed to directly tied to ground.

The picoammeter data was noisy, as the signal was subjected to long cables and no troubleshooting. However, if the noise is trustworthy, the picoammeter showed spurious spikes of less than 8 pA after charging, with an average consistent with zero. During a charging cycle, the picoammeter data ebbed and flowed with the movement of the charge onto the C electrode (albeit also noisily). I made no attempts to fix the noise, as the leakage current was less useful than a measurement of the total charge leakage afterwards such as Fig. 3.9. Picoammeter data may be much more useful for the a cryogenic Cavallo apparatus with voltages an order of magnitude higher than these.

Beyond the charge leakage through the air and through the insulating posts, other flaws impacting the agreement between the capacitance-calculated prediction and the measured C voltage include the precision of the wiggling capacitive voltmeter calibration, and errors in the capacitance measurements especially at the extrema of the B electrode's journey.

Finally, an additional ground electrode underneath the C electrode was introduced, which is hiding under the C electrode on a LabJack in Fig. 3.5. Its function was to change the C_{CG} capacitance to change the gain of the Demonstrator Apparatus. A salient concept was illustrated with this addition; as we can see on the right side of Fig. 3.10, the gain is not only limited by capacitance, but also by breakdown.

3.5 The Full-Scale Cryogenic Prototype

A Cavallo multiplier designed specifically for the nEDM experiment must operate cryogenically, with electrodes made of thin conductive shells instead of eddy-current-filled bulk conductors. Thought must be given to the electrode shapes to maximize their gain and minimize their sparking probability. The purpose of our cryogenic prototype is not simply to operate a Cavallo multiplier cryogenically, but to also test a design for the full-scale nEDM Cavallo electrodes.

The space assigned the Cavallo system in the nEDM experiment is cylindrical, with two ends sectioned off for light connection fibers, SQUID connections, and other engineering services, illustrated in 3.11. The distance between those two straight

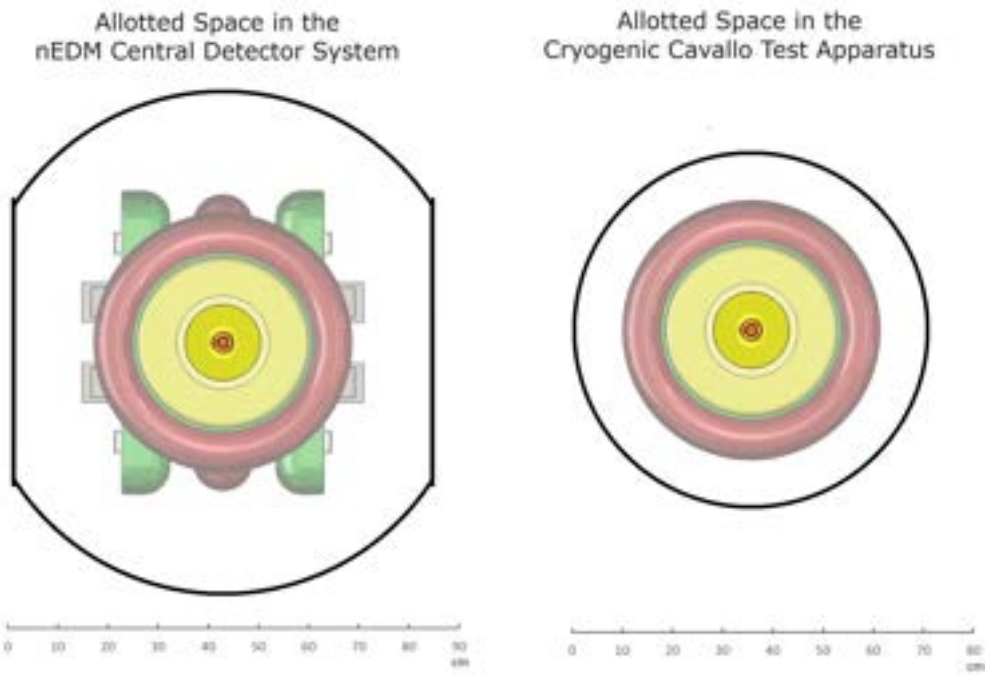

Figure 3.11: Size Comparison for the Cavallo Apparatus: Left, the 86 cm space for the Cavallo Apparatus in the nEDM@SNS Central Detector System. Right, the 74 cm-diameter Central Volume for the Full Scale Cavallo Cryogenic Prototype.

walls—the "tightest diameter" for the Cavallo apparatus—is 86 cm. The cryogenic prototype uses a similarly sized bucket dewar with a liquid nitrogen and liquid helium jacket recycled from the Caltech cryomagnet tests, which has an inner diameter of 83.3 cm. This cryostat, pictured in Fig. 3.12 became the starting point for the Cavallo cryogenic prototype. The details of the cryogenic system are discussed in subsection 3.5.4.

The optimization of the electrode shapes was done focusing on the reduction of electric field hotspots (detailed in subsections 3.5.1 and 3.5.2), as Phan et al. [57] showed that electrical breakdown depends, not only on the strength of the electric field at the electrode's surface, but also on the integrated surface area at that field strength. This comprehensive method to calculate the probability for electrical breakdown (detailed and implemented in subsection 3.5.3) works for arbitrary electrode geometries, using data on breakdown field distributions from a set of small electrodes that take into account the other variables of electrical breakdown (material, surface quality, LHe pressure, etc.). For this analysis, we focused on electropolished stainless steel electrodes with varying LHe pressures due to the team's extensive experience with their performance [72] [57].

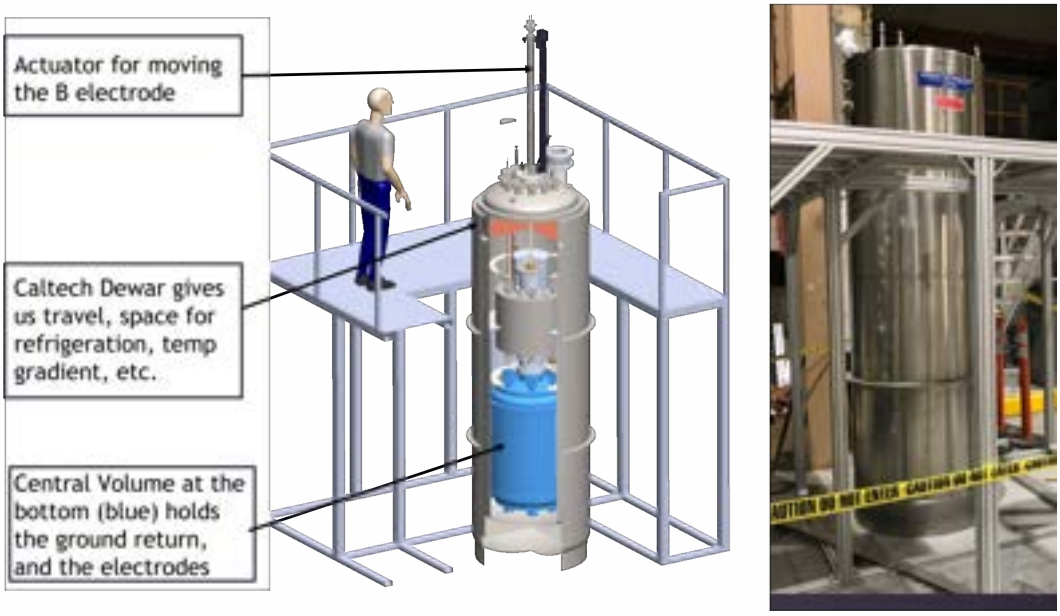

Figure 3.12: Overview of the Full Scale Cryogenic Prototype. Left: to-scale model of the important features of the full scale cryogenic prototype by our engineer Chris O'Shaughnessy. Right: a photograph of the Caltech Cryostat.

For the cryogenic prototype, the first set of Cavallo electrodes were also created out of stainless steel. This allows the apparatus to survive electrical breakdown, testing and verifying the predictions of Phan et al.'s method, while exploring breakdown prevention strategies outlined in subsection 3.3.1. Once these goals are met, and breakdown prevention is comfortable, a set of conductive-coated plastic electrodes (the specific materials and coating techniques currently under study) will be fabricated [78].

It is especially prudent for the nEDM measurement to ensure that the limiting voltage of the experiment lies with the neutron measurement cell electrodes, and not on the voltage-generating apparatus; we should have the option to use the measurement cell to its limit. Therefore, we initially designed the Cavallo apparatus electrodes to maximize the possible geometric gain while still operating with electric fields below those of the measurement cell electrode (120 kV/cm [72]), with the nEDM experimental space constraints in mind.

3.5.1 Design Methods

The design goal of the nEDM Cavallo Apparatus is to maximize the geometric gain produced by the electrode capacitances, while keeping the electric field below $\tilde{1}20$

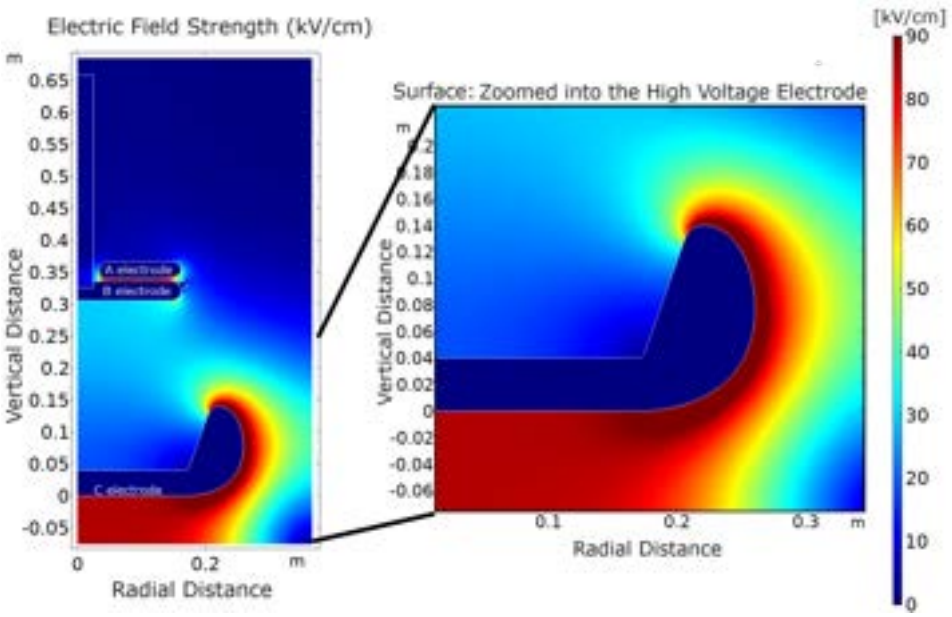

Figure 3.13: The axisymmetric physics model for the Cavallo electrodes. The electrode shapes were tailored with the influences of the other electrodes. Left, we show the C electrode at 650 kV within the physics model. Right, the C electrode in detail: Created with a large lobe as a result of the relationship between C_C/C_B and Q_C/Q_B to maximize the geometric gain, while using two parametric tanh-based curves to minimize electric field hotspots.

kV/cm to minimize the probability of breakdown. The constraints include:

- A restricted volume to emulate the nEDM@SNS experimental engineering constraints while optimizing for a specific recycled cryostat
- A seed voltage (A electrode) of 50 kV to reach the 650 kV goal on the high voltage electrode (C electrode) in a reasonable number of cycles.
- A constraint of about 120 kV/cm, minimizing all hotspots, chosen to ensure that the measurement cell geometry is the voltage limiting factor in the final experiment, not the Cavallo multiplier.

To achieve these goals, we used the finite element analysis simulation software COMSOL [76], which allowed us to create and fine-tune electrode profiles in the Cavallo Apparatus. We produced simulated capacitances and visualizations of voltage distributions and electric fields in the Cavallo Apparatus.

Two kinds of COMSOL simulations were run—two dimensional axisymmetric models and three dimensional models. Two dimensional axisymmetric simulations

are models computed in two dimensional space that represent three-dimensional space by rotating the plane about the r=0 axis as in Fig. 3.13. These models informed the electrode shapes and engineering constraints, and working in two dimensions is easier to visualize and saves computation time. A Solidworks model, Fig. 3.21 was created using the result of the 2D axisymmetric studies, which was nearly axisymmetric, with a few exceptions. This model was imported into a full three dimensional simulation, and cross-sectional results of that model are presented below.

The basic shape of the C electrode combines electrostatic necessity (a corona ring) with a strategy to maximize the gain. At 650 kV, the C electrode needs a corona ring because its width is too narrow to handle the fringe electric field at its outside edge. However, the inclusion of this ring has an added benefit of increasing the gain by screening the B electrode from ground when the B electrode is touching the C electrode. This screening increases the charge transferred from the B electrode to the C electrode: When the C electrode cradles the B electrode on contact, the ratio of the $C_C G/C_B G$ increases, and so the ratio of Q_C/Q_B increases. The distance between the C electrode and the bottom of the ground return was chosen to approximately simulate the electrostatic "load" of the measurement cell. Together, these considerations informed the ear-like shape of the C electrode's lobe.

Crawford [79] proposed a heuristic family of functions that smoothly join a horizontal asymptote with a vertical one, which the Nab experiment [80] [79] previously used for their electrodes. This family of curves is based on an intuitive desire for ellipse-like curvature:

$$\left[\frac{x}{a}\right]^{m_x} + \left[\frac{y}{b}\right]^{m_y} = 1 \tag{3.16}$$

We set the first and second addends in Eq. 3.16 equal to $\cos^2(t)$ and $\sin^2(t)$, respectively, to get:

$$x = a\cos^{2/m_x}(t) \tag{3.17}$$

$$y = b\sin^{2/m_y}(t) \tag{3.18}$$

where t has a range of $\pi/2$ within one of the four quadrants depending on the orientation of the asymptotes. A tanh curve has the asymmetric rectangular-box boundary behaviors that a corner-cutting curve desires, so we enveloped the x and y formulas in Eq. 3.17 and 3.18 in a "tanh envelope" as seen below. Furthermore, closed curves on the two-dimensional plane revolved around the x=0 axis produce three-dimensional (electrode) shapes; therefore the x and y in the above equations

correspond to r and z in the model. We call the result the "Crawford Curve:"

$$r = R_o \left[\frac{\tanh(k_x \cos t)}{\tanh(k_x)} \right]^{2/m_x} \tag{3.19}$$

$$z = z_o \left[\frac{\tanh(k_y \cos t)}{\tanh(k_y)} \right]^{2/m_y} \tag{3.20}$$

These parametric curves contain parameters k_x,k_y,m_x,m_y that can be fine-tuned for an empirically driven electrode shape. COMSOL's graphical user interface includes a study method allowing COMSOL to loop through values for these parameters.

For the C electrode, we used two of these "Crawford Curves" to create the outside of the lobe, and the z transition coordinate between the two curves was also fine-tuned. The final choice of curve parameters is included in the results section. Crawford curves were explored for other electrode and engineering surfaces as well, such as in the A electrode (see Results).

3.5.2 Simulation Results

The most effective approach to balancing the geometric gain while minimizing the electric field included designing the A and C electrodes with fine-tuned Crawford curves, while the B electrode was chosen to have circular fillets.

The C electrode has a high electric field on the outside of the lobe when it is fully charged, and due to its bowl-like shape, it required a balance of two parametric Crawford curves. The C electrode is depicted in Fig. 3.13, and the formula for the outside lobe is as follows:

$$\begin{cases} r_{top} = 21\text{ cm} + d_i + 4\text{ cm}\dfrac{\tanh(0.2\cos t)}{\tanh(0.2)} \\ z_{top} = 7.65\text{ cm} + 6.35\text{ cm}\dfrac{\tanh(0.3\sin t)}{\tanh(0.3)} \\ \qquad\qquad\qquad\qquad\qquad\qquad\qquad\qquad t \in (0, \pi/2) \\ r_{bottom} = 17\text{ cm} + (d_i + 4\text{ cm})\dfrac{\tanh(0.5\cos t)}{\tanh(0.5)} \\ z_{bottom} = 7.65\text{ cm} + 6.35\text{ cm}\dfrac{\tanh(0.3\sin t)}{\tanh(0.4)} \end{cases} \tag{3.21}$$

Note that d_i is the distance from the flat inner part of C to the top of the lobe held at a 20 degree angle, found to be ≈ 5.177 cm. For this parameter sweep, in addition to

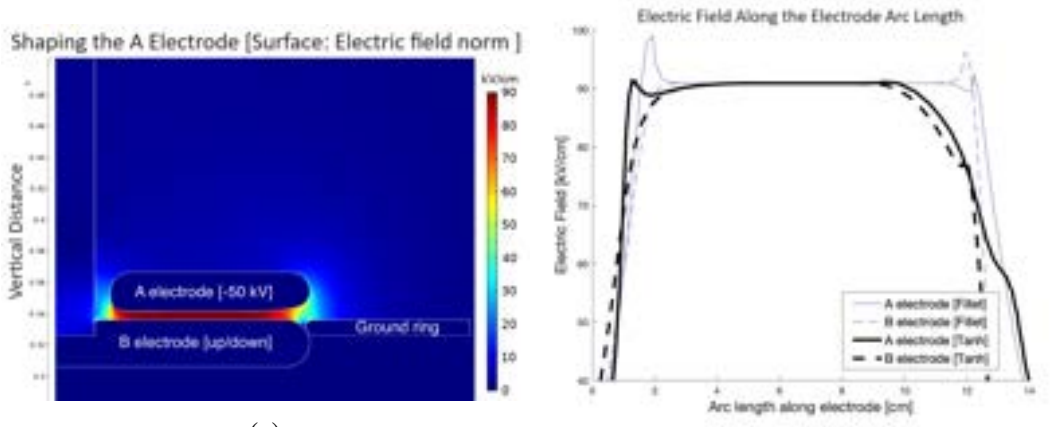

(a) (b)

Figure 3.14: Shaping the A electrode: The strong electric field between the A and B deposits a large charge on the B electrode, but any electrical hotspots may result in electrical discharge.
Left (a): Axisymmetric simulation of the electric field between the A and B electrode. Crawford curves were chosen to decrease the hotspots on the electrode edges. Right (b): Electric field along the A and B electrode as a function of the arc length along the cross-sectional edge along the electrode shown on the left. The A electrode's arc length is measured from the innermost point of the A electrode (the leftmost in Fig. a), and the B arc length is measured from the bottom corner of the B electrode shaft's borehole. Note the difference between circular fillets and Crawford Curves in eliminating electrical hotspots.

the free parameters in Eq. 3.19 and 3.20, we also swept through the point at which the two curves should join, and found it to be (26.177 cm, 7.65 cm).

The A electrode's bottom surface experiences a high electric field when the B electrode is docked on the ground ring as shown in Fig. 3.14a. The ground ring and the shaft driving the B electrode also distorts the electric field, so a different Crawford Curve is required for both the inner and outer lower surface of the A electrode. They both take the form of:

$$\begin{cases} r_{Ai} = -4.32\text{ cm}\dfrac{\tanh(k_x \cos t)}{\tanh(k_x)} \\ z_{Ai} = 1.25\text{ cm}\dfrac{\tanh(k_y \sin t)}{\tanh(k_y)} \end{cases} \qquad t \in (0, \pi/2) \tag{3.22}$$

where k_x, k_y is (0.8,3) for the inner curve and (1,1) for the outer curve.

These two Crawford "fillets" smoothed the electric field hotspots between A and B. This is shown especially in the comparison between this geometry and a perfectly

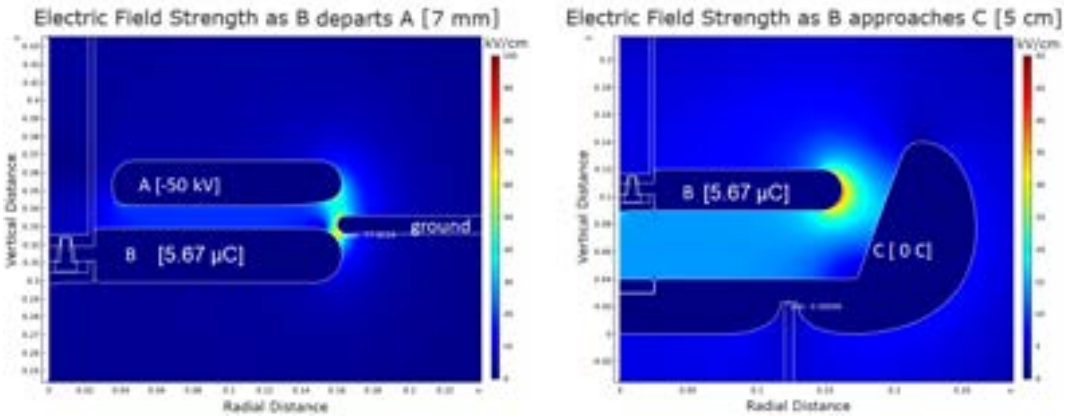

(a) B electrode approaches the ground ring (b) B electrode approaches the C electrode

Figure 3.15: Pseudo-axisymmetric simulations of the electric field strength for two positions of the B electrode. The B electrode experiences high electric field on both its upper and lower faces as it traverses the distance between the ground ring and the C electrode. Therefore its best edge shape is a circular fillet.

circular fillet geometry. Fig. 3.14b is a line graph that traces the stressed edges of the A and B electrode cross sections of Fig. 3.14a and plots the electric field normal to the surface as a function of position along each electrode's arc length. It clearly shows that for a circular fillet graphed in blue, there are two large electric field maxima at arc length 2 cm and 12 cm. Conversely, for the tailored Crawford Curve "fillets" (denoted "Tanh" in the legend), the inner hotspot greatly reduced to less than 91.5 kV/cm (and moved to 1.3 cm due to the shape of the arc). The outer curve eliminated the hotspot on the outer edge of the electrode.

Electrode B, unlike the other two electrodes, was chosen to be a circular electrode. This is because its topside experiences a high electric field when it returns to a docked position on the ground ring near A as in Fig. 3.15a, and its downside experiences higher electric fields when it approaches the C electrode as in 3.15b. To maximize the radius of curvature for both its topside and downside, the solution is a circular fillet.

Because the Crawford Curves are useful in smoothing high electric fields, one may want to employ them in all engineering surfaces on the electrodes. However, it is not always necessary, and the curves are more expensive to implement.

Two engineering surfaces where the curves were worth the cost to implement are the grooves of the C and D electrodes, because the region in between the electrodes experiences high electric fields when charged as depicted in Fig. 3.16. The D

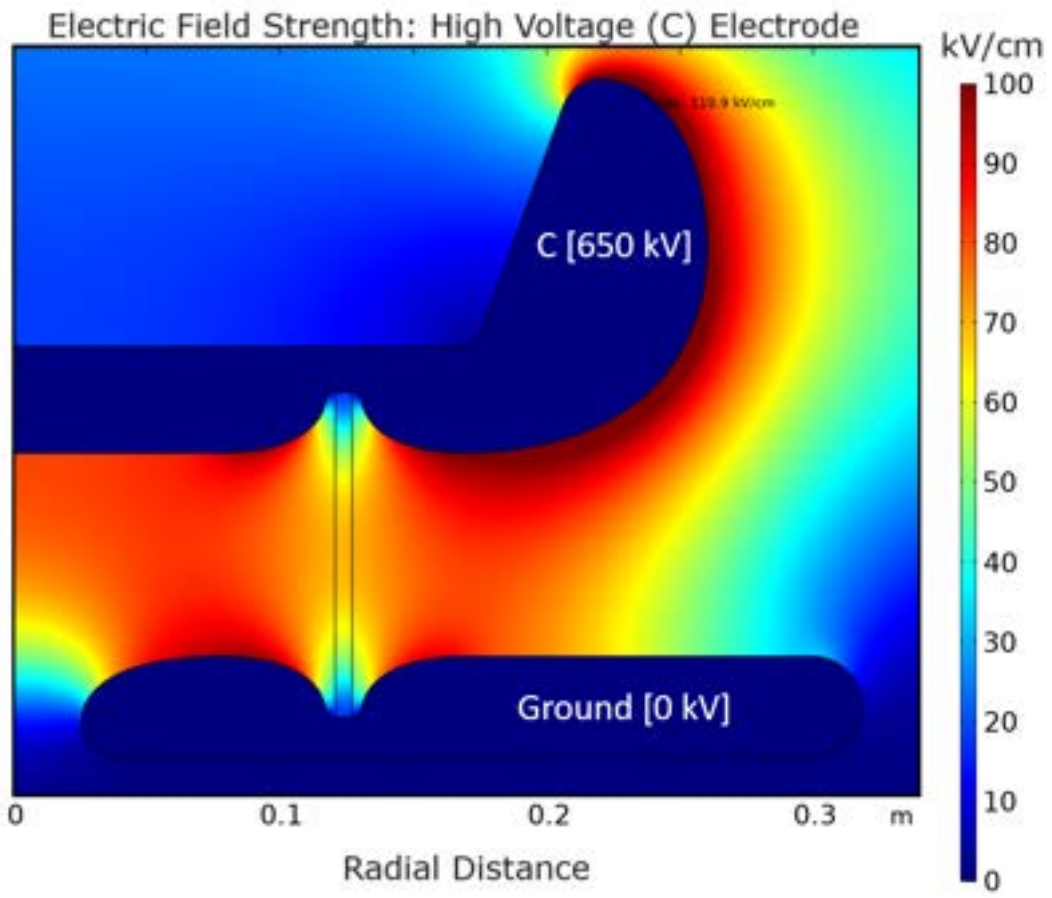

Figure 3.16: Electric field map of the C electrode in the test stand, held up by an acrylic cylinder from a ground electrode (electrode D). The engineering surfaces, including a hole in the D electrode, all employ Crawford Curves.

electrode is part of the ground return of the system, but is stood off from the rest of the ground in order to measure leakage currents. It holds up the C electrode at a distance of 7.6 cm with an acrylic cylinder to approximate the "load" of the nEDM measurement cell capacitance. This cylinder mates with both electrodes in a groove carved out by a Crawford Curve mirrored about the center of the groove. It was optimized to be:

$$\begin{cases} r_{gr} = 2.97031 \text{ cm} \dfrac{\tanh(0.5\cos t)}{\tanh(0.5)} \\ z_{gr} = 2.28346 \text{ cm} \dfrac{\tanh(0.5\sin t)}{\tanh(0.5)} \end{cases} \quad t \in (-\pi/2, 0) \tag{3.23}$$

Note that the groove itself was chosen to be 2.28 cm deep and 2.97 cm wide.

Furthermore, a Crawford Curve was also employed for some holes in the D electrode, to make measurements of the C electrode voltage using a field mill (such as [81]). Here h_D is the thickness of the D electrode:

$$\begin{cases} r_{gr} = \frac{3}{2} h_D \dfrac{\tanh(0.5 \cos t)}{\tanh(0.5)} \\ z_{gr} = \frac{2}{3} h_D \dfrac{\tanh(0.5 \sin t)}{\tanh(0.5)} \end{cases} \quad t \in (\pi/2, pi) \tag{3.24}$$

While we explored Crawford curves for all engineering surfaces, such as for where the B electrode's driving rod attaches to B, and for the edges of the button as in Fig. 3.17, these surfaces were not high-field enough or sensitive enough, respectively, to warrant the extra expense and fabrication difficulty.

A flawless B electrode approaching a flawless C electrode, perfectly parallel, will not produce any electrical discharge in the medium (a spark) [59]. However, engineering tolerances reflect real-world imperfection; a spark between these two surfaces is inevitable. The electrodes needed for the nEDM experiment will be made of nonconductive material with a thin alloy film, so we need to protect them from spark damage.

Rather than destroying the coating of the electrodes, we have elected to force the spark to occur on a thicker-coated replaceable button that screws into the bottom of B and the top of C as depicted in Fig. 3.17.

The energy of the spark, despite the reinforcements, must still be minimized. The energy of the system is depicted in Fig. 3.18. In Fig. 3.18(a), the total energy of the system and the energy of each electrode was calculated using $U = \frac{1}{2}QV$ as a function of the B's position as it decreases the distance to the C electrode. However, not all of that energy is available for the spark; the spark's energy is the difference between the potential energy before and after the charges moved, calculated assuming that the spark took all of the energy available to it to eliminate the potential difference between the B and C electrodes. The result is the blue curve in Fig. 3.18b. Plotted against the electric field between B and C, an estimate of the spark's probability (by over-applying[c] the analysis presented in the next section) shows that the spark might occur around the 2 mm separation with 0.07 J. This configuration is simulated in Fig. 3.20, where you can see that the high electric field occurs exactly where we

[c]The methodology applies to a stationary electrode geometry that increases its voltage (and therefore charge) to increase the electric field. Here, the geometry is moving with a stationary charge to increase the electric field. The assumption of this equivalence is untested.

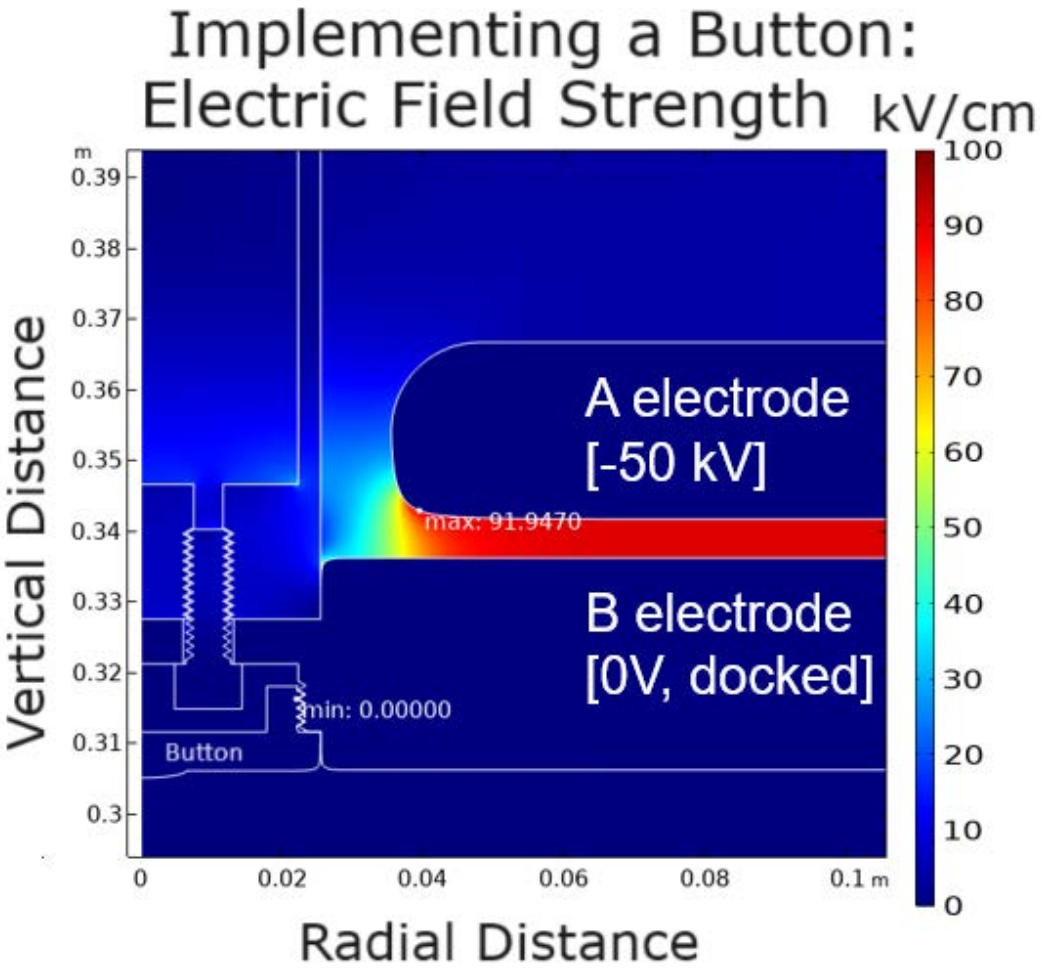

Figure 3.17: Quasi-axisymmetric close-up of the B electrode: Here we can see that a sparking button (left side of the figure) can also hide the hardware surfaces such as shaft screws for the B electrode. Note, however, that these screws are suggestive only, and are not correct in the 2D-axisymmetric framework.

want the spark to be—on the spark button. An added benefit to the removable button is that it can hide other engineering requirements. For example, shown in Fig. 3.19 on the B electrode, the button electrostatically hides the hardware connecting B to its rod. And the C electrode's stainless steel prototype will be very heavy, but we can move it around using a screw hole hidden by that spark button.

Our final design is depicted in Fig. 3.21, with the high voltage electrode shown in red. The ground return on the outer wall is created using 24 flat slats to facilitate access to the inner volume, and the COMSOL simulation in Fig. 3.22 shows that the total engineering surfaces work as designed. The final geometric gain is 18, and our final Emax is 116 kV/cm. The apparatus will reach our 650 kV target at around

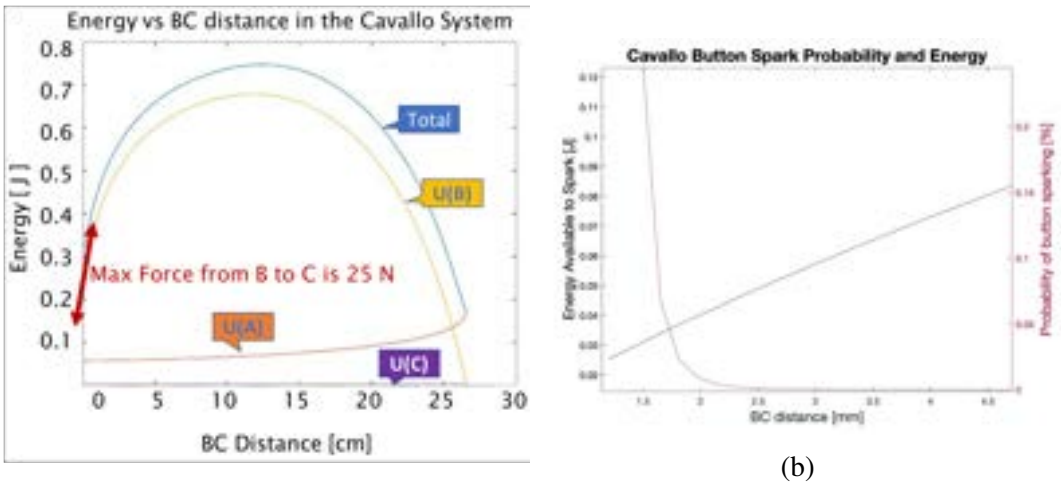

(a) (b)

Figure 3.18: Potential Energies in the first charge cycle of the Cavallo apparatus.

Left (a): Total electrostatic energy of each electrode as a function of the distance between the B and C electrodes. The force between the B and C electrodes is the derivative of U(B)-U(C), calculated to be less than 25 N.

Right (b): Electrical Discharge profile: The black curve (left) is the amount of energy available to a spark between the B and C electrodes, as a function of the distance between the B and C electrodes. The red curve (right) is the probability of a spark between the B and C electrodes at the fixed distance between them upon ramping. The closer the electrodes become, the lower amount of energy available to the spark; the probability curve implies the spark may occur when the BC distance is less than 2 mm, with only 30 mJ available.

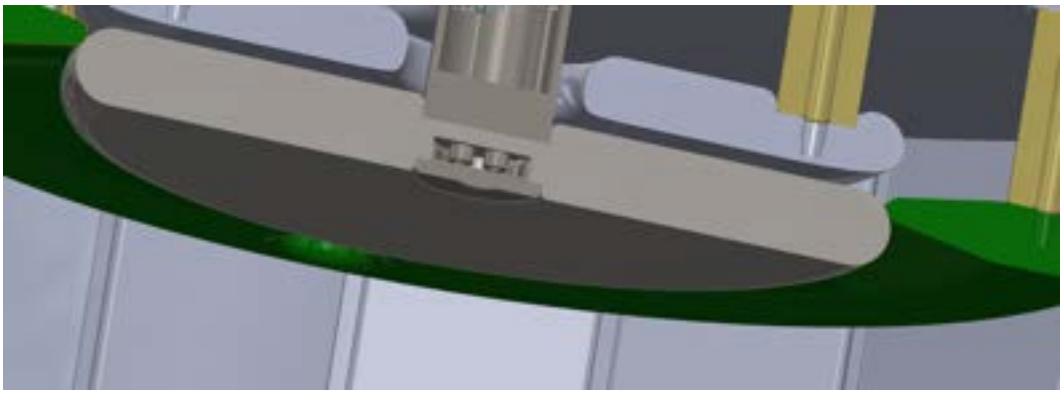

Figure 3.19: A Computer-Aided Drawing of the spark button and the shaft hardware for the B electrode.

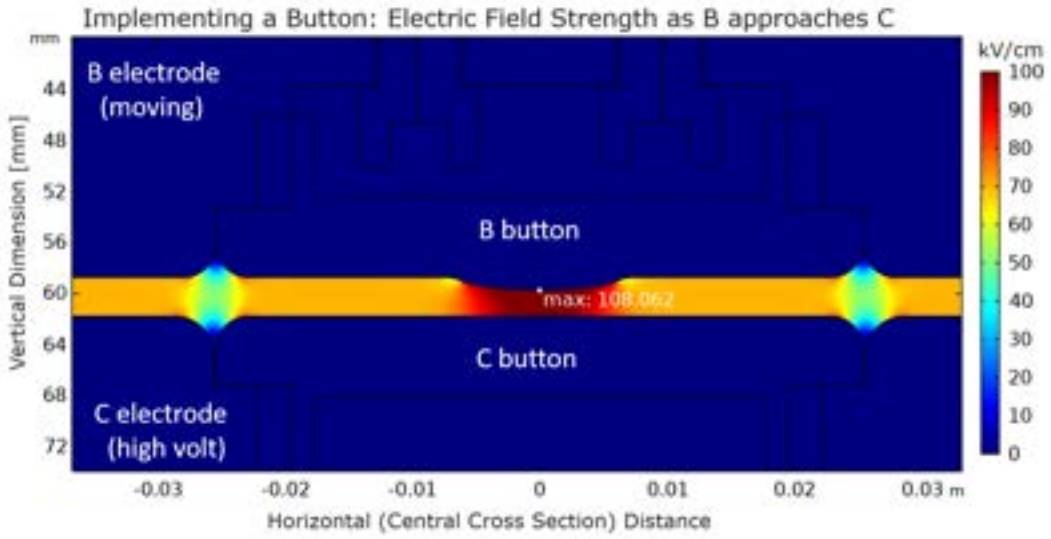

Figure 3.20: Sparking buttons: A replaceable button installed on both the B and C electrodes can protect electrodes by forcing a spark to happen on the buttons' thickened and replaceable surface. Note the high electric field to produce the spark in the desired location.

fourteen cycles.

3.5.3 Simulation Analysis

The probability of breakdown is often conceptualized as an electric-field threshold effect, but a comprehensive analysis of electric field ramping done by Phan et al. [57] at Los Alamos National Laboratory showed that not only does the strength of the electric field matter, but also the integrated surface area at that electric field strength via:

$$P_{breakdown} = 1 - \prod_{E_i} e^{-S(E_i)W(E_i)} \tag{3.25}$$

where effects on the breakdown probability such as the electrode roughness or the pressure of the medium are grouped heuristically into the $W(E_i)$ function. $S(E_i)$ is the surface area experiencing the electric field strength E_i. By using a measured curve (with the same measured helium pressure and similar electrode material and polishing) for the W function above, we can use Eq. 3.25 to calculate a breakdown probability for reaching[d] a certain voltage for an arbitrary electrode geometry.

[d]This work had low statistics to study time-dependent effects, such as holding the electric field once reached

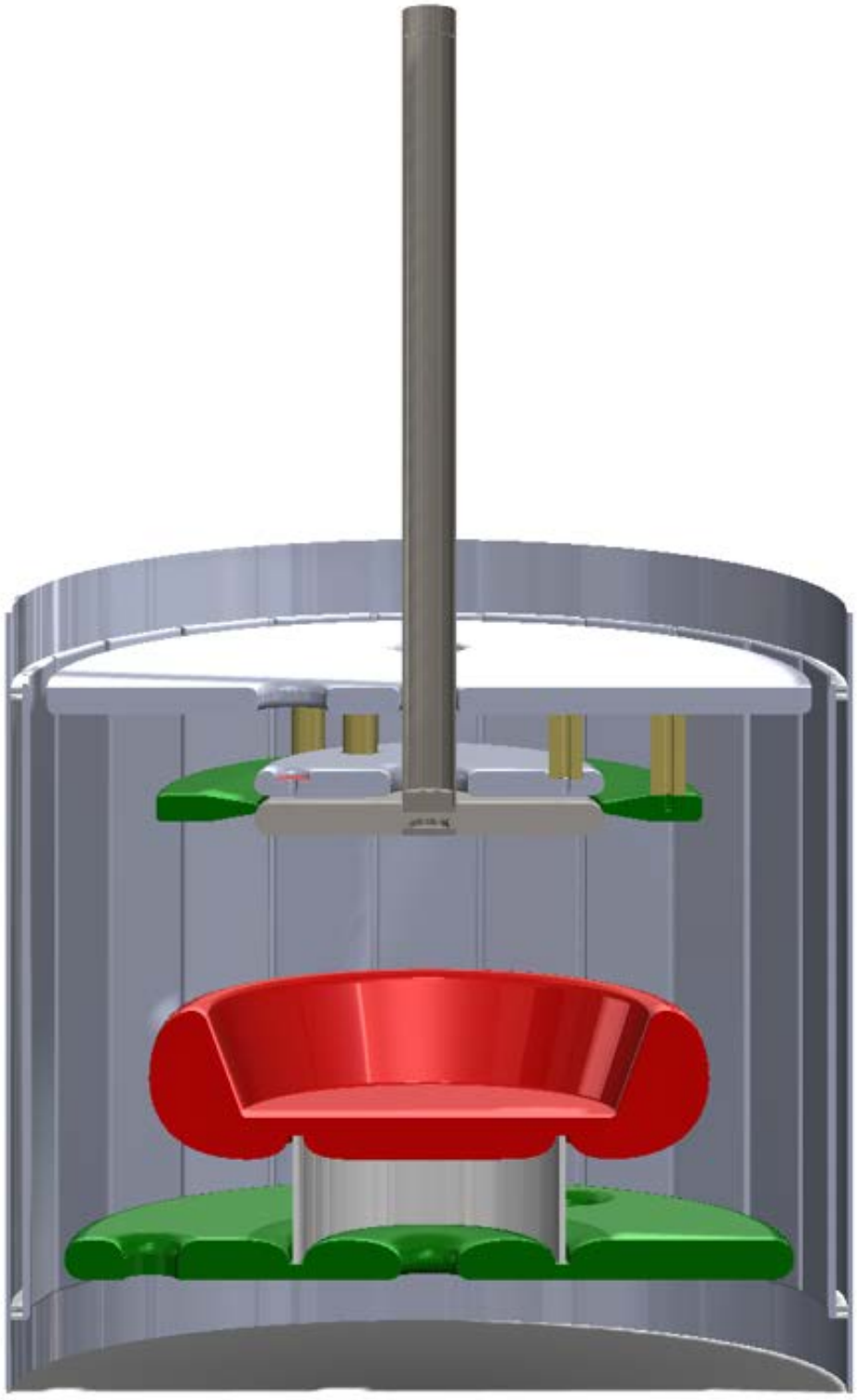

Figure 3.21: Final Computer-Aided Design: The electrodes are shown with their engineering surfaces, as well as a ground return made of 24 slats instead of a perfect cylinder for real-world access.

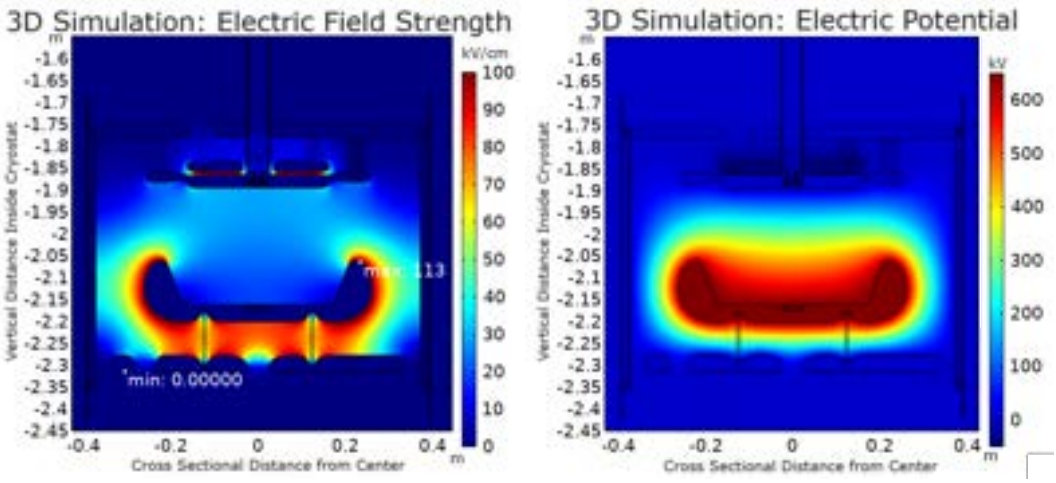

(a) Electric Field Cross Section (b) Voltage Cross Section

Figure 3.22: 3D cross-section simulation: Fig. 3.21 was imported into the finite element analysis program, and the running voltages of $V_A = -50$ kV and $V_C = 650$ kV were applied

Fig. 3.23 graphs the surface area of the Cavallo apparatus electrodes at the fully charged configuration depicted in Fig. 3.22a, as a function of electric field strength (binned to the nearest kV/cm). The most correct application of Eq. 3.25 assumes that the breakdown begins with a field emission at the cathode, so the highest probability of sparking occurs when the C electrode is the cathode. For this configuration, only the surface area of the C electrode matters.

However, if we allow the idea of a spark originating at the anode, note that most of the surface area for the anode surfaces (Grounds) are at the low end of the graph while a large portion of the C electrode's surface area is between 100 kV/cm and 113 kV/cm. The C electrode (sparking at the cathode) still dominates the breakdown probability calculation due to the shape of the W function—negligibly small for small values of E_i, but rapidly increasing for large values of E_i. Including the total surface area of all the electrodes gives us a generous upper bound of the breakdown calculation.

Processing the surface area fields of Fig. 3.23 into Eq. 3.25, we calculate the following predicted probabilities for the Cavallo apparatus breakdown:

	C electrode	All Surfaces
He at 12 torr	98.1772%	99.2525%
He at 600 torr	0.7169%	0.7828%
He at 1520 torr	0.0003%	0.0003%

The apparatus will certainly spark in vacuum, and studies at the three pressures will yield insight into charging up practices and minimizing sparking at both the B-C contact button and when the B electrode docks at the top ground ring. Future experimental tests will include a first set of electrodes fabricated out of stainless steel and electropolished for this exploration, before the more delicate coated plastic electrodes are ordered.

Furthermore, the physical asymmetry in anode (ground) and cathode (C electrode) geometry can make the breakdown origination surface obvious. If the discharge must originate at the cathode, then flipping the anode and cathode (charging the C electrode to a negative voltage as required in the final experiment) results in a significantly smaller breakdown prediction. If the discharge can originate at either the anode or cathode, then the breakdown prediction is equal in both charging configurations (positive or negative).

Eq. 3.25 was also used to create Fig. 3.18b, the probability of sparking as the B electrode approaches the C electrode. The surface area vs. electric field strength $SA(E_i)$ was calculated for each physical step of the B electrode as it approached the C electrode, using the initial loaded charge on B. This initial charge is equivalent to the first stroke of the Cavallo apparatus, where the strongest difference in charge between B and C (and therefore most energy available to spark) happens. However, note that Eq. 3.25 was derived from a charge up of a voltage from an electrical power source, NOT from an in-situ change of voltage via a change in geometry. We caution that the equation (or its W curve) might not hold in this case, and therefore further tests of the button design hold merit.

Following the results of the test apparatus simulations, we placed these electrodes in a finite element analysis of their position in the final nEDM experimental apparatus, shown in Fig. 3.24. Note that the electric field around the Cavallo electrodes is less than that in the Cavallo test apparatus (Fig. 3.22a) due to more space, but also that the electric field is on the order of the test apparatus (120 kV/cm) around the measurement cells. This is ideal because the voltage multiplication should not be the limiting factor in the final nEDM experiment as it pushes the limits of neutron electric dipole moment sensitivity.

The survivability of the nEDM high voltage electrodes—$1 - P_{breakdown}$ of Eq. 3.25 is plotted in Fig. 3.25 as a function of the final voltage stored on the high voltage electrodes (including the C electrode and the high voltage cell electrode from Fig. 3.24). Note that for tests in “vacuum” (<12 torr), it is prudent to stay well below the

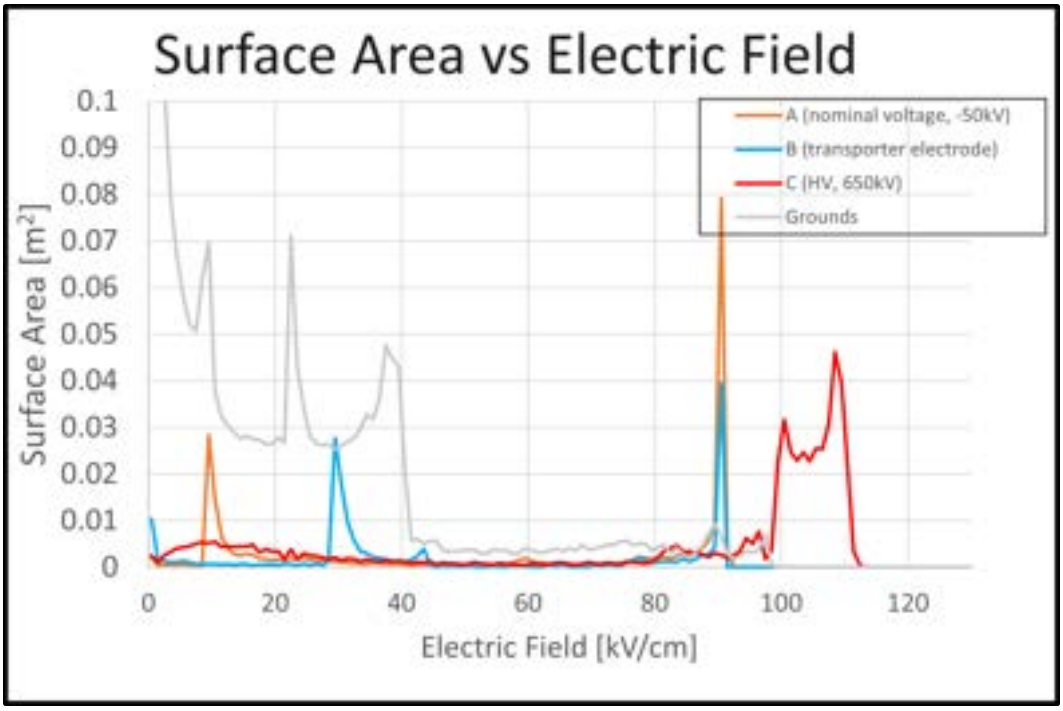

Figure 3.23: Surface Area of the Electrodes: Surface area as a function of electric field strength. The finite element analysis program integrated through each surface area element, and histogrammed that surface area by its surface electric field strength.

desired 650 kV, but for "atmosphere" (600 torr) we can choose our breakdown risk approaching that desired 650 kV. Furthermore, by doubling the pressure (1520 torr), the system is predicted to be robust as the knee in the survival probability curve is far from the desired 650 kV. The probability of breakdown (Eq. 3.25) at 1520 torr for the system for the system to ramp to 650 kV is on the order of 10^{-6}.

3.5.4 Cryogenic Test Apparatus

The Cryogenic Test Apparatus will let us run the full-scale electrode prototypes at superfluid helium pressures up to 2 atm. Recall that the apparatus was designed around a recycled bucket-type Dewar of 3 m height and 1 m outer diameter, the Caltech "Half Scale" Cryostat [82] of Fig. 3.12. While the inside of the cryostat may be held at vacuum or hold cryogens during operation, its walls contain cooling loops to flow cryogens as thermal shielding for its inside volume—one set attached to the bucket, and the other for a liquid nitrogen–temperature shield.

The rest of the instrumentation, including the refrigeration devices, are attached to the lid as a few–thousand-pound insert depicted in Fig. 3.26. The upper half of the insert consists primarily of the refrigeration devices such as the 4 K bath, while the

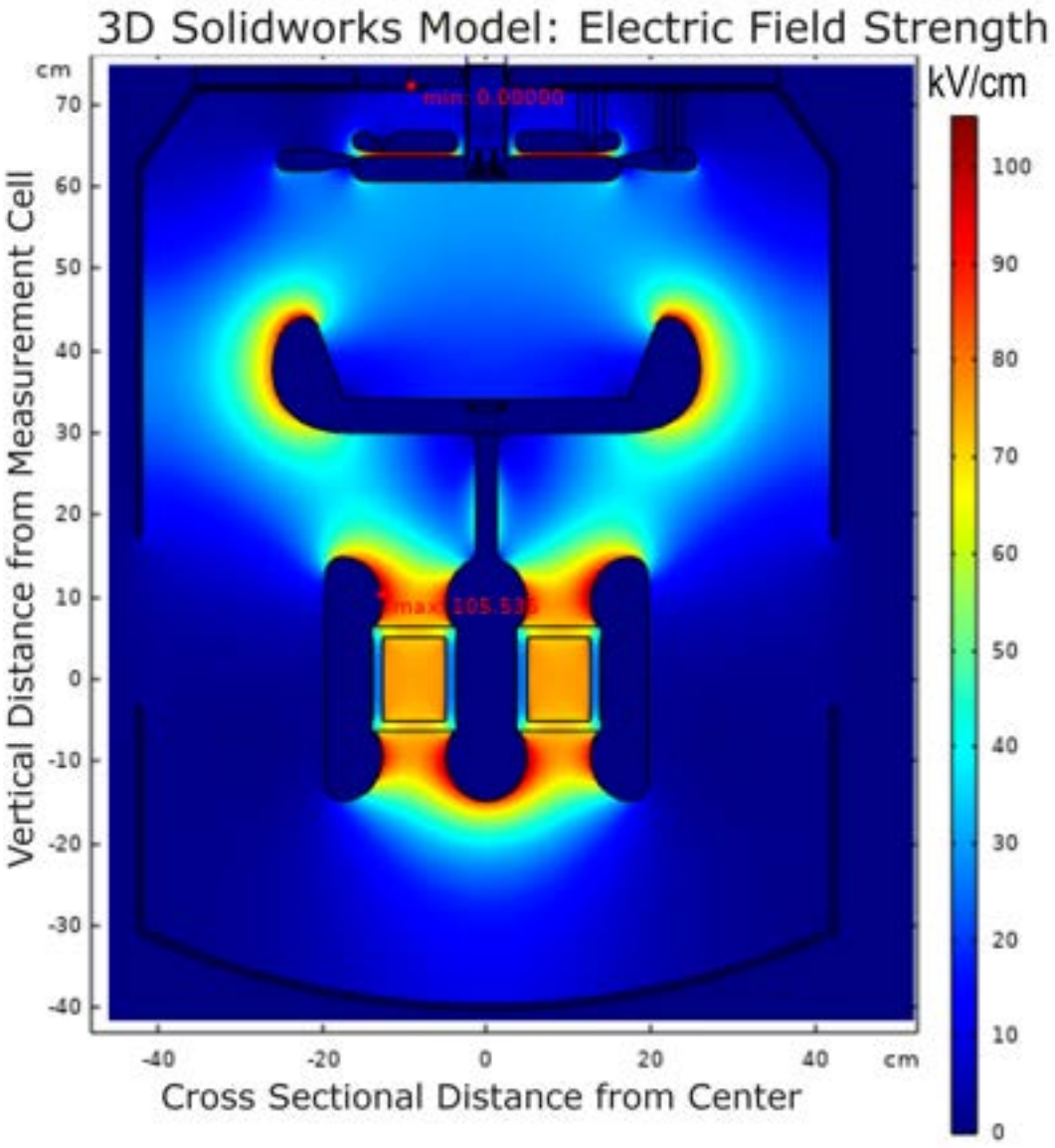

Figure 3.24: Electric Field in the Future nEDM Experimental Volume: 3D Model cross-section of the Cavallo Electrodes in their space in the final nEDM experiment, with the measurement electrodes attached below.

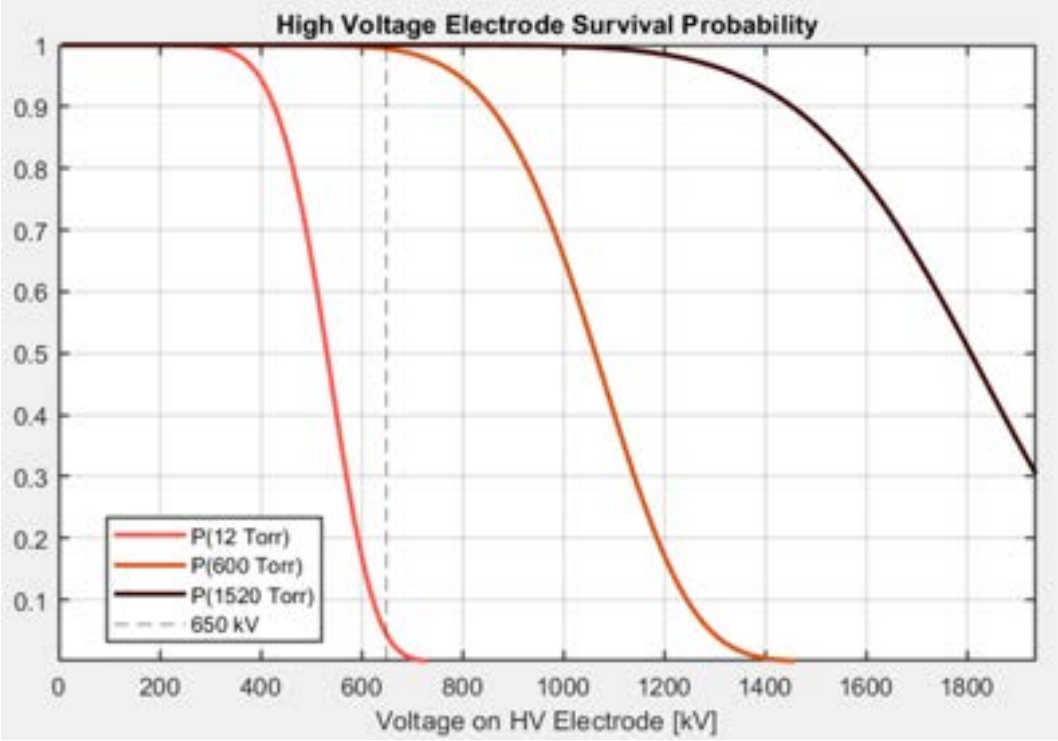

Figure 3.25: High Voltage Electrode Survival Probability: As the ramped voltage increases on the high voltage electrodes (the measurement and C electrode connected together in Fig. 3.24), the probability of reaching that voltage is calculated, to create these probability curves.

Figure 3.26: Center: CAD model of the Cryogenic Insert for the Cavallo Cryogenic Test Apparatus. Left: Photograph of the refrigerator for the insert at present. Right: Photograph of the CV for the insert being used at room temperature, with hard working students for scale.

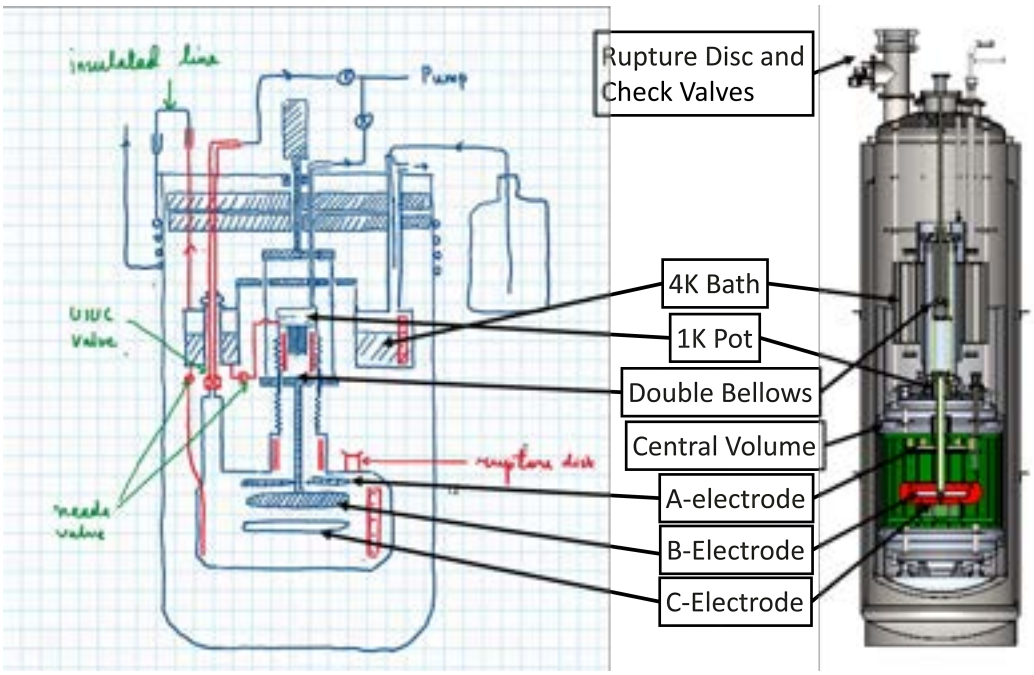

Figure 3.27: The Inner Workings of the Cryogenic Apparatus. Left, an illustration of the operation of the cryogenic apparatus drawn by our Cryogenic Physicist, Weijun Yao. Right, a Computer-Aided Design created by our Cryogenic Engineer, Chris O'Shaughnessy.

lower half is the central volume (CV) where the Cavallo multiplier electrodes and ground return reside. The figure includes photographs that depict the current state of this insert; the 4 K bath hangs from the lid on a stand, and the CV is independently prepared for room-temperature Cavallo charging tests.

The fundamental operation is best understood with Fig. 3.27. Liquid helium cools the insert to 4 K, and accumulates in the doughnut-shaped 4 K bath in the center of the insert. A smaller 1 K pot is fed from this 4 K bath by a 1/8 inch tube, and cooled evaporatively down to about 1.5 K by pumping on the helium in the volume. This 1 K pot is in thermal contact surrounding the top of the CV, cooling the bottom of the insert to superfluid temperatures. The UIUC valve depicted is a large (3 cm aperture) nonmagnetic, superfluid-helium tight valve developed by the University of Illinois with Bartoszek Engineering [83].

The Cavallo electrodes are nestled in that CV, with a double-bellows assembly maintaining the total bath volume and pressure constant while an external linear actuator drives the B electrode as illustrated in Fig. 3.28. While the CV is rated for a 40 psi differential, the double-bellows assembly will not survive a full 2 atmosphere pressure differential. For this reason, it may eventually be advantageous to fill the

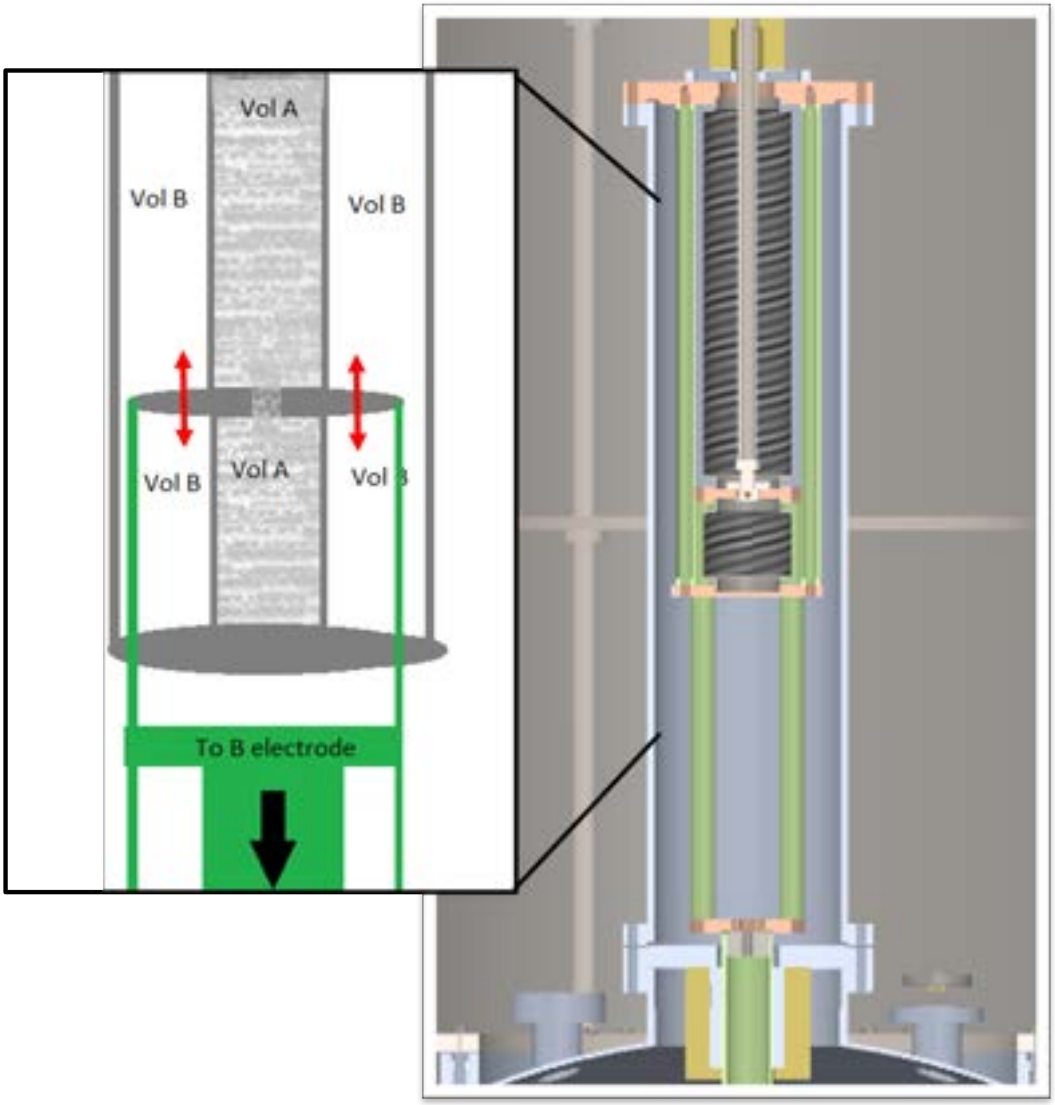

Figure 3.28: Double Bellows Assembly: the Computer Aided Design (zoomed in from an earlier version of Fig. 3.27) shows the workings of the double bellows assembly, which keeps the volume of the CV constant as the B electrode is moved from an actuator outside of the volume. In the foreground, the zoomed illustration better depicts the conservation of volume by explicitly showing the volumes of the double bellows assembly.

vacuum inside the Caltech Cryostat with cryogens, allowing us to put the CV at an absolute of 2 atm but a differential of only 1 atm, and is reflected in procedure documents.

It is unnecessary, time consuming, and difficult to cool down to 2K for every measurement required of the Cavallo Multiplier. Many tests can be done with just the CV acting as a vacuum chamber, including a lower voltage multiplication

(geometry) test in room temperature N_2 or SF_6. A higher voltage multiplication test can occur in liquid nitrogen, which has similar electrically insulating properties to the liquid helium quantified [84] [85].

3.5.5 Initial Measurements at Room Temperature

3.5.5.1 Central Volume Setup

The room temperature low-voltage tests used the central volume (CV) of the cryogenic apparatus as a standalone vacuum-tight apparatus, driving the B electrode directly with the linear actuator as seen in Fig. 3.29. Fig. 3.31a shows a view of the top of the CV from below, so you can see the B electrode on its G10 rod, followed by the ground ring, and then the top of the ground return, polished and ready for high voltage. The bottom of the ground return, with the C and D electrodes, is also photographed in Fig. 3.31b. Take special note of the sacrificial button the C electrode (there is also one on the B electrode that may not be as visible), and the holes in the D electrode for no-contact voltmeter installations.

The transition from simulation to reality included designing the ground return as a set of 24 slats instead of a cylindrical shell for access as photographed in Fig. 3.31b. Note in Fig. 3.30b as in the CAD model (Fig. 3.21), how the C electrode is held up by an acrylic cylinder. All electrodes were machined (see Fig. 3.30a) by Hand Precision Machining, mechanically polished (Irving Polishing) and electropolished (Able Machining), such that optical faceting from the machining process disappeared. A strain gauge was used to calibrate the B electrode's position in the apparatus.

3.5.5.2 Voltage Multiplication Measurements

The "voltage to be multiplied"—the A electrode's voltage—was fed from a Matsusada power supply (AF-100R0.1-LCG) into the central volume by a Ceramtec feedthrough [75]. The no-contact voltage measurement device providing the voltage readings on the C electrode was a field mill, discussed in section 3.6. Early tests were done in gaseous nitrogen, since sparking happened more readily when the central volume was evacuated assumedly due to charge motility. We decided to run the tests in Sulfur hexafluoride (SF_6) for its great insulating properties.

Recall from subsections 3.5.2 and 3.5.3 that our two approaches for charge-transfer sparking protection include removable/thicker-coated buttons between the B and C electrodes, and managing the voltage on the A electrode as the B electrode returns

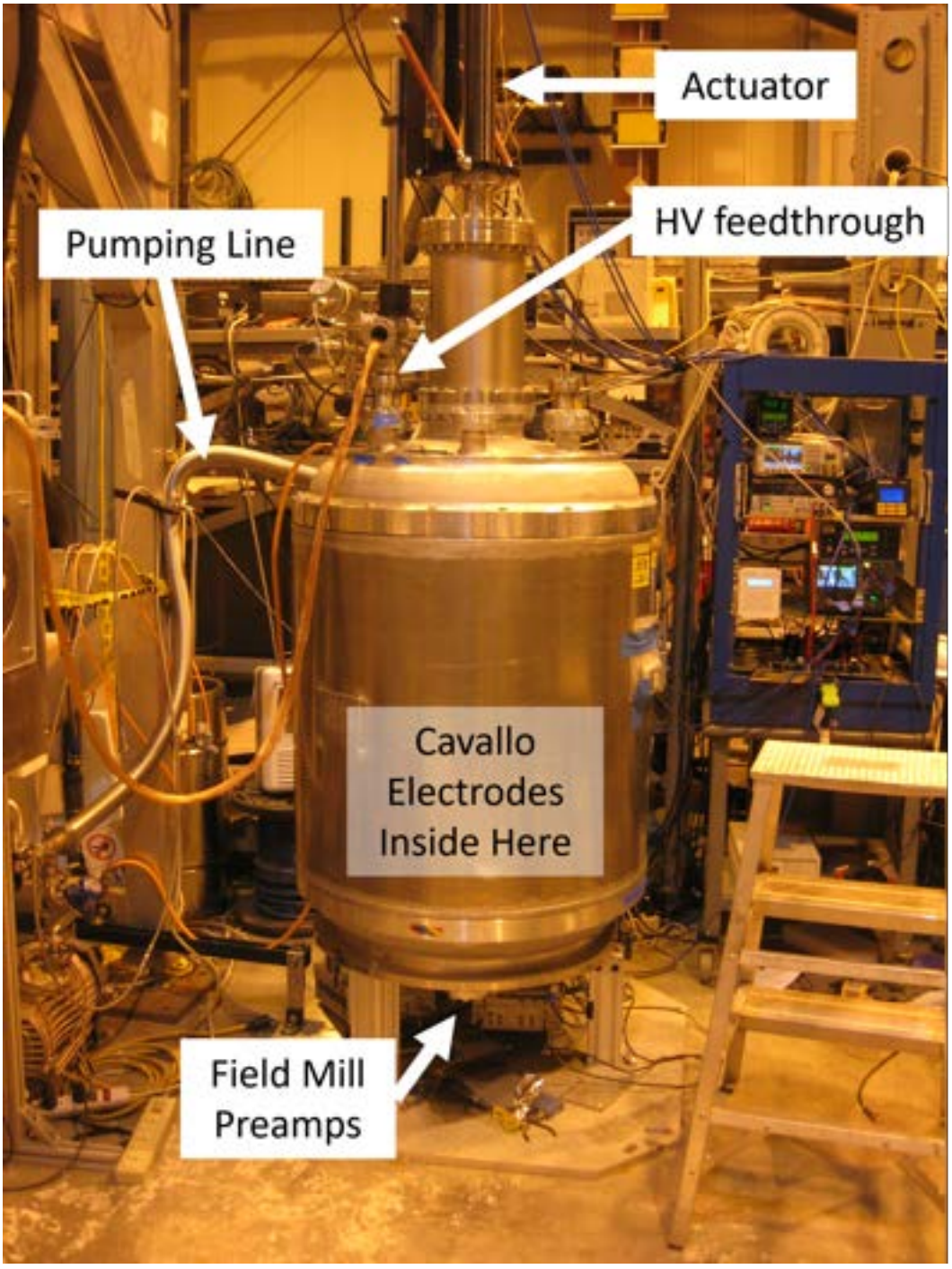

Figure 3.29: The CV in the laboratory: Eventually to hang from the Cryogenic Insert, the Central Volume was outfitted with a temporary pumping line, actuator, and electrical instrumentation to test the Cavallo apparatus in non-cryogenic conditions.

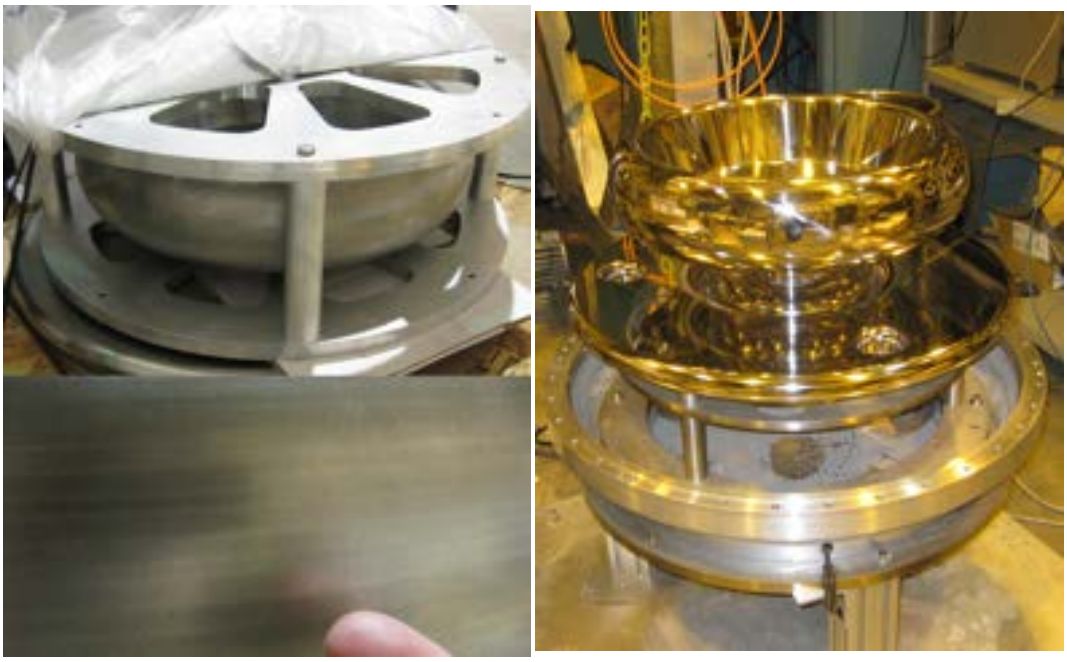

(a) Before Polishing

(b) After Polishing and Assembly

Figure 3.30: Inside the apparatus (bottom) before and after polishing. Top Left: The C and D electrodes as shipped. Bottom Left: Zoom in of the C electrode facets. Right: The bottom of the CV before the ground return and can are installed.

back to the ground ring near the A electrode. The latter turned out to be more important than we initially imagined.

Fig. 3.32 graphs some early data with obvious discharges at ~230 s and ~880 s. The top of each bump corresponds to each half-cycle of the Cavallo multiplier—the B electrode touches the C electrode. The bottom of each bump corresponds to the B electrode returning to the ground ring near A. The large instantaneous drops in voltage correspond to a partial discharge that affected the C electrode. The discharges occurred as the B electrode approached the C electrode, before docking with the C electrode, about when the B electrode's theoretical voltage is at its highest. It is not clear where these sparks occur, or who is sparking to whom, but one discharge can produce x rays that can prompt discharge in other places of very high electric field. The heuristic solution that post-baccalaureate scholars Theresa Sandborn and Isaac Smythe, and postdoctoral scholar Jason Surbrook discovered, was to turn down the voltage on the A electrode (but non-zero as the B electrode returns with some residual charge).

Being careful to not spark—a smaller voltage on the A electrode, turning down the voltage after the B electrode begins its journey, etc.—cleaner runs are plotted in

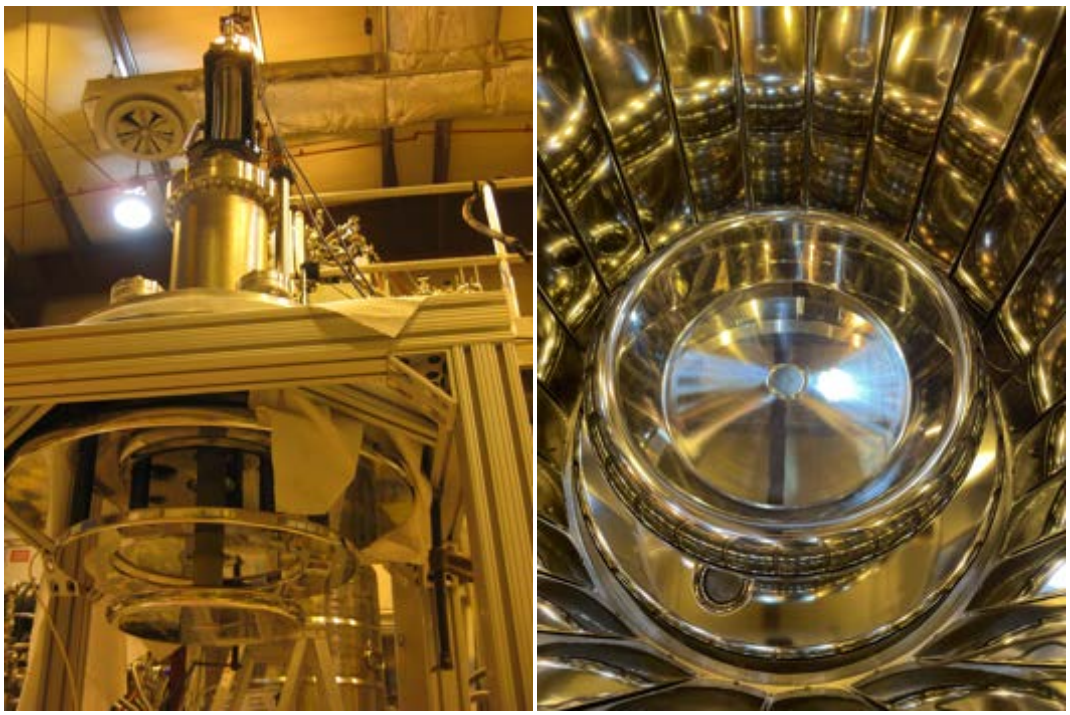

(a) Top of CV (b) Bottom of CV

Figure 3.31: Inside the apparatus. Left, top of CV, including the B electrode, the docking ground ring, and the lid of the ground return. Right, downward view of the bottom of the CV, including the C and D electrodes, and the ground slats.

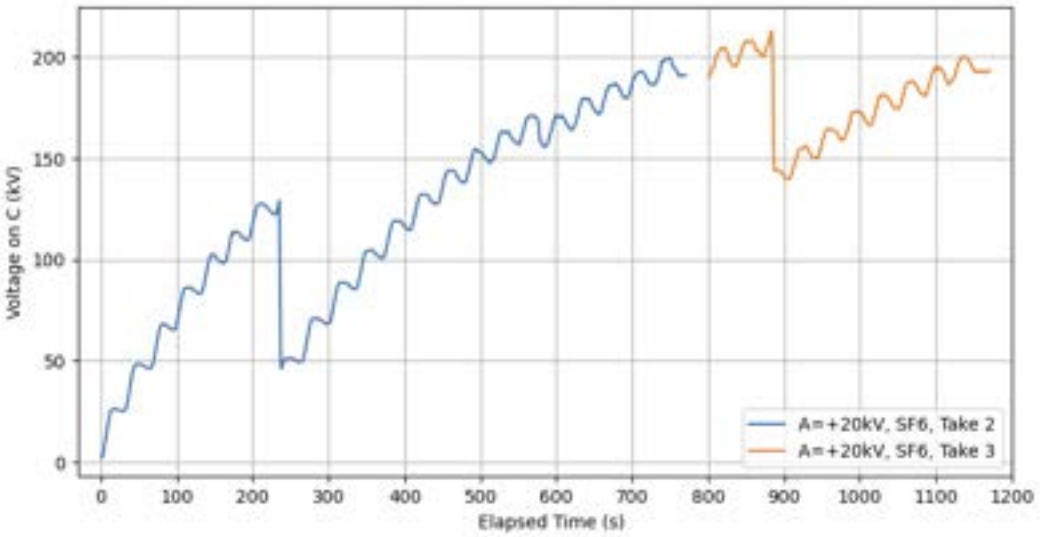

Figure 3.32: Voltage Multiplication in the Cavallo multiplier for fixed V_A = 20 kV. Note the frequent breakdowns as B traveled towards the C electrode.

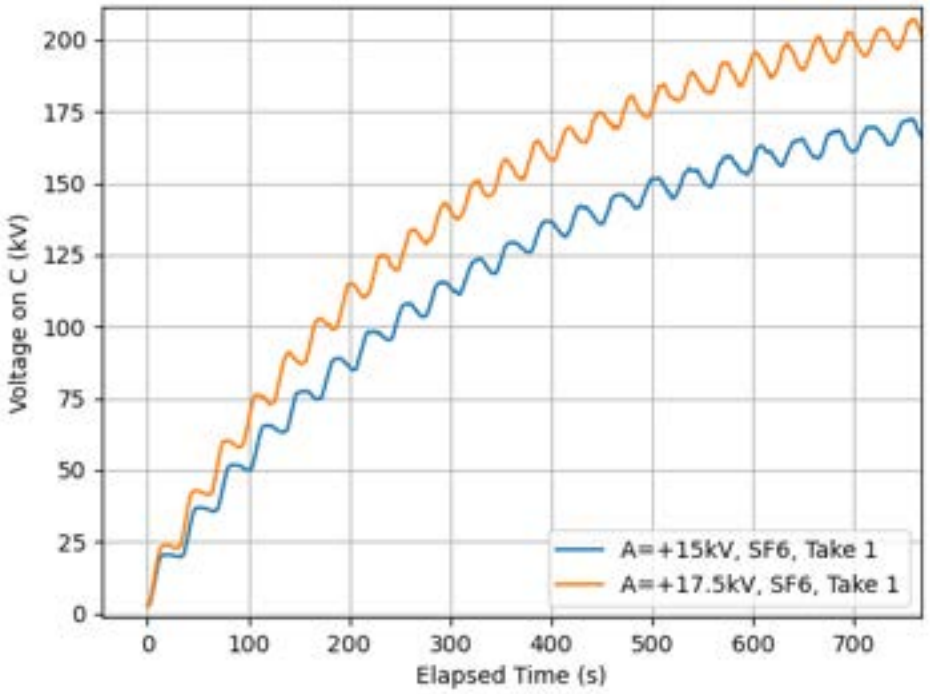

Figure 3.33: Voltage Multiplication in the Cavallo Multiplier in SF6 for a few initial voltages on the A electrode.

Fig. 3.33. The different initial voltages on the A electrode produce similarly shaped charging curves, scaled by that initial A electrode voltage.

The Cavallo Multiplier's capabilities were pushed in Fig. 3.34. With the A electrode voltage turned up to 25 kV, the Cavallo Multiplier reached 250 kV before a large discharge. After this discharge, subsequent charging cycles at the initial V_A= 25 kV and lower voltages suffered a cutoff at about 120 kV, with discharging evident by the rough shape of the bumps. Burn marks could be seen on the ground ring and the C electrode, and surprisingly, mechanical hand polishing with a Dremel of fine-grit sandpaper (1000 and then 2000) removed this cutoff ceiling, restoring the previous performance without the steps taken in Fig. 3.30a.

The degradation of the smoothness of the bumps in the initial run in Fig. 3.34 are not significant for the charging voltage of the C electrode. They, instead, signify that the field mill measuring the voltage needed some maintenance.

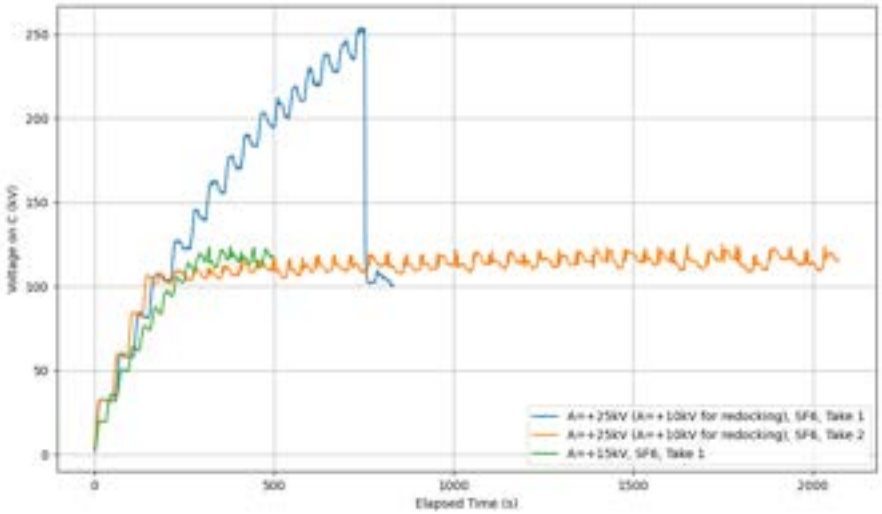

Figure 3.34: Voltage Multiplication in the Cavallo Multiplier in SF6 for a large initial voltage and subsequent breakdown activity.

3.6 Non-Contact Voltage Measurements of the Cavallo Apparatus

Voltage verification inherits the same feedthrough struggles as the measurement electrodes; if one cannot support a 650 kV feedthrough for an input, one cannot support one for an output. For at least the room temperature and cryogenic Cavallo tests, it is essential to measure the multiplied voltage produced for analysis.

Furthermore, the scope of future work on no-contact voltage measurement is up for debate in the nEDM@SNS collaboration. The scintillation produced by the capture products (the proton and triton) gives us an in-situ measurement of the electric field inside of the measurement cell. Scintillation light yield is inversely proportional to the experienced electric field [86].

The scintillation damping does not give a measurement of the voltage applied outside of the cell, just of the electric field felt inside of the cell. Relying only on the scintillation light leaves the experiment blind to high voltage issues. One cannot differentiate between charge buildup cancelling the field inside of the cell, or the high voltage electrode discharging. How does one tell when the Cavallo apparatus needs to recharge the high voltage electrode? Consider, if upon commissioning, no scintillation light is detected? A way to externally measure the voltage in the central volume is advantageous for a variety of troubleshooting issues.

Various schemes were considered to create a no-contact voltage measurement device,

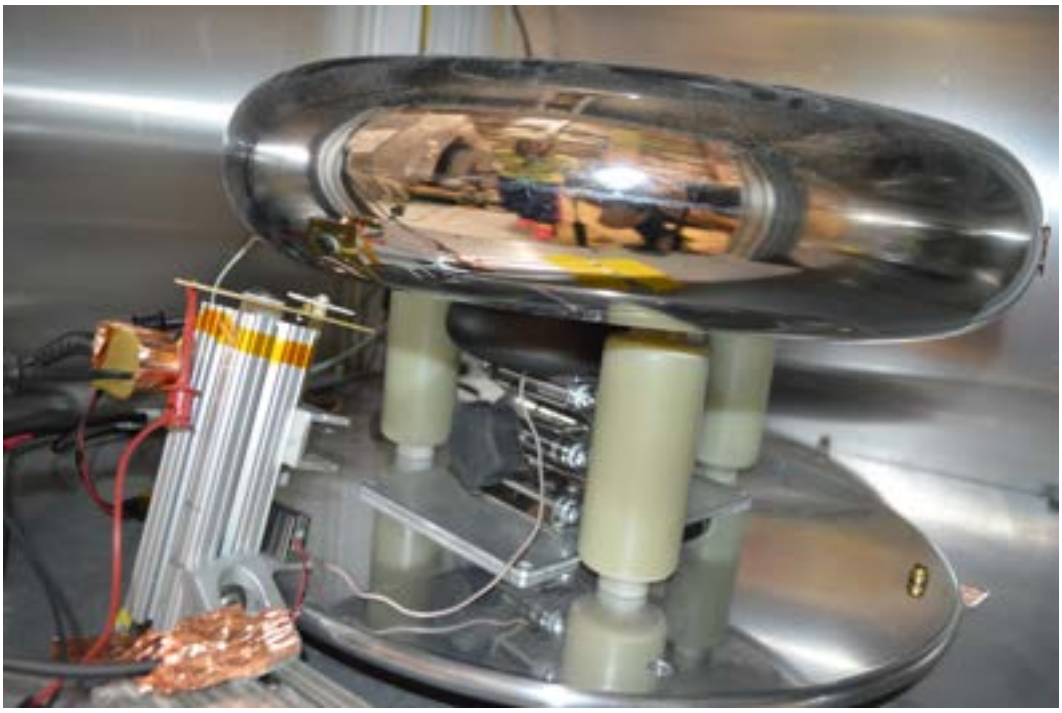

Figure 3.35: Photograph of the wiggling capacitor voltmeter in position near the high voltage electrode. Note the grounded plate above the extruded aluminum base, and the delicate wiggling plate above it (appearing white in the photo towards the right side of the grounded plate).

including a wiggling capacitor for the room temperature demonstrator, a field mill for the cryogenic apparatus, and a micro-electromechanical system (MEMs) for the final nEDM measurement.

3.6.1 Wiggling Capacitor Voltmeter

A wiggling capacitor voltmeter consists of a sense electrode disk that is vibrated in the fringe field of the high voltage electrode by a piezo-actuator. The change in capacitance drives a change in charge, which one measures in a preamplifier connected to the disk providing a virtual ground:

$$\frac{dQ}{dt} = V\frac{dC}{dt} \tag{3.26}$$

A hypothetical cryogenic wiggling capacitor "voltmeter" could use a PD410 ceramic from Potomac Instruments [87], which would have an oscillation amplitude around 25 microns at 4 K.

A prototype of this device provided measurements for the room temperature demonstrator prototype discussed in section 3.4, photographed for figure 3.35. In this

prototype, the sense electrode disk (plated circuit board material with 1 inch radius) was driven at a 40 micron amplitude at 40 Hz by a room-temperature piezo-actuator (Thorlabs' PK2FVF1), and the output of the preamplifier (Stanford Research SR556) was quantified by a lock-in amplifier (Stanford Research SR556). The lock-in amplifier shared a reference oscillator with the piezo-actuator's driver (an operational amplifier, TI OPA548), yielding a voltage amplitude proportional to the lock-in amplifier's out-of-phase signal.

The signal was calibrated in-situ by an electrometer (Keithley 617) temporarily connected to the high-voltage electrode, which reported the voltage as the electrode was charged. This calibration was heavily dependent on the exact position of the prototype, as the difference between the electric field at the top and bottom of the sense electrode disk's 40 micron sinusoid is very small; in simulation, that difference is 1 V/mm. Examples of these calibration curves are shown in Fig 3.36. Note how the slopes of the different calibration curves are similar, but the offset varies widely depending on the exact voltmeter position. With the large scaling between lock-in voltage to kilovolts, a small bump was enough to void the calibration. For the March calibration shown (the black set of points and line), the voltmeter was moved much closer to the C electrode in trying to keep the voltmeter's wiggling plate parallel to the C electrode's surface tangent. The other three calibration curves were used with the voltmeter further away (and not pointed directly at the C electrode).

External noise was limited by a grounded plate separating the piezo actuator from the sense electrode disk. Its extruded aluminum base was also grounded, and the preamplifier was enclosed within the Cavallo demonstrator apparatus enclosure. Its output to the lock-in amplifier fed through a small hole on top of the box.

The wiggling capacitive voltmeter clearly has its limitations of calibration between a very large value (100 V to measure kilovolts) and a very small value (thousandths in a lock-in amplifier amplitude). The signal is very small, measuring $\Delta E = E(x(top)) - E(x(bottom))$. The rest of the non-contact voltmeters in this section instead measure the difference between the electric field at its location and E = 0, yielding a much larger signal.

3.6.2 Field Mills

Field mills are already a well-developed tool, both in climate science [88] to measure atmospheric charge buildup [89] (including applications such as rocket and spacecraft launching protection by predicting lightning [90]), and also in high volt-

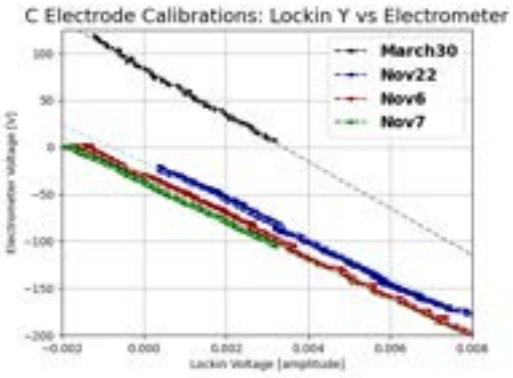

Figure 3.36: Calibration Curves for the wiggling capacitor voltmeter.
The fits for the calibration are as follows:

March (top curve):	-24859.1 V/amplitude + 84.4 V
Nov_22 (2nd from top):	-20451.0 V/amplitude - 16.2 V
Nov_6 (2nd from bottom):	-20951.1 V/amplitude - 31.0 V
Nov_7 (bottom):	-20780.3 V/amplitude - 37.4 V

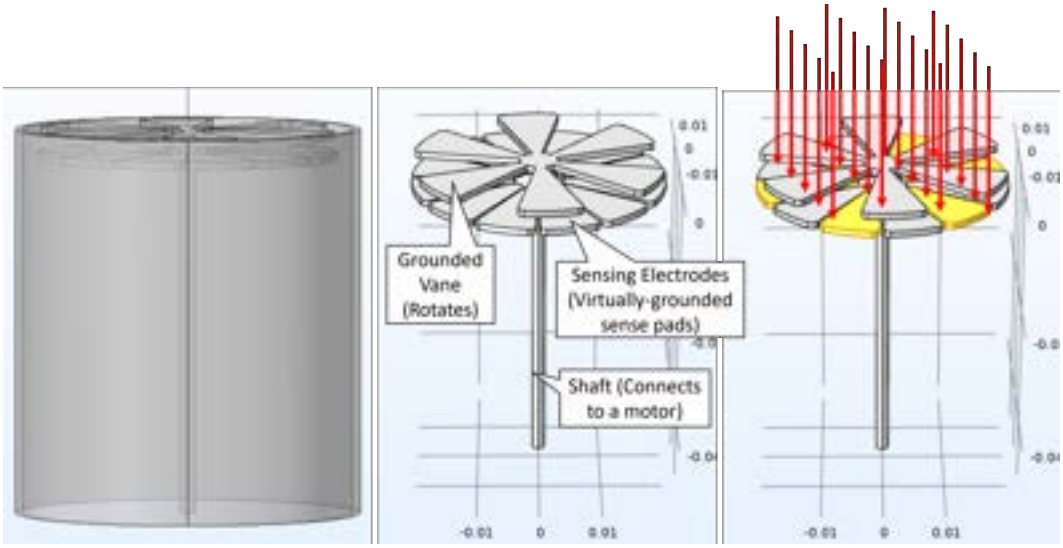

Figure 3.37: A Stereotypical Field Mill: Left, field mill in guarded enclosure (only electric field lines above make it to the sense electrodes). Center, field mill anatomy. Right, field mill cartoon showing one set of ganged sense petals in yellow (and the other set in grey), with the electric field lines coming in from above (in red), getting partially blocked by the field mill vane.

age generation where they are known as “Generating Voltmeters” [91] [92]. An appropriate application for these devices is to measure the high-voltage electrode in the cryogenic Cavallo apparatus, and we built three prototypes:

- Proof of concept demonstrator using a conventional (vacuum-incompatible, cryogen-incompatible) stepper motor
- An intermediate prototype with a homemade cryogenic-safe saddle coil motor
- Robust field mill, with a strong motor used for the measurements in the cryogenic apparatus (first at room temperature, but eventually at liquid nitrogen temperatures).

All of these field mills operate on the same principle: a grounded vane rotates a small distance above a set of sense electrodes. As it rotates, symmetric holes in the vane expose or shield the sense electrodes from the electric field above, with its rotational symmetry being half that of the sense electrodes. Every other sense electrode is ganged to “multiply” the signal, as they are experiencing the same amount of shielding from the vane.

This operation is illustrated in Fig. 3.37. All the field mill’s parts are labeled in the center graphic of the illustration, and the left shows how the radial field lines are shielded from the sense electrodes by a conducting cylinder, allowing only field lines that pass through the field mill vane to find the sense electrodes. On the right, those field lines are depicted as red arrows descending onto the field mill’s vane and sense electrodes. The yellow sense electrode “petals” are ganged together, as are the grey sense electrode “petals” in the figure. This illustration shows how each of the ganged “petals” are experiencing the same electric field “shadow” from the field mill’s vane, and is further depicted in Fig. 3.38. One can imagine the “shadow” evolving as the field mill vane rotates as seen in the figure, completely covering and uncovering every other sense electrode.

To design a field mill for the Cavallo apparatus, one must be wary of corona points and edges producing high electric fields. The conventional “flower petal” field mill design as in Fig. 3.37 contains an unnecessary number of external edges. Consider, instead, its reverse: a waffle-shape at the bottom left of Fig. 3.40; it allows the same number of electric field lines to the sense electrodes, but has guarded internal edges and larger external radii. Fig. 3.39 illustrates the electric field hotspots for both types of field mills in the same simulated environment; both field mill vanes were

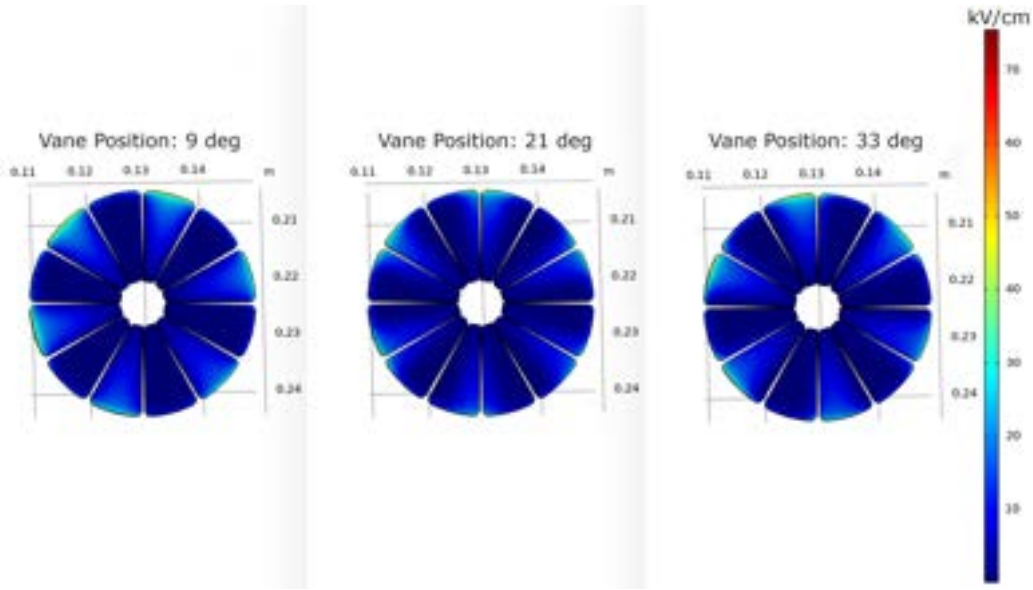

Figure 3.38: "Shadows of the Field Mill Vane:" This finite element analysis simulation measured the electric field lines the sense petals experience from a voltage source above, as a function of the position of the field mill vane.

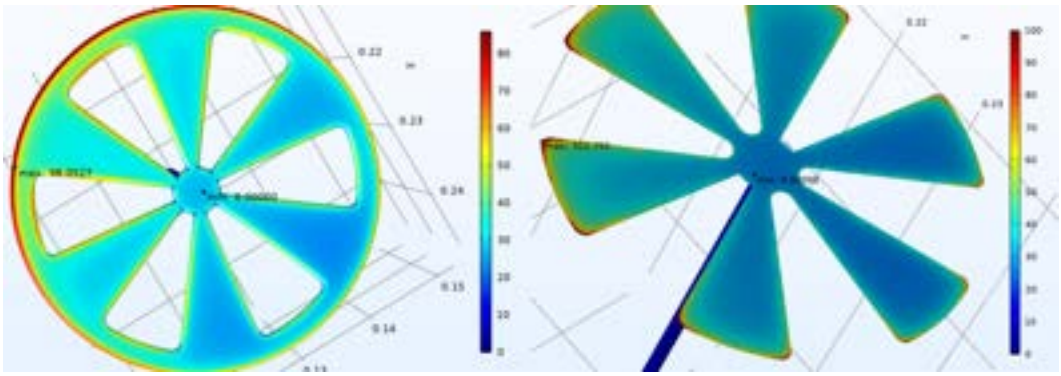

Figure 3.39: Electric Field Experienced at the Surface of the Field Mill Vane (as simulated in COMSOL): Left, the waffle shape guards its internal edges and has a larger external edge radius. Right, the flower shape has many sharp corners that act as corona points.

exposed to the same conditions within the simulation, but the flower created much higher electric field hotspots (313 kV/cm) than the waffle (98 kV/cm).

These electric field hotspots can be further managed by managing how deep into the shield (or D electrode) these field mills sit. However, the deeper they sit, the weaker their output signal. This balance is best done by practice instead of simulation.

The waffle shape is difficult to machine, and we could not produce it in-house. A 3-hole punch is much simpler to machine ourselves, and performs almost as well as

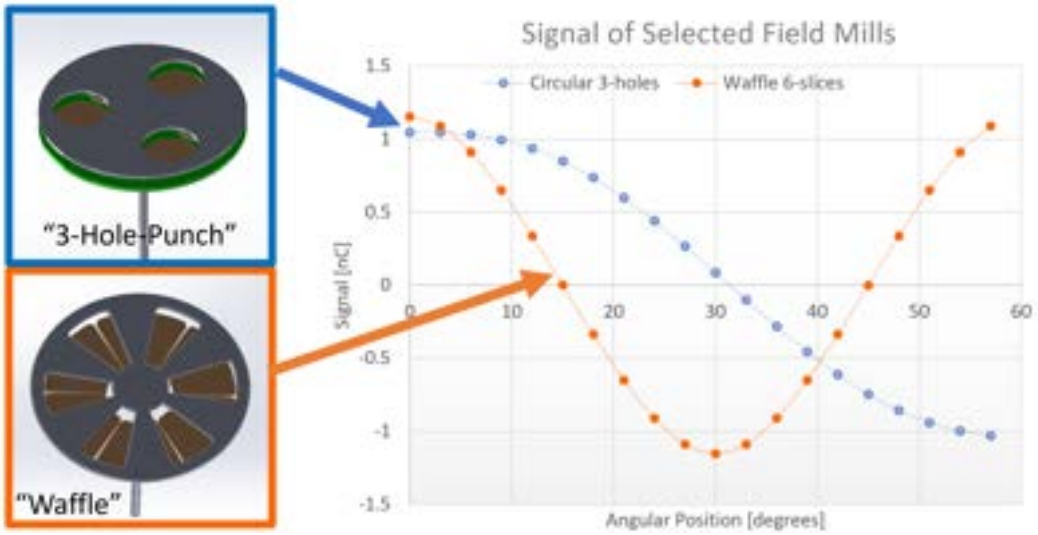

Figure 3.40: Simulated Signal for Selected Field Mills. These sinusoids represent the charge simulated on the virtually grounded sense pads of their respective field mills, measured in nC. However, a real signal will be the time-derivative of this shape, a current whose size is also dependent on the vane rotational speed.

the waffle as depicted in Fig. 3.40. It worked so well that we ordered the 3-hole punch design from manufacturers (instead of the waffle) in addition to the one we produced ourselves.

The waffle shape is further compared to the 3-hole punch shape in Fig. 3.40. Note that the 3-hole punch has half the number of sense petals, and so its period is twice as long as the waffle. The signal depicted in this graph is the signal as measured by the electrostatic finite element analysis simulation; it calculates the amount of charge on each of the virtually grounded sense petals. A real-life signal will actually be the time-derivative of this simulated signal, as we measure charge movement, not raw charge. It will depend also on the rotational speed of the field mill vane. The area of the sense petals matter, as the waffle shape's petals have more surface area and therefore a larger-amplitude sinusoid. However, the difference is small—less than 0.45 nC in the simulation.

Each of the three field mill prototypes created use the 3-hole punch design. The differing details of the field mills include the motor for the rotational motion and the housing materials and shielding.

(a) (b)

Figure 3.41: The Demonstrator Prototype Field Mill. Left, the CAD model of the prototype—note the small hole for wires, the motor underneath, and the smooth housing meeting the field mill vane. Right, photograph of the prototype as built—note the thick field mill vane and the large gap between the vane and the housing.

3.6.2.1 Demonstrator Prototype Field Mill

The design for the demonstrator prototype field mill was centered around its motor and its field mill vane. The vane for the field mill was created in-house milling three holes into a slice of aluminum cylinder from McMaster-Carr. The sense pads consisted of six radially symmetric circular pads placed by ExpressPCB CAD. The rotational motion for the vane was provided by a Portescap bipolar stepper motor (44M100D2B), around which the rest of the mechanics was designed. The two coils of the motor were driven out of phase through two operational amplifiers (Stanford Research SR556) [e].

The housing was produced by Xometry, with a lip created for the printed circuit board sense pads to press-fit against at the top, guaranteeing the sense pads normal to the motor shaft. The motor screwed into the bottom of the housing, with spacers allowing the screws to act as legs for the field mill.

Threads were cut into an 1/8 inch aluminum shaft to mount the vane in an attempt

[e]The "quadrature generator"—the 90° out-of-phase signals for each SR556—were created by two outputs from a single signal generator (T3AFG40), set at 50 Hz, with 2.2 Vpp, offset from each other by 90°.

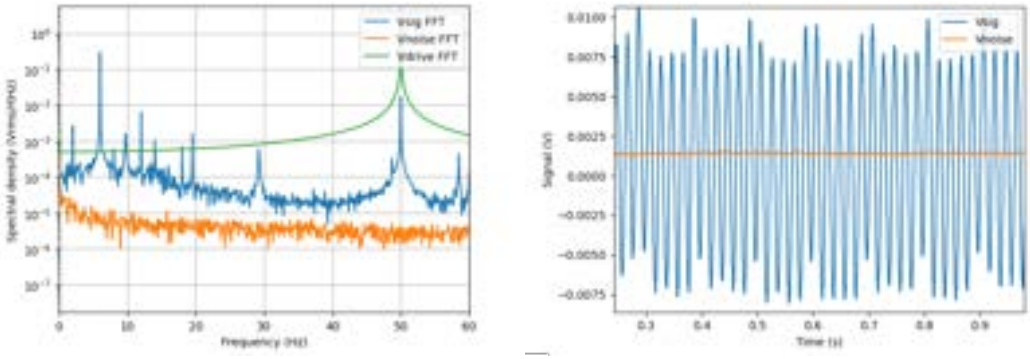

(a) Field mill signal FFT at V_C = 2 kV. (b) Field mill signal vs. time, V_C = 2 kV.

Figure 3.42: Demonstrator Field Mill Example Signals. Left, the fast Fourier transform of the signals, including the driving frequency (50 Hz), the electronic noise, and the differential field mill signal (peaking at 6 Hz with several noise/background peaks). Right, the time domain signal and electronic noise.

to keep the shaft normal to the vane. However, an extra nut and bending pressure was needed to force this normal; future iterations took advantage of the precision of Xometry (future vanes were designed with a slide-fit collar and set screws for shaft mounting). This increased the distance between the vane and the sense pads to about 6 mm.

This field mill was placed under the C electrode of the Cavallo Demonstration Prototype of section 3.4. Its vane was almost 3 inches from the bottom of the C electrode. The Bertan High Voltage output was connected to the top of the electrode to apply voltage for the field mill to measure.

The signal produced by the field mill differs from the frequency that we drive the motor. First, note that each 120° rotation of the field mill vane produces the same electrostatic condition on the sense pads; one revolution of the vane equals three cycles for the sense pads. Secondly, the stepper motor steps at 3.6°/step. The driving signal is at 50 Hz, with four steps per complete pulse on both sets of coils, yielding 200 steps per second, or 2 Hz/revolution. The field mill signal, therefore, will come at 6 Hz. This agrees with Fig 3.43.

The difference between the 50 Hz driving signal and the 6 Hz field mill signal made using cross-correlation with a lock-in amplifier troublesome. Instead their signal was fed into a low-noise preamplifier (Stanford Research Systems 570) through a BNC cable; the differential was produced by wiring one set of ganged pads to the ground of the cable, while the other set was wired to the signal wire of the cable.

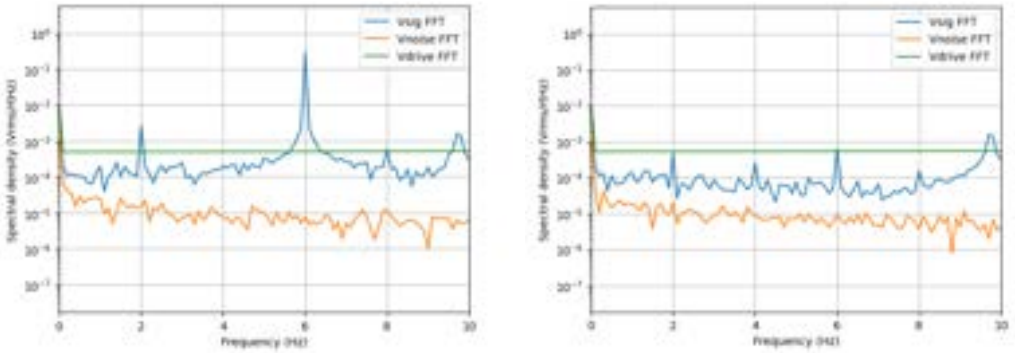

(a) Field mill signal FFT at V_C = 2 kV. (b) Field mill signal FFT at V_C = 0 kV.

Figure 3.43: Fast Fourier Transforms (FFTs) of the Field Mill Signal. Note the large peak at 6 Hz corresponding to applied voltage on C, that mostly goes away when the voltage on C is 0 V.

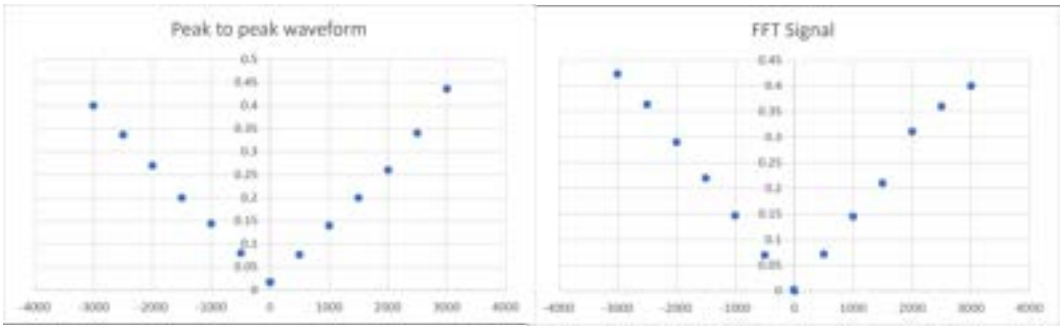

Figure 3.44: Field Mill Calibration: We applied different voltages to the C electrode, and measured the resulting signal for both the FFT and the time domain amplitude. The resultant linear relationship can be used to measure the voltage on the C electrode.

This preamplifier also included a low pass filter (6 dB), which we set to 100 Hz. The output signal was then recorded with a D-tAcq data acquisition system (ACQ2106).

Figures 3.42 and 3.43 represent a typical signal output for this field mill. The green curve is simply a copy of the driving signal, useful for cross-correlation measurements or to see that the fast Fourier transform (FFT) is working properly. The orange curve is the measure of the electronic noise in the system. The blue curve is the field mill differential signal—a little noisy as one can see in the time domain in Fig. 3.42b. The FFT of that signal is much cleaner, as one can pick out the amplitude specific to the signal expected at 6 Hz. Fig. 3.43 shows a zoom in of that 6 Hz signal—one for the same C voltage as in Fig. 3.42, and one where the C voltage is zero; it is clear that the signal is real.

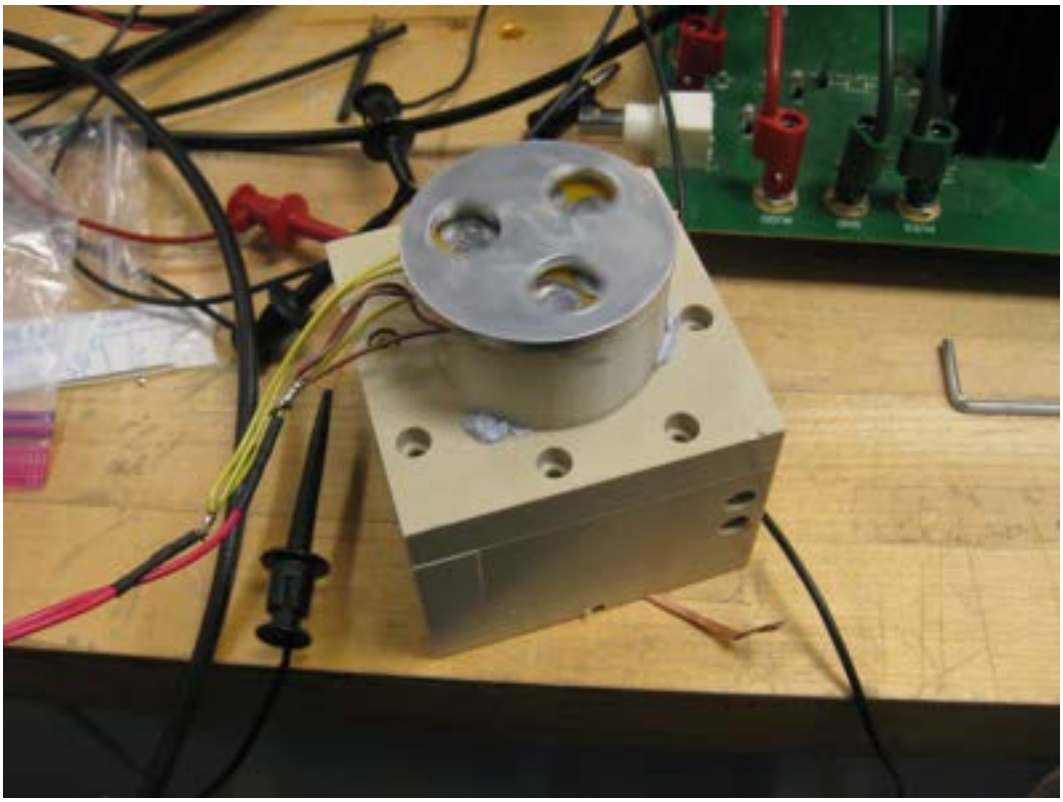

Figure 3.45: Saddle Coil Field Mill. The motor inside the PEEK box is run with two 90° out-of-phase sinusoids, and the sense electrode stand was epoxied for testing.

Furthermore, as the voltage on C increased, the field mill signal also increased, both in the FFT and in the time domain voltage amplitude. This is plotted and looks very linear in Fig. 3.44. One thing to note, however, is that the field mill is not sensitive to the direction of the normal electric field that it is measuring; positive and negative voltages yield the same signal. This is why Fig. 3.44 appears to be an "absolute value" graph.

3.6.2.2 Saddle Coil Prototype

The Saddle Coil Prototype depicted in Fig. 3.45 was an exercise in making our own cryogenic-safe motor. A small magnet bead was glued with DP190 to a stainless steel shaft (which can be seen in Fig. 3.46a inside the saddle coil). Its dipole was perpendicular to its hole where the shaft went through. Two coils were wound perpendicularly to each other around a saddle coil form as shown in Fig. 3.46. Driving these coils sinusoidally 90° out of phase with each other produces a rotating magnetic field in the plane of the magnetic dipole, yielding a torque on the magnet that turns the shaft.

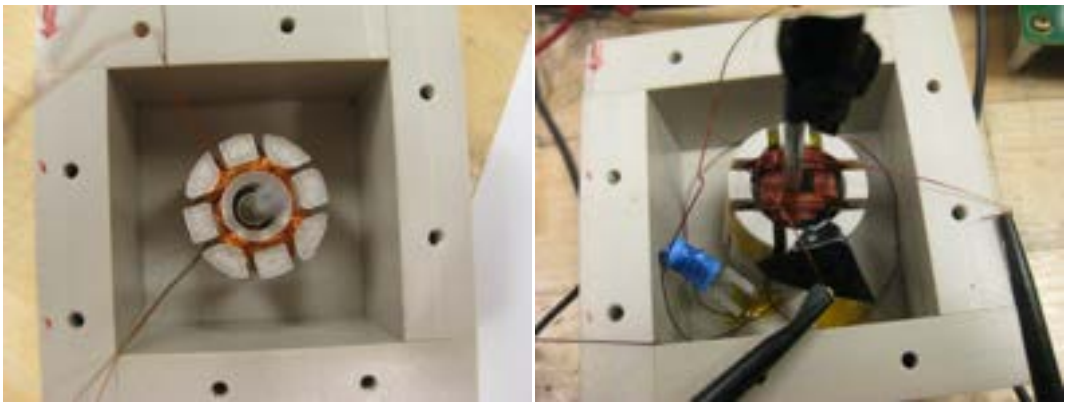

(a) Copper Magnet Wire Coils (b) Superconducting Wire Coils

Figure 3.46: Two saddle coil configurations for the Saddle Coil Prototype: On the left, the original copper magnet wire was wound around a 3D printed form. On the right, superconducting wire was would around a machined PEEK form.

We drove the two saddle coils in a similar way to the stepper motor of the Demonstrator Field Mill in the previous subsection—using the same two operational amplifiers driven out of phase (Stanford Research SR556). [f] This setup is depicted in Fig. 3.47.

The housing was made out of PEEK because it was cryogenically safe and nonmagnetic (in hopes for future upgrades). The box was outfitted with two Teflon bearings for the vane shaft—one at the bottom of the box, and one through the lid. The original saddle coil form and sense petal PCB stand were 3D printed, later to be replaced by PEEK and aluminum, respectively. The initial saddle coil was created out of 40 turns (per coil) of copper magnet wire, and later out of 0.3 mm diameter Niobium (STI 56S52) superconducting wire.

The vane was attached to the shaft first in the same way as the previous field mill, but later by a screw collar. It was successfully grounded by drilling a grounded pin through the bottom of the PEEK box.

The motor has turned with a constant speed, but it was very sensitive to the bearings' friction and alignment; any small amount of misalignment created too much friction for the motor to spin properly. For this reason, many of the documentation and videos depict the Saddle Coil Field Mill without screwing the device completely together. A better housing was required.

[f] The "quadrature generator"—the 90° out-of-phase signals for each SR556—were created by two outputs from a single signal generator (T3AFG40), set at 1 Hz, with 200 mVpp, 90° out of phase.

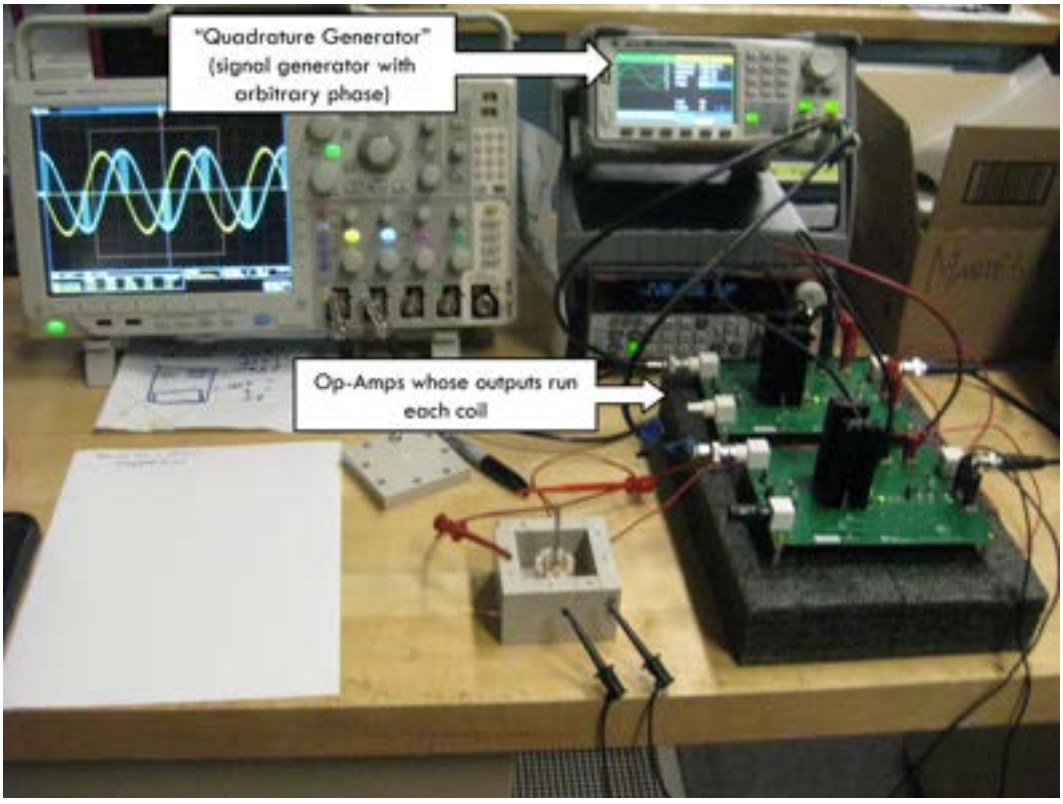

Figure 3.47: Setup for the Saddle Coil Motor: The signal generator feeds two Operational Amplifiers each a sinusoid 90° out of phase with each other.

In addition, plastics turned out to be a large issue. In other failed non-contact voltage measurement schemes, nonconductors appeared to charge up, to the point where most of them needed to be eliminated. The PEEK box, the PEEK saddle coil form, and the 3D printed stand were all deemed unreliable.

However, the motor proof-of-concept was promising. If we find it necessary to continue down this path of creating our own cryogenic motor, a new aluminum housing must be produced, taking careful account of bearing choice and alignment. However, two identical commercial motors were harvested out of commercial hardware with a potential to be cryogenic-safe, providing a significantly larger torque and less required engineering. We used those instead for the final prototype in the following section.

3.6.2.3 Cryogenic-safe Robust Field Mill

Scientist Steven Clayton harvested inductance motors from his basement humidifiers to form the foundation for the robust field mill for the cryogenic Cavallo apparatus. These motors have survived dunk tests in liquid nitrogen, appear to be clean, and

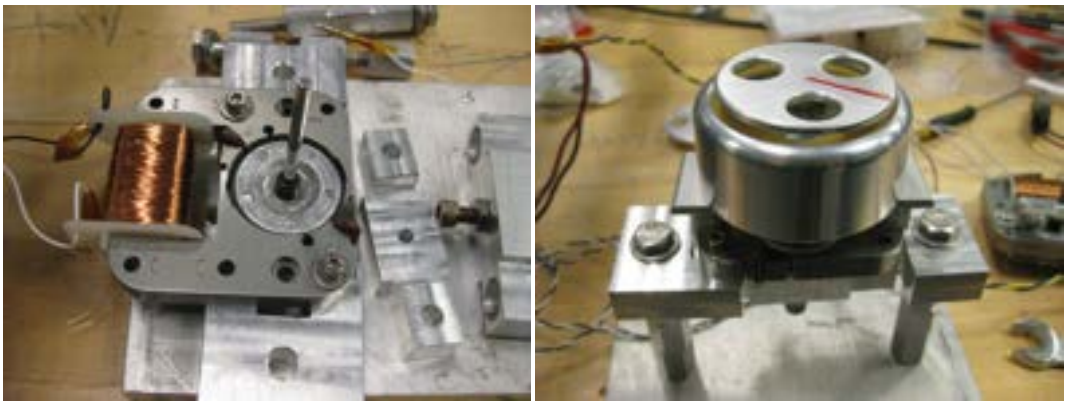

(a) (b)

Figure 3.48: Left: Inductance Motor from an old humidifier—appears suitable for cryogenic operation. Right: Field mill based on the inductance motor on the left. Red line is for measuring frequency of rotation.

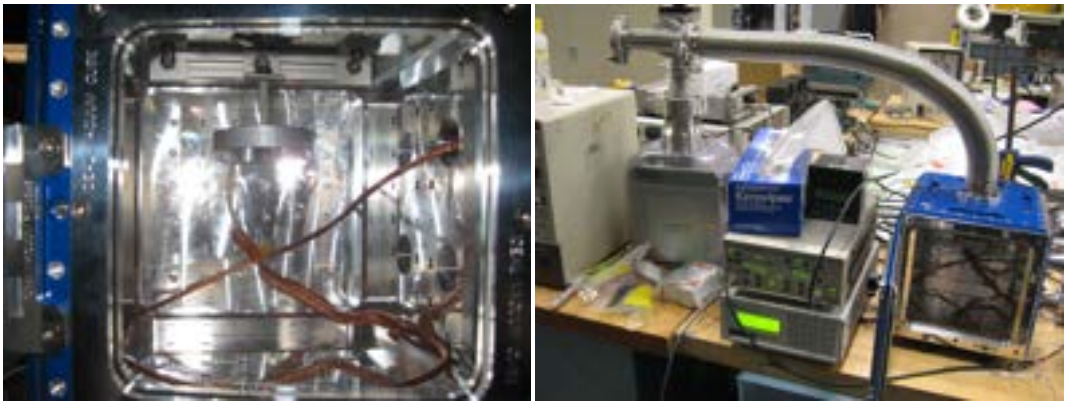

(a) Inside the Vacuum Test Box (b) Vacuum Test Box Set Up

Figure 3.49: Vacuum Test Box for High Voltage. Right: The set up used to test the Robust Field Mill in vacuum, including the high voltage power supply, the pump, the preamplifier, and the chamber (from left to right). Left: Inside the test box, where you can see a shielded copper sleeve guarding the high voltage line as it connects to a high voltage electrode (center top).

do not have oils that will freeze or compromise a vacuum. One of these two motors are shown in Fig. 3.48a. The field mill built on top of it is shown in Fig. 3.48b and 3.50a.

The field mill housing and vane were produced by Xometry to ensure professional rounded edges, with the vane including a collar and set screw as learned in previous iterations. Two full ceramic R144 bearings were chosen for their cryogenic tolerance, with a spring-and-plug assembly designed by postbaccalaureate scholar Theresa Sandborn to ground the shaft and minimize friction.

This motor was accustomed to house power, and so required a single-phase sinusoid instead of the usual quadrature generator. Given the limitations of our operational amplifiers, we still used two channels from the signal generator (T3AFG40) at 180° out of phase to drive the operational amplifiers (SR556). Attaching each amplifier to each side of the coil allowed us to double the power output to the coil.

The field mill motor and initial engineering were tested in a vacuum box equipped with a high voltage electrode as depicted in Fig. 3.49. The vacuum experienced no significant outgassing from the motor, and the motor experienced no overheating in the vacuum chamber.

While the motor was being driven at 50 Hz, a red line was drawn on the face of the field mill vane as shown in Fig. 3.48b to measure the field mill's frequency. The measurement is done using a strobe light; as the frequency of the strobe light changes, the red line dances around. When the frequency of the strobe light matches the frequency of the field mill, the red line appears to stop moving. A driving frequency of 50 Hz corresponds to a field mill frequency of 104 Hz ±1 Hz, with the uncertainty dictated by the bearing fit and grounding spring engagement, which differs slightly with every rebuild.

The field mill's ganged sense electrode output was connected to the low-noise preamplifier (Stanford Research Systems 570) in the same way the demonstrator field mill was (through a BNC cable with one set of ganged pads attached to the signal wire, and the other to the ground of the cable). Its voltage output was measured with an oscilloscope. The Bertan 377X High Voltage Supply provided the voltage to the test box through a feedthrough. The field mill experienced electrode voltages from 0 to 2 kV, and responded in a linear fashion.

The field mill was then installed into the central hole in the D electrode, pointing to the center of the C electrode. However, the setup underneath the C electrode in the Cavallo Apparatus differed somewhat from the test setups; putting one set of ganged sense petals on a BNC guard/ground increased the possibility of noise. Instead, each ganged set of sense petals received its own shielded signal cable, passed through a feedthrough outside of the central volume to its own preamplifier (SR570). Each preamplifier was separately read into the D-tAcq data acquisition system (ACQ2106), as well as the voltage output from an optical position sensor (Sick DT-35).

Calibration was done using the Booper (official name), a magnetically actuated

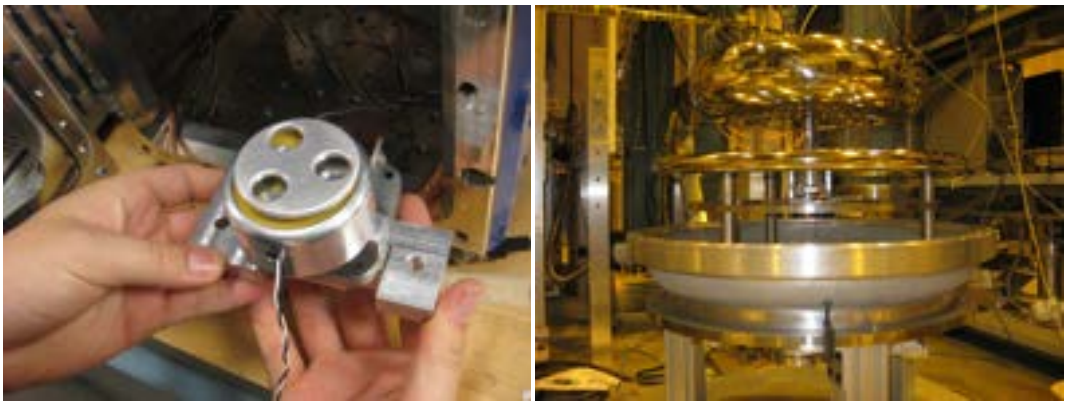

(a) (b)

Figure 3.50: Robust Field Mill for the Cryogenic Cavallo Apparatus. Left: Photograph of the cryogenic field mill before installation. Right: The field mill was installed underneath the center hole in the D electrode.

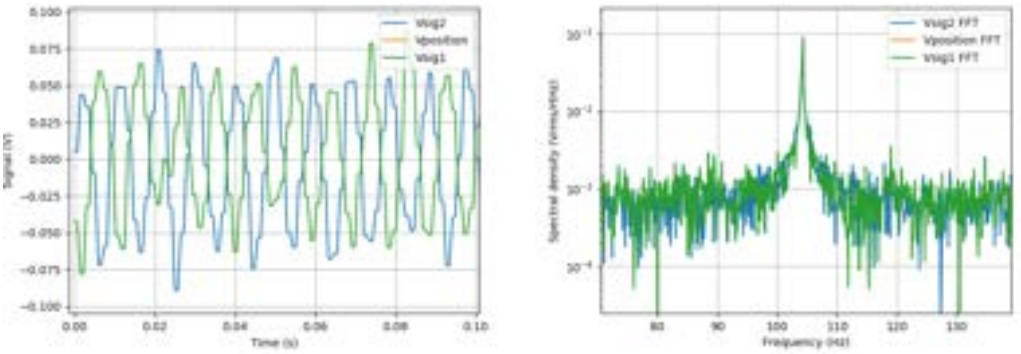

(a) Field Mill Signal: Time Domain (b) Field Mill Signal: Frequency Domain

Figure 3.51: A characteristic field mill signal output at V_C = 2 kV.

grounding rod stored at the top of the central volume. Its primary purpose is to ground the high voltage electrode by coming down and touching the top of the C electrode lobe, but it can be isolated from ground and instead connected to the Bertan High Voltage Supply. In this manner, we descend the Booper onto the C electrode, give it a range of voltages through the Bertan High Voltage Supply, and measure the output of the field mill.

The result is the signal of Fig. 3.51. Note the strong FFT peak significantly shy of 60×3 Hz. We found that, surprisingly, the signal is cleaner if we take the two sets of sense petals independently instead of their differential—we have plenty of signal to spare. The result of the Booper calibrations are shown as the 2024Feb8 and 2024Feb26 lines in the plot shown in Fig. 3.52. Note how

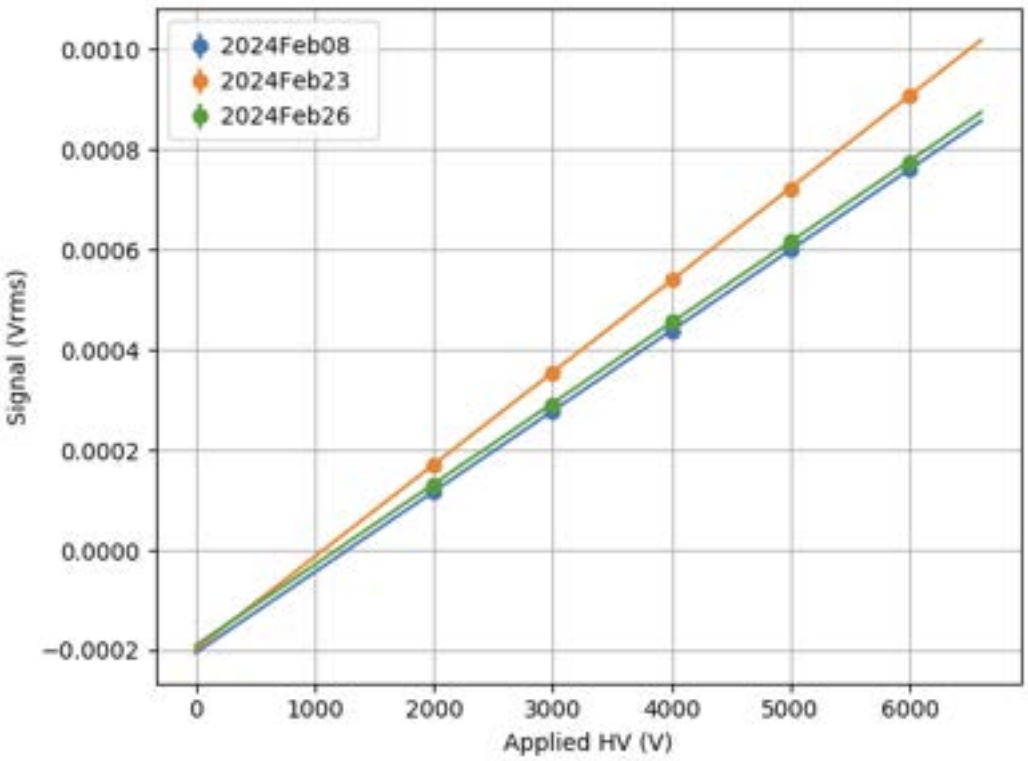

Figure 3.52: Selected Calibration curves for the Robust Field Mill. Note the agreement between datasets for the 2024Feb08 and 2024Feb26 measurements, and the deviation for the 2024Feb23 dataset. The 2024Feb23 data was taken when the field mill ran at an alternate frequency (52.5 Hz).

closely these two datasets agree with each other, despite being a month and some Cavallo rebuilding/troubleshooting apart. The 2024Feb23 dataset, however, deviates significantly from the other two calibrations because it was taken with the field mill frequency at 52.5 Hz instead of 104.

The current iteration of this field mill is being used to measure the voltages produced by the Cavallo Apparatus in SF6, and will be used to measure the voltages in cryogenic nitrogen. However, it currently has a "running life" due to the soft brass of one of its vital parts—the spring and plug being used to ground the field mill vane and ensure the shaft's only contact is with bearings. This soft brass eventually breaks down and starts gauging into the aluminum housing; stronger materials are being studied to replace it.

3.6.3 MEMs

A field mill cannot live in the final nEDM experiment; the motor is highly magnetic, and a large amount of engineering would be required to figure out how the mechanical

structures could be fabricated out of conductive-coated plastic. Perhaps a "MEMs device" could fill this need, instead.

Micro-electromechanical systems (MEMs) are "tiny integrated devices or systems that combine mechanical and electrical components... fabricated using integrated circuit (IC) batch processing techniques and can range in size from a few micrometers to millimetres [93]." These devices are small enough that "dynamic electrostatics"[g] could produce the locomotion for a pseudo-fill mill (no large magnetic motor required).

In fact, this has already been done [94] [95] [96]. At Boston University, Horenstein and Stone created "a micro-aperture electrostatic field mill based on MEMS technology [94]." This tiny "field mill" uses a conductive "shuttle"—a 200 μm plate with three holes in it—as their field mill vane. Rather than rotate, this shuttle is driven from side to side, covering and uncovering the sense electrodes underneath its holes.

The shuttle is driven by a comb drive. A comb drive consists of two sets of interspaced conductive fingers. One set is fixed onto the lithography substrate, while the other is attached to a "MEMs spring" of folded metal bars. A voltage is applied between the two, resulting in an attractive force between the two sets of combs; this voltage is oscillated to produce the back-and-forth rocking required of the tiny field mill.

We as a collaboration have some potential opportunities to make one of these devices; Caltech has a MEMs laboratory [97], as does Los Alamos National Laboratory [98]. Professor Yu Chong Tai of Caltech said that the smaller the device, the more expensive it is to make [99]; the largest comb drives in existence are well within the nEDM material constraints. The biggest constraint hindering this effort is manpower; perhaps this need can be circumvented by acquiring one from a research MEMs lab such as Tao Chen of the University of Manitoba [95].

3.7 Conclusions

The Cavallo Apparatus developed in the 18th century can be modernized to provide the necessary high voltage for the nEDM@SNS experiment. A 50 kV feedthrough can meet the stringent constraints of the nEDM central detector volume, and be electrostatically multiplied into the 650 kV required for the experiment.

[g] In the MEMs field, they use the term "electrostatic forces" to describe the driving forces of motion.

We showed a mathematical understanding of this process with a demonstrator apparatus, and designed and created a novel set of full-scale electrodes with shapes appropriate for the final nEDM experiment. These electrode shapes were fine-tuned using parametric hyperbolic-tangent-based curves within finite element analysis simulations. This allowed us to smooth and spread out the electric field lines, eliminating hotspots.

The shapes were incorporated into the engineering of both a test apparatus and into the final nEDM experimental design. The engineering design was then simulated in the finite element analysis program, and analyzed for a probability of breakdown. These calculations are very promising, as they suggest that the Cavallo apparatus would break down in vacuum, but rarely at 2 atm of liquid helium. Experiments can be done to fine-tune that probability of breakdown by changing the pressure of the liquid helium, allowing us to study the limitations and impact of breakdown in the apparatus.

The calculations are also promising for the final nEDM apparatus, as the breakdown probability of the Cavallo apparatus in the final experiment is even lower. However, the predictive power of this calculation is incomplete, as it does not include the probability of being able to hold that voltage for the lifetime of the experiment. The published data [57] includes a double-exponential fit that suggests that if electrodes hold a voltage for more than 20 seconds, it will stay indefinitely; more data is needed to understand this mechanism and probability.

The final nEDM measurement goals include a measurement cycle of 2400 s, and ten thousand cycles. One might be tempted to establish an upper bound on the electrode breakdown probability for the lifetime of the experiment by using the results of Fig. 3.25, but more studies are needed to understand the post-charging cycling of electrodes in liquid helium. Specifically, the helium study suggests that once an electrode survives charging to some voltage V, then the probability of survival to that same voltage V approaches 1 [57].

Despite these interpretation limitations, the metrics of this design are promising and appear to meet the goals: a geometric gain of 18 allows for us to reach the high voltage goal of 650 kV in 14 strokes. When the B electrode delivers the charge to the C electrode, and any resulting spark is limited to the order of 10 mJ on a reinforced replaceable button.

A set of stainless steel electrodes were fabricated with a test apparatus with pressured

liquid helium capabilities, towards testing the geometry and its charging operation, as well as breakdown profiles in operation. Once a good understanding is established, a set of conductive-coated plastic electrodes can be fabricated and tested as is required for the final nEDM experiment.

Of the three methods of no-contact voltage measurement considered and developed, the field mill is the most robust and confidence-inspiring, but it is also inappropriate for the final nEDM experiment. It is implemented for the Cavallo test apparatus. However, more work is required to use either the wiggling capacitive electrode cryogenically, or a MEMs device.

In conclusion, the Cavallo multiplier would enable us to apply a record-breaking electric field to the neutron measurement cell, allowing us to achieve unprecedented nEDM sensitivity.

Chapter 4

CREATING THE MAGNETIC FIELDS

Neutrons may have a measurable electric dipole moment, but they definitely have a magnetic dipole moment measured to be $\mu = -1.9130427(5)\mu_N$ [100], where μ_N is the nuclear magneton $e\hbar/2m_p$. In experimentalist-convenient units, this is $\mu = -1.45824$ kHz/G or 6.03077×10^{-8} eV/T. This magnetic dipole moment is the "handle" to manipulate neutrons' spins using magnetic fields.

Our experiment takes advantage of that magnetic dipole moment by precessing the neutron in a constant 3 μT magnetic field in the "free precession" mode, and by dressing the neutron spin states in an AC magnetic field in the "critical spin dressing" mode. The Hamiltonian for the neutrons in the measurement cell, for a magnetic field $\vec{B}$ and electric field $\vec{E}$, is as follows:

$$\mathcal{H} = \vec{\mu} \cdot \vec{B} + \vec{d} \cdot \vec{E} \tag{4.1}$$

where μ is the neutron's magnetic dipole moment and d is the neutron's electric dipole moment. The ^{3}He nucleus experiences a negligible amount of the electric field due to its electron cloud shielding.

When running in free precession mode, the first addend in the equation is familiar as textbook Larmor precession [101], and its eigenvalue at B=3μT is of the order of

$$(6 \times 10^{-8} \text{ eV/T})(3\ \mu\text{T}) \approx 10^{-13} \text{ eV}$$

while the limits on d that we hope to impose are on the order of 10^{-28} e cm. The second addend in Eq. 4.1 (with E=75 kV/cm) is of the order of:

$$(10^{-28} \text{ e cm})(75 \text{ kV/cm}) \approx 10^{-23} \text{ eV}$$

The second addend is a perturbation ten orders of magnitude smaller than our "controlling" magnetic field energy. One needs to be very careful that any of our magnetic field perturbations do not resemble that of our electric field.

4.0.1 Signal

The perturbation in Eq. 4.1 is linear with respect to the electric field; so is our signal. Recall from Chapter 2 that the primary signal monitored by the experiment

is scintillation light from the products of the spin-dependent capture cross section of polarized ^{3}He and polarized neutrons.

For the free precession measurement, the signal is a beat frequency whose strength is proportional to the polarization of both the ^{3}He and the neutrons, and directly changed as a linear function of electric field [60]:

$$\omega = \omega_3(1 - \gamma_3/\gamma_n) \mp 2dE/\hbar \tag{4.2}$$

where ω_3 is the SQUID-measured ^{3}He frequency, and ω is the frequency of the scintillation light—the beat frequency of the neutron and ^{3}He precession. The gyromagnetic ratios, γ_3 for ^{3}He and γ_n for the neutrons, are related to above magnetic dipole moments by the spin of the species ($\vec{\mu}_i = \gamma_i \vec{S}_i$).

Further sensitivity is established by switching the direction of the electric field, with the change in frequency given by:

$$\Delta\omega = \frac{4dE}{\hbar} \tag{4.3}$$

Given the applied electric field and a measured $\Delta\omega$, one can use this equation to find the electric dipole moment d.

For the critical dressing measurement, in the absence of an electric field (E) or an nEDM (d), the scintillation light is constant for each measurement cycle. Recall from Chapter 2 that the neutrons and ^{3}He have been tipped to have the same effective gyromagnetic ratio we call γ^{eff} [102]:

$$\gamma^{eff} = \gamma_n \, J_0(\gamma_n \frac{B_{RF}}{\omega_{RF}}) = \gamma_3 \, J_0(\gamma_3 \frac{B_{RF}}{\omega_{RF}}) \tag{4.4}$$

where J_0 is the zeroth order Bessel Function, and B_{RF} and ω_{RF} are the strength and frequency of the spin-dressing magnetic field. The angle between the spins of the neutrons and the ^{3}He is arbitrary, but we set it to be "critical"—the steepest point of the sinusoid. Any extra phase acquired will increase the amount of scintillation light, and an electric dipole moment will change that set phase by:

$$\Delta\phi = 2J_0 \, d \, E \, t/\hbar \tag{4.5}$$

Note this extra phase accumulation is linear with respect to time, and that it is problematic to make a direct fit to this accumulation. Instead, we can repeat the measurement for the same amount of time (t) in the above equation, but swap the spins of the neutrons and ^{3}He. In other words, we can alternate which spin (the

neutrons or the ^{3}He) is leading or lagging—the same initial phase producing the same initial amount of scintillation light—while Eq. 4.5 has the opposite effect on each run. An asymmetry measurement falls out naturally, directly proportional to the electric field and the nEDM [60].

For both the free precession measurement and the spin dress measurement, the signal should change as a linear function of electric field for a nonzero nEDM.

As a final note on the nEDM mechanics, Thomas precession is often applied to elementary particle Larmor precession; it is a relativistic correction to the angular velocity of the particles in precession, proportional to

$$\frac{1}{c^2}\left(\frac{\Gamma^2}{\Gamma+1}\right) \tag{4.6}$$

where I have chosen Γ to be the Lorentz factor $1/\sqrt{1-v^2/c^2}$ because its usual symbol is occupied. With the majority of the UCN moving at significantly less than 7 m/s, this translates to a correction on the order of 10^{-19}Hz. The neutron precession frequency is 87 Hz, with a sensitivity to a frequency shift above 7×10^{-9} Hz; we cannot detect the Thomas precession.

4.0.2 Not the Signal: Sources of Error

The only important systematic sources of error are ones that mimic an nEDM—in other words, those that are linear in the electric field like the nEDM is. Other effects can be corrected away. These effects are enumerated and quantitatively explored in Ahmed et al. [60].

The largest systematic source of error (that is linear in the electric field E) comes from a Bloch–Siegert shift [103], which is a deviation in the Larmor precession frequency produced by a time-varying magnetic field perpendicular to B0. The frequency shift is proportional to the quadratic of this field.

This systematic is often called the "geometric phase" because the time-varying magnetic field comes from particle motion. "Geometric phase" in laymen quantum physicists' terms is a phase change produced by/over the course of a particle's movement through a geometry [104]. The neutron's magnetic dipole moving with velocity v through the experiment's electric field E produces a magnetic field in the radial direction with respect to the particle's precessional circle:

$$\vec{B}_v = \frac{-\vec{v}}{c^2} \times \vec{E} \tag{4.7}$$

which we call the motional magnetic field B_v. To first order, this motional magnetic field would not produce a false nEDM signal on its own because its affect is quadratic with respect to the electric field. (To second order, it is sensitive to the misalignment of B0 and E [60]).

However, paired with any other radial magnetic fields, like those required by the Maxwell Equations given a nonuniformity in the B0 field ($\nabla \cdot \vec{B} = 0$), there is a cross term that is linear in E:

$$B_{total}^2 = (B_v + B_{maxwell})^2 = B_v^2 + B_{maxwell}^2 + 2B_v \cdot B_{maxwell} \tag{4.8}$$

where $B_{maxwell}$ can be expressed as [60]:

$$B_{maxwell} = -\frac{1}{2}\frac{\partial B_z}{\partial z}\vec{r} \tag{4.9}$$

Note, then, that the gradient in the above equation can be minimized to limit the effect of the geometric phase systematic. Ahmed et al. therefore calculated the phase shift to be [60]:

$$\delta\omega_{avg} = -\frac{\gamma_n^2 \left(\frac{\partial B_z}{\partial z}\right) E R^2 \omega_r^2}{c^2 \left(\omega_0^2 - \omega_r^2\right)} \tag{4.10}$$

where R is the radial travel of the neutrons (not to exceed the size of the cell, so about 10 cm), and ω_r is the angular velocity of that travel, $\omega_r = v/R$. The UCN have an average velocity about v =3 m/s, the electric field is E =75 kV/cm in the measurement cell, and the B0 field is 3 μT. This B0 field translates to a Larmor precession frequency of $\omega_o = \gamma_n B0$ = 87 Hz = 549 rad/s.

A tolerable geometric phase from Eq. 4.10 is of the order of the floor of our target sensitivity, d_n on the order of 10^{-28} e cm. Plugging that into Eq. 4.3, and using the resultant phase shift as the higher bound in Eq. 4.10 yields an acceptable level for the B0 gradient of:

$$\frac{\partial B_z}{\partial z} \approx 10^{-11} \text{ T/cm} \tag{4.11}$$

Experimentally, this is a stringent constraint. It is met with carefully engineered and constructed B0 coils, a superconducting lead shield to keep out external disturbances, and a magnetic shield room with active shielding to house the entire apparatus.

4.1 Building the Cryomagnet

The cryomagnet is designed around a set of "Matryoshka" or Russian nesting dolls, with the outer layers serving cryogenic purposes, the innermost layer reserved for the

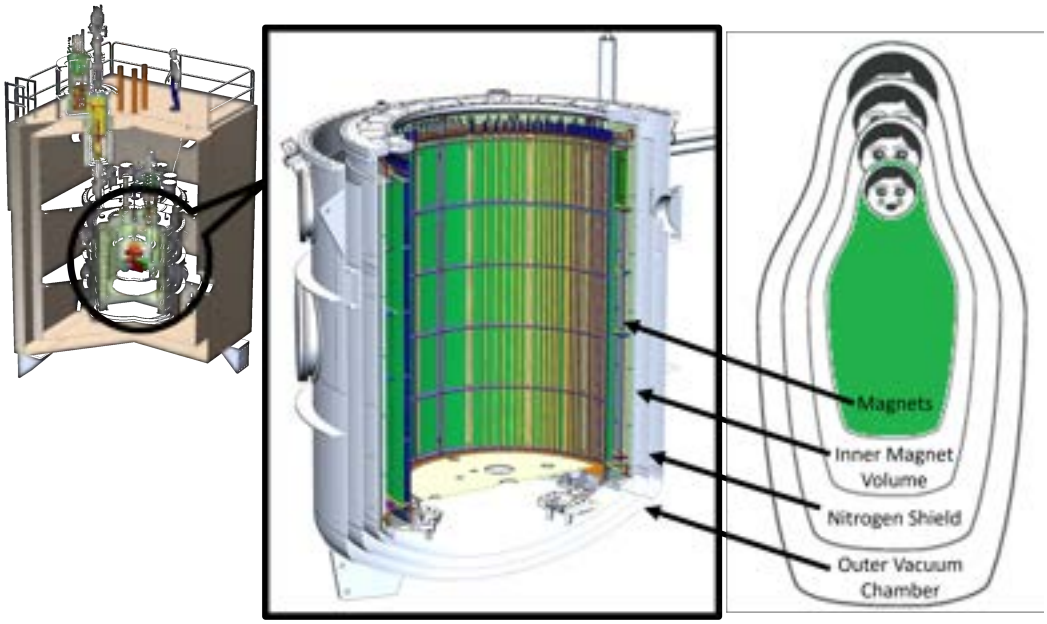

Figure 4.1: The cryomagnet as compared to a set of nesting dolls. Credit to engineer John Ramsey for the cryomagnet graphic, and nesting dolls adapted from [105].

central detector system (where the Cavallo multiplier and measurement cells live), and the middle layers for the magnet package itself. The magnet package layers are contained in their own separate volume, called the "inner magnet volume" (IMV). For their study, special lids have been created to isolate the cryomagnet (including the cryogenics) from the rest of the experiment.

Fig 4.1 puts these layers into perspective: in the far left is an icon of the full experiment from Fig 2.4, with the cryomagnet circled and brought to the center, enlarged. The layers of interest are highlighted by the adjacent nesting doll on the right, with the electromagnets inside.

The magnet package consists of the B0 coil (for making the uniform precession field), B0 shim coil(s) (to mitigate any magnetic field gradients in the B0 field), and the Spin-Dress coils (for the AC spin manipulation)—all wound from superconducting Cu-clad NbTi wire. It also includes cylindrically wrapped 35 μm copper sheets (for AC shielding), and 0.8 mm superconducting lead sheets "welded" together to the outside with two lead end caps (for maximal magnetic field line rejection). To prevent magnetic field distortion due to the superconductor boundary conditions, a high-mu flux return was created out of a thin engineered alloy called Metglas, discussed in the next subsection. Yet another set of coils are wrapped toroidally (in three bunches) around the package for degaussing the Metglas, also discussed in the

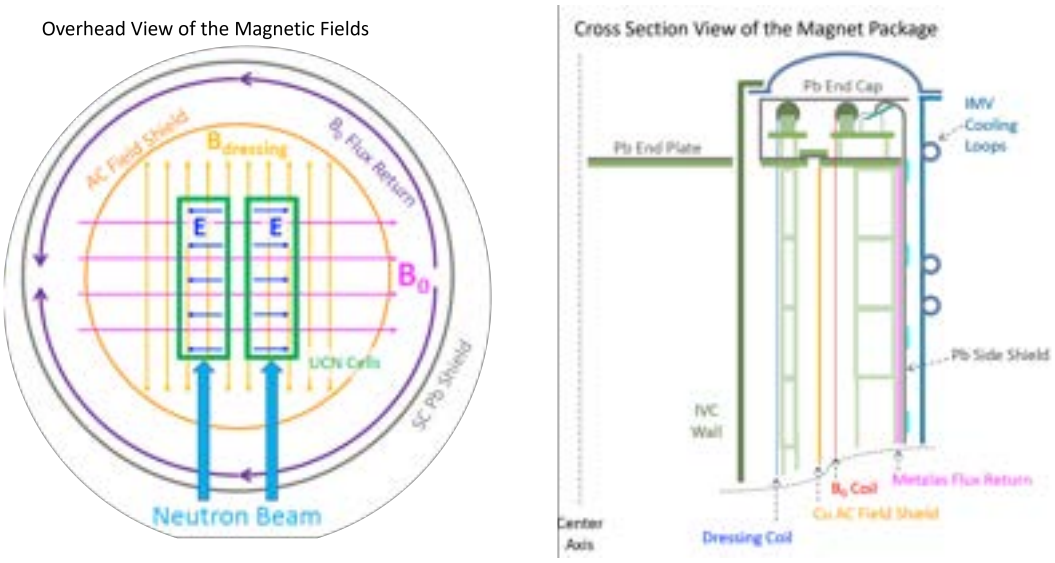

Figure 4.2: Diagrams of the Magnetic Field Package. Right, the cross sectional view of the inner cylinder of the magnetic field package inside of the IMV. Left, an illustration of the magnetic field package and their resultant magnetic fields inside of the experimental volume as they relate to the neutron beam and measurement cells.

next section. All of these components are illustrated in Fig. 4.2.

Fig. 4.2 shows the B0 and spin-dress coils creating uniform magnetic fields across the measurement cells; they are modified 'cosine-theta' coils designed by former Research Assistant Professor Chris Swank [82]. He modified the B0 coil to compensate for the image current effects in the outer Metglas later. For the spin-dress coil, he used finite element analysis [76] to optimize the coils' wire placement for the longest coherent holding times by applying Redfield relaxation theory [106]. He calculated achievable wire positioning tolerance [0.25 mm] for both coils, with good uniformity and holding times.

Photographs of the magnet package are included in Fig. 4.3. Recalling the physical magnitude of the cryostat, the B0 coil is also 2.5 m tall by 2 m in diameter. Care was taken to ensure that the wire positioning along these multi-meter lengths stayed within the tolerances even after cooldown to 6 K. The approach was twofold: the wires were guided into place by the engineering of the coil's G10 support frame as shown on the left side of Fig 4.3, and wire tensioners (shown in the bottom right of Fig 4.3) were engineered from Torlon pulleys and PEEK springs to keep the wires in place as the package cooled. The G10 support frame was created out of G10 rings called "hoops" held at fixed repeated distances by scaffolding called "story

Figure 4.3: The Magnet Package, with emphasis on B0. Left, the B0 coil wound in its G10 support frame. Center, the outside of the magnet package, with the wound Metglas outer layer. Top right, the inside view of the magnet package, with the (currently innermost) AC shield layer. Bottom right, a close-up view of the wire tensioners made of Torlon pulleys and PEEK springs.

sticks[a]" and gussets as shown. Both the wire tensioners and the hoop assembly are well documented in former graduate student Xuan Sun's thesis [108]. The raw material for the G10 hoops was unable to be commercially obtained at such great diameters, so they were glued together from segments with high precision using a vacuum table, and their tolerances verified with a robotic ROMER arm [108]. The B0 magnetic field profile was verified in-house. Similar work is ongoing for the Spin Dress coil, whose dimensions fit inside this coil and shield, and is constructed similarly.

The copper AC shield was created with copper-coated G10 support sheets, which were attached to the inside of the B0 magnet as shown in Fig. 4.3. The superconducting lead shield was similarly glued to G10 support sheets, and will surround the outside of the B0 magnet. However, a flux return is imperative to maintain the required magnetic field homogeneity inside the experiment, as the B0 field is perpendicular to the superconducting cylinder. Simulations showed that this flux return could not tolerate beam port holes and had to fit in the thin space between the magnets and the superconductor, necessitating a thin layer with no neutron-depolarizing

[a]This moniker is suitably derived from the woodworking concept of Story sticks/Story poles [107].

domains. Metglas, a family of proprietary engineered alloys, was chosen for this purpose. The chosen alloy was wound around the magnet package. Analysis of this material and a competing alloy is discussed in subsection 4.1.1.

The spin-dress coil is not yet installed and so is not depicted in Fig. 4.3, leaving the AC shield as the innermost layer. The superconducting lead shield is also not yet installed or depicted, leaving the Metglas as the outermost layer.

Finally, four sets of degauss coils were wrapped toroidally around the package. Degauss coils are used to "remove magnetization" by applying a decaying AC magnetic field to magnetic materials—while it is thought of as "removing" the magnetization, it is really reaching equilibrium in its magnetic environment. In actuality, the process provides the "activation energy" for the magnetic domains to flip positions to minimize their magnetic energy in the field. Here, the coils initially create about a 1 gauss field to saturate the Metglas.

4.1.1 Flux Return Analysis: Metglas Studies

Metglas is a series of proprietary alloys invented at Caltech [109] whose name comes from a portmanteau of "metal" and "glass" (because it is an FeNi alloy, but amorphous like glass). Its manufacturing process attempts to prevent magnetic domains or crystalline structures from forming in the metal by cooling the entire ribbon instantaneously ("a million degrees per second" [109]), though a study by Kronmüller studied this more closely [110]. Its thin profile, high resistivity, amorphous structure, and high magnetic permeability (μ) make it an ideal material for the magnet package flux return.

Two Metglas alloys considered were 2705M (which boasted a very high mu-as-cast, but contained cobalt) and 2826MB (which still had a high mu, but contained no cobalt). Cobalt is a concern for the flux return because cobalt gets activated by neutrons, creating large and long-lasting gamma backgrounds [111]. Some manufacturer specifications are in the table below, but it is important for us to measure our own shielding factors and consider the Metglas' magnetization curves. Properties of two Metglas alloys given by their technical sheets [112] [113] are as follows:

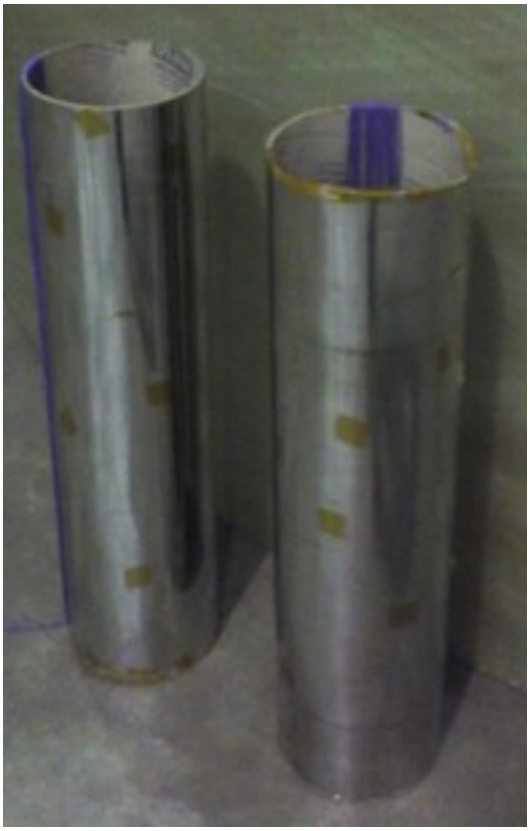

Figure 4.4: Photograph of the two Metglas sample shields, created for characterization. The purple wire is the degaussing circuit, and the right cylinder is the 2826MB while the left is 2705M.

Metglas Alloy	2705M	2826MB
Cobalt Content	75%-80%	<0.3%
Mu-as-cast	290,000	50,000
Resistivity	0.136 $\mu\Omega$ cm	0.138 $\mu\Omega$ cm
Thickness	20 μm	29 μm

4.1.1.1 Magnetic Shielding

To characterize the two Metglas alloys, shields were created out of six layers of Metglas and 15 cm diameter sonotubes, 60 cm tall. Two circumferential base layers were wound, followed by two layers of strips laid parallel to the tube (axially), followed by two more final circumferential layers. Degaussing circuits for the shields were wound from 20 toroidal loops of coil. These shields are photographed in Fig. 4.4, where the shiny grey "foil" is the Metglas, and the purple wire is the degaussing circuit.

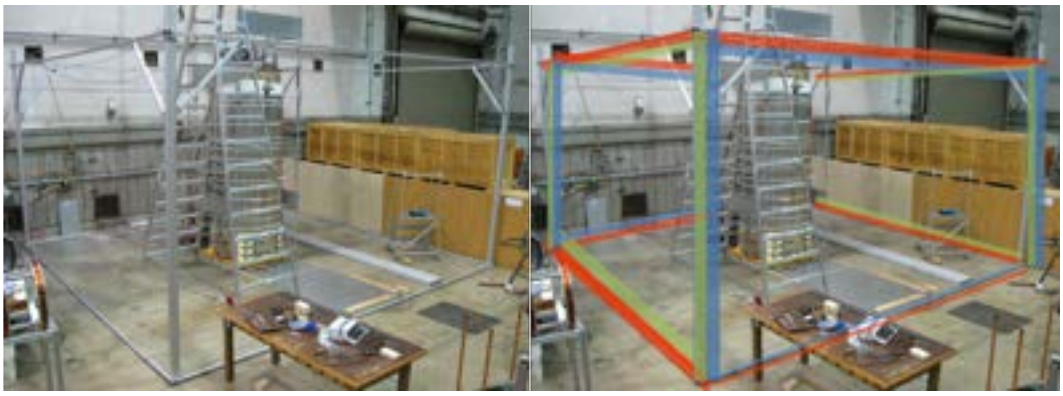

Figure 4.5: Photograph of the bucking coil frame at Caltech, with the three coils (in the three Cartesian directions) highlighted in color on the right side.

The shields were tested with the Caltech Bucking Coil laboratory, depicted in Fig. 4.5. These are 128" tall Cartesian coils in the x, y, and z directions to create or cancel magnetic fields. Each direction (colored in Fig. 4.5) contains two sets of coils—a main and a shim coil. These coils are attached to current-controlled power supplies (main = Harrison 6274A and HP6269, shims = Kepco JQE 150-3M and ATE 75-3M), either running independently or controlled by a signal generator. DC electric current was run through the main coils to cancel or add to Earth's magnetic field, while a perturbation was created using AC current through the shim coils. In this manner, varying AC and DC magnetic field conditions could be applied to the shields to measure quasistatic shielding factors.

A magnetic field probe was attached to a linear actuator in the center of the bucking coils—a calibrated 3-axis flux gate magnetometer (Bartington Mag-03). A shield was placed on a wooden table such that the magnetic field probe was in the center of the shield (±2 cm). Using the flux gate magnetometer, the magnetic field was measured with and without a shield present.

An illustration of this measurement is sketched in Fig. 4.6. The magnetic field without the shield is the higher sinusoid, with a transverse DC magnetic field component labeled H_0^{DC} and a transverse AC magnetic field component labeled H_0^{AC}. When the shield is installed, however, both the DC magnetic field component drops and the AC magnetic field component is reduced—this is seen as the smaller, lower sinusoid in Fig. 4.6. Its shielded DC component is labeled H_1^{DC}, and its AC magnetic field component labeled H_1^{AC}. These sinusoids can be used to calculate the shielding factors for the two Metglas shields.

There are two categories of magnetic shielding, and each type has a different per-

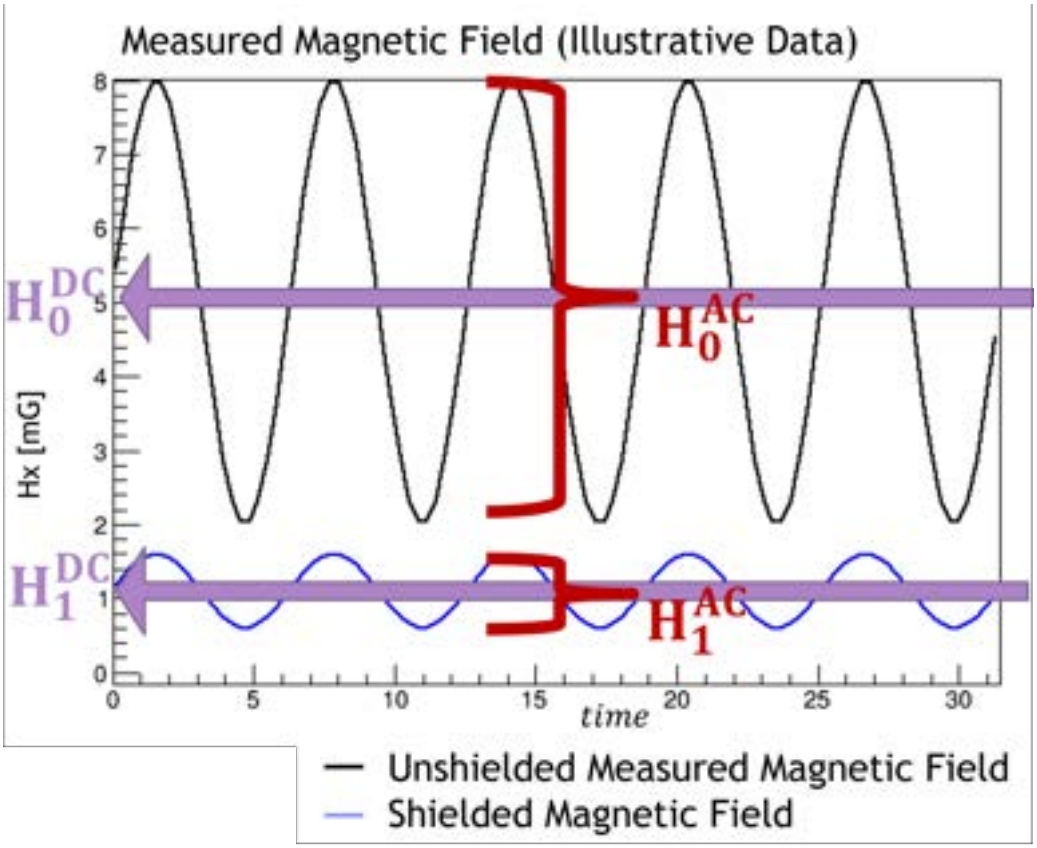

Figure 4.6: Illustrative sketch of the magnetic field shielding data. Without the shield present, the flux gate magnetometer reads the top sinusoid with DC component H_0^{DC} and AC component H_0^{AC}. With the shield present, the flux gate magnetometer reads the bottom (smaller) sinusoid with DC component H_1^{DC} and AC component H_1^{AC}.

meability:

1. Static Shielding

   Static Shielding can be conceptualized as H_0^{DC}/H_1^{DC} from Fig. 4.6 [114].

   One may object that this shielding factor is not particularly meaningful, as hysteresis dictates the materials' location on the μ vs. H curve and therefore changes the shielding factor. However, degaussing the shield every time it is placed relaxes the domains, forcing the material onto the anhysteretic curve [114] seen in Fig. 4.7, which is reproducible. These measurements are too difficult for small H_0 in our setup, and quasistatic data is more reliable.

   Furthermore, this shielding factor is still not particularly meaningful for the nEDM experiment, since the flux of the B0 magnet is running through this "shield"/flux return, manipulating the domains. The quasistatic shielding

factor is more meaningful for characterizing shielding against the slowly varying external fields.

2. Dynamic Shielding

   - Quasistatic Shielding:

     Quasistatic fields are slowly evolving perturbations in the magnetic field, and they trace out tiny hysteresis loops as seen in Fig. 4.7. When measured and extrapolated into the limit of zero frequency, these curves represent the original, initial permeability.

     The shielding factor associated with them using the sinusoids depicted in Fig. 4.6 is H_1^{AC}/H_1^{AC}.

     For a cylindrical shield of radius R and thickness t, the transverse shielding is:

     $$S^T = 1 + \frac{\mu t}{2R} \tag{4.12}$$

     From this, we can measure the effective μ of the Metglas.

   - Skin Effect:

     For alternating fields, the eddy currents and the skin effect may be taken into account. The frequencies applied in our quasistatic measurements are mostly less than 1 Hz. The skin depth can be calculated from:

     $$\delta = \sqrt{\frac{\rho}{\pi f \mu}} \tag{4.13}$$

     where ρ is the resistivity of the material, f is the frequency, and μ is the magnetic permeability ("mu as cast" times $4\pi 10^{-7}$ N/A^2. For our sinusoidal magnetic field at 1 Hz, the skin depth is 34 μm for the 2705M and 84 μm for the 2826MB. Comparing these depths to the thickness of the material ($20\mu m$ and $30\mu m$, respectively), the skin effect is very small. Furthermore, the copper shield in the magnet package prevents the Metglas from being exposed to AC fields for spin manipulation in the nEDM experiment.

Static Shielding Factor

The static shielding factor is simply derived from the difference in the static magnetic field before and after the shield is applied and degaussed. For the two Metglas species, plotting the shielded vs. unshielded magnetic field yields Fig. 4.8, and

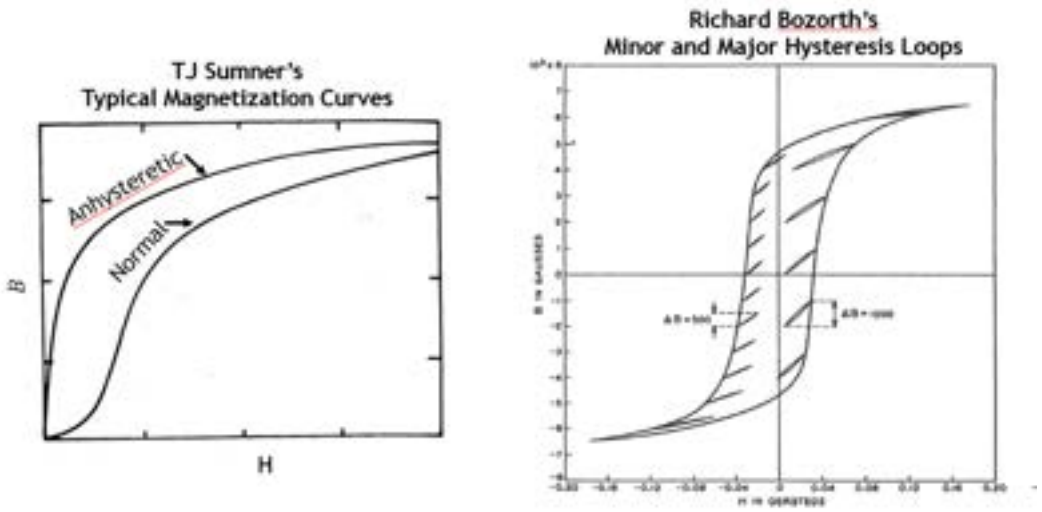

Figure 4.7: Left, typical (hysteretic) vs. anhysteretic H vs. B curves, taken from [114]. Right, the large hysteresis loop vs. small quasistatic loops, taken from [115].

the shielded field measured is relatively flat—far from saturation. Calculating the shielding factor from Fig. 4.8 yields Fig. 4.9.

Applying Eq. 4.12 to Fig. 4.9, the resultant magnetic permeability corresponds to between 300,000–1,000,000 for the 2705M Metglas, and 50,000–150,000 for the 2826MB Metglas. These numbers are consistent with the manufacturer's specifications.

Quasistatic Shielding Factor

The quasistatic shielding factor is derived from small perturbations of the H_0^{DC} field. For our dynamic setup, these perturbations for each of the H_0^{DC} fields are summarized by the left plot in Fig. 4.10. On the right, the shielding data reveals some frequency dependence, but less so for our frequency range (left side of the plot). This allows us to correct the quasistatic shielding measurements for "RF" shielding effects.

Beginning with high H_0^{DC} = 680 mG, H_0^{AC} was varied from 12 mG to 56 mG, with the resultant shielded magnetic fields plotted on the left side of Fig. 4.11. The shielding factors for this data are calculated for the plot on the right side of Fig. 4.11. Note the linearity of the data, evidencing that we are far from saturation. Applying Eq. 4.12 to Fig. 4.11, the resultant dynamic mu is plotted in Fig. 4.12.

As we drop in H_0^{DC}, similar behavior is measured for H_0^{DC} = 300 mG. The shielding factor for 2826MB continues to be flat, and the shielding factor for 2705M continues

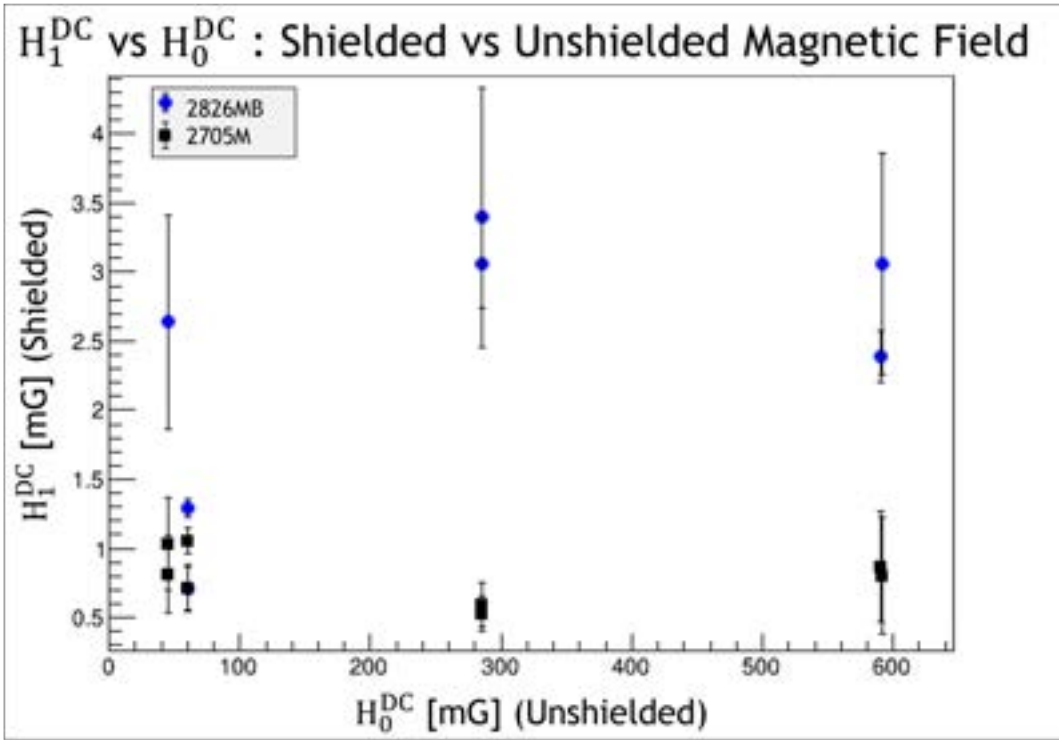

Figure 4.8: H_1^{DC} vs. H_0^{DC}: Flux-gate measurements of the Shielded vs. Unshielded Magnetic Field for two Metglas species.

to be linear, as seen in the left hand side of Fig. 4.13. However, for the low value of H_0^{DC} = 44 mG, both Metglas species have a flat shielding factor as seen in the right hand side of Fig. 4.13.

Note especially that the shielding factor for 2705M is low for small values of H_0^{AC}, and especially at the low value of H_0^{DC} = 44 mG, which is approximately the value of our operating field. This is not ideal for our flux return choice.

The manufacturer hysteresis curve measurements of 2705M as seen on the left side of Fig. 4.14 do not reveal this poor performance at low field. However, comparing the 2705M behavior to the 2826MB behavior on the right side of the figure, 2705M has a more rectangular curve than 2826MB. The 2826MB curve has the same slope over a longer range in H (applied magnetic field), while the 2705M slope is steep for a much shorter range. As the slope of this curve is defined as the μ of the material, it explains why the shielding factor of 2826MB is flat, while the 2705M exhibits a more linear response. The shielding factor of 2826MB of 2.8 surpasses the shielding factor of 2705M at low field, making it the more suitable material both in magnetic characteristics and cobalt content.

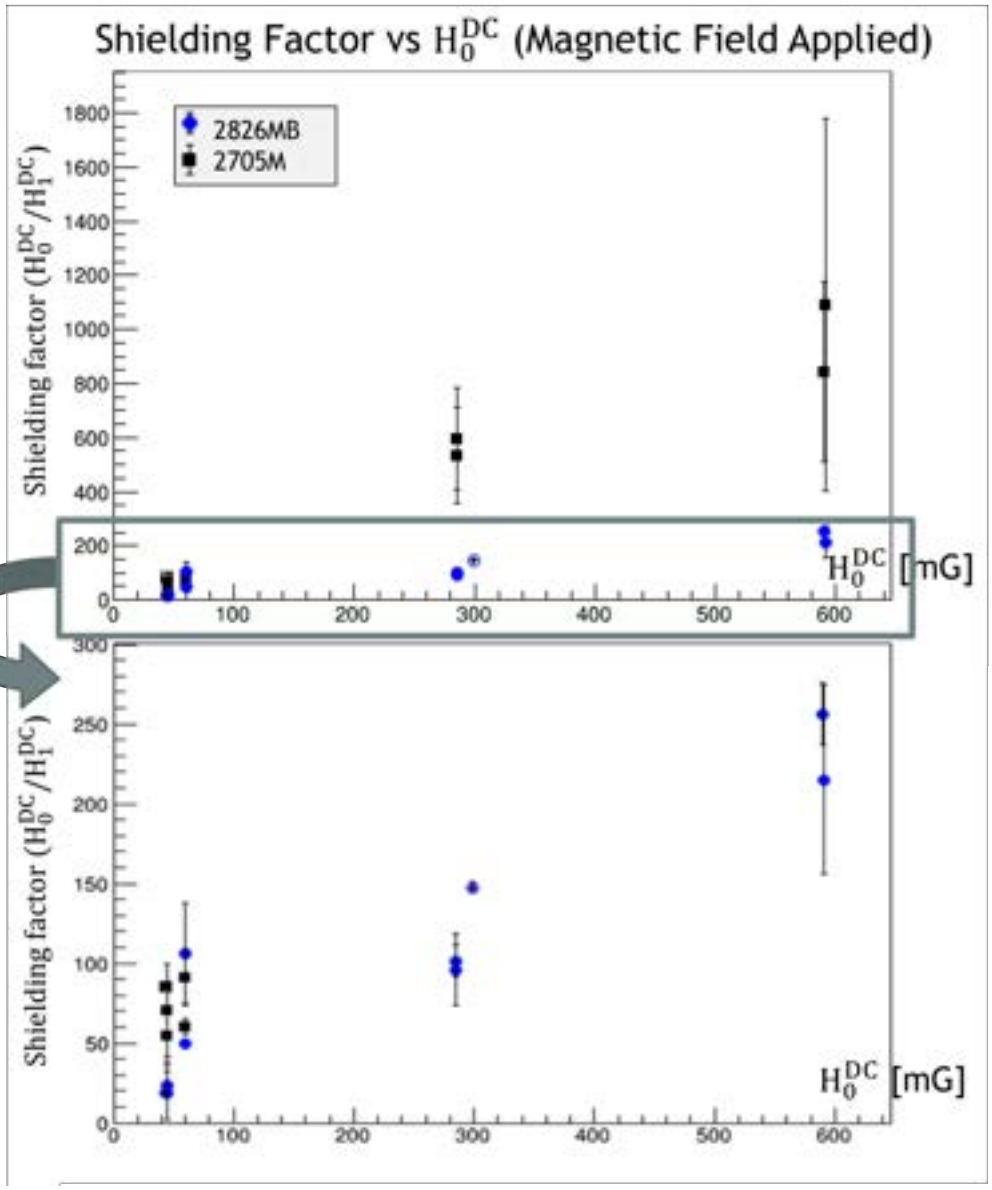

Figure 4.9: Static Shielding Factor vs. H_0^{DC}: Above, full measurement range, lower values zoomed below.

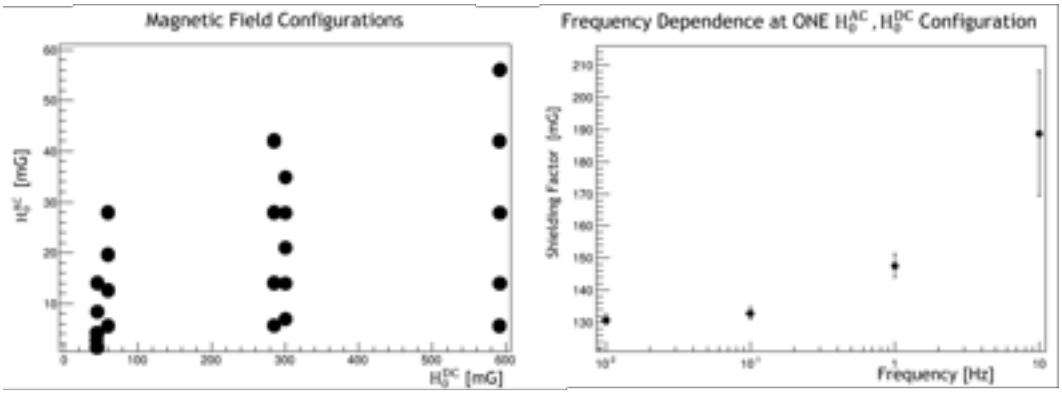

Figure 4.10: Quasistatic shielding measurement considerations: Left, summary of measurement conditions applied. Right, sample shielding factors as a function of frequency.

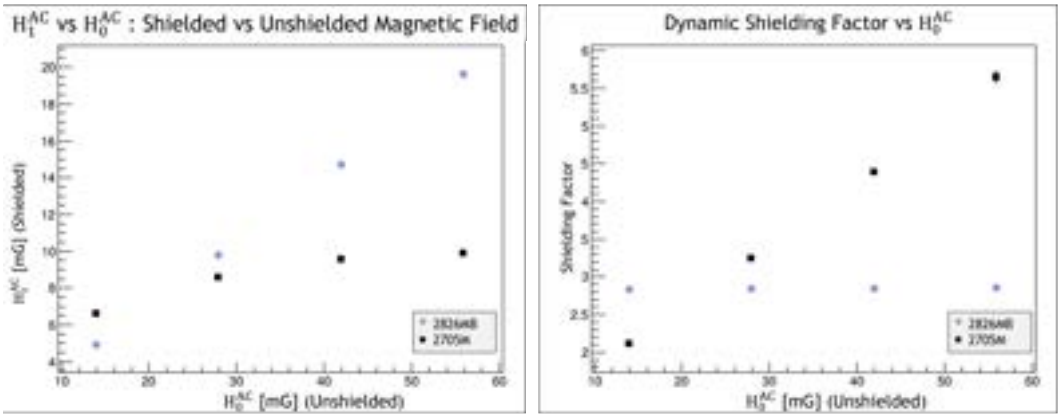

Figure 4.11: Dynamic Data for H_0^{DC} = 680 mG. Left, H_1^{AC} vs. H_0^{AC}. Right, shielding factor vs. H_0^{AC}.

In summary, the results are as follows:

Metglas Species	DC Permeability*	Quasistatic Shielding
2705M	μ =300,000 to 1,000,000 (good at high field)	High Fields Range from 2 to 6. Constant at Low Fields—1.75
2826MB	μ = 50,000 to 120,000	Constant for all fields measured—2.8

*For H^{DC} = 30 mG to 600 mG.

The error bars are due to the repeatability of the exact transverse placement of the 15 cm diameter cylinder compared to the approximately 2 cm diameter of the flux gate magnetometer. This could be better controlled with a larger diameter shield and wooden guides to better control the placement.

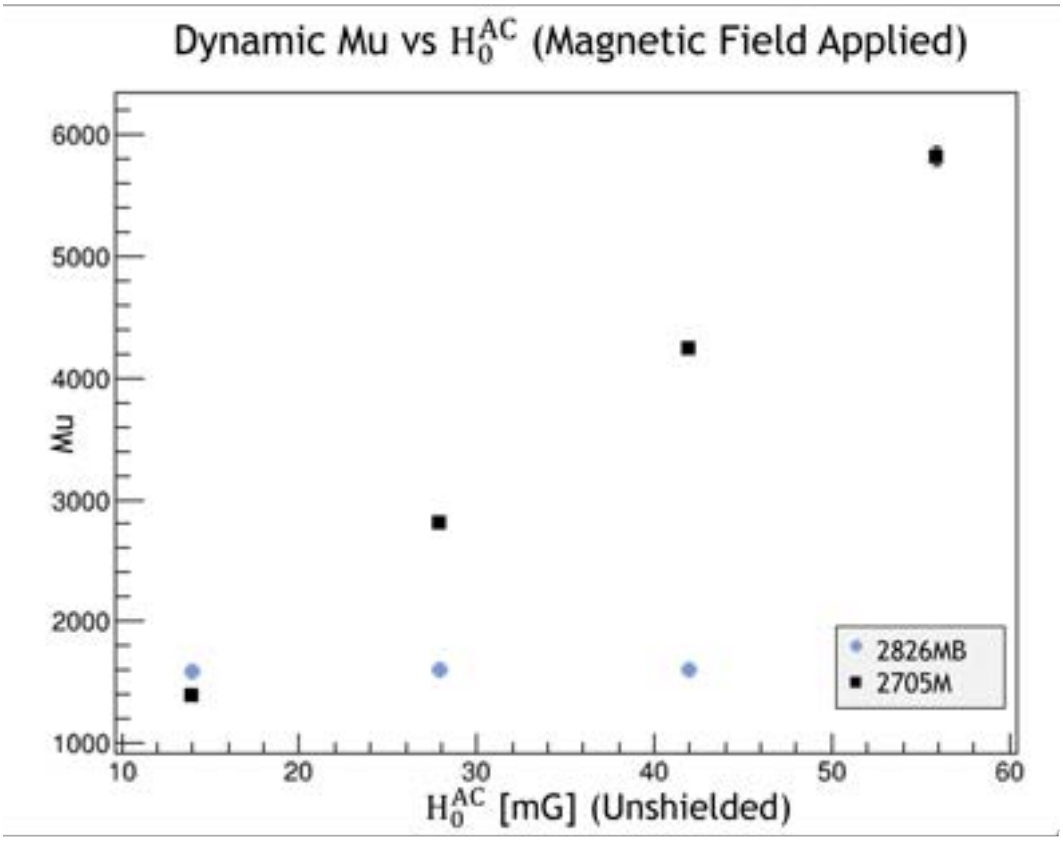

Figure 4.12: Dynamic Mu for H_0^{DC} = 680 mG.

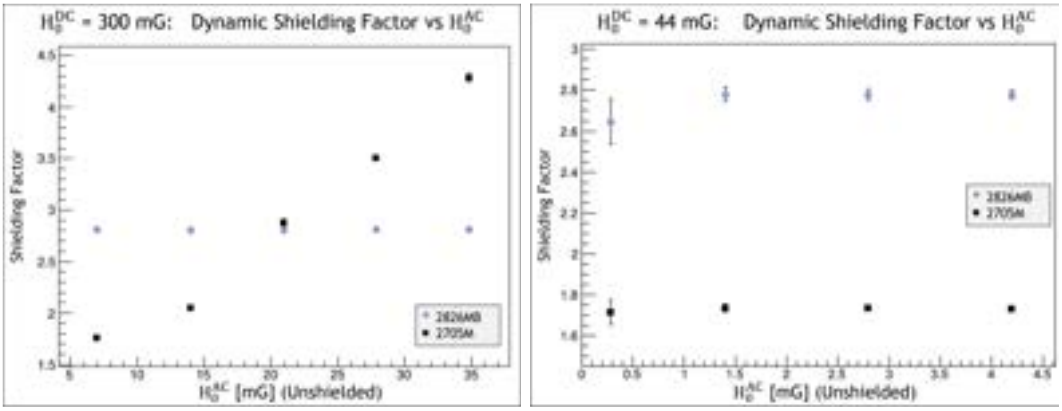

Figure 4.13: Shielding factors for different H_0^{DC}. Left: 300 mG. Right: 44 mG.

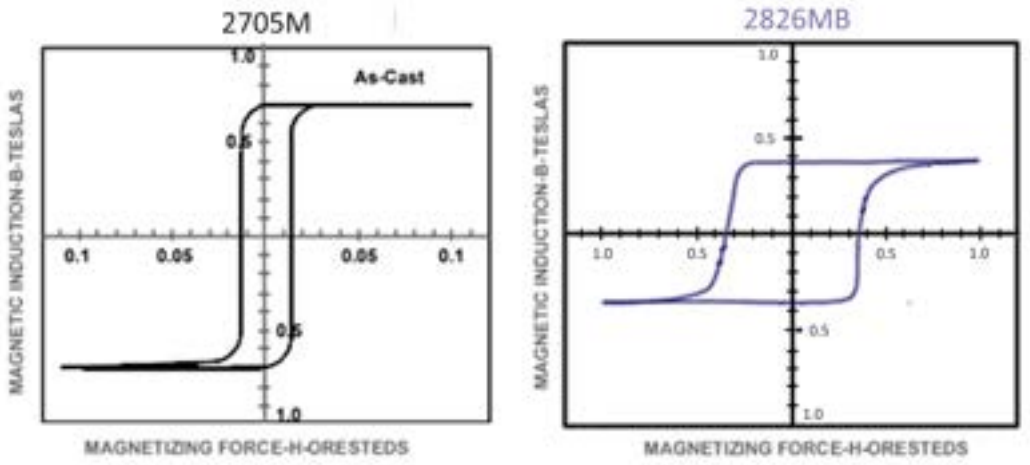

Figure 4.14: Hysteresis curves for 2705M (left) and 2826MB (right) provided by Metglas.com in [113] and [112].

4.1.1.2 Boron Content

The 2826MB Metglas alloy chosen for the flux return, while having perhaps trace amounts of cobalt, contains another element of concern—boron. Natural boron is a mix of isotopes, with about 80% boron-11 (^{11}B) and 20% boron-10 (^{10}B). For neutrons below 10 keV, the neutron capture cross section for ^{10}B is 5 or 6 orders of magnitude greater than for ^{11}B [116]. This makes ^{10}B a great neutron absorber, and is used in everything from shielding to neutron detection. It is not good for high neutron transmission through a flux return.

How much boron is in the 2826MB ribbon? A measurement was done using an Americium-Beryllium (AmBe) neutron source at Los Alamos National Laboratory, housed in a steel enclosure attenuating some of the emitted neutrons and gamma rays. Outside of the enclosure, it supplied about 60 Hz into a detector setup as described below.

A ^{6}Li-based detector (Eljen EJ-420) counted neutrons into a multichannel analyzer (Ortek Easy-MCA 2k), surrounded with lead and borated plastic bricks. The lead and borated plastic shielded the detector on all sides except for a 5 cm x 5 cm "transmission" square, where clips were installed to place sheets of Metglas ribbon. With all of the shielding and the transmission square blocked with borated plastic, the background rate of neutrons in the detector is 3.5 ± 0.1 Hz.

Eight squares of 2826MB Metglas ribbon covered the (unblocked) transmission window, and neutrons were tabulated in the MCA histogram for 2 hours. A pair of Metglas squares were removed, and the measurement repeated until all the Metglas

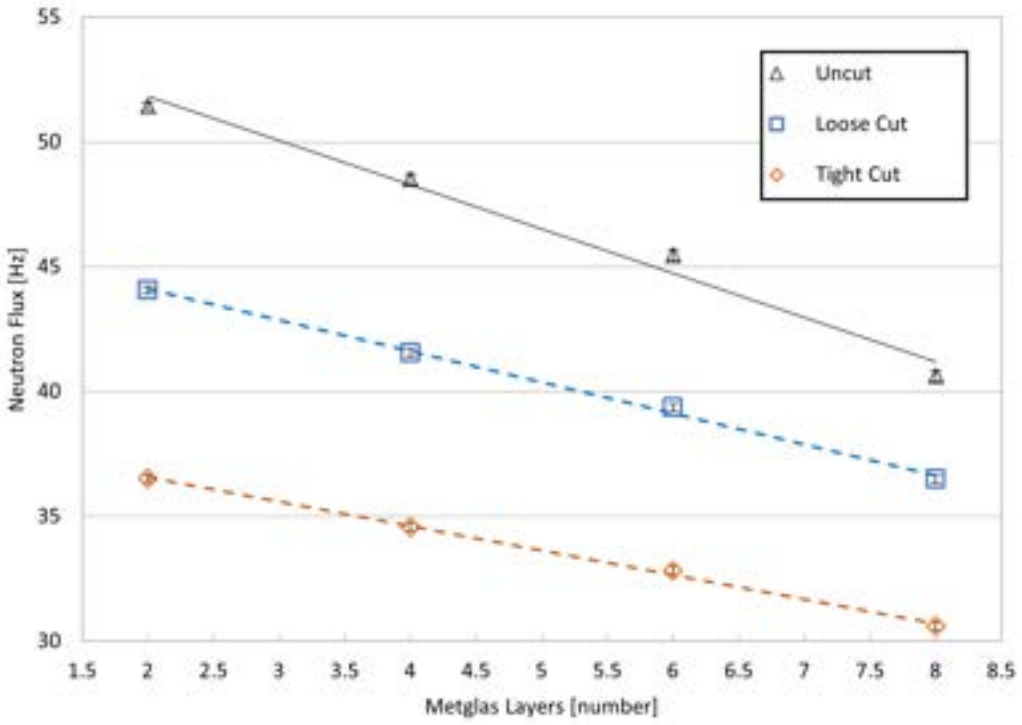

Figure 4.15: Neutron flux as a function of Metglas layers; note the decrease in neutron flux as more Metglas layers are added.

was removed. The background-subtracted counts (normalized by time) are plotted in Fig. 4.15.

The top dataset in Fig. 4.15 contains the total counts of the background-corrected histogram, and includes some background artifact at the low-energy tail of the histogram. The next two datasets are two potential cuts to the dataset: one just cutting off the low energy artifact, and the other getting close to the shoulder of the histogram's Gaussian shape—these two cuts yield the same results.

For ease of analysis, one does not need to establish the efficiency of the detector or the absolute flux of the neutrons if one compares only the data runs with varying amounts of Metglas foil; these trickier parameters cancel out. From the linear regression in Fig. 4.15 (given the thickness of the Metglas), the absorption length is calculated to be 1.13 mm ± 0.04 mm.

The cross section of boron is (7.67±0.08) $\times 10^{-22}$ cm^2 [117], yielding a density of ^{10}B of 1.16×10^{22} atoms/cm^3. Recall that we are only sensitive 20% of the total boron in the Metglas; the total density of boron atoms is therefore (1.45±0.05) $\times 10^{22}$ atoms/cm^3 or (0.26±0.01) g/cm^3. The total density of 2825MB is 7.9 g/cm^3, so the

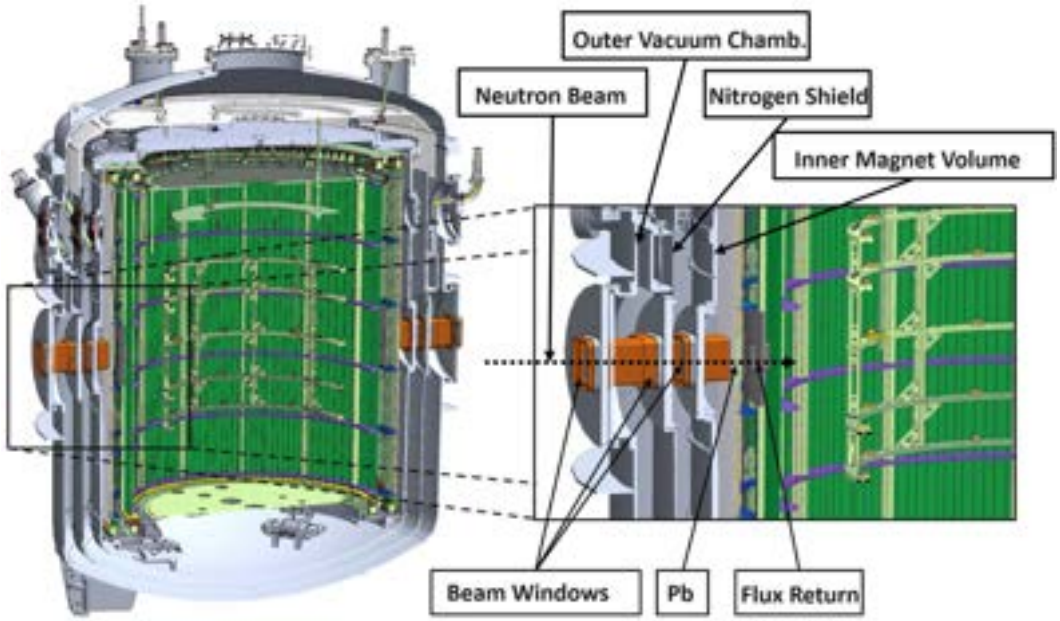

Figure 4.16: Cryomagnet Diagram: The cryomagnet layers are enlarged on the right to illustrate the neutron beam's path through the cryomagnet.

total boron content is 3.3% ± 0.1%. This results in a 2.7% loss in the single layer of the flux return, which is acceptable.

2826MB is a good material for the flux return; its properties boast a high magnetic permeability to capture the B0 flux, acceptable quasistatic shielding, and trace amounts of cobalt with and a small fraction of boron. The neutrons passing through the material will not activate it, and the number of neutrons captured is small. But what about the spin interactions of the material? What about polarization effects of moving through the magnetic domains of the Metglas? This concern is addressed by a polarization and transmission measurement through the cryomagnet.

4.2 Motivation for a Polarization and Transmission Measurement Through the Cryomagnet

Fig. 4.1 shows the concentric layers of the cryomagnet, inside which sits the measurement cells of the experiment. It is clearly depicted in Fig. 4.2 that the polarized cold neutron beam passes through those layers, interacting directly with beam windows, an alloy foil flux return, and magnetic fields on their way to downscattering into the measurement cell. All of these layers and stages could negatively impact their flux and polarity as they get "loaded" into the system.

This journey is illustrated in more detail in Fig. 4.16. They enter through the outer

vacuum chamber (OVC) through a thin engineered window, pass through the hole in the nitrogen shield, and then encounter a second engineered window at the inner magnet volume (IMV). Passing through the magnet package, a hole in the Metglas flux return would be too damaging to the homogeneity of the magnetic field inside the experiment. A decision to pass the neutrons directly through the Metglas is preferred, if the neutrons' depolarization is modest.

Neutron transport through all of these materials must be evaluated. Recall that the neutron flux is important to the experiment because the number of neutrons available to downscatter into UCN directly affects the statistical sensitivity of the experiment (Eq. 2.4); greater flux results in a higher density of UCN in the measurement cell. Transmission loss is also concerning because those captured neutrons can activate the experiment's materials, creating large backgrounds.

The polarization factors into both signal strength and coherence time. More in sync n-^{3}He captures produce more scintillation, yielding a larger signal over the background light. Depolarized neutrons will create background captures at the "wrong" time, and these captures slightly decrease the neutron population.

Some studies can be done using small samples of the in-beam materials that the neutrons must penetrate, but those measurements are not necessarily a great representative of the experiment as a whole. Graduate student Kavish Imam performed transmission measurements through thin metal window samples, including Magnesium/Aluminum AZ31B and Zircaloy-4 at a neutron flux reactor [118]; these measurements, as nonmagnetic components, are expected to be representative.

Superconducting lead [119] and some Metglas ribbons [120] were also previously studied. However, these samples are sensitive to the magnetic environment in which they are tested, and a small sample may not be able to reproduce it. For the lead, it may be expected that the neutron experiences the magnetic transitions through the boundary so quickly that the spin is unaffected ("non-adiabatically"). Simulations might be able to predict diabatic spin-flips by reproducing the current density along the superconductor and the microscopic magnetic domains in the Metglas, given the high field applied within. Columbia University undergraduate Jason Gao, a summer student at Caltech, simulated the spin transport of a neutron through these Metglas domains of different domain strengths and sizes. His results for domain strength in Fig. 4.17 show that as the Metglas is more saturated (x axis), the neutron spin (y axis) is more likely to stay polarized; this makes intuitive sense because less of the domains are randomly oriented, and more are oriented in the direction of the neutron

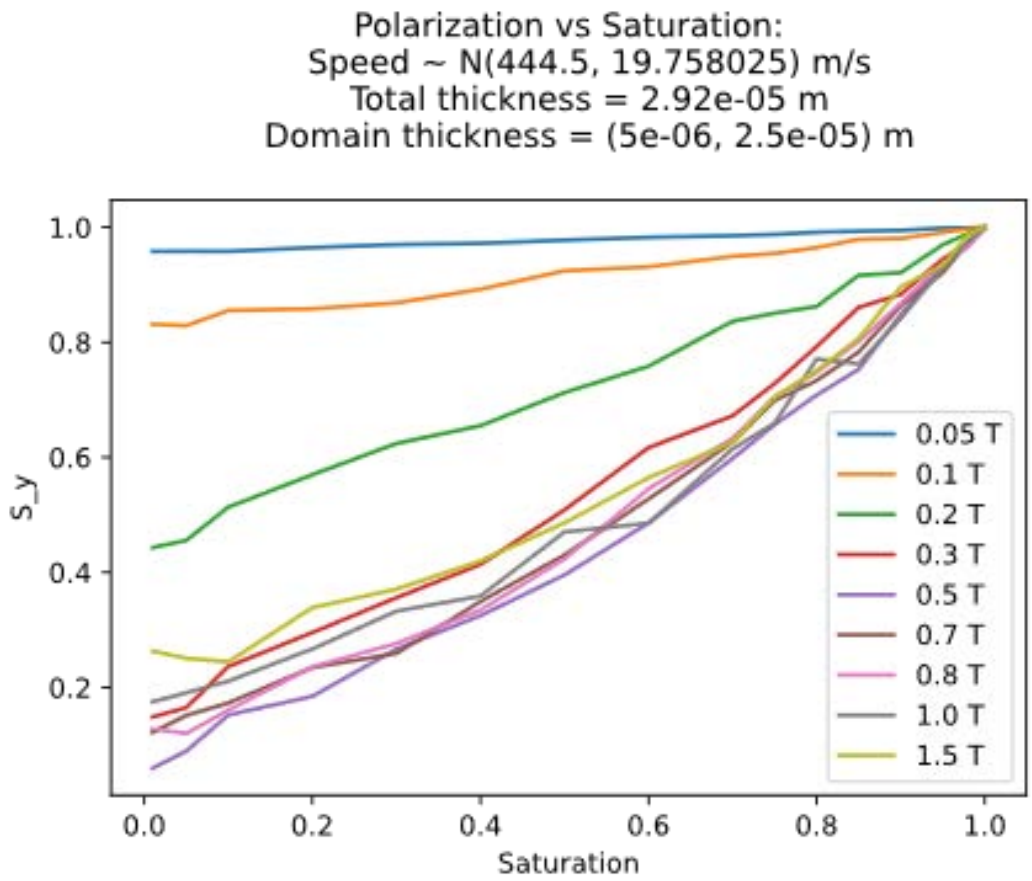

Figure 4.17: Metglas Saturation vs. Polarization of the neutron spins through the Metglas, courtesy of Jason Gao.

spin. However, the flux return will operate around the midpoint of this saturation graph. For differing domain strengths specified in the legend, these randomized domains have more depolarization effect the stronger they are. His simulations also suggested resonances at different domain sizes.

All of this uncertainty poses a risk to the needed polarization and transmission of the neutrons through the apparatus; this uncertainty can be eliminated by testing the polarization and transmission through the apparatus and reducing any polarization and transmission losses observed.

A meaningful polarization and transmission test requires an environment that approaches the magnetic characteristics of the real nEDM experiment. Recall that the experiment takes place in a magnetic shield enclosure that removes the magnetic field of the earth, and includes active shielding. To approximate this, bucking coils paired with a concentric cylindrical mu-metal shield can cancel out the Earth's field

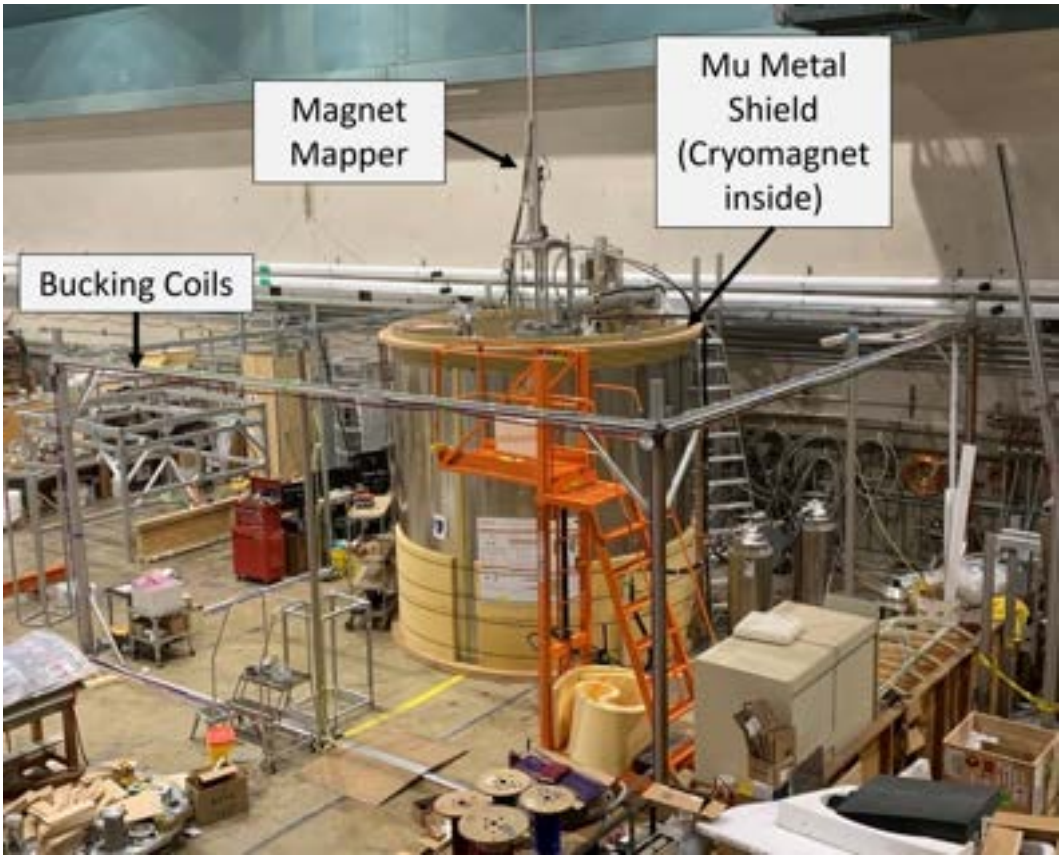

Figure 4.18: Photograph of cryomagnet setup at Caltech. Note the bucking coils and mu-metal shield to cancel the Earth's field and provide shielding for the cryomagnet inside.

and provide shielding for the cryomagnet. The idea was developed and implemented in Caltech lab space, pictured in Fig. 4.18. Note the Bucking Coils, when recreated at Oak Ridge National Laboratory, required currents of the order of 20 A (12 turns), 20 A (12 turns), and 10 A (4 turns) in the vertical, northern, and eastern directions.

The mu-metal shield was constructed of 0.8 mm mu-metal, wrapped around a G10 cylinder strengthened by wooden supports. Caltech graduate student Alston Crowley designed a magnet wound on the inside of the G10 cylinder to aid in the neutron transport inside the mu-metal shield's volume.

To make the polarization and transmission measurement, this system—the mu-metal shield, bucking coils, and the cryomagnet setup—needed to be installed and commissioned in a location providing a 9.8 Å cold neutron beam, with various configurations of the magnet package to isolate each layer's effect.

4.3 Commissioning of the Caltech Cryostat

The commissioning of the Caltech Cryostat took place in an experimental hall attached to Beamline 13 of the Spallation Neutron Source, called "External Building 1" (8713 on an Oak Ridge campus map). This is not the Caltech Cryostat's final location for the nEDM@SNS experiment; its final location "External Building 2" would be constructed adjacent to the existing building. However, this initial location is ideal for studying the systematics involved with the cold neutron transport into the future nEDM@SNS experimental cell—its transmission and polarization through the nested layers of the apparatus.

This building is sufficiently large with adequate overhead space, equipped with an overhead crane for construction of the nested layers of the apparatus, power for the Helium system, access to Nitrogen bottles, and most importantly, access to 9.8 Å neutrons from Beamline 13A discussed in section 4.5. Installing the Caltech Cryostat in External Building 1 allowed us to gain operational experience, further develop that data acquisition control infrastructure, and measure the cold neutron transmission and polarization through the nEDM experiment as we add each layer to the magnet package.

This operational experience is essential in producing a working experimental apparatus, and I received a Department of Energy Office of Science Graduate Science Research Fellowship (SCGSR) to relocate to Oak Ridge National Laboratory to commission the system. With so many layers and interwoven systems (depicted in Fig. 4.1), we assembled, leak checked, and installed it in the experimental hall. To accomplish this work, I attended two onsite workshops, "Training for Overhead Crane Operations" and "Basic Hoisting and Rigging" class. These workshops were very useful in assembling the nested layers of the cryostat and allowed us to make installation progress on schedule.

This also involved setting up a slow control system for the apparatus cool down. The data acquisition's slow control system is a software infrastructure that allows computer control of the hardware of the experiment, such as the temperature sensors, valves, flow controllers, and power supplies.

The commissioning of the Caltech Cryostat included:

- the mapping and troubleshooting of the magnetic field in the External Building 1 experiment hall
- the installation and leak checking of the nested layers of the apparatus

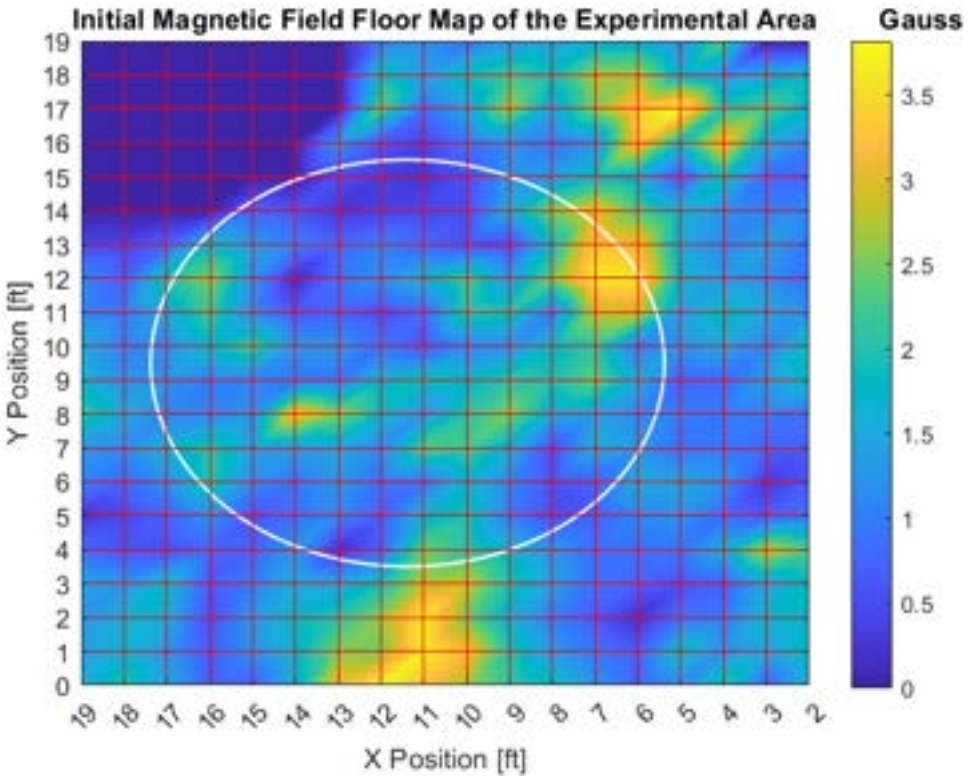

Figure 4.19: Initial Magnetic Map of the Experimental Hall. Here the X axis is parallel to the wall closest to the SNS target hall (approximately East–West), and Y is perpendicular to that wall (approximately North–South). Note the significant magnetic field maxima along the mu-metal shield position, drawn as a white circle for reference. Also note that there is no data at the upper left hand corner of the graph.

- cooling the system, ultimately into the single Kelvin range
- slow control communication with every major device in the cooldown and an array of sensors

4.3.1 External Building 1—Initial Magnetic Troubleshooting

First, the polarization and transmission measurements are only valid characterizations for the final nEDM installation if the environment of the apparatus is controlled to limit the extraneous magnetic field gradients and disturbances that are not present in the final nEDM experimental environment. The technical approach to control these conditions include cubic bucking coils surrounding the experimental space, a cylindrical mu-metal shield around the apparatus itself, and surprisingly, steel plate shielding on the floor.

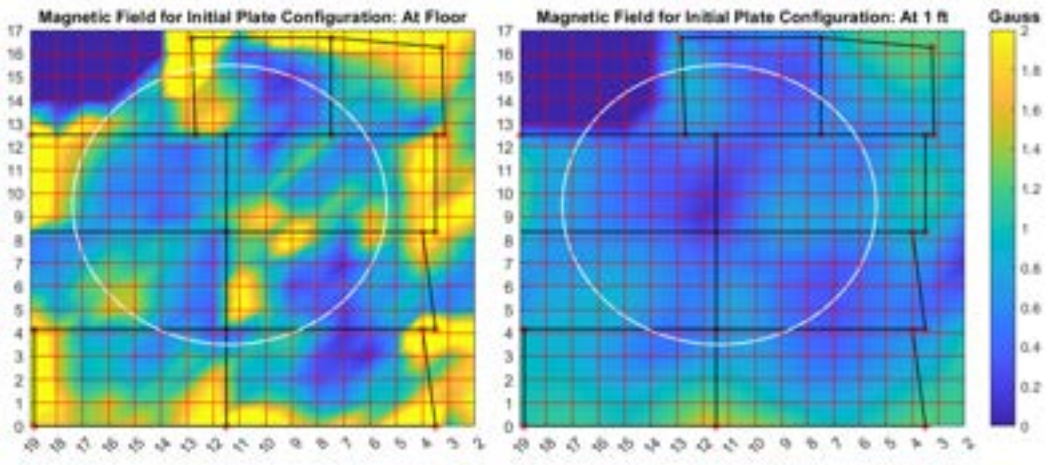

Figure 4.20: Magnetic Maps for the Initial Configuration of Steel Plate Shielding. Left, at floor level. Right, at 1 ft above the plates.
Note that the magnetic field hotspots from Figure 1 have dissipated from the graph on the right, and further fall away at 1 ft on the left. The cylindrical mu-metal shield (drawn as a white circle) actually begins about 1 ft off of the ground, and so this magnetic field depicted would work perfectly. As in Figure 1, there is no data in the upper left corner of the plot.

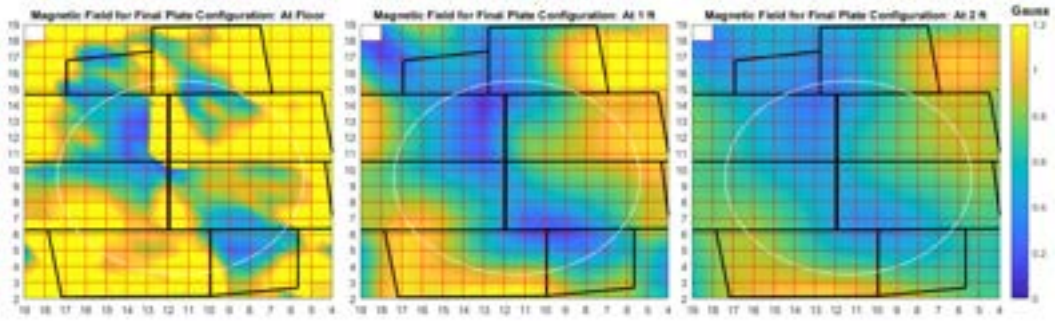

Figure 4.21: Magnetic Maps for the Final Configuration of Steel Plate Shielding. Left, at floor level. Middle, at 1 ft above the plates. Right, at 2 ft above the plates. Note that the configuration does not do as well as the initial configuration at 1 ft but still does not saturate, but does well at 2 ft above the ground.

An initial magnetic field map of the floor of the experimental area, shown in Fig 4.19, suggested that some of the steel rebar used in its construction was heavily magnetized, showing magnetic field hotspots of around 4 gauss. The cylindrical mu-metal shield would saturate around 1 gauss, so more shielding was required.

A finite element analysis simulation, run in the COMSOL [76] magnetic framework, showed promise that laying steel plates on the ground would help shield the experiment as shown in Fig 4.22, and plates of C1010 steel shielding left over

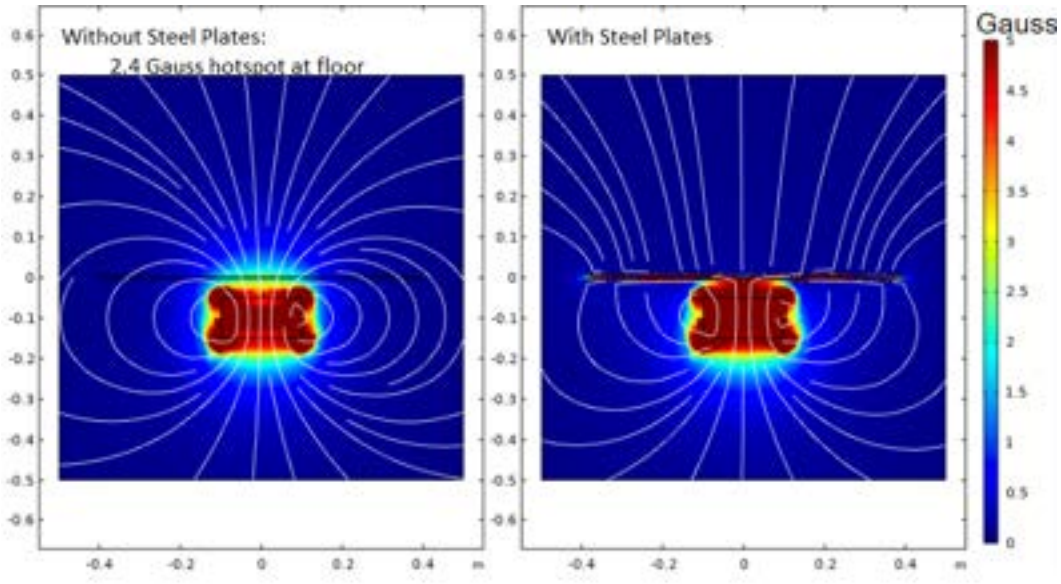

Figure 4.22: Finite Element Analysis of a Steel Plate on a Dipole:
Left, plate absent. Right, plate present.
Note how the 2.6 gauss field above the plate location on the right is suppressed on the left as the magnetic field lines get sucked into the plate.

from a previous experiment were laid out over the experimental area and found to be adequate in their initial "proof of concept" configuration as shown in Fig 4.20. However, some of the plates became magnetically contaminated (magnetized) during handling after a series of water leaks in the building necessitated their painting; the facility painters flipped the plates directly over the magnetized rebar. Studies were done using many degaussing methods to remove this contamination without success, including using an AC-powered magnetic tape eraser, a bar magnet, and a solenoid magnet.

Limited success came from removing the most contaminated of the steel plates and reconfiguring the remaining steel as shown in Fig 4.21—the new configuration was not as good as the initial proof of concept from Fig 4.20, but adequate to not saturate much of the mu-metal shield. One must take care to not magnetize steel in the presence of magnetic field hotspots.

4.3.2 Outer Vacuum Chamber—Placement

After the magnetic map over the steel plates configuration proved adequate, the apparatus could be installed on top of them. We call the outermost layer of the apparatus the Outer Vacuum Chamber, denoting its function. An abundance of caution led us to preventing unnecessary stress on the inner components of the

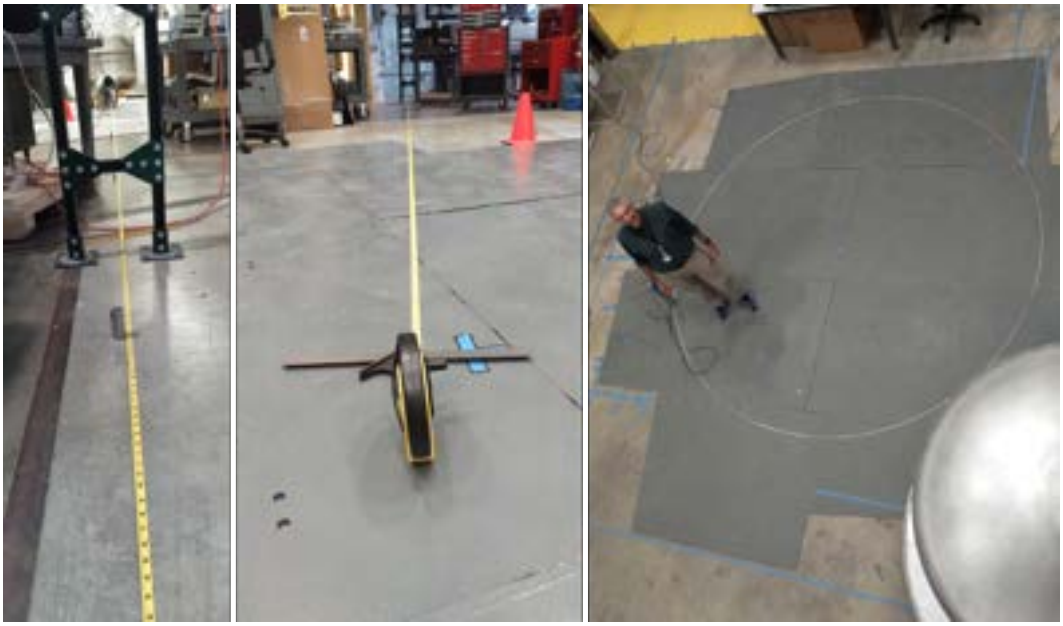

Figure 4.23: Photographs of the OVC position with respect to the experimental hall. Left: Downstream view from the beamline cave towards the experimental hall. Center: Upstream view from the experimental hall, including the square to measure the 18 cm offset from beampipe-center. Right: A chalk ring representing the circular extent of the apparatus (the edges of the mu-metal shield), with a professor for scale.

apparatus by placing the vacuum chamber before installing the inner components.

The vacuum chamber was craned onto the plates, and then Oak Ridge National Laboratory's Survey and Alignment team used their laser alignment system to aid in optimal positioning (to a tolerance level of 0.5 cm by successive lift-taps); this was a tedious alignment due to the coarse control of the crane, exacerbated by a quasi-random pattern of whether a successive corrective lift would bring us closer or further away from our optimal placement.

The optimal placement was calculated based on where the beam came out of the Beamline 13 cave[b], and adjusted for both the off-axis window placement and the reflection angle (critical angle of one spin state) of the supermirror polarizer. I estimated this position using the neutron flight tube supports and some crude measuring devices (measuring tape and square) as seen in Fig. 4.23, and the Survey and Alignment Team found this to be correct to less than 5 cm. Fig 4.24 shows the Survey and Alignment laser at work, as well as a photograph of the outer vacuum chamber (OVC) placement on the steel plates.

[b]Concrete structure for radiation safety with beam access within

Figure 4.24: Photographs of the OVC placement. Left, the survey and alignment team affixing their laser alignment system to the outside of the OVC. Right, the completed placement of the OVC on the steel plates in the experimental hall.

However, two major misalignments occurred vertically and rotationally. The Survey and Alignment team found that the rotation of the vessel to be out of alignment by over 2.5 cm. Furthermore, External Building 1 and the Target Building (where the neutrons originate) had an unaccounted floor difference of 4 cm, and the introduction of the steel plates raised the vessel at least another 2/3 cm. This caused the neutron beam to pass through the vessel lower than designed. Beam geometry calculations appeared to tolerate this misalignment, putting the neutron beam in the lower right corner of the windows. Extra material was removed from the external mu-metal Shield as seen in Fig. 4.25 in attempt to ameliorate this misalignment.

4.3.3 Cryogenic Layers—Installation

The cryogenic layers of the apparatus include the outer vacuum chamber, the nitrogen shield, and the inner magnet volume. Each of these 3 layers consist of a shell, a lid, and some multilayer insulation (MLI) wrapped between them. They nest together like Matryoshka dolls, requiring precise crane maneuvers to bring each "doll" into position inside the next one.

The nitrogen shield ("100K shield") is the first layer inside of the Outer Vacuum Chamber. It consists of an aluminum "bucket" with a non-sealing "mushroom"-shaped lid (shown in the bottom left of Fig. 4.27 held at around 100 K by two LN_2 pathways. The first pathway is a series of welded coils on the top of the mushroom, as seen in the top left of Fig. 4.27 for a liquid nitrogen flow-based cooling. The second pathway contains a reservoir "belt" around the aluminum bucket, which

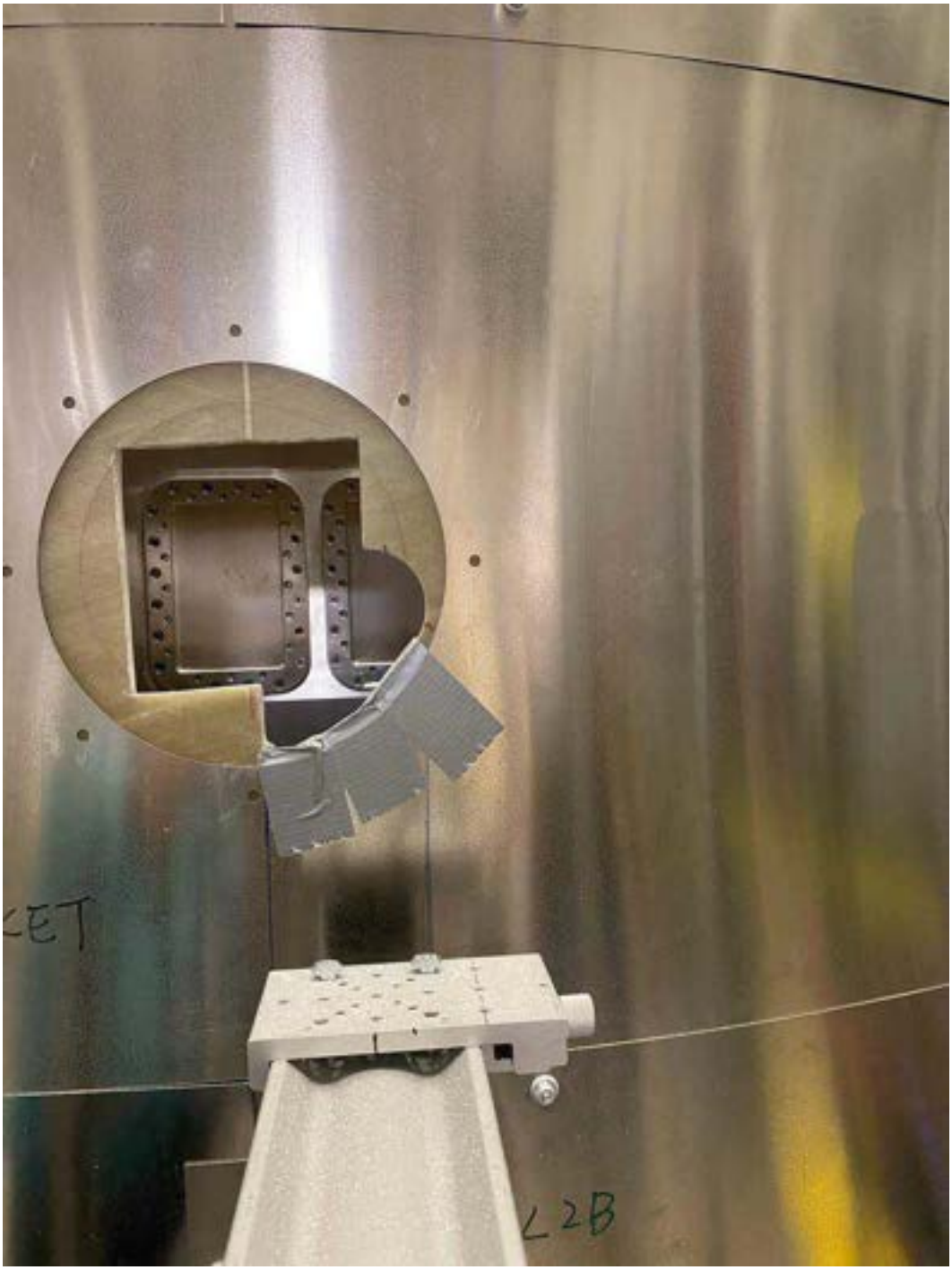

Figure 4.25: Photograph of the upstream view of the mu-metal shield and cryomagnet. Note the extra cutout for the neutron beam.

Figure 4.26: Nitrogen shield installation: a photo montage of the careful maneuver as the liquid nitrogen shield is lowered into the outer vacuum chamber and secured with cold mass support rods.

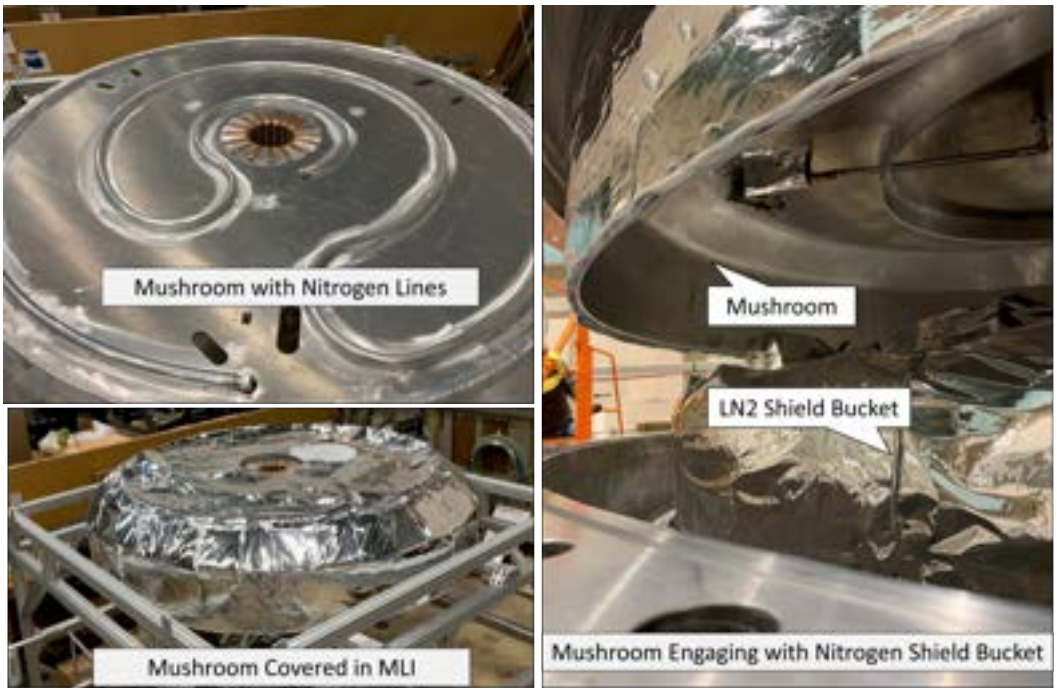

Figure 4.27: Photographs of the Mushroom. Upper Left: The naked mushroom showing its welded nitrogen coils. Lower Left: The mushroom dressed in 60 layers of MLI. Right: Lowering the mushroom onto the bucket of the liquid nitrogen shield; the two cylinders mate loosely.

holds the liquid nitrogen for a more stable cooling reservoir less sensitive to flow. The bucket and the mushroom of the nitrogen shield do not form a hermetic seal, but instead nest together as shown in the right side of Fig. 4.27.

The nitrogen shield's aluminum body is suspended inside of the vacuum chamber by three G10 cold mass support rods, connecting to the shield by way of three straight clevis pins. The nitrogen shield's mushroom is suspended from the vacuum

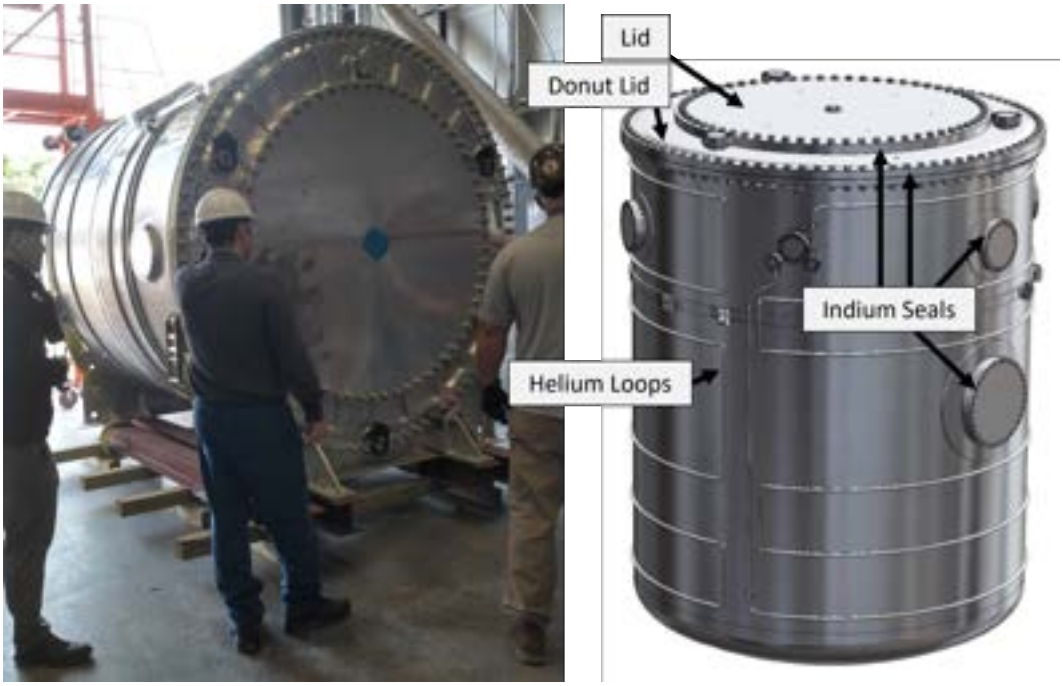

Figure 4.28: Inner Magnet Volume: Left, photograph of the IMV as shipped (on its side). Right, model of the IMV with its double lid, beam ports, and helium loops labeled.

chamber's lid via three G10 pole supports. Fig 4.26 shows the installation of the nitrogen shield (already covered with MLI) into the apparatus. Despite the MLI, the belt tank is clearly visible in the first photo on the left. Both the pole supports and the cold mass support rods are made of the composite G10, minimizing the conductive heat load to the shield. The radiative heat load is also minimized with 60 layers of MLI.

The second layer inside of the cryostat is the IMV. This aluminum vessel is capped with two large indium seals on the "lid" and "doughnut lid" as pictured in Fig 4.28. It has its own three clevis-pinned cold mass support rods also suspended from the room-temperature vacuum chamber, and ten layers of MLI. The Inner Magnet Volume is cooled by loops of near-critical helium, using a Cryomech closed-loop helium expansion system consisting of two cold heads with a central compressor, and two auxiliary compressors. The Cryomech system is discussed in detail in Section 4.3.5. Fig 4.29 shows two photographs of the IMV installation, including installation of the Helium service ports (left) and the lid's MLI (right). Note on the left, the two sets of nuts that compress the indium seals and other features are all covered with MLI on the right.

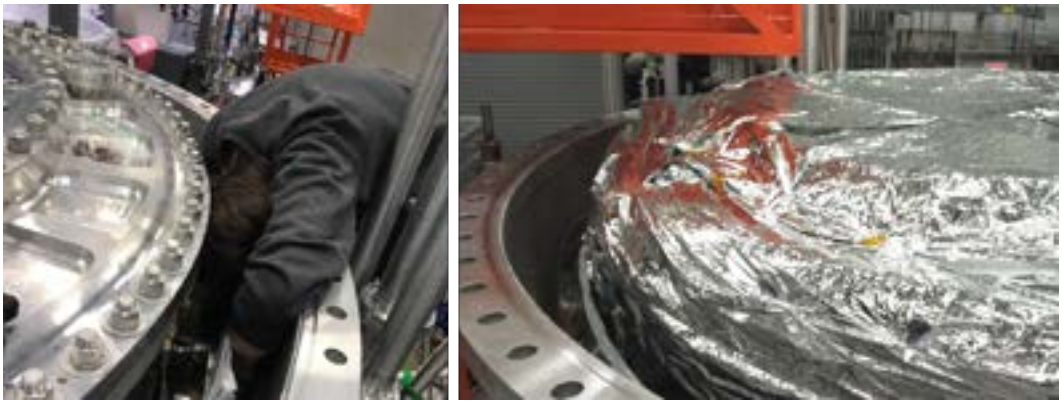

Figure 4.29: Photographs of the Installed Inner Magnet Volume: Left, student Alston Crowley reaches into the space between the IMV and nitrogen shield to install the Helium services into the IMV. Right, the IMV covered with ten layers of MLI.

The physical scale of this work can be felt from these photos, and it helps to have height-advantaged people on the team. Graduate Student Alston Crowley, pictured reaching into the abyss between the IMV and OVC in Fig. 4.28, is 6.5 feet tall. Any magnetic components such as tools were tied to the team's wrists to prevent them from falling into the annulus. However, one or two items problematic to the final experiment fell into the void—such as a stainless steel KF O-ring assembly. An equivalent O-ring assembly was tested with the flux gate, revealing a contaminating adjacent field of only 20 nT.

The innermost layer is the B0 Magnet Package, discussed in section 4.1. The installation of the B0 Magnet Package also included careful cranework, with three posts in the G10 magnet frame lowering into three holes on engineered hinging brackets called "lobsters." These lobsters fasten to the bottom of the IMV.

The magnet package's present configuration—for the initial test—include the copper shield, the B0 magnet, and the flux return. This is installed in Fig. 4.30 and in Fig. 4.31. Note from Fig 4.31 that the flux return blocks the line of sight through the beam window ports: the neutrons go through it. The left photograph shows the cryostat before the beam windows are installed, and one can see a pipe on the other end of the room. However, the right side shows the same view with the magnet package installed; the beam windows of the magnet package are covered with a layer of Metglas. This high-mu material, with the flux of B0 running through it, will depolarize the neutrons at some level suggested by Jason Gao's simulations discussed in Section 4.2. One can even observe a shape indenting the Metglas

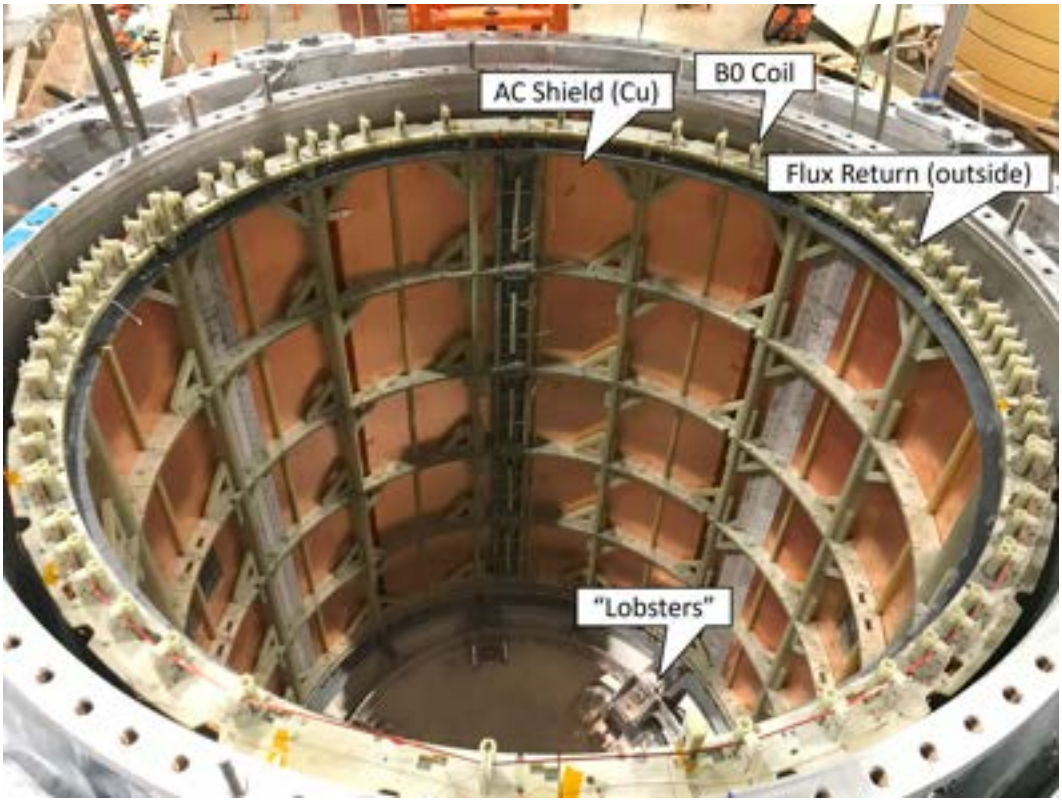

Figure 4.30: Photograph of the Magnet Package installed in the cryostat, with all lids off.

slightly on the right photograph in Fig. 4.31; this is the cutout of the beam windows through the G10 and copper of the package.

Future iterations of the polarization and transmission measurements will include the spin-dress magnet coil and the superconducting lead shield, after we isolate the effect of the currently installed components.

Buttoning everything up includes installing the beam windows, the lid to the IMV, and lid to OVC. Their installation is as follows:

The IMV lid is a double-lid with a doughnut lid on the outside and an inner circle lid on the inside. A double lid allows for configurations that involve installing room temperature instrumentation in an inner bore inside of the cryostat at Caltech. Here, both lids are sealed with indium and are treated as one piece. This is shown on the left in Fig. 4.32 on the overhead crane. Before installation, a magnetic field probe array photographed in Fig. 4.33 was attached to the inside of the IMV lid, to monitor the magnetic field inside of the IMV [61].

The next layer, the nitrogen shield's non-hermetic sealing lid discussed above (called

Figure 4.31: View through the open beamports before (left) and after (right) the magnet package was installed in the cryostat. The beam window flanges are not installed, allowing a view straight through the apparatus without the magnet package. Note, however, with the magnet package installed, the view is blocked by the Metglas flux return.

Figure 4.32: Lid installations. Left, the IMV lid before the magnetic field probe array is installed. Middle, the nitrogen shield mushroom (lid) covered in MLI, being craned by graduate student Marie Blatnik. Right, the OVC lid with the nitrogen shield mushroom attached.

Figure 4.33: Photograph of the magnetic field probe array hanging from the IMV lid.

the "mushroom"), is shown mid-maneuver in the center photograph of Fig. 4.32 as I craned it onto a stand to prepare for installation. It hangs from the OVC by G10 support poles, and you can see it underneath the OVC lid in the left photograph of the figure. After the mushroom is installed, both lids (the mushroom and OVC lid) are craned as one into place. The delicate descent involves first ensuring that the mushroom delicately surrounds the opening of the nitrogen shield and its MLI, and then aligning the bolt holes of the OVC as the descent culminates. The maneuver included four people at the North, East, South, and West ends of the cryomagnet on ladders to ensure that their bolt holes aligned; their communication was especially important with a slight paraboloid (potato chip shape) distortion of the lid.

Once these surfaces were sealed, an initial cool down was done, using a side port on the cryomagnet to pump out the OVC as discussed in section 4.4. Lessons from this first cool down were applied to the beam cool down, which required the OVC to be pumped from above due to the installation of the magnetic environment.

A final note on the installation: I received hoisting and rigging training, which removed a stressful source of uncertainty and delay working with the SNS facilities personnel. It allowed me to better coordinate and perform these delicate maneuvers myself, and is highly recommended for future installation activities.

4.3.4 Installation of the Magnetic Environment

Once the Outer Vacuum Chamber was sealed and leak checked, but before the vacuum system and Cryomech system could be installed, the mu-metal shield needed to be installed. This consists of a 12-foot diameter, 12-foot tall G10 cylinder covered in mu-metal sheets, with wooden stiffening rings to reinforce the cylindrical shape. It can be seen at Caltech in Fig. 4.18.

Its installation at the beamline was nontrivial, as the lift was constrained by the hook height in the building. Including the lifting fixtures, the clearance between the fully hoisted mu-metal shield and the top of the OVC lid was only 4 to 5 cm. Further complication was created by the IMV cooling lines depicted in Fig. 4.38; these pipes intruded high into the space needed for the lift. Rather than fight to reinstall them at height with no clearance (a potentially impossible feat), we cut a "mouse hole" in the mu-metal shield to pass the shield's cylinder over them. This mouse hole appears in Fig. 4.34, with a postdoctoral mouse for scale in the bottom right photograph.

The montage of photographs in Fig. 4.34 shows that some mu-metal panels were

Figure 4.34: Photographs of the mu-metal Shield Installation. Top left, the shield is lifted with a spreader bar. Top right, the shield is lowered around the cryomagnet. Bottom left, the shield is rotated so the IMV services pass through the mouse hole. Bottom right, postdoctoral mouse peeks through the hole for scale.

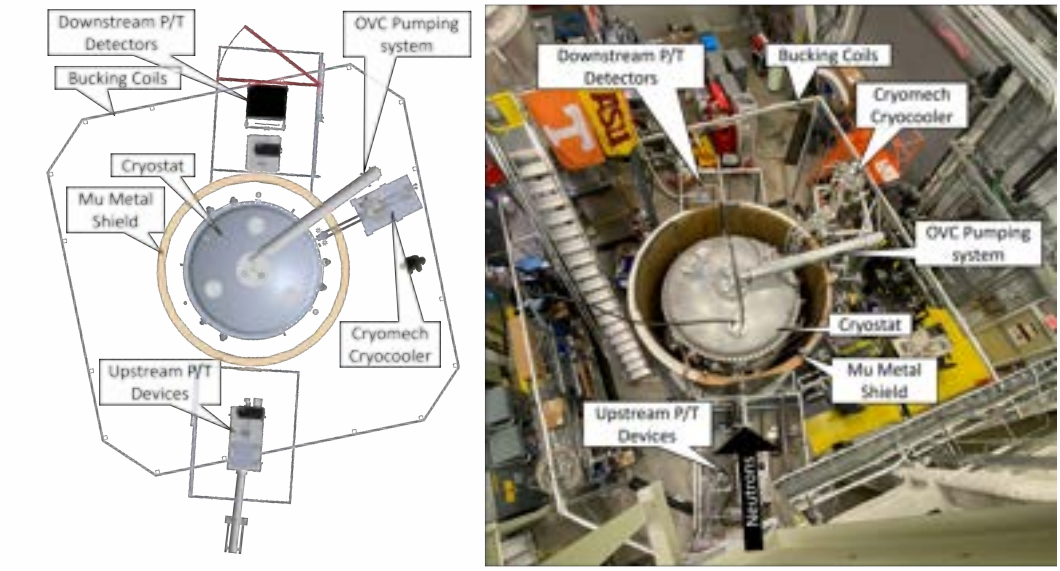

Figure 4.35: Final P/T Configuration: Left, CAD representation of the polarization and transmission set up. Right, photograph of the set up.

removed to make the mouse hole. The shield was lifted with a spreader bar (top left), rotated such that the IMV cooling lines passed through the mouse hole (bottom left), and lowered around the cryomagnet (top right). Finally, after the crane operation was completed, the panels were replaced onto the G10 form, and Caltech graduate student Alston Crowley's neutron transport coil was installed.

The final requirement for the magnetic environment was the bucking coils as in Fig. 4.18. These electromagnetic coils were wound along the x, y, and z directions with 12 AWG wire on 80/20 aluminum supports as depicted in the frame in Fig. 4.35.

4.3.5 Cryomech Cryocooler System

The Cryomech cryocooler system (based on the pulse-tube Cryomech PT420) provides the cooling for the IMV by pumping near-critical helium through the tubes welded to the outside of the IMV. Its system includes a circulator with heat exchangers and two stages of cold heads (Cryomech PT420) within a multi-cylindrical setup above the cryostat on an 80/20 [121] frame as labeled in Fig. 4.35, called the circulation package. The cold heads are supported by two auxiliary compressors, CPA1114 A and B, and the circulator is supported by a CP103 compressor. These compressors sit in a tower in the northeast corner of the building, near the building's water cooling supply (see Fig. 4.39).

The system is illustrated in Fig. 4.36, and a CAD diagram provided solely by

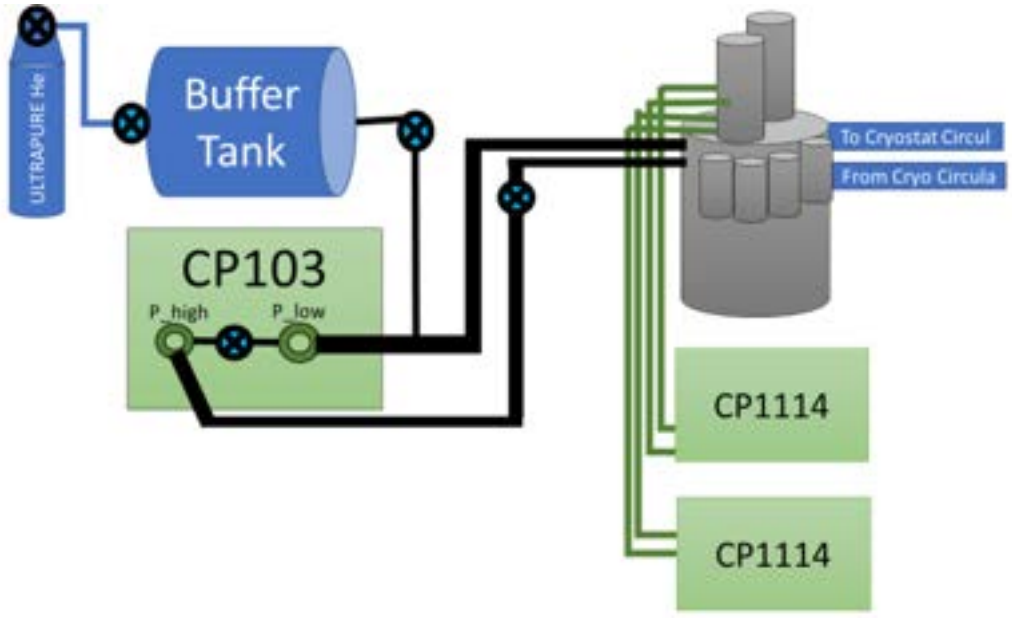

Figure 4.36: Illustration of the Cryomech Cryocooler System. The circulation package is the grey multi-cylindrical tower in the top right, pushing helium into the blue rectangles going into the IMV cooling loops. The compressors remove heat and send compressed helium into the circulation package, where it expands in the cold heads inside. The buffer tank adds ultrapure helium to the system.

Cryomech is reprinted with permission in Fig. 4.37. The circulation package is represented by the grey multi-cylindrical tower in the top right, and the blue rectangles off to the right are the helium lines/stingers going into the IMV cooling loops via the IMV service ports. This is further illustrated in the photographs of Fig. 4.38.

The three compressors are represented by green boxes and labeled in the figure; each compressor has a pair of flex hoses to the circulation package with Aeroquip fittings. These fittings allow the whole system to become connected/disconnected while trapping the ultrapure helium in the volumes to prevent spoiling the purity of the helium in the system. Special care is paramount when installing or reconfiguring the system to ensure that only Aeroquip connections are connected/disconnected to prevent gas contamination.

Note that the CPA1114 compressor flex hoses feed directly into the system as they remove heat and compress the helium for the cold head expansion. These two compressor loops are completely closed, and the volume of helium that cools in these loops is very small. Therefore, no additional helium is needed to balance the

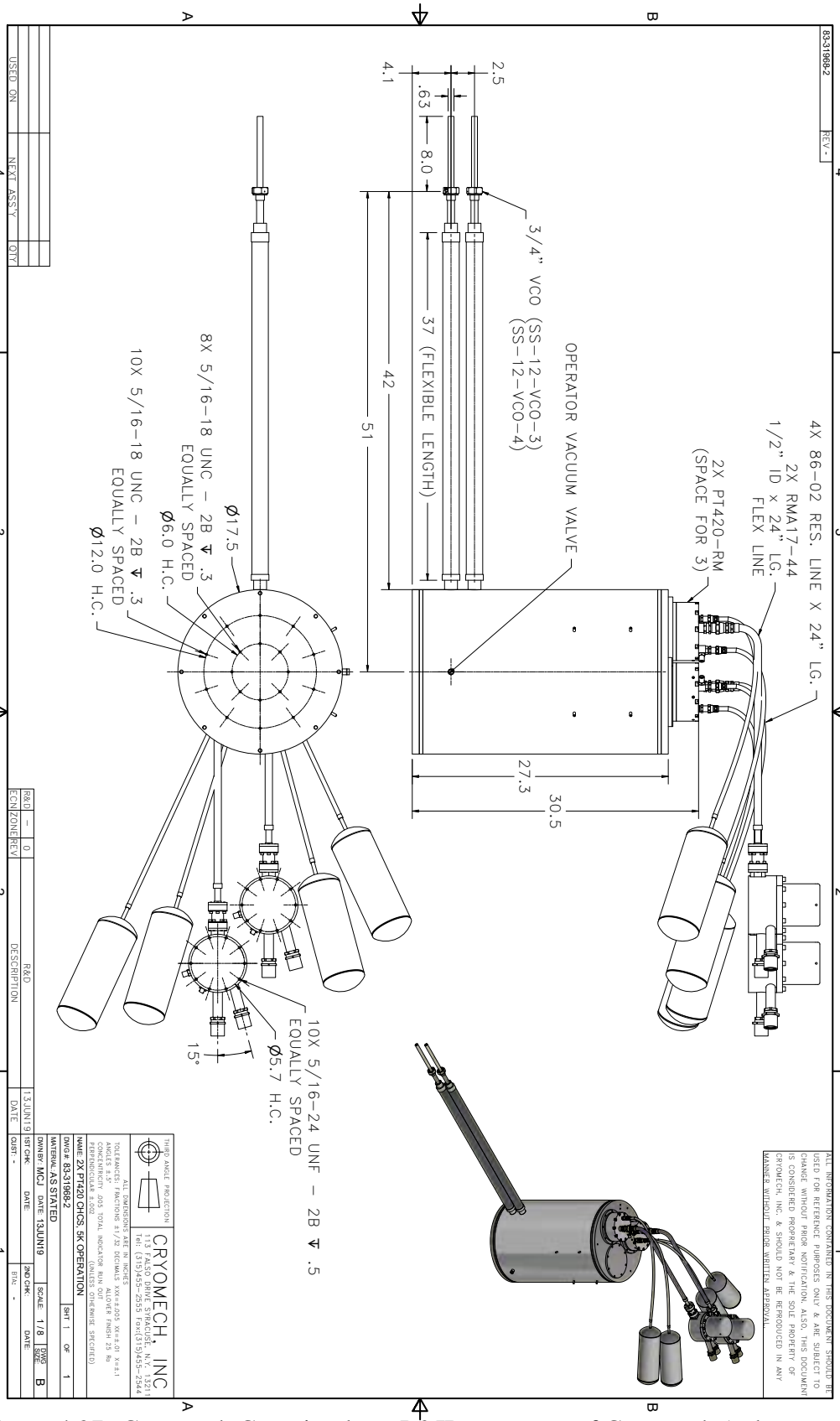

Figure 4.37: Cryomech Cryocirculator P&ID, courtesy of Cryomech (sole source)

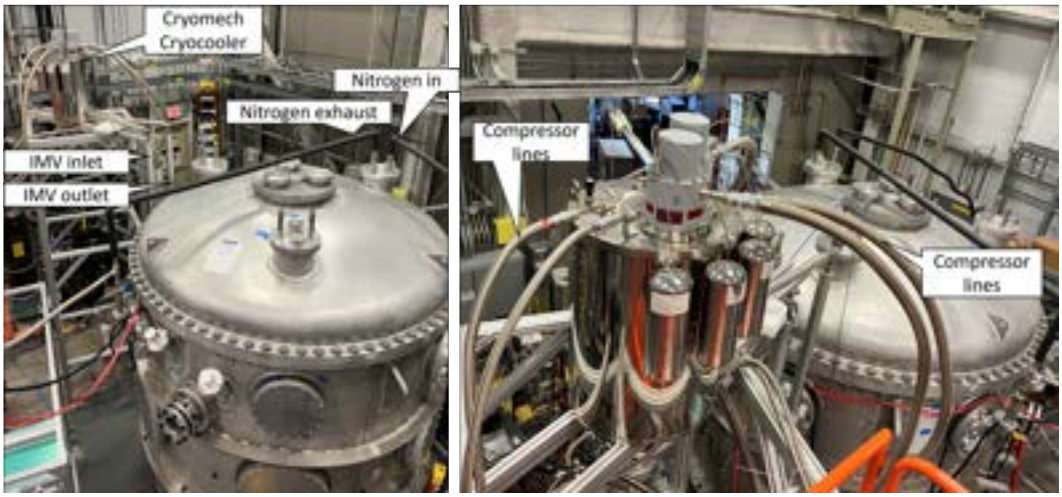

Figure 4.38: Photographs of the Cryomech Cryocooler System installed. Left, view from the west side of the cryomagnet. Note the circulation package on its stand, and the tubes feeding into the IMV services. Right, view from the east side of the cryomagnet—a closer view of the circulation package.

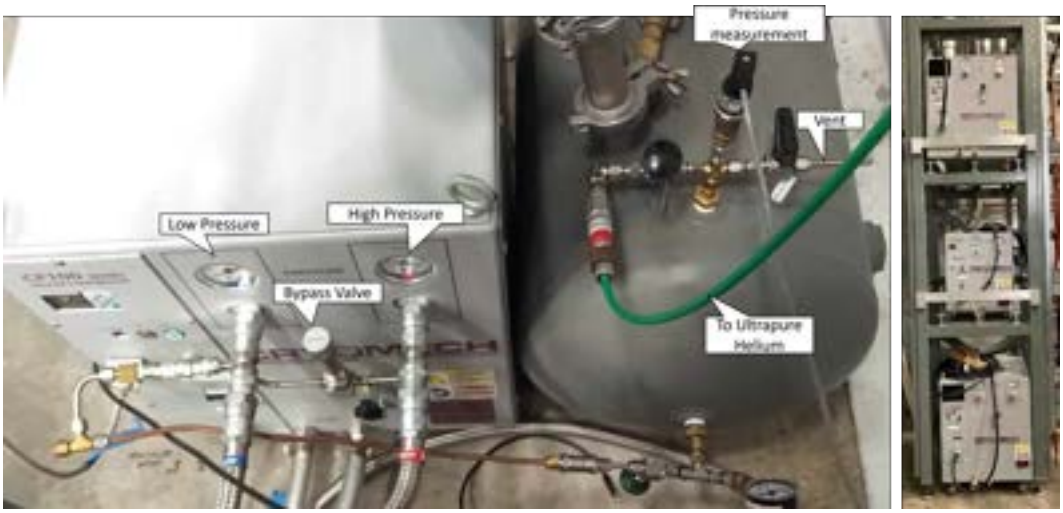

Figure 4.39: Photographs of the Cryomech Compressor System. Left, the CP103 compressor with the Buffer tank. Right, the three compressors in their tower.

small density change as the system cools.

The CP103 loop has two valves, each represented by a circle with a cross shape in the illustration. These two valves allow us to tune or bypass the flow through the circulation package and therefore through the IMV cooling loop. This circulation loop requires additional helium as the temperature of the system drops, provided through the buffer tank. This recharging is necessary when the high pressure output of the CP103 drops near 175 psi, or if the difference between the high and low side may drop below 75 psi. The frequency for required recharge depends on how leak-tight the buffer tank manifold is, and how quickly the temperature of the system is dropping, but is on the order of a couple of days. These recharges are done using the buffer tank and its ultrapure helium bottle, which are represented by the blue labeled shapes in Fig. 4.36 and photographed in Fig. 4.39. Recharges must happen very slowly (5 psi/minute) to keep the compressor oil from contaminating the system.

This cryogenic system required commissioning twice at the beamline—once for an initial cool down before the mu-metal shield was installed, and once after the shield was installed. The goal of the first cool down was to verify operation post-shipping, troubleshooting issues ahead of the beam schedule. The second cool down was for the polarization and transmission measurement. These cool downs are detailed in Section 4.4.

4.4 Cool Down of the Caltech Cryostat

4.4.1 Slow Controls and Instrumentation

The slow controls system communicates with all the major devices involved in the cryogenic and cool down operations, including the turbo pump and its gate valve, the Cryomech cryocooler and its compressors, and a variety of temperature and pressure sensors installed in the system. It stores data in a SQL database architecture, which populates using python scripts that communicate serially with each instrument's digital readout. Once the database is set up (see setup_tables.py and instruments_DBNAME.pl where DBNAME is the database name), initialized (see initialize_tables.py), and populating (see mag_start_progs.py), the data can be accessed with the QT-based graphical user interface (executable SlowDaqDisplay_v5) shown in Fig. 4.40 [c].

[c] QT (pronounced "cute") is a C++-based development architecture for creating graphical user interfaces [122].

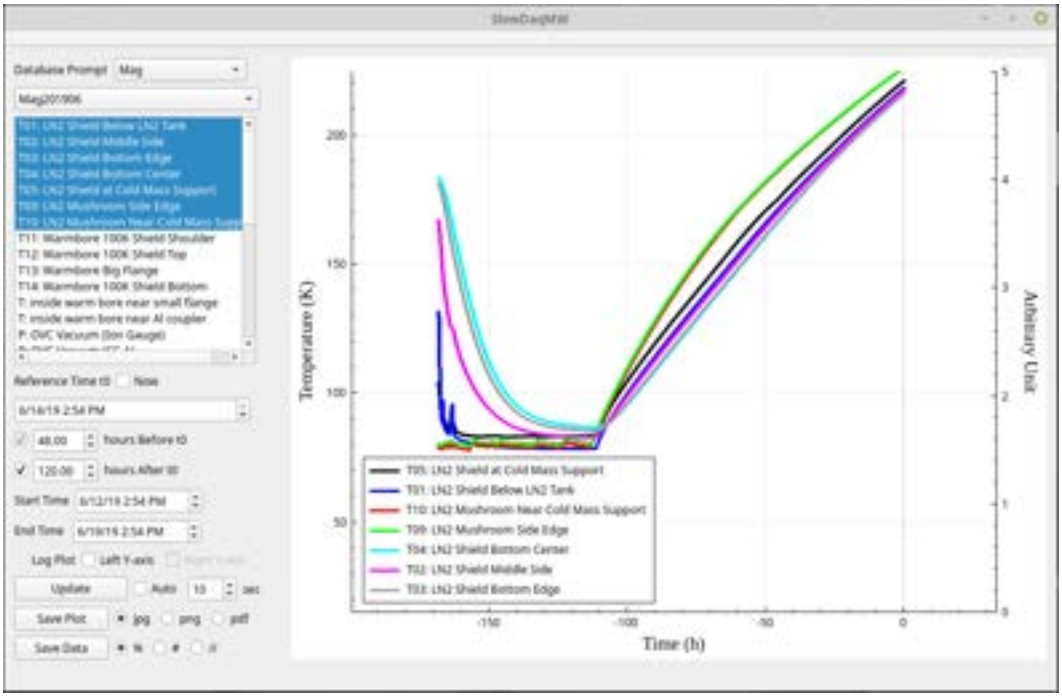

Figure 4.40: Graphical User Interface for the slow control system. Temperatures are plotted from a Caltech cool down; each cool down can have its own database.

The instrument list and the variables stored are written in an XML file that feeds into the Perl scripts. For these cool downs, the important instruments include:

- Cryomech CTC100 temperature controller for the Cryomech circulator system
- Cryomech CPA1114 Compressors
- CP103 Compressor Monitor (Arduino)
- Lakeshore cryogenic temperature monitors (two Lakeshore 240 units and two Lakeshore 218 units)
- Agilent LCR meter (attached to a capacitive level meter)
- Turbo Pump Controller
- Gate Valve Monitor (Arduino)
- Three vacuum gauge controllers (Granville-Phillips, MKS, and Heise)

The Cryomech CPA1114 compressors use ModBus protocols and can be communicated serially (RTU using RS232) or over Ethernet (TCP/IP). The slow control

system communicates with them using serial Modbus RTU protocol, which was convenient at Caltech where the computer was sufficiently close to the compressors. However, at Oak Ridge National Laboratory, the compressors sit in the northeast corner of the room while the slow control computer sits at the southeast corner—significantly over 50 feet away. Thankfully, both serial-to-USB converters and USB hubs work as serial "repeaters" which allows a graduate student to cheat the distance limitations of serial communication. It may be prudent to switch to Ethernet Modbus TCP/IP communication to eliminate the tight distance restriction for the final experiment; the pain of checksums and writing directly to registers can be skipped by modifying the current python object (CPA_ModBus_v2.py).

The CP103 compressor has an even more primitive communication protocol—essentially a row of output and input pins on a DB9 connector that flag errors in the system. Each input pin represents a simple primitive command (e.g., "shut off"), and simply requires a completed circuit to the first pin to send a "true" to the system. The output pins represent only error flags, and read "high" or "low" compared to that first pin. An Arduino was employed to record the Boolean of these output pins. This Arduino was given a double-duty of reading the output of a pressure sensor (Ashcroft G2 Pressure Transducer) on the buffer tank, converting the output voltage of the sensor to a pressure reading.

The temperature sensors consist mostly of DT470 AND DT670 silicon diodes, measured by Lakeshore (LS218 and LS240) Cryogenic Temperature Monitors. They were placed in diagnostic locations throughout the cryostat as depicted in Fig. 4.41, allowing us a good understanding of the cool down. A list of these temperature sensors are included in Appendix A.1.1.

Recall also that the liquid nitrogen shield has a tank around its belt to accumulate liquid nitrogen. The level of liquid nitrogen in this belt tank is measured using a capacitive level sensor, which is read out by an Agilent LCR Meter (U1733C).

The turbo pump (Agilent Turbo-V 2300 Twistorr)—primarily involved in providing vacuum for the OVC, but also pumping out the IMV before cooling commences—removes 1800 L/s for He and 2050 L/s N_2. It requires a chiller with a recommended water flow temperature between 15° C to 30° C—we ran at 17° C. The turbo pump, however, will not overheat—its controller box uses a thermistor to cut power to itself when it exceeds safe operating temperatures. The slow control system remains in contact with that controller box throughout its operation.

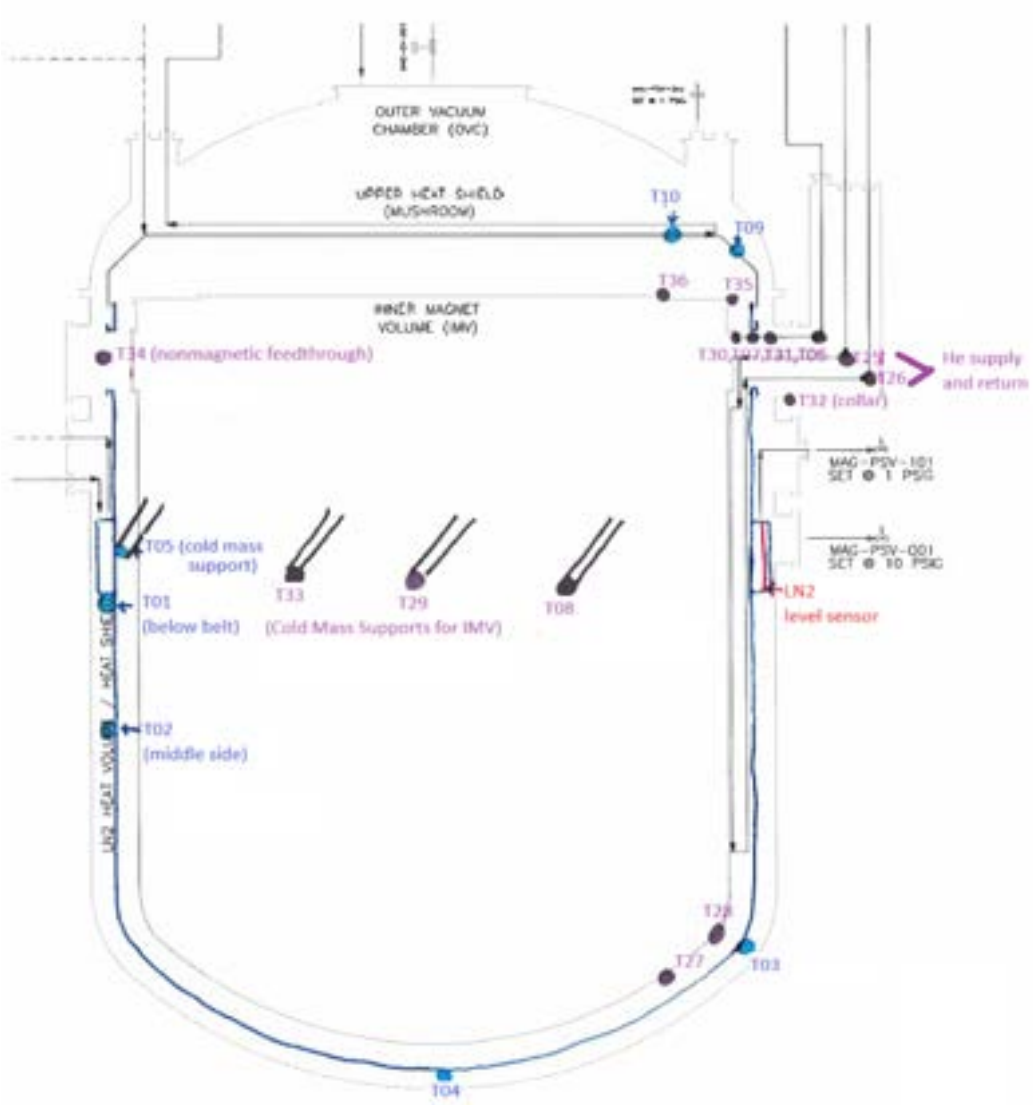

Figure 4.41: Illustration of the temperature sensors in the cryomagnet. The complete list can be found in Appendix A.1.1.

The pneumatic ISO-250 linear gate valve (Pfeiffer Vacuum GVAP-10002), chosen for matching throughput to the turbo pump, requires compressed air (80–100 psi) to operate. While the slow control system does not directly command the gate valve to open or shut, a controlling Arduino reports the "open or shut" state to the slow control system measured from the gate valve's monitor circuit. It has a Caltech-made "turbo pump safety" feature in addition to the usual "open/shut" operations; if the pressure upstream of the turbo pump exceeds 0.1 torr, the Arduino sends a command to shut the gate valve and power down the pump.

In addition to the buffer tank pressure sensor, three other pressure sensor monitors are

employed in the system. The Granville-Phillips Micro-Ion Vacuum Measurement System (PG358) measures two cathode gauges and an ion gauge. One cathode gauge monitored the line above the roughing pump, while the other two gauges measured the OVC pressure (one for the safety feature discussed in the preceding paragraph). The IMV pressure was measured with a DualMag (inverted magnetron transducer, DualMag 972) read by an MKS Vacuum Gauge Controller (PDR900). Finally, a Heise Dual Display Digital Pressure Indicator (PM1) was employed to keep a more precise online monitoring of the CP103 inlet and outlet pressures ("P_high" and "P_low"), using two piezoresistive sensors.

The full P&ID (Piping and Instrumentation Diagram) is attached in Fig. 4.42. Note that a burst disk protects the OVC from catastrophic overpressure (and a Circle Seal relief valve from non-catastrophic mistakes at 1 psig), while a check valve (Circle Seal, 0.1 psig) protects the IMV from external overpressure.

A vacuum manifold allows the turbo pump and/or the roughing pump (a scroll pump) to evacuate the IMV and/or the Outer Vacuum Chamber. This is the first step to cooling down, and is more clearly illustrated by the black lines and labeled valves assembled in the P&ID for leak checking in Fig. 4.43. However, while simpler, this PNID differs significantly from the final experiment. For example, the pressure gauges for the IMV and OVC are swapped, and the check valve is not yet in place to protect the IMV from overpressure.

4.4.2 Diagnostic Cool Down at Oak Ridge National Lab

Due to the large scale of these cryogenic components, a cool down is a multi-week effort even after assembly, leak-checking, evacuating and/or purging the spaces. During this time, the slow control system monitors the cool down behavior closely as temperatures drop and cryogens flow. The system is designed to achieve inner magnet volume temperatures in the single digits to allow the lead shield to go superconducting.

The system was previously cooled down at Caltech with the B0 magnet installed, but included a warm bore in the center for magnet mapping. The Caltech cool down achieved magnet temperatures of about 8–9 K. A cool down was prudent ahead of the polarization and transmission measurement to verify the system operation after shipping, and troubleshoot issues ahead of the beam schedule. This was done without the spacial constraints of the mu-metal shield, allowing thorough leak checking, ease of access to components, and ease of assembly.

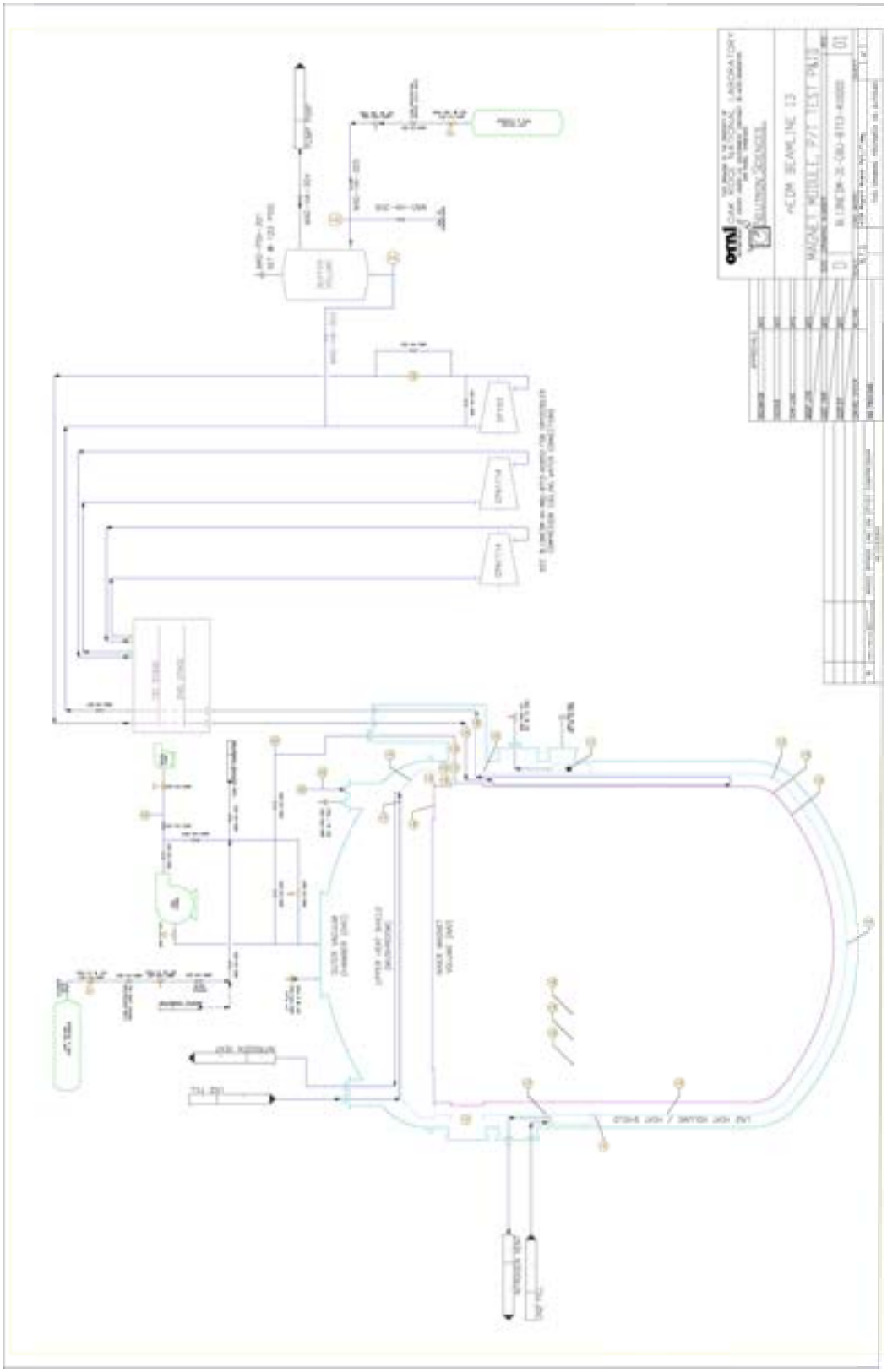

Figure 4.42: Official P&ID for the system cool downs. Created by Engineer John Ramsey of ORNL.

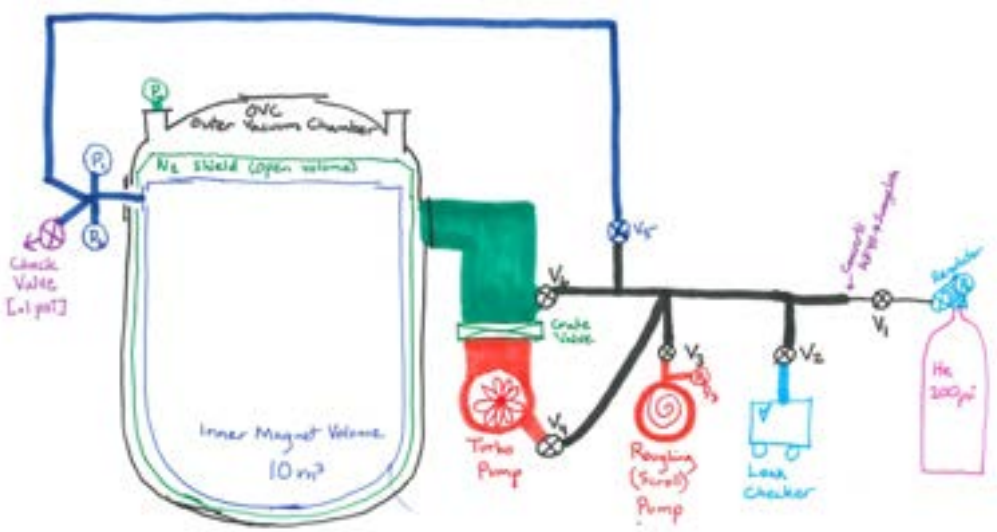

Figure 4.43: P&ID for leak checking the IMV. The black lines depict the manifold, and the valves (V3 through V6) allow the roughing pump to operate on its own or back up the turbo pump.

A photograph showing the setup, including the turbo pump manifold easily mounted to the side of the OVC, demonstrates this access in Fig. 4.44. The left photograph shows the Cryomech circulator package feeding into the service port of the inner magnet volume. The right photograph shows the leak checker hooked up to the IMV vacuum port.

The left side of Fig. 4.44 shows the cryostat sealed, pumped down, and ready to cool. The tower leading into the upper side port is the helium services for the inner magnet volume, and the manifold affixed to the side of the system (on the lower port) is the pumping port assembly. That manifold allowed us to pump on the OVC and IMV together or separately, with full access to easily leak check everything on the way. Furthermore, the magnet package was not yet installed into the IMV, reducing the amount of outgassing G10 moisture to pump out.

After the system is under vacuum, the cryogens can begin to flow. Recall that the nitrogen shield has two ports to input liquid nitrogen: one continuous flowing pathway on top of the mushroom, and one reservoir called the “belt tank” around the center of the shield. The nitrogen lines were vented to the outside for safety. After assembly and purging, the cold helium circulation system is ready to turn on when water cooling is established to all the compressors, and does not require the nitrogen shield to be completely cold before commencing. More details of the cryomagnet

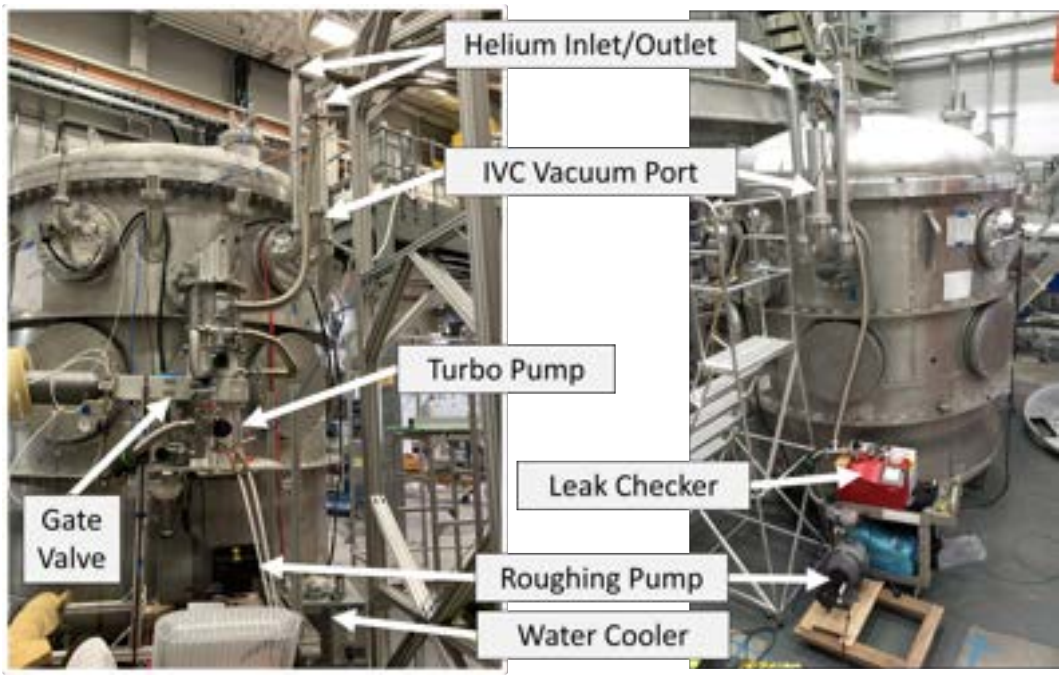

Figure 4.44: Photographs of the first cool down setup. Left, northwest view of the cryostat and instrumentation—note the turbo manifold with the gate valve and turbo pump to pump out the OVC and IMV. Right, southwest view of the cryostat and instrumentation—note the helium inlet and outlet stingers for the IMV cooling loops, as well as the IMV vacuum port.

operation can be found in the Standard Operating Procedure, found in Appendix A.3.

The first cool down was only successful down to the freezing temperature of nitrogen. This was due to contamination in the system, to which no definitive cause was established. Two hypotheses are as follows:

1. I accidentally partially discharged the CP103 compressor by connecting the buffer tank copper tube to the CP103 without the buffer tank attached (see Fig. 4.39). This allowed a slow escape of the ultrapure helium out of the compressor (thankfully, slow enough that the compressor's oil did not contaminate the compressor), and could have saturated the compressor's absorber (which removes trace impurities from the helium). Note that this mistake was repeated by another graduate student, so it is an easy mistake to make; DO NOT REPEAT IT.

   However, the Cryomech support engineers were unconvinced that this mistake was enough to account for the helium contamination, because no air was forced

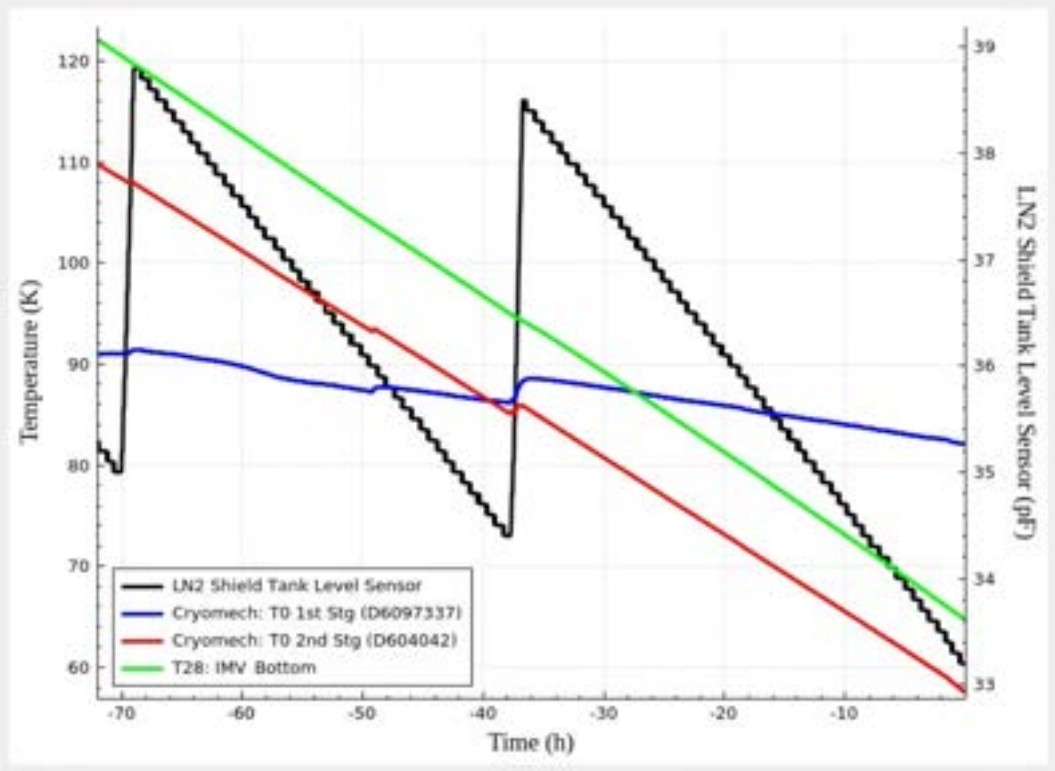

Figure 4.45: Slow Control Output for the last 3 days of the first cooldown. The three colored curves are temperatures at different points in the cooling assembly, with the black sawtooth shape being the level of the nitrogen in the belt tank as measured by a capacitance level sensor.

through the absorber—we did not operate the compressor in this state at all.

2. At the time of the initial cool down, only a partially used ultrapure helium bottle was available. We therefore flushed the system three times after it was completely assembled, by filling it with ultrapure helium, and then evacuating it with a roughing pump to 10^{-2} torr. Perhaps the vacuum allowed air to leak into the system between flushes; filling and purging corrects this.

Both hypotheses were addressed in preparation for the next cool down.

4.4.3 Cool Down for the Polarization and Transmission Test

This cool down was successful, with the B0 magnet reaching temperatures of <5.9 K. It took 28 days and 9000 L of LN_2.

This cool down required the full magnetic environment to be installed, which involved reinstallation of the Cryomech circulation package and pumping the OVC from the overhead port instead of the side port. A large “trunk” ISO pipe was

Figure 4.46: Computer Aided Design of the Magnet System. Note the large pipe ("trunk") going from the top of the OVC to the manifold on the side.

installed above the OVC and over the mu-metal shield, bringing the top port to gate valve level as seen in the Computer Aided Design model in Fig. 4.46.

For this cool down, a more thorough process was undergone to flush the system with ultrapure He and prevent contamination. First, the absorber was regenerated by removing it from the compressor and attaching it to the OVC manifold's turbo pump, where we directly pumped on it for 48 hours[d]. Secondly, each Aeroquip-delineated section of the circulation system in Fig. 4.36 was separately flushed five times using an ultrapure helium bottle and a portable manifold pictured in Appendix A.2. They were then connected together at the airtight Aeroquip-fittings. Details of this procedure are in Appendix A.2.

Temperatures dropped as cryogens flowed, as seen in Fig. 4.47. On the left, the temperature sensor on the B0 magnet is particularly important, as this is representative of the temperature of the magnet system inside of the inner magnet volume. In other words, this magnet is the "target" to cool.

[d]Cryomech recommends going to millitorr pressures and pumping on both sides of the absorber. We, however, only pumped on one side but achieved microtorr pressures

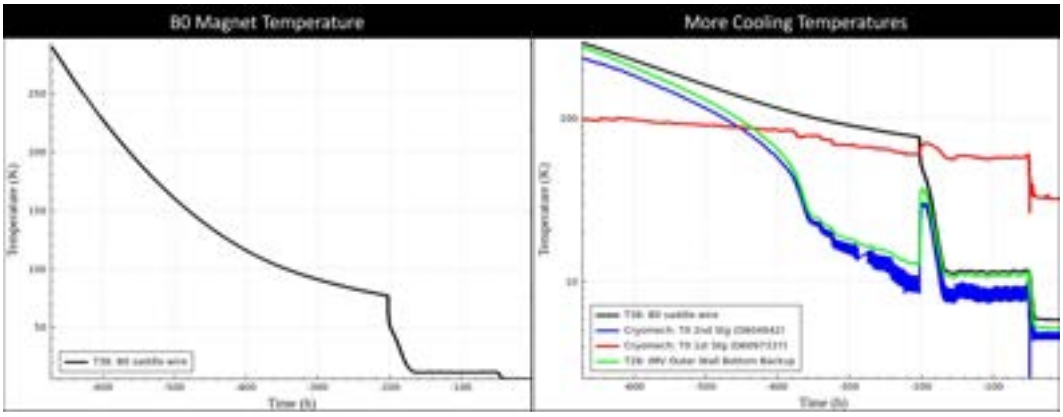

Figure 4.47: Temperatures measured during the cooldown. Left, the B0 temperature is representative of the temperature inside of the IMV. Right, other temperatures of interest in the cryomagnet.

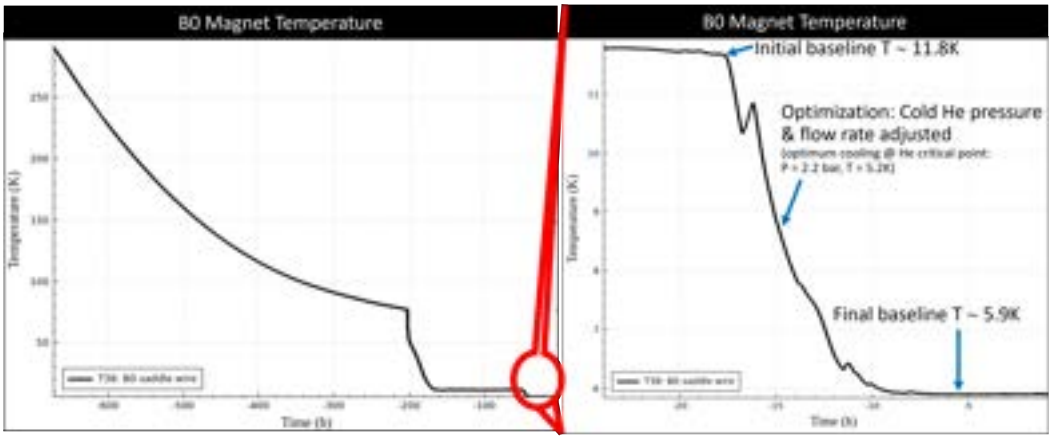

Figure 4.48: B0 magnet temperature measured in the cooldown. Left: for the entire cooldown. Right, zoomed into the bottom right corner of the left graph.

The right side of Fig. 4.47 contains other interesting and diagnostic temperatures. Note that the precipitous drop of B0 around the -200 hour mark was correlated with some warming of the IMV outer wall and the 2nd stage of the cryocooler. The cause of this was a purposeful introduction of a little bit of gaseous helium injected into the IMV; we spoiled the vacuum to help the heat transfer inside of the IMV. The B0 magnet temperature behavior showed that it worked as intended.

Fig. 4.48 shows another precipitous drop around -18 hours. This is due to tuning the helium flow through the IMV by the cryocooler. Recall from Fig. 4.36 that a needle valve on the high pressure side of the CP103 line allows us to modulate the flow. At these low temperatures, maximum helium flow is no longer maximum cooling—the most efficient cooling happens closest to the critical point of the helium, when the

specific heat of the helium is maximized. Tuning the needle valve is tuning the velocity and pressure of the helium to maximize its specific heat. The result is a final B0 below 5.9 K, well within the target of superconducting lead.

4.5 Polarization and Transmission Measurement through the Caltech Cryostat

The polarization and transmission measurement of cold, downscatter-able neutrons through the cryomagnet apparatus took advantage of a parasitic beamline off the neutron fundamental physics beamline at Oak Ridge National Laboratory's Spallation Neutron Source, 13A. Moderated polychromatic neutrons from the spallation source [54] come to beamline 13 where they first encounter a chopper, and then a double crystal monochromator set sends them down beamline 13A.

The chopper wheel, often referred to as a "mechanical velocity selector" in the literature, has the shape of a full pizza minus a 130° slice. It rotates in tune with the proton beam (60 Hz), with a phase delay (5.3 ms) chosen to allow only the transmission of 7.6 Å–12.0 Å neutrons via their time of flight.

The monochromator system is a potassium and a rubidium intercalated graphite monochromator system [54] [118], which uses Bragg diffraction to divert specific neutron wavelengths (λ) out of the main beamline. The monochromator's 'intercalated' spacing chooses the wavelength according to the Bragg condition:

$$n\lambda = 2d\sin(\theta_B) \tag{4.14}$$

where d is the lattice spacing, n is the integer diffraction order, and θ_B is the Bragg angle. The lattice spacing d was engineered (with a few mosaic crystals to give the wavelength peak a small variance [54]) for 9.8 Å neutrons.

The system is composed of two of these Bragg-diffracting monochromators, with different Alkalis for two different lattice spacings and therefore two different Bragg angles. The first monochromator is lowered directly into Beamline 13 to kick out the desired wavelengths and to transmit the rest. The second monochromator directs those neutrons down beamline 13A at an angle of 9° with respect to their original beamline trajectory.

The first step of operating the parasitic beamline is to determine the optimal position of the monochromator that kicks the neutrons out of Beamline 13 by taking some neutron flux data for the neutrons coming into beamline 13A. Using an n-^{3}He proportional detector provided by the SNS facility services, Fig. 4.49 shows the

Figure 4.49: Neutron counts as a function of monochromator position. The monochromator was slowly lowered into the cold neutron beam at Beamline 13, and the neutrons reflected were counted in parasitic Beamline 13A. The optimal position is -25 mm as further up on the curve distorted the neutron spectrum.

neutron counts as a function of monochromator position, as the monochromator was lowered into the neutron beam.

This measurement, paired with the future measurements of the neutrons at the end of the beamline at the apparatus position, begins the baseline understanding of the neutrons traveling down the 13A beampipe. The flux of neutrons at the beginning of the beamline at our detector is shown in Fig. 4.50, and the neutrons entering the apparatus are shown in the left side of Fig. 4.52.

The neutrons in this test require polarization. This was accomplished using a supermirror polarizer, flipped using a diabatic spin flipper, and analyzed using a ^{3}He Spin-Exchange Optical Pumping (SEOP) system. The supermirror polarizer was provided from a previous Beamline 13 experiment [56]. The spin flipper was developed by graduate student Kavish Imam [118], who also ran the SEOP system provided by the accelerator's polarization team. He reports an initial neutron polarization of:

$$P_n^o = 0.83 \pm 0.07$$

Transmission measurements were taking using an "8-pack" (set of eight vertical) ^{3}He proportional detectors provided by the SNS facilities [123]. The gaseous ^{3}He

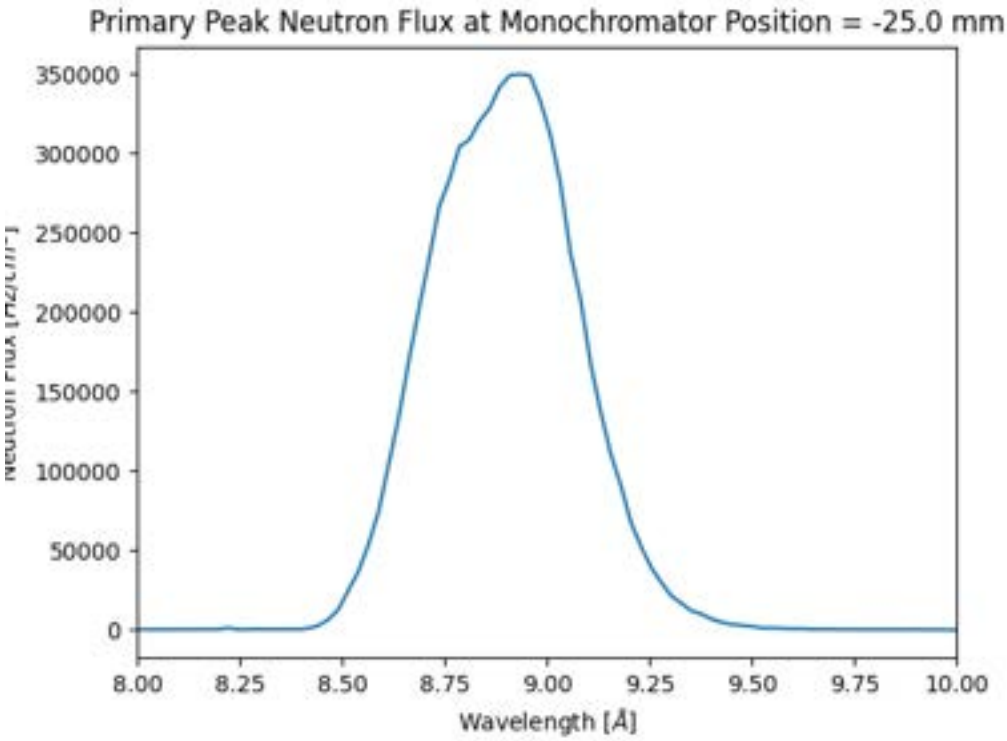

Figure 4.50: Primary Peak Neutron Flux in Beamline 13A with the monochromator in position at -25.0 mm. The monochromator was designed to select the 8.9 Å neutrons from Beamline 13 because this wavelength is optimal for downscattering into ultracold neutrons in the liquid helium measurement cell.

tubes contain additional gasses and an inner high-voltage wire spanning the length of the tube. When the ^{3}He captures a neutron, its charged particle products migrate to the high-voltage wire, creating a charge avalanche. Both ends of the high-voltage wire contain preamplifiers, and the difference in the timing of the signal from the preamplifiers is used to determine where along the wire the avalanche occurred—giving a "position" determination.

The 8-pack was moved along the beamline upstream and downstream of the cryo-magnet in the enclosures of the final configuration depicted in Fig. 4.35. The results are plotted in Fig. 4.52. Not only do they show a significant decrease from the initial flux on the left hand side to the transmitted flux on the right hand side of the figure, but also the Gaussian flux shape has distorted, implying a scattering effect. The flux of the neutrons detected is less than half of those predicted by Imam's simulations [118]. Furthermore, the downstream neutrons were completely depolarized.

To figure out what happened to our neutron beam to produce such poor transmission

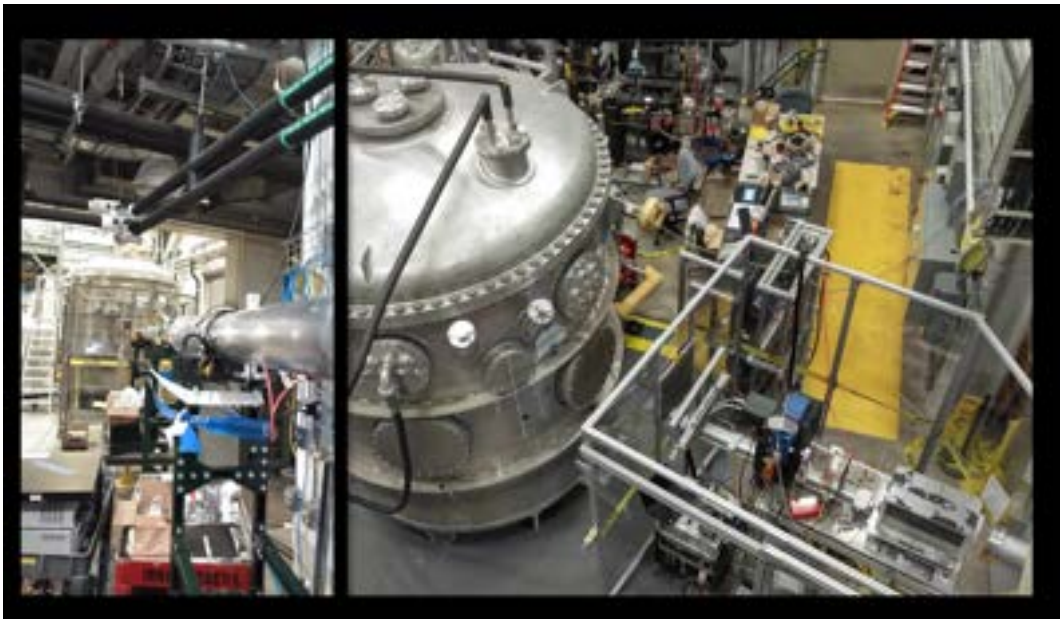

Figure 4.51: Photographs of the Initial Beamline Characterization. On the left is a photo of the perspective of the beamline coming towards the nEDM apparatus. On the right is the perspective from above, with the supermirror polarizer at the end of the beamline (rightmost object), followed by the spin analyzer. The structure is a radiation protection boundary.

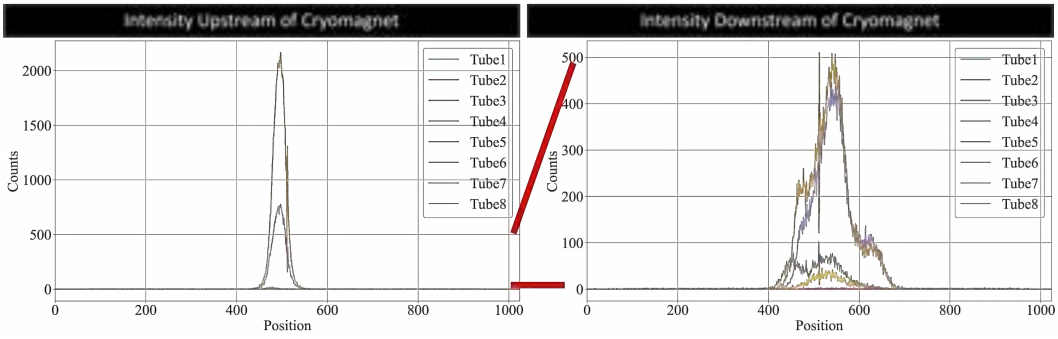

Figure 4.52: Transmission Measurements: 8-pack position data for the upstream (left) and downstream (right) neutron flux.

and polarization transport through the cryomagnet, neutron absorbing ribbons (^{6}Li) were placed around the beam window, and a Gadolinium Oxysulfide scintillator "beam plate" was used to "photograph" the beam spot. The imagine is shown in Fig. 4.53. Note that the beam is on the low side of the image (which could be expected), and that the two ^{6}Li strips are seen in the image.

More telling, however, is the ragged anti-circular shadow cast in the lower left (beam right) side of Fig. 4.53. Note how it looks like the cutout of the G10 cylinder and its mu-metal shield in the beam right of Fig. 4.25. Recall from Section 4.3.2 that the cryomagnet was rotated over 3 cm from its optimal placement, 4 cm higher than designed, and that a larger hole was cut into the mu-metal shield in attempt to fix this. Clearly, however, the beam is getting too close to the depolarizing edge of the mu-metal, experiencing large magnetic field gradients. The measurement will be repeated at the next beam cycle, after more alignment efforts are performed.

4.6 Conclusions

A large component of the nEDM experiment is in the manipulation of precise magnetic fields with very low gradients. The cryomagnet was engineered and fabricated for a superconducting lead shield, with a central volume to house the measurement cells and its related light collection and high-voltage creation components.

Polarized neutrons are required to pass through the layers of this cryomagnet to get to the measurement cell. The most concerning layer of this transport is the Metglas flux return for the inner spin manipulation magnets. With high fields running through it, avoiding a beam port cut out of it was preferred. The material for the flux return was specially chosen to minimize neutron losses and activation; the alloy chosen had at most, trace amounts of Cobalt. The amount of boron in the alloy was measured to be 3.3%±0.1%.

A polarization and transmission test of the apparatus at the Beamline 13A of the Spallation Neutron Source at Oak Ridge National Laboratory was attempted. This involved preparing an external building—"External Building 1" of the collaboration's naming scheme, or "8713" of the Oak Ridge National Laboratory's labels—to have similar magnetic field conditions to the final experiment. It involved installing the cryomagnet in that space, complete with its vacuum and cryogenic systems. It involved characterizing the parasitic monochromatic neutron beam coming out of the 13A beamline.

The building's magnetic field was prepared by installing steel plates on the floor

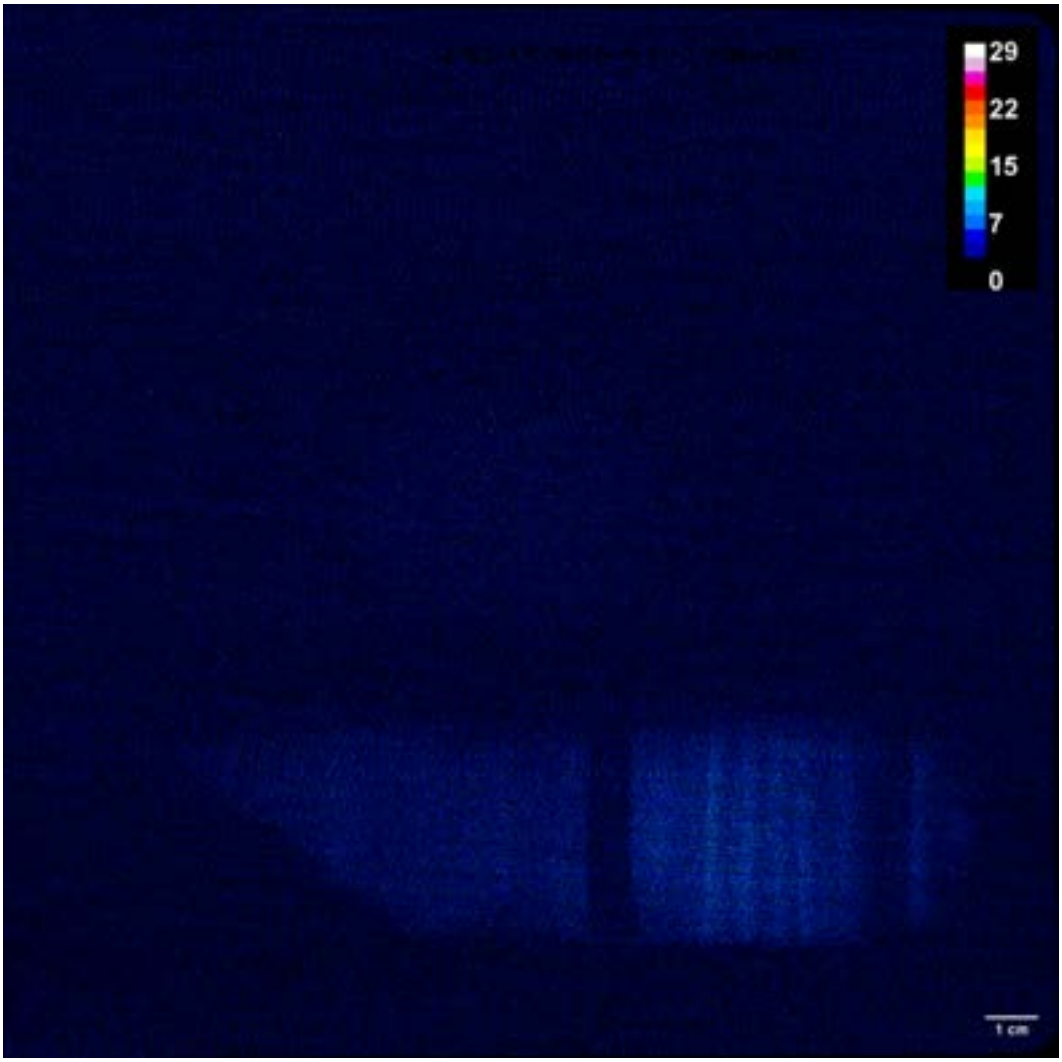

Figure 4.53: Gadolinium Oxysulfide Scintillator Image of the Downstream Beam Spot.

to shield the system from any magnetic field hotspots. Post cryostat installation, it involved installing a cylindrical mu-metal shield and a set of external bucking coils to cancel Earths magnetic field.

The cryomagnet was installed, commissioned, and cooled in the building, reaching a final temperature below 5.9 K. This is well within the target temperature to create a superconducting lead shield.

Misalignments between the cryomagnet, the cylindrical mu-metal shield, and the beam pipe hampered the neutron transport through the system. Many more neutrons were lost than expected, with an odd non-Gaussian scattered shape after traveling through the cryomagnet. The neutrons were completely depolarized by their trans-

port.

Another beam cycle is upcoming for the summer of 2024. These misalignments can be corrected with the help of the Survey and Alignment team, and a better measurement can be performed.

The measurement from the 2023 dataset is a proof of concept and was successful in commissioning the cryomagnet. These measurements provide the baseline understanding of the neutrons traveling down our beampipe, as well as experience in the cryomagnet system's operations.

Chapter 5

SUMMARY AND OUTLOOK

This work took place in the context of the nEDM@SNS Collaboration, a multi-institution effort with an ultimate goal to put new limits on the neutron electric dipole moment (nEDM) at the Spallation Neutron Source (SNS) to an order 10^{-28} e cm, two orders of magnitude better than the current best measurement [31]. The neutron electric dipole moment (nEDM) is sensitive to new sources of CP violation proposed by a medley of theorists [124]. These theories attempt to explain the matter/antimatter asymmetry by introducing new sources of CP violation, and consequently predict the nEDM has a magnitude in a (barely) measurable range. The impact of measuring this observable earned the nEDM@SNS experiment the highest priority in neutron physics recommended to the Nuclear Science Advisory Committee [125].

The predicted sensitivity improvement results from clever techniques such as creating trapped ultracold neutrons in situ from a cold neutron beam interacting with phonons in superfluid helium, holding them at less than 1 K, sustaining high electric fields in liquid helium, and taking precession measurements using two separate spin precession techniques. One precession technique takes advantage of ^{3}He's spin-dependent capture cross-section to measure the precession beat frequency. These techniques are all possible with a collaborative effort involving many interwoven systems that operate cryogenically inside a large cryostat.

Two of the key challenges that this ambitious experiment must address are the focus of this thesis—the production of high voltage for the nEDM measurement itself, and the magnetic environment created for the polarized neutrons as they are delivered into the measurement cell through the many nested layers of the apparatus. The former included designing, implementing, and measuring an electrostatic voltage multiplication device called the Cavallo Apparatus to produce the required high voltage from a smaller feedthrough electrically isolated from the experiment. The latter includes emulating the magnetic conditions for the nEDM@SNS experiment in an existing experimental target hall, sending the neutrons through, and measuring the resultant transmission and polarization loss. These two challenges feature directly in the experiment's sensitivity; the neutron flux through the apparatus directly impacts

the number of stored neutrons, and the polarization and electric field strength feature linearly in the uncertainty parameter.

For the nEDM@SNS to reach its target sensitivity, the neutrons must experience 75 kV/cm in the measurement cell, corresponding to a measurement electrode voltage of 650 kV. This voltage is too large to pipe directly into the magneto-sensitive subkelvin measurement region, so it will come from the electrostatic multiplication of a more reasonable 50 kV feedthrough. The Cavallo Multiplier is an electrostatic multiplication device fashioned after the 18th Century set of electrodes that Tiberius Cavallo used to turn immeasurable triboelectric charges into large enough voltages to be seen by electroscopes [58].

This work brings the device into this century, using electrodes designed by tuning parametric asymptotic tanh curves using a finite element analysis program. A proof of concept demonstrator apparatus was built and its voltage data compared to its capacitive predictions with good agreement. The full-scale electrodes for the final experiment were then designed and simulated, with a predicted gain of 18 and magnetic field hotspots of 116 kV/cm at the target voltage. With this simulated geometry, the hotspots can be sustained in 2 atm of LHe with a probability of breakdown on the order of 10^{-6}.

To verify the design, test the electrodes, and explore breakdown control, a cryogenic apparatus was designed and constructed. The apparatus performed in Sulfur Hexafluoride, achieving 250 kV, with a lower gain than predicted due to misalignment of the electrodes.

That cryogenic apparatus requires voltage measurements, but the 650 kV feedthrough embargo also applies to measurement feedthroughs. Non-contact voltage measurement devices were explored, with the most success found using a field mill. The field mill has a vane that turns to block electric field lines repetitively from a set of sense electrodes, with the input voltage measured proportional to the charge movement on those electrodes.

The future steps for the Cavallo Apparatus are clear; after further troubleshooting the alignment and analyzing the charging and discharging behavior of the test apparatus, pressurized cryogens will be introduced to the system in a methodical program, with the ultimate goal of reaching 650 kV in the apparatus.

For the final nEDM@SNS experiment, the cryostat will sit in a large magnetically shielded enclosure with a field compensation system to reduce the ambient mag-

netic field, a superconducting lead shield to greatly reduce external magnetic field variations, and a high-permeability magnetic flux return for the neutron and He-3 spin-manipulation coils inside the superconductor. The cold neutron beam must reach the measurement cell, so it must penetrate through these components. These components could decrease our flux and polarization. Vital sensitivity calculations, as well as troubleshooting the nested layers of the apparatus, depend on measuring the neutron beam's transmission and polarization as it traverses the components before downscattering to UCN in the measurement cell.

The experimental building for this experiment does not yet exist, and the large magnetically shielded room is currently overseas. Instead, the essential layered components were installed and commissioned at Oak Ridge National Laboratory's SNS, Beamline 13A, which is a 9.8 Å parasitic beamline off of the main Beamline 13's polychromatic cold neutron beam. The 9.8 Å neutrons were selected and redirected into Beamline 13A by a double crystal Alkali-intercalated graphite monochromator.

This work involved shielding the magnetic field in the measurement hall to mimic the conditions of the final experiment, assembling the nested layers of the cryostat, and setting up the interwoven cryogenic systems. Magnetic field hotspots from magnetized rebar in the floor were attenuated using steel plates. A mu-metal cylinder was installed around the apparatus to roughly approximate the shielding of the magnetically shielded room. Bucking coils were installed around the setup to attenuate Earth's and other magnetic fields. Then the apparatus was cooled to gain operational experience, and controlled with a slow control system that will be the impetus for the slow control system of the entire experiment. The cryostat required liquid nitrogen and a helium cryocooler system, especially to get the magnet package below the transition temperature of a superconducting lead shield to be installed next summer.

Finally, neutrons traveled through the apparatus and were detected and analyzed for flux and polarization loss using neutron detectors and He-3 spin filters. The procedure was to first measure the flux of the neutrons coming into the apparatus and measure the flux getting to the location of the nEDM measurement cell. Then, the He-3 spin filters gave us access to the spin content of that flux—measuring the number of neutrons that made its way through the layers with the correct and incorrect polarization.

While the ultimate goal was to characterize the sensitivity of the future nEDM mea-

surement by understanding the impact of the magnet package layers on our neutron flux and polarization as they travel to the measurement cell, a major misalignment obscured that data. A more preliminary goal was achieved as a proof of concept for this measurement, allowing us to discover the misalignment and troubleshoot the apparatus. Future work includes re-aligning the cryostat and mu-metal shield and repeating the measurement, after gaining all of this operational and troubleshooting experience.

The major accomplishments that took place included: 1) the mapping and troubleshooting of the magnetic field in the experiment hall, 2) the installation, leak checking, and cooling of the nested layers of the apparatus, achieving magnet temperatures <5.9 K, 3) slow control communication with every major device in the cooldown and an array of sensors, 4) the measurement of the neutron flux coming into Beamline 13A and into the apparatus, as well as a preliminary measurement of the neutron beam's polarization through a supermirror polarizer.

A new hurdle for the nEDM@SNS experiment is the abrupt loss of funding at the very end of this graduate student's tenure. This loss of funding created the loss of the nEDM@SNS's home at the SNS. However, there is a great amount of interest to rehome the experiment in Europe, potentially at the European Spallation Source. An experiment this important to the advancement of science will get done somewhere, someday, and the work in this thesis informs the cryogenic effort.

BIBLIOGRAPHY

[1] D.J. Schwarz. "The first second of the Universe". In: *Annalen der Physik* 515.4 (2003), pp. 220–270. DOI: 10.1002/andp.20035150402.

[2] Antonio Riotto and Mark Trodden. "Recent Progress in Baryogenesis". In: *Annual Review of Nuclear and Particle Science* 49.1 (1999), pp. 35–75. DOI: 10.1146/annurev.nucl.49.1.35.

[3] Mirco Cannoni. "Relativistic and nonrelativistic annihilation of dark matter: a sanity check using an effective field theory approach". In: *The European Physical Journal C* 76.3 (Mar. 2016), p. 137. DOI: 10.1140/epjc/s10052-016-3991-2.

[4] Planck Collaboration et al. "Planck 2015 results. XIII. Cosmological parameters". In: *Astronomy & Astrophysics* 594 (Oct. 2016), A13. DOI: 10.1051/0004-6361/201525830.

[5] Edward Kolb and Michael Turner. "Big Bang Nucleosynthesis –4.5 Abundances: Observations". In: *The Early Universe*. Frontiers in Physics 69. Addison-Wesley Publishing Company, 1990, pp. 100–105.

[6] A. D. Sakharov. "Violation of CP invariance, C asymmetry, and baryon asymmetry of the universe". In: Pis'ma Zh. Eksp.Teor. Fiz., 5, pp. 32-35. JETP Letters 5, pp. 24-27. (1967).

[7] Graham Albert White. *A Pedagogical Introduction to Electroweak Baryogenesis:* Morgan & Claypool Publishers, Nov. 2016. DOI: 10.1088/978-1-6817-4457-5.

[8] Marco Sozzi. *Discrete Symmetries and CP Violation: From Experiment to Theory*. Oxford Graduate Texts. Oxford, New York: Oxford University Press, July 2012.

[9] J. H. Christenson et al. "Evidence for the $2\ensuremath{\pi}$ Decay of the K_{2}^{0} Meson". In: *Physical Review Letters* 13.4 (July 1964), pp. 138–140. DOI: 10.1103/PhysRevLett.13.138.

[10] Soeren Prell. "CP VIOLATION AT BABAR AND BELLE". In: (2003).

[11] Ta-Pei Cheng and Ling-Fong Li. *Gauge Theory of Elementary Particle Physics*. 1st edition. Oxford Oxfordshire : New York: Oxford University Press, Jan. 1988.

[12] Peter Arnold and Larry McLerran. "The sphaleron strikes back: A response to objections to the sphaleron approximation". In: *Physical Review D* 37.4 (Feb. 1988), pp. 1020–1029. DOI: 10.1103/PhysRevD.37.1020.

[13] Michael J. Ramsey-Musolf. *Particlegenesis: Why is there more matter than anti-matter?* UMass Amherst, June 2014.

[14] Edward Kolb and Michael Turner. *The Early Universe*. Frontiers in Physics 69. Addison-Wesley Publishing Company, 1990.

[15] Marco Drewes. "The phenomenology of right handed neutrinos". In: *International Journal of Modern Physics E* 22.08 (Aug. 2013), p. 1330019. DOI: 10.1142/S0218301313300191.

[16] Tsutomu Yanagida. "Horizontal Symmetry and Masses of Neutrinos". In: *Progress of Theoretical Physics* 64.3 (Sept. 1980), pp. 1103–1105. DOI: 10.1143/PTP.64.1103.

[17] Steven R. Elliott and Petr Vogel. "Double Beta Decay". In: *Annual Review of Nuclear and Particle Science* 52.1 (Dec. 2002), pp. 115–151. DOI: 10.1146/annurev.nucl.52.050102.090641.

[18] M. Carena and C. E. M. Wagner. "Electroweak Baryogenesis and Higgs Physics". In: *Perspectives on Higgs Physics II* CERN-TH/97-74, FERMILAB-Pub-97/95-T (Dec. 1997), pp. 320–358. DOI: 10.1142/9789812819505_0010.

[19] Borut Bajc et al. "Threshold corrections to dimension-six proton decay operators in non-minimal SUSY SU(5) GUTs". In: *Nuclear Physics B* 910 (Sept. 2016), pp. 1–22. DOI: 10.1016/j.nuclphysb.2016.06.017.

[20] Johann Rafelski. "Melting Hadrons, Boiling Quarks". In: *The European Physical Journal A* 51.9 (Sept. 2015), p. 114. DOI: 10.1140/epja/i2015-15114-0.

[21] Jonathan Allday. *Quarks, Leptons and The Big Bang, Second Edition*. 2nd edition. New York, NY: CRC Press, Dec. 2001.

[22] P. F. de Salas et al. "Status of neutrino oscillations 2018". In: *Physics Letters B* 782 (July 2018), pp. 633–640. DOI: 10.1016/j.physletb.2018.06.019.

[23] Carmen García-Recio and Lorenzo Luis Salcedo. "CP violation in the effective action of the Standard Model". In: *Journal of High Energy Physics* 2009.07 (July 2009), p. 015. DOI: 10.1088/1126-6708/2009/07/015.

[24] Jihn E. Kim et al. "Jarlskog determinant and data on flavor matrices". In: *Modern Physics Letters A* 35.31 (Oct. 2020), p. 2050261. DOI: 10.1142/S0217732320502612.

[25] J. M. Pendlebury and E. A. Hinds. "Particle electric dipole moments". In: *Nuclear Instruments and Methods in Physics Research Section A: Accelerators, Spectrometers, Detectors and Associated Equipment* 440.3 (Feb. 2000), pp. 471–478. DOI: 10.1016/S0168-9002(99)01023-2.

[26] V. Andreev et al. "Improved limit on the electric dipole moment of the electron". In: *Nature* 562.7727 (Oct. 2018), pp. 355–360. DOI: 10.1038/s41586-018-0599-8.

[27] D. E. Maison, L. V. Skripnikov, and V. V. Flambaum. “Theoretical study of $^{173}\mathrm{YbOH}$ to search for the nuclear magnetic quadrupole moment”. In: *Physical Review A* 100.3 (Sept. 2019), p. 032514. DOI: 10.1103/PhysRevA.100.032514.

[28] J. H. Smith, E. M. Purcell, and N. F. Ramsey. “Experimental Limit to the Electric Dipole Moment of the Neutron”. In: *Physical Review* 108.1 (Oct. 1957), pp. 120–122. DOI: 10.1103/PhysRev.108.120.

[29] W. B. Dress et al. “Search for an electric dipole moment of the neutron”. In: *Physical Review D* 15.1 (Jan. 1977), pp. 9–21. DOI: 10.1103/PhysRevD.15.9.

[30] J. M. Pendlebury et al. “Geometric-phase-induced false electric dipole moment signals for particles in traps”. In: *Physical Review A* 70.3 (Sept. 2004), p. 032102. DOI: 10.1103/PhysRevA.70.032102.

[31] C. Abel et al. “Measurement of the Permanent Electric Dipole Moment of the Neutron”. In: *Physical Review Letters* 124.8 (Feb. 2020), p. 081803. DOI: 10.1103/PhysRevLett.124.081803.

[32] C. A. Baker et al. “Improved Experimental Limit on the Electric Dipole Moment of the Neutron”. In: *Physical Review Letters* 97.13 (Sept. 2006), p. 131801. DOI: 10.1103/PhysRevLett.97.131801.

[33] N. J. Ayres et al. “The design of the n2EDM experiment”. In: *The European Physical Journal C* 81.6 (June 2021), p. 512. DOI: 10.1140/epjc/s10052-021-09298-z.

[34] T. M. Ito et al. “Performance of the upgraded ultracold neutron source at Los Alamos National Laboratory and its implication for a possible neutron electric dipole moment experiment”. In: *Physical Review C* 97.1 (Jan. 2018), p. 012501. DOI: 10.1103/PhysRevC.97.012501.

[35] Ryohei Matsumiya et al. “The Precision nEDM Measurement with Ultra-Cold Neutrons at TRIUMF”. In: *Proceedings of the 24th International Spin Symposium (SPIN2021)*. Dec. 2022. DOI: 10.7566/JPSCP.37.020701.

[36] Jacob Yoder. “Measurement of wall relaxation times of polarized 3He in bulk liquid 4He for the Neutron Electric Dipole Moment experiment”. In: (Jan. 2010).

[37] M. G. D. van der Grinten. “CryoEDM: A cryogenic experiment to measure the neutron electric dipole moment”. In: *Nuclear Instruments and Methods in Physics Research Section A: Accelerators, Spectrometers, Detectors and Associated Equipment*. Particle Physics with Slow Neutrons 611.2 (Dec. 2009), pp. 129–132. DOI: 10.1016/j.nima.2009.07.040.

[38] Philip Harris. Private Communication. Mar. 2024.

[39] *SUPERSUN, A Super Ultra Cold Neutron source*. URL: https://www.ill.eu/users/instruments/instruments-list/supersun/description/instrument-3d (visited on 04/17/2024).

[40] R. Golub and Steve K. Lamoreaux. "Neutron electric-dipole moment, ultracold neutrons and polarized 3He". In: *Physics Reports* 237.1 (Feb. 1994), pp. 1–62. DOI: 10.1016/0370-1573(94)90084-1.

[41] M. Batz et al. "3He Spin Filter for Neutrons". In: *Journal of Research of the National Institute of Standards and Technology* 110.3 (2005), pp. 293–298.

[42] *NIST data: shielded helion gyromagnetic ratio in MHz/T*. URL: https://physics.nist.gov/cgi-bin/cuu/Value?gammahpbar (visited on 12/11/2023).

[43] *NIST data: neutron gyromagnetic ratio in MHz/T*. URL: https://physics.nist.gov/cgi-bin/cuu/Value?gammanbar (visited on 12/11/2023).

[44] Clark Hickman. *Update on Characterization of measurement cells for the nEDM@SNS experiment*. Nov. 2023. URL: https://indico.miserver.it.umich.edu/event/5/contributions/15/ (visited on 04/17/2024).

[45] Fritz Riehle. "Optical Atomic Clocks Could Redefine Unit of Time". In: *Physics* 5 (Nov. 2012), p. 126. DOI: 10.1103/PhysRevLett.109.203002.

[46] Young Jin Kim and Steven Clayton. "A SQUID-based 3He Co-magnetometer Readout for the SNS nEDM Experiment". In: 2014 (Mar. 2014). Conference Name: APS April Meeting Abstracts ADS Bibcode: 2014APS..APRS12004K, S12.004. DOI: 10.1103/BAPS.2014.APRIL.S12.4.

[47] Douglas Wong. "THE NUTS AND BOLTS OF THE NEUTRON ELECTRIC DIPOLE MOMENT EXPERIMENT AT LOS ALAMOS NATIONAL LABORATORY". PhD thesis. Bloomington, Indiana: Indiana University, June 2023.

[48] S. Eckel et al. "Time dependent spin-dressing using a ^3He atomic beam". In: *Phys. Rev. A* 85 (2012), p. 032124. DOI: 10.1103/PhysRevA.85.032124.

[49] C. Cohen-Tannoudji and S. Haroche. "Absorption et diffusion de photons optiques par un atome en interaction avec des photons de radiofréquence". In: *J. Phys. France* 30.2-3 (1969), pp. 153–168. DOI: 10.1051/jphys:01969003002-3015300.

[50] W. Schott et al. "UCN production in superfluid helium". In: *The European Physical Journal A - Hadrons and Nuclei* 16.4 (Apr. 2003), pp. 599–601. DOI: 10.1140/epja/i2002-10128-3.

[51] E. Korobkina et al. "Production of UCN by downscattering in superfluid He4". In: *Physics Letters A* 301.5 (Sept. 2002), pp. 462–469. DOI: 10.1016/S0375-9601(02)01052-6.

[52] Elizabeth Blackburn. “Excitations in the Ultimate Quantum Fluid”. In: *Physics* 14 (Mar. 2021), p. 45. DOI: 10.1103/PhysRevB.103.104516.

[53] P. Schmidt-Wellenburg, K. H. Andersen, and O. Zimmer. “Ultra cold neutron production by multiphonon processes in superfluid helium under pressure”. In: *Nuclear Instruments and Methods in Physics Research Section A: Accelerators, Spectrometers, Detectors and Associated Equipment*. Particle Physics with Slow Neutrons 611.2 (Dec. 2009), pp. 259–262. DOI: 10.1016/j.nima.2009.07.085.

[54] N. Fomin et al. “Fundamental Neutron Physics Beamline at the Spallation Neutron Source at ORNL”. In: *Nucl. Instrum. Meth. A* 773 (2015), pp. 45–51. DOI: 10.1016/j.nima.2014.10.042.

[55] Drew Winder. “Evolution of the High-Power Spallation Neutron Mercury Target at the SNS”. In: *Proceedings of the 12th International Particle Accelerator Conference* IPAC2021 (2021), 5 pages, 0.752 MB. DOI: 10.18429/JACOW-IPAC2021-THXC03.

[56] S. Balascuta et al. “The implementation of a super mirror polarizer at the SNS fundamental neutron physics beamline”. In: *Nuclear Instruments and Methods in Physics Research Section A: Accelerators, Spectrometers, Detectors and Associated Equipment* 671 (Apr. 2012), pp. 137–143. DOI: 10.1016/j.nima.2011.12.088.

[57] N. S. Phan et al. “A study of DC electrical breakdown in liquid helium through analysis of the empirical breakdown field distributions”. In: *Journal of Applied Physics* 129.8 (Feb. 2021), p. 083301. DOI: 10.1063/5.0037888.

[58] Tiberius Cavallo. *A complete treatise on electricity in theory and practice; with original experiments*. Vol. III. London : C. Dilly, 1795.

[59] Steven M. Clayton et al. “Cavallo’s Multiplier for in situ Generation of High Voltage”. In: *Journal of Instrumentation* 13.05 (May 2018), P05017–P05017. DOI: 10.1088/1748-0221/13/05/P05017.

[60] M. W. Ahmed et al. “A New Cryogenic Apparatus to Search for the Neutron Electric Dipole Moment”. In: *Journal of Instrumentation* 14.11 (Nov. 2019), P11017–P11017. ISSN: 1748-0221. DOI: 10.1088/1748-0221/14/11/P11017.

[61] Alina Aleksandrova. “Magnetic Field Monitoring in the SNS Neutron EDM Experiment”. PhD thesis. Lexington: University of Kentucky, Jan. 2019.

[62] I. Bernard Cohen. “The Eighteenth-Century Origins of the Concept of Scientific Revolution”. In: *Journal of the History of Ideas* 37.2 (1976), pp. 257–288. ISSN: 0022-5037. DOI: 10.2307/2708824.

[63] J. L. Heilbron. *Elements of Early Modern Physics*. Mar. 2022.

[64] Isaac Newton. “Philosophiæ Naturalis Principia Mathematica”. In: *Royal Society, London [Cambridge Digital Library]* (1686).

[65] Herbert Meyer. *A History of Electricity and Magnetism*. Cambridge, MA: MIT Press, 1971.

[66] William Gilbert. *On the loadstone and magnetic bodies, and on the great magnet the earth; a new physiology, demonstrated with many arguments and experiments. A translation by P. Fleury Mottelay*. Trans. by P. Fleury Mottelay. London, England: B. Quaritch, 1893.

[67] J. L. Heilbron. *Electricity in the 17th and 18th Centuries: A Study in Early Modern Physics*. Mineola, N.Y: Dover Pubns, Jan. 1999.

[68] Charles Francois De Cisternay Du Fay and Thomas Stack. “V. A letter from Mons. Du Fay, F. R. S. and of the Royal Academy of Sciences at Paris, to his Grace Charles Duke of Richmond and Lenox, concerning electricity. Translated from the French by T. S. M D”. In: *Philosophical Transactions of the Royal Society of London* 38.431 (Jan. 1997), pp. 258–266. DOI: 10.1098/rstl.1733.0040.

[69] Alexander Volta. “On the Electricity Excited by the Mere Contact of Conducting Substances of Different Kinds. In a Letter from Mr. Alexander Volta, F. R. S. Professor of Natural Philosophy in the University of Pavia, to the Rt. Hon. Sir Joseph Banks, Bart. K. B. P. R. S.” In: *Philosophical Transactions of the Royal Society of London* 90 (1800), pp. 403–431.

[70] Antonio Carlos M. de Queiroz. *Nicholson’s doubler*. URL: https://www.coe.ufrj.br/~acmq/nicholson/ (visited on 05/09/2024).

[71] William Nicholson. *A Journal of Natural Philosophy, Chemistry, and the Arts, 1804, Vol. 9*. Forgotten Books, Jan. 2019.

[72] T. M. Ito et al. “An apparatus for studying electrical breakdown in liquid helium at 0.4 K and testing electrode materials for the neutron electric dipole moment experiment at the Spallation Neutron Source”. In: *The Review of Scientific Instruments* 87.4 (Apr. 2016), p. 045113. DOI: 10.1063/1.4946896.

[73] S Janos and F Nydegger. “High-pin density feedthrough for superfluid helium applications”. In: *Cryogenics* 43.8 (Aug. 2003), pp. 463–464. DOI: 10.1016/S0011-2275(03)00121-8.

[74] *Energy to Power Solutions (e2pco.com)*. URL: https://www.e2pco.com/ (visited on 05/04/2024).

[75] *Ceramtec Feedthrough*. URL: https://shop.ceramtec.us/product?sid=234 (visited on 03/14/2024).

[76] *COMSOL Multiphysics® v. 5.4. www.comsol.com. COMSOL AB, Stockholm, Sweden*. Stockholm, Sweden, 2019.

[77] M. Niemetz and W. Schoepe. “Stability of Laminar and Turbulent Flow of Superfluid 4He at mK Temperatures Around an Oscillating Microsphere”. In: *Journal of Low Temperature Physics* 135.5 (June 2004), pp. 447–469. DOI: 10.1023/B:JOLT.0000029507.98543.1d.

[78] Takeyasu M. Ito et al. *High Electric Field Research and Design Program for the nEDM@SNS Experiment*. Oct. 2021.

[79] C. Crawford. *Private Communications*. 2018.

[80] J. Fry et al. “The Nab Experiment: A Precision Measurement of Unpolarized Neutron Beta Decay”. In: *EPJ Web of Conferences* 219 (2019), p. 04002. DOI: 10.1051/epjconf/201921904002.

[81] P. Sarma Maruvada, R.D. Dallaire, and R. Pedneault. “Development of Field-Mill Instruments for Ground-Level and Above-Ground Electric Field Measurement Under HVDC Transmission Lines”. In: *IEEE Transactions on Power Apparatus and Systems* PAS-102.3 (Mar. 1983), pp. 738–744. DOI: 10.1109/TPAS.1983.318035.

[82] S. Slutsky et al. “Cryogenic magnetic coil and superconducting magnetic shield for neutron electric dipole moment searches”. In: *Nuclear Instruments and Methods in Physics Research Section A: Accelerators, Spectrometers, Detectors and Associated Equipment* 862 (Aug. 2017), pp. 36–48. DOI: 10.1016/j.nima.2017.05.005.

[83] Larry Bartoszek. *The SNS Neutron Electric Dipole Moment Experiment (nEDM), https://bartoszekeng.com/nEDM/nEDMvalve.htm*. URL: https://bartoszekeng.com/nEDM/nEDMvalve.htm.

[84] J. Gerhold. “Properties of cryogenic insulants”. In: *Cryogenics* 38.11 (Nov. 1998), pp. 1063–1081. DOI: 10.1016/S0011-2275(98)00094-0.

[85] Masanori Hara et al. “Electrical Breakdown Mechanism of Cryogenic Liquid Coolants in the Presence of Thermal Bubbles”. In: *IEEJ Transactions on Power and Energy* 111.4 (1991), pp. 352–357. DOI: 10.1541/ieejpes1990.111.4_352.

[86] N. S. Phan et al. “Effect of an electric field on liquid helium scintillation produced by fast electrons”. In: *Physical Review C* 102.3 (Sept. 2020), p. 035503. DOI: 10.1103/PhysRevC.102.035503.

[87] *PD410 Round PICMA(R) Multilayer Bender Actuators, PI*. URL: https://www.physikinstrumente.com/en/products/piezoelectric-transducers-actuators/bender-actuators/pd410-round-picma-multilayer-bender-actuators-103050 (visited on 05/04/2024).

[88] K. A. Nicoll et al. “A global atmospheric electricity monitoring network for climate and geophysical research”. In: *Journal of Atmospheric and Solar-Terrestrial Physics* 184 (Mar. 2019), pp. 18–29. DOI: 10.1016/j.jastp.2019.01.003.

[89] NASA Global Hydrology Resource Center. *CAMEX-4 MIPS Field Mill*. URL: https://ghrc.nsstc.nasa.gov/uso/ds_docs/camex4/c4gmipfm/c4gmipfm_dataset.html.

[90] S. Handel, Kenneth Cummins, and E. Krider. "Surface Potential Gradients and NEXRAD Radar Reflectivities Before the Onset of Lightning at the KSC-ER". In: *Journal of Geophysical Research: Atmospheres* 127 (Sept. 2022). DOI: 10.1029/2022JD036681.

[91] C.E. Hollandsworth, S.G. Buccino, and P.R. Bevington. *Precision Accelerator Voltage Measurements with a Generating Voltmeter*. Jan. 1963. URL: https://www.osti.gov/servlets/purl/4054896.

[92] Xiaoang Li et al. "Design and testing of a high-precision generating voltmeter for metal-enclosed megavolt level DC voltage source". In: *Review of Scientific Instruments* 95.4 (Apr. 2024), p. 045008. DOI: 10.1063/5.0190171.

[93] Raveena Rao. *Prime Faraday Technology Watch: An Introduction to MEMS (Micro-electromechanical Systems)*. PRIME Faraday Partnership, 2002.

[94] Mark N. Horenstein and Patrick R. Stone. "A micro-aperture electrostatic field mill based on MEMS technology". In: *Journal of Electrostatics*. Electrostatics 2001: 9th International Conference on Electrostatics 51-52 (May 2001), pp. 515–521. DOI: 10.1016/S0304-3886(01)00048-1.

[95] Tao Chen and Cyrus Shafai. "A Flexible Printed Circuit Board Based Microelectromechanical Field Mill with a Vertical Movement Shutter Driven by an Electrostatic Actuator". In: *Sensors* 24.2 (Jan. 2024), p. 439. DOI: 10.3390/s24020439.

[96] Xianxiang Chen et al. "Thermally driven micro-electrostatic fieldmeter". In: *Sensors and Actuators A: Physical* 132.2 (Nov. 2006), pp. 677–682. DOI: 10.1016/j.sna.2006.02.044.

[97] MEMs Caltech. *https://www.mems.caltech.edu/*.

[98] Los Alamos National Laboratory. *Materials Science and Technology*. URL: https://organizations.lanl.gov/physical-sciences/materials-science-technology/.

[99] Yu Chong Tai. *Private Communications*. 2019.

[100] R. L. Workman et al. "Review of Particle Physics". In: *PTEP* 2022 (2022), p. 083C01. DOI: 10.1093/ptep/ptac097.

[101] Louis N. Hand and Janet D. Finch. *Analytical Mechanics*. Cambridge University Press, Nov. 1998.

[102] Raymond Tat and C. M. Swank. "Quantum control of two critically dressed spin-1/2 species in magnetic fluctuations". In: *Physical Review A* 105.5 (May 2022), p. 053120. DOI: 10.1103/PhysRevA.105.053120.

[103] F. Bloch and A. Siegert. “Magnetic Resonance for Nonrotating Fields”. In: *Physical Review* 57.6 (Mar. 1940), pp. 522–527. DOI: 10.1103/PhysRev.57.522.

[104] J. C. Solem and L. C. Biedenharn. “Understanding geometrical phases in quantum mechanics: An elementary example”. In: *Foundations of Physics* 23.2 (Feb. 1993), pp. 185–195. DOI: 10.1007/BF01883623.

[105] Andrew Herod. “Scale: The local and the global”. In: *Key Concepts in Geography*. SAGE Publications Ltd, Jan. 2008.

[106] A. G. Redfield. “On the Theory of Relaxation Processes”. In: *IBM Journal of Research and Development* 1.1 (Jan. 1957), pp. 19–31. DOI: 10.1147/rd.11.0019.

[107] Spike Carlsen. *Woodworking FAQ: The Workshop Companion: Build Your Skills and Know-How for Making Great Projects*. Storey Publishing, Apr. 2012.

[108] Xuan Sun. “Measurements of Beyond Standard Model Interactions with the UCNA and nEDM@SNS Experiments”. phd. California Institute of Technology, 2022. DOI: 10.7907/n87j-gh29.

[109] Inc. Metglas. *Metglas (metglas.com)*. URL: https://metglas.com/ (visited on 05/04/2024).

[110] H. Kronmüller et al. “Magnetic properties of amorphous ferromagnetic alloys”. In: *Journal of Magnetism and Magnetic Materials* 13.1 (Sept. 1979), pp. 53–70. DOI: 10.1016/0304-8853(79)90029-5.

[111] D. Duffey, P. F. Wiggins, and A. A. El Kady. “Spectral enhancement of cobalt neutron capture gamma rays”. In: *Nuclear Instruments and Methods* 105.1 (Nov. 1972), pp. 23–28. DOI: 10.1016/0029-554X(72)90485-5.

[112] Metglas.com. *Metglas 2705M Tech Note*. 2014. URL: https://metglas.com/wp-content/uploads/2021/06/2705M-Magnetic-Alloy-updated.pdf.

[113] Metglas.com. *Metglas 2826MB Tech Note*. 2011. URL: https://metglas.com/wp-content/uploads/2016/12/2826MB-Magnetic-Alloy.pdf.

[114] T. J. Sumner, J. M. Pendlebury, and K. F. Smith. “Conventional magnetic shielding”. In: *Journal of Physics D: Applied Physics* 20.9 (Sept. 1987), p. 1095. DOI: 10.1088/0022-3727/20/9/001.

[115] Richard M. Bozorth. *Ferromagnetism*. Hoboken, NJ: Wiley-IEEE Press, Aug. 1993.

[116] Elizabeth C. Auden et al. “Thermal Neutron-Induced Single-Event Upsets in Microcontrollers Containing Boron-10”. In: *IEEE Transactions on Nuclear Science* 67.1 (Jan. 2020), pp. 29–37. DOI: 10.1109/TNS.2019.2951996.

[117] NIST. *NIST: NCNR for Boron (Neutron Scattering Lengths and cross sections)*.

[118] S. K. Imam. "A Measurement of Neutron Polarization and Transmission for the nEDM@SNS Experiment". PhD thesis. Knoxville, TN: University of Tennessee Knoxville, Dec. 2023.

[119] Wolfgang Treimer et al. "Polarized neutron imaging and three-dimensional calculation of magnetic flux trapping in bulk of superconductors". In: *Physical Review B* 85.18 (May 2012), p. 184522. DOI: 10.1103/PhysRevB.85.184522.

[120] Vince Cianciolo et al. *nEDM Design Evaluation Task Force Report*. Technical Report. nEDM Collaboration, Sept. 2014.

[121] 80/20. *80/20 Aluminum T-slot Building Systems and 80/20 Aluminum Extrusions*. URL: https://8020.net/ (visited on 05/08/2024).

[122] QT Group. *QT Group*. 2024. URL: https://www.qt.io/.

[123] Kevin D. Berry et al. "Characterization of the neutron detector upgrade to the GP-SANS and Bio-SANS instruments at HFIR". In: *Nuclear Instruments and Methods in Physics Research Section A: Accelerators, Spectrometers, Detectors and Associated Equipment* 693 (Nov. 2012), pp. 179–185. DOI: 10.1016/j.nima.2012.06.052.

[124] T. E. Chupp et al. "Electric dipole moments of atoms, molecules, nuclei, and particles". In: *Reviews of Modern Physics* 91.1 (Jan. 2019), p. 015001. DOI: 10.1103/RevModPhys.91.015001.

[125] Krishna Kumar et al. *Report to the Nuclear Science Advisory Committee: Submitted by the Subcommittee on Fundamental Physics with Neutrons*. Tech. rep. 2011.

APPENDICES

Appendix A

RESOURCES FOR REBUILDING AND COMMISSIONING THE NEDM CRYOSTAT

This appendix is useful for running the cryomagnet system, and for the eventual rebuilding of the nEDM cryostat in its new home.

A.1 IMV Accessories

A.1.1 Temperature Sensors on IMV and LN_2 Shield Components

- LN2 shield sensors:
  T01: Below LN2 Tank
  T02: Middle Side
  T03: Bottom Edge
  T04: Bottom Center
  T05: at Cold Mass Support

- At Mushroom (LN2 shield):
  T09: Mushroom side edge
  T10: Mushroom near cold mass support

- IMV sensors:
  T06: IMV pump port (on N2 shield)
  T07: Sleeve on IMV pump ports
  T08: IMV cold mass support N-Mid@5k

  T25: IMV He Circulation Supply
  T26: IMV He Circulation Return
  T27: Outer Wall Bottom
  T28: Outer Wall Bottom Backup (also called “Inner shell bottom” but is on the outside)
  T29: IMV Cold Mass Support East@5K
  T30: IMV Pump Port Ti bellows @5K
  T31: IMV Pump Port Ti bellows @100K
  T32: 100K Shield on IMV He Circulation Supply
  T33: IMV Cold Mass Support SW-Mid@5K

T34: IMV non-mag feedthrough South@5K

T35: Outer Edge of Doughnut lid

T36: Inner edge of Doughnut Lid

- Within IMV:

T37: Not working (Upstream Metglas)

T38: B0 Saddle wire

T39: Not working (Probe Array)

Preparing the CP103 Compressor:

Marie From Caltech (Blatnik) and Parker From Cryomech

Current State of the System:

CP103 compressor is discharged (TWICE!!! Ugh. And I promise NEVER AGAIN.)

Absorber has been removed and pumped down (only one one side) to 10^-6 torr for a couple of days.

Last time the system was run (with CP103, Buffer Tank, Small Aeroquip Hoses, Heat Exchanger), there was a nitrogen clog (at about 63 K).

Constraints:

→ WE WANT TO LIMIT THE AMOUNT OF STORED GAS ENERGY OF THE SYSTEM AT LESS THAN 73 psi ft^3

The CP103 compressor (including the absorber) has a physical Helium volume (in physical space) of 11.01 Liters. THIS MEANS WE CANNOT GO OVER 73psi*ft^3 /11.01 L*(28.317 L/1ft^3) = 187 psi. (I rounded down)

Procedures for preparing ABSORBER separately from the CP103 Compressor. DO NOT REATTACH ABSORBER TO COMPRESSOR UNTIL BOTH ABSORBER AND COMPRESSOR ARE INDEPENDENTLY PREPARED!!!!

PURGING Caltech Manifold Procedure: FOLLOW THIS ANY TIME THE INSIDE OF THE MANIFOLD HAD AIR IN IT.

1. Caltech has created the “Caltech Manifold,” shown in orange on the drawing (at the end of this packet). The first step is to (replace the pressure gauge and then) leak check the Caltech Manifold. To move on with the procedure, no leaks can exist and the leak checker (and everything) must be disconnected from the Caltech manifold.

2. Ensure that C1, C2, and C3 are all closed.
3. Attach the helium bottle's "quick connect" to the Caltech Manifold.
4. Turn on the Helium bottle with the regulator.
5. Open C3 to flush out the Polyflo Helium bottle line.
6. Close C3 and then open C2 and C1 to flush out the rest of the Caltech Manifold for a little bit of time.
7. Close C1 and pressurize manifold (controlled with the regulator and C2) to 90 psi.
8. Open C1 slowly and drain the pressure to 10 psi.
9. Repeat steps 6 and 7 for a total of 5 charge-discharge cycles.
10. Ensure C2 is closed before disconnecting the Helium bottle's quick connect.

Prepare the Absorber Procedure:

1. IF NEEDED, purge the Caltech Manifold as defined above.
   If not needed, this assumes that ultrapure helium is entrapped in the volume between the two aeroquip hoses and the C1 and C2 valves – C1 has not been reopened to atmosphere since a purge.

   If the Helium bottle needs reattached, follow steps 2-4 of the Caltech Manifold Purge procedure above and then close C3 when finished.

2. Attach the two aeroquip hoses to the two ends of the absorber. (Cryomech says both is best)

3. Pressurize to over 80 psi. (Appendix A says 220 but the quick start says 120, our bottle only seems to allow 80 in a reasonable timeframe). Do this by opening C2 slowly. Close when finished.

CP103 Preparation Procedure:

1. IF NEEDED, purge the Caltech Manifold as defined above.
   If not needed, this assumes that ultrapure helium is entrapped in the volume between the two aeroquip hoses and the C1 and C2 valves – C1 has not been reopened to atmosphere since a purge.

   If the Helium bottle needs reattached, follow steps 2-4 of the Caltech Manifold Purge procedure above and then close C3 when finished.

2. Connect the two aeroquip hoses on the Caltech Manifold to:
   → P_low on the CP103 compressor front,
   → P2 located inside of the CP103 compressor, near the right panel.

3. VERY SLOWLY increase the pressure to 80 psi, at a rate of 5 psi per minute, by slowly opening the C2 valve. (Cryomech external document says 20 but I think the manual says 5. Not verified).

4. Close the C2 valve and slowly open the C1 valve such that the compressor discharges at a rate of 5 psi per minute, UNTIL THE PRESSURE REACHES 2 psi.

5. When the pressure reaches 2 psi, close C1. Repeat Steps 3 and 4 for 5 total cycles.

6. Repeat Step 3 one final time for the final pressure to be 120 psi.

MERGING THE ABSORBER AND THE COMPRESSOR:

BECAUSE WE CAN USE THE SAME PRESSURE INDICATOR ON THE CALTECH MANIFOLD, WE CAN SET BOTH THE CP103 and its absorber TO 120 PSI, THE SAME PRESSURE. Then when that is true, we can plug them in.

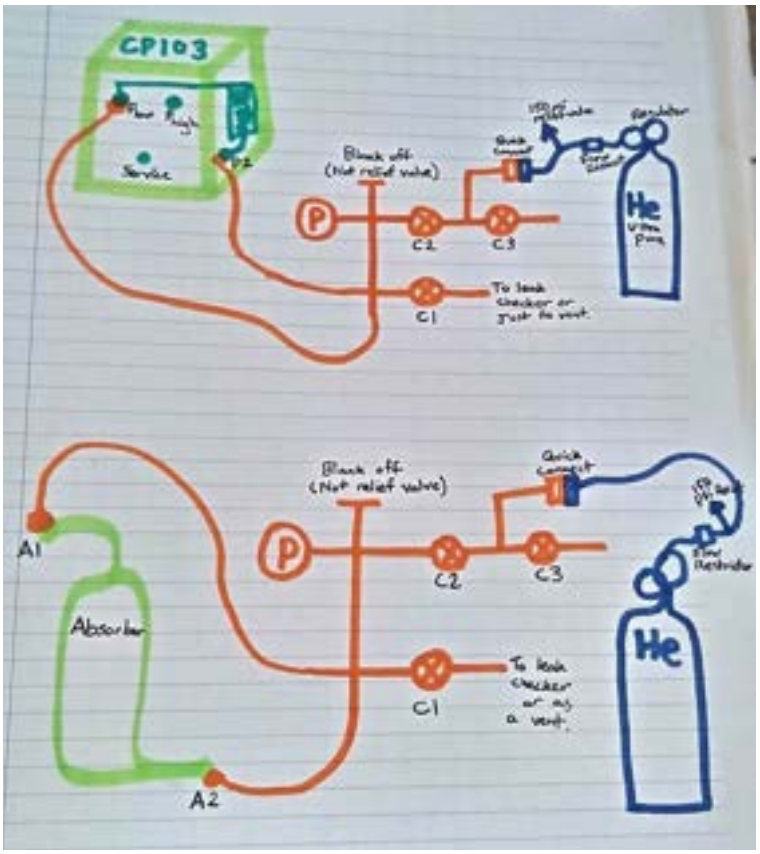

PARTS LIST AT PRESSURE:

1. 3000 psi Matheson Model 1L-580 Regulator (on the He bottle)
2. ½'' Pipethread Union
3. ½'' to ¼'' Pipethread adapter
4. ¼'' Pipethread union
5. ¼'' Pipethread elbow
6. ¼'' Pipethread to swagelok adapter.
7. 1'' of copper pipe with two brass swagelok fittings (¼'')
8. PSV-007267 Relief Valve set at 150 psi.
9. **2 x ¼'' swagelok fitting on Kinoflo Plastic Pipe ¼'' WEATHERHEAD PT24044 6N 0523 07 A687**
10. ¼'' swagelok to ½'' Pipethread adapter
11. **½'' quickconnect fitting**
12. ½'' brass swagelok pipe with 2 swagelok fittings (½'')
13. ½'' swagelok to pipethread adapter (¼'')
14. ¼'' Swagelok/Pipethread elbow
15. ¼'' swagelok T with 3 x ¼'' brass swagelok pipe with ¼'' swagelok fittings
16. Whitey 200 PSI ¼'' Valve
17. Whitey ¼'' Valve SS-1KS4 rated to 3130 psi
18. ¼'' swagelok cross with 3 x ¼'' swagelok pipe with ¼'' swagelok fittings
19. stainless ¼'' swagelok plug
20. ¼'' swagelok to ½'' pipethread adapter
21. **MATHESON 60 PSI GAUGE!!!!**
22. ¼'' swagelok to ¾'' swagelok
23. ¾'' swagelok cross with 4x 3/4'' swagelok pipe with 3/4'' swagelok fittings
24. Whitey B-1kS8 3000 psi
25. 2 x ¾'' Swagelok to VCR adapters
26. 2x "Helium" flexhose.
27. 2x Brazed VCR to ¾'' pipethread adapters
28. 2x ¾'' Aeroquip Fittings.

A.3 Standard Operating Procedure for the Cryomagnet at Oak Ridge National Laboratory: March 2023

MAGNETIC FIELD SYSTEM COOLDOWN PROCEDURES		
BL13NEDM-31-PCD10000	**Prepared by:** *A. Aleksandrova & B. Filippone*	**Checked by:** *A. Saunders*

0. Introduction

The nEDM experiment at SNS will conduct a series of cryogenic tests of the Magnetic Field System (MFS) prior to the installation of the actual experiment. These cryogenic tests will be performed initially without beam in order to first test the cryogenic performance of the cryostat and associated cooling systems of the MFS. Later, with the neutron beam, additional cooldowns will be performed to test the neutron transmission and transport of neutron polarization through the MFS and its vacuum cryostat. The MFS and its cryostat are comprised of multiple layers, including the coils that will apply the very small external magnetic field to the ultimate experiment, the superconducting lead shield that will help exclude unwanted magnetic fields, and the insulating layers that will enable the internal components to stay in a superconducting state.

The MFS cryostat is cooled by a combination of liquid nitrogen shields and a pair of Cryomech PT420 pulse-tube cryocoolers. Cryogenic testing will be performed in SNS Bldg 8713 with cryogenic operation supervised by users from California Institute of Technology. The system is monitored with a PC based Unix program (Slow Control Readout) that monitors pressures, temperatures, gas flow rates, etc. A detailed P&ID diagram BL13NEDM-31-G8U-8713-A10000 documents the hardware components and helps inform the "nEDM@SNS Design Analysis and Calculation – Magnet Test Vacuum and Cryogenic Overpressure Protection" document: BL13NEDM-31-DAC10001. This system was operated at Caltech for more than 2 years as various components came online and were tested. A series of four cooldowns were performed there to demonstrate performance prior to shipping to SNS last year. Details on the components of the system are described in the "nEDM@SNS Magnetic Field System (MFS) Commissioning Hazard Analysis" document: BL13NEDM-31-ESH10001 The procedures for operating the cryostat and its associated vacuum and cooling systems are described below.

1. Vacuum Procedure

Pumping on Inner Magnet Volume (IMV) and Outer Vacuum Can (OVC)

1. Start with all IMV and OVC vacuum valves closed
2. Power-up the scroll pump (rough pump in P&ID, see Fig. 2) and open HA-002, HA-003, HA-004, HA-005, and gate valve CV-001 (by pulling the red button, marked 1 in Fig.1) to pump on the IMV and OVC to rough vacuum.
1. After the pressure drops below 0.5 torr [see P1:OVC Vacuum (CG A) and P1: 972B DualMag on IMV in slow controls]
    - Connect and turn on the the chiller for the turbo pump. Wait for the temperature of the chilled water to reach 17°C.
    - Close HA-003.
    - Open the gate valve
    - Flip up both of the override (bypass) switches, marked 4* in Fig. 1, on the gate valve control box to “Open”.
    - Turn on the turbo pump by pushing the green button marked 3 in Fig. 1.
    - For overpressure safety, remove all bolts from the lift-plate which is labeled and is the 10.25” flange that is above and beam left of the large beam entrance flange. Confirm that drop lines are connected.
    - **Note:** Both of the override (bypass) switches can be flipped down after pressure in the OVC [see P1:OVC Vacuum (CG A) in slow controls] drops below 0.1 torr.
    - **Note:** Once the pressure is below 1e-4 torr, the turbo power should stay <50 W (see Turbo Power in slow controls) If it is noticeably higher, there could be a leak in the system.
    - **In case of emergency:** you can close the gate valve and shut down the turbo by pressing the red buttons marked 1 and 2 in Fig. 1.

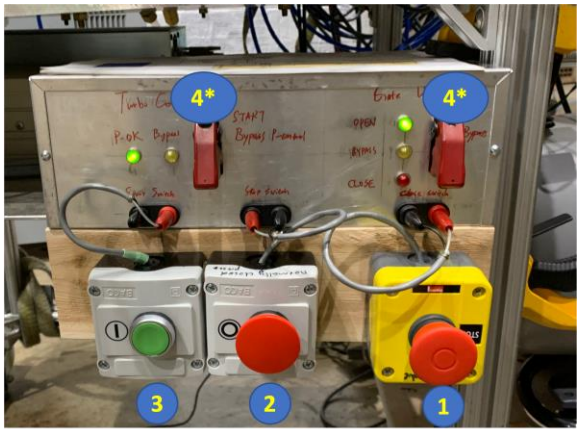

Figure 1: Gate Valve Control Box

2.0 Cooldown Procedure

Initial Checklist (prior to beginning cooldown):

1. Be sure that HA-005 and HA-006 are open and install tag to indicate that these valves must remain open during cooldown for overpressure protection.
2. Confirm OVC and IMV pressures are below 2 x 10^{-4} torr.
3. Confirm lift plate (PSV-003 in P&ID) bolts are removed.
4. Confirm LN2 house exhaust valve open and tagged that valve must remain open during cooldown.
5. Confirm that Mu-metal Shield is closed (Mouse Hole covered with Mu-metal) and marked with appropriate signage to prevent any entry inside. Should entry inside the Mu-metal shield be needed during cooldown, SME will need to approve new procedures.

Note: Once cool-down begins HA-005 and HA-006 must remain open for IMV overpressure protection. Confirm that tag is installed to indicate this.

2.1 Preparing the Cryomech Vessel

1. Pump on the helium circulation line in Cryomech vessel and on IMV for 2 hours.
2. Fill the helium circulation line 3 times with Ultra High Purity (UHP) He to 70 psig and vent (purge) down to 10 psig.
3. Charge the helium circulation line with 30 psig pressure of helium gas. Check how the pressure holds in the helium circulation line over night.
4. Connect the large compressors (CPA1114) to the Cryomech vessel.

   Note: If the helium charging is not done through the Buffer tank, e.g. if Cryomech is servicing the unit and wants to charge from a gas bottle, then we will need to review their process and protections with our pressure safety SMEs

2.2 Start Cryomech Compressors and Cold Heads

1. Turn on chilled water for the Cryomech compressors.
2. Close valve HA-303 to isolate the He buffer tank from the IMV He circulation.
   Note: Buffer tank must be closed off before turning on the CP103. Otherwise, it will overcharge the IMV circulation line to too high a pressure.
3. Fully close the IMV He circulation bypass valve HA-307.
4. Fully open the needle valve on the Cyomech vessel for the IMV He circulation HA-301

5. Switch on the "MAIN BREAKER" on each compressor.
6. Turn on the Cryomech cold head compressors A and B by pushing the green "ON" button.
7. Turn on the IMV He circulation compressor CP103 by pushing the green "ON" button.

Note: During the entire duration of the cooldown, you must maintain the pressure difference between P high and P low above 75 psid to allow for proper oil flow in the circulation compressor (CP103). To do so, charge the IMV He circulation line with helium from the buffer volume. Charge P_high to 185 psig and no higher than 200 psig. This will usually need to be done once a day. **Note:** Once final tuning is complete and the IMV is at low temperatures (< 10K) the ideal situation is to leave the buffer tank fully open to the system. This will prevent the pressure from overshooting.

2.3 Start cooling with LN2

NOTE: 1st day need ~ 5 low pressure 160L dewars of LN2. 2nd day needs 4. After LN2 shield gets cold, 1-2 dewars per day are enough to maintain cooling.

1. Confirm that house LN2 exhaust vent (attached to the mezzanine) is opened.
2. Flush the mushroom cooling line with one dewar of LN2.
3. Flush LN2 belt tank with one dewar of LN2.
4. Keep flushing the LN2 belt tank until the LN2 starts to accumulate (see LN2Shield TankLevel Sensor in slow controls and LT 101 in P&ID).
    - When filling the belt tank, fill to ~36pF. **Note:** Stop fill before 37pF.
    - A typical fill of the belt takes ~1hr.
    - **NOTE:** The LN2 level sensor baseline is 31.3 pF which corresponds to 0.5" above the bottom of the belt tank. The increment is 0.8 pF/inch. 1 inch of LN2 = 12 Liters.
5. Keep flushing the mushroom with 1 dewar of LN2 per day. Tune the flow of the LN2 for a slow flush.
    - **Note:** It is OK to let the mushroom warm up slightly while changing out the LN2 dewar.
6. Once a day charge the He circulation line with UHP helium from the buffer tank to P_high ~ 185psig. During the day, check that the ΔP = (P_high – P_low) of the He circulation compressor (CP103) is above 75 psid. If it drops below that, charge more helium from buffer tank.

- If you need to charge more gas into the buffer tank:
  - Be sure that line from UHP bottle has remained pressurized (otherwise the line will need to be filled and purged 4-5 times.
  - Close the buffer volume tank to circulation line HA-303, indicated with red in Fig.3.
  - Open the fill valve HA-305 and add ~2 psid to buffer tank.
  - Close valve HA-305 to gas supply.
  - Slowly open valve HA-303 to the circulation system. The rate of pressure increase should be <5 psi/min. Close valve when finished.
  - When buffer tank valve is fully open, keep P_high – P_low > 75psid. If the difference is too low, start closing the inline needle valve above the Cryomech vessel, indicated with green in Fig. 3.

7. Twice daily, check the LN2 shield tank level sensor (see LN2Shield TankLevel Sensor in slow controls and LT 101 in P&ID). **Note:** Usually it is sufficient to fill the belt tank once daily. You can estimate the refill time based on the level sensor data from the previous day.

8. During the cool down, the OVC pressure ion gauge [see P1:OVC Vacuum (Ion Gauge)] in slow controls] should stay ~10^{-5} - 10^{-6} torr. If it starts rising rapidly or is too high, check for frosting on the OVC lid flange. The o-ring there can start to freeze due to the dripping from the mushroom cooling lines. Use a heat gun to defrost.

9. Once the temperature of the IMV drops below 70K, exchange gas can be introduced into the IMV. Typically we fill to 7 mtorr of helium gas. To do this close HA-004 and the He gas cylinder and open the needle valve HA-201. Now close HA-001 to isolate the Turbo pump and open HA-003. Slowly open HA-204 to pump out the He line with the scroll pump to below 0.01 torr (see Turbo foreline in slow control) This should only be done for a few minutes so that Turbo doesn't overheat. Now close the needle valve HA-201 and HA-003 and then open HA-001 to continue pumping out the Turbp pump. Open the He gas cylinder and slowly open the needle valve to introduce the He exchange gas up to the desired value, typically < 10 mTorr. You may see the OVC pressure rise due to the introduction of the warm gas releasing some cryopumped gasses. Close the needle valve when you are done and then close HA-204. **Note:** HA-004 must remain closed when exchange gas is in the IMV.

10. Once the temperature of the IMV reaches below 20K see (T27 Outer Wall Bottom in slow controls), one may try to very slowly close the flow meter bypass valve (see HA-302 in P&ID) on the CP103 compressor, indicated with green in Fig. 4, and read the actual flow rate. Open the bypass valve if the flow rate is still too high.

11. Once the temperature of the IMV reaches <10K (T27 Outer Wall Bottom in slow controls), the inline (see HA-301 in P&ID) and bypass needle valves (see HA-302 in P&ID), and the charging/bleeding valve (see HA-305 in P&ID) from buffer volume can be adjusted to achieve the optimum settings (see App 1).

    Inline Needle Valve: Closing the in-line needle valve (see HA-301 in P&ID) will reduce the flow rate and the pressure on the low-pressure side of the circulation compressor (CP103) and will increase the pressure on high-pressure side of the circulation compressor (CP103). **Note:** max (7+17/25)x turns. Each 1/5 turn increase P high sharply by 8 psi and decrease P low by 0.15-0.2 psi

    Bypass Needle Valve: Opening the bypass valve will reduce the flow rate and the pressure on the high- pressure side of the circulation compressor (CP103) and will increase the pressure on the low-pressure side of the circulation compressor. **Note:** max 7x turns. Each 1/5 turn will decrease P high sharply by 3 psi and increase P low by 0.2 psi.

    Buffer Tank: Charge more helium gas to increase both the high and low-pressure sides of the circulation compressor (CP103). Bleeding the buffer tank very very slowly via HA-306 will decrease P_high and P_low.

12. The goal is for the IMV He circulation flow rate to be around 210-230 SLPM, for the T0 of 1st stage to be around 30K (see Cryomech: T0 1st Stg in slow controls), and T0 of the 2nd stage to be around 5K (see Cryomech:T0 2nd Stg in slow controls), and P_low to be about 30psi.

13. **In case of cooling problems:** If the chilled water gets too hot, the SlowControls will display a warning "T Coolant is High"
    - If this is a temporary issue, you can shut down one of the compressors (CPA1114) and run off of one large compressor while the issue is being fixed. → check water filter
    - If the coolant water temperature is still too high, turn off He circulation compressor CP103 followed by the remaining large compressor CPA1114 until the issue is fixed.

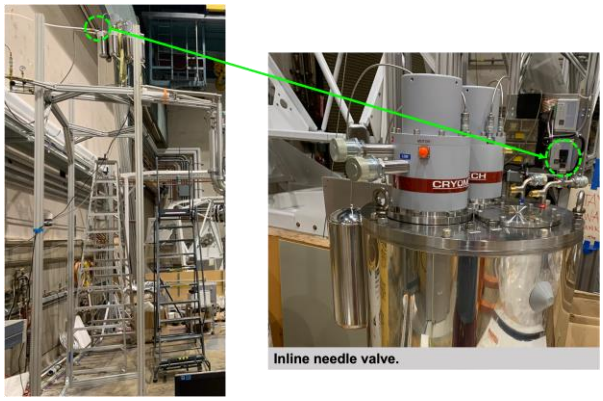

Figure 3: Inline Needle Valve

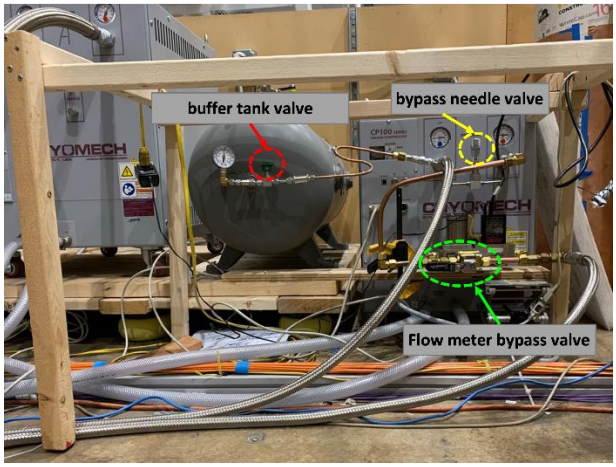

Figure 4: Bypass Needle Valve and Buffer Tank Valve

3. Warm-up Procedure

1. Turn off both Pulse Tube compressers CPA1114. Leave CP103 compressor on.
2. Stop flushing the mushroom.
3. Ensure that control needle valve HA-301 is fully open and circulation bypass valve HA-302 is fully closed.
4. Turn on heater of the 2nd stage and set it to 10W.
5. Turn on heater of the 1st stage and set to 10W.
6. Start pumping out IMV exchange gas of helium with scroll pump when T_IMV ~55K (T27 Outer Wall Bottom in slow controls).
7. Once T_IMV ~ 80K, fill IMV with N2 gas up to 100 torr maximum. **Note:** Flush multiple times first. It is best to flush out the helium gas before it gets absorbed

onto any G10 in the system (applies when B0 is installed in IMV). It will make the next leak check easier.

8. Occasionally pump and refill some N2 gas to help increase the warm-up rate.
9. Once the system is warm and heaters are no longer needed, turn off heaters and stop compressor CP103.
10. Before venting the OVC, install several bolts on the liftplate.

3. Summary of Off-normal/Emergency Procedures

Here we list actions to be taken in case of off-normal or emergency. All are included in the above, but we list them here so workers don't need to read through the full document to perform corrective action.

.

1. **In case of emergency (OVC pressure too high)** you can close the gate valve and shut down the turbo by pressing the red buttons marked 1 and 2 in Fig. 1.
2. **Note:** If the helium charging is not done through the Buffer tank (e.g. if Cryomech is servicing the unit and wants to charge from a gas bottle), then we will need to review their process and protections with our pressure safety SMEs.
3. **In case of cooling problems:** If the chilled water gets too hot, the SlowControls will display a warning "T_Coolant In High":
    a. If this is a temporary issue, you can shut down one of the compressors (CPA1114) and run off of one large compressor while the issue is being fixed. → check water filter
    b. If the coolant water temperature is still too high, turn off He circulation compressor CP103 followed by the remaining large compressor CPA1114 until the issue is fixed.

Sub-Appendix (Alston Croley): Final Descent Process:

Begin by adjusting the inline needle valve and bypass valve to 11/25 and 2 ⅛ turns open, respectively. Then bleed out enough pressure from the lines through the buffer tank to reach approximately 97.5 psig and 9.7 psig for P high and P low. From this point on there shouldn't be much needed in the way of valve adjustments and you will largely just be adding helium to the lines whenever they get low. Watch the descent of the 1st and 2nd stage temperatures as well as the IMV temperature and keep the largest possible temperature difference between the two stages while the IMV is slowly decreasing to match the temperature of the 2nd stage. Based on the past three cool-downs, lower 2nd stage temperatures find stability at higher 1st stage

temperatures. Maintaining a large temperature difference between the two stages will allow the IMV to reach a lower temperature by the time the system reaches stability. If the 1st stage is decreasing too fast and the IMV needs time to catch up to the second stage, slowly leak helium into the lines through the buffer tank. If the leak rate is slow enough the 1st stage temperature should remain roughly constant while the IMV continues to drop. Optionally you can also do this if the cooling is inefficient to save time. When the IMV temperature is around 5.3 K the system is ready to stabilize and you should notice that P high appears to behave asymptotically. At this point pay attention to how the 1st stage temperature changes as you add more helium to the lines, and only add the minimum amount needed to maintain a pressure difference of more than 80 psi and keep the 1st stage temperature above 35 K.

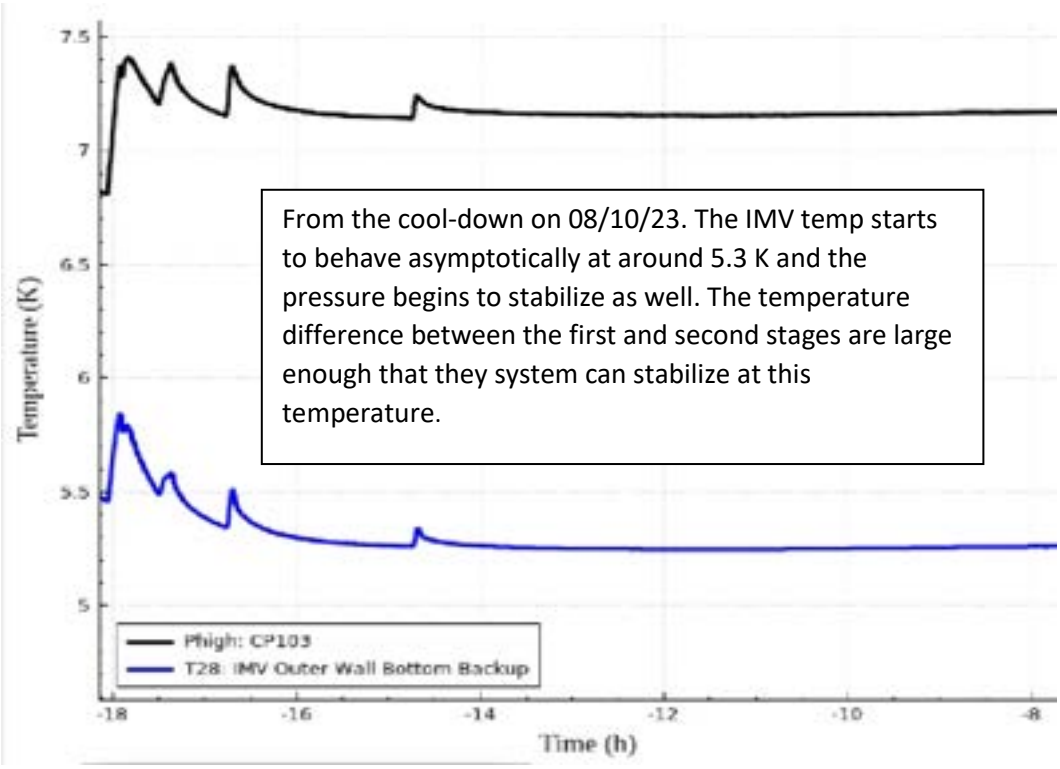

From the cool-down on 08/10/23. The IMV temp starts to behave asymptotically at around 5.3 K and the pressure begins to stabilize as well. The temperature difference between the first and second stages are large enough that they system can stabilize at this temperature.

From the cool-down on 08/16/23. Once again the IMV temperature begins to behave asymptotically at 5.3 K. This time the temperature difference between the two stages is much lower than before and the system cannot find stability at this temperature. The temperature must increase before finding stability.

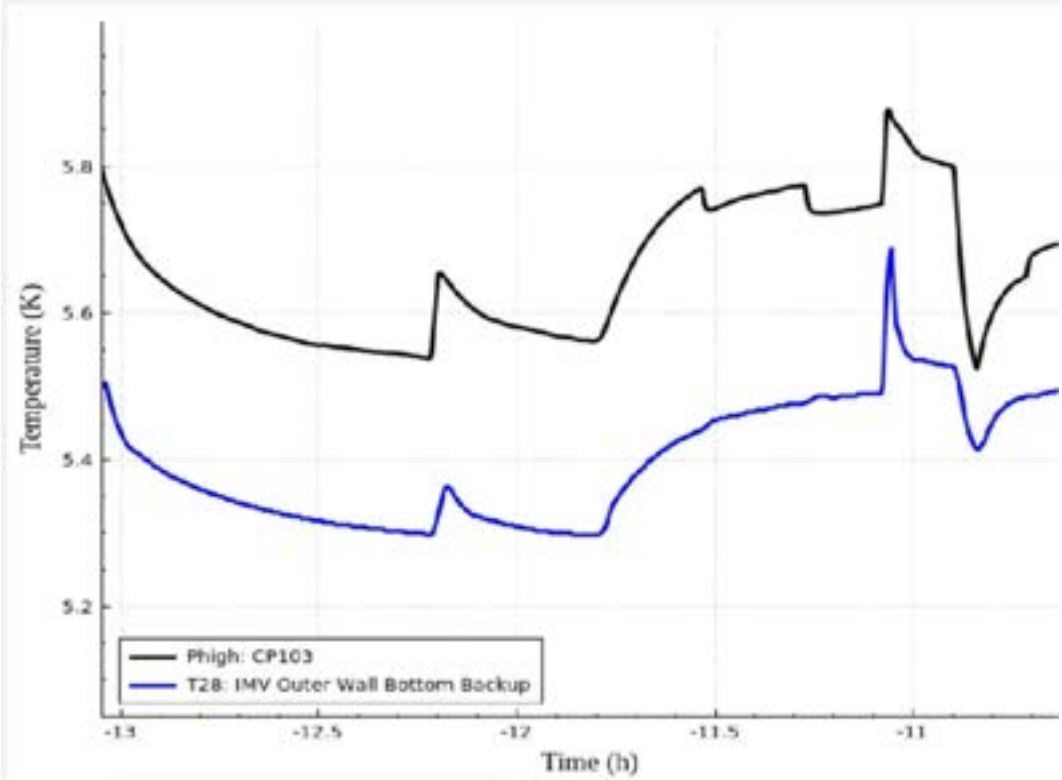

Cryomech test data in the manual suggests we would like to reduce but not necessarily minimize flow rate. We didn't have a flow rate monitor this time, but reading through Wanchun's notes from the 04/22 cool-down a lower delta_P roughly corresponded to a lower flow rate.